THE UNIVERSITY *of* EDINBURGH

POST-OROGENIC TOPOGRAPHY AND SEDIMENT FLUX OF MOUNTAIN-FORELAND SYSTEMS: MIOCENE EROSION AND SEDIMENT YIELD FROM THE PYRENEES

Thomas Bernard

Doctorate

The University of Edinburgh

2020

ABSTRACT

Considerable research has been focused on the syn-orogenic evolution of mountain belts in order to explore interactions between tectonic, climate and surface processes. Comparatively, limited work has been carried on the post-orogenic stage of mountain ranges. Because of the relatively small-sized of the orogen, the good quality of exposure and large volume of dataset, the Pyrenees are a natural laboratory to study orogenic processes. Moreover, the Pyrenees are characterized as a post-orogenic system since at least 20 Ma and constitute a perfect target for this thesis. Our aim in not to solely resolve the post-orogenic history of the Pyrenees, but rather provide an understanding of fundamental behaviours and processes of the late syn- to post-orogenic systems. The purpose of this study is to better constrain the transition from crustal thickening to post-orogenic decay in mountain ranges in term of topographic and sediment flux toward foreland basins and surrounding continental margins. This is achieved through a multi-disciplinary approach combining analyses of low-temperature thermochronological data (apatite and zircon fission track, apatite helium and $^{4}He/^{3}He$ apatite data), topographic analyses from digital elevation model of the Pyrenees and landscape evolution models.

Thermal histories inferred using a similar inverse modelling from pre-existing apatite and zircon fission track and apatite (U-Th)/He data document the syn-exhumation history and reveal the late syn- to post-orogenic transition in the Central Pyrenees. The main exhumation associated with the orogenic growth is diachronous in the Central Pyrenees and younging from north to south. In the Northern Pyrenean zone, the main exhumation occurred during Middle Miocene times (i.e. 40-45 Ma) whereas in the southern Axial Zone, main exhumation is recorded during Oligocene times (i.e. 30-25 Ma). Thermal histories also reveal an abrupt and diachronous cooling cessation across the Central Pyrenees. Cooling cessation, associated with the post-orogenic transition occurred from 36-37 Ma in the northern Pyrenees (Arize massifs) to 23 Ma in the southern Pyrenees (southern Axial Zone). Because of late laboratory difficulties,

$^4He/^3He$ data were not available for the thesis publication. However, implications of these results for potential late post-orogenic exhumation signals are discussed.

Extraction of topographic indices from digital elevation models of the Pyrenees allowed us to observe a systematic correlation between river channel steepness, elevation and rock strength associated to variation of lithologies. Rock strengths were determined using Schmidt hammer measurements. This correlation demonstrates that rock types have affected the topographic development of the Pyrenees since cessation of orogenesis. The landscape of the Pyrenees reveals this behaviour with the main drainage divide tracking the granitoid plutonic massifs which have the highest rock strength. We propose also that the abrupt deceleration of exhumation recorded through thermal histories could be associated with the exhumation of these high resistant plutonic massifs. Landscape numerical modelling confirms that exhumation of harder rocks results in catchment vulnerabilities during transient landscape response and that readjustment is principally made by divide migrations. Other mountains range as the Western European Alps show similar drainage divide patterns.

Analysis of a coupled mountain range and foreland basin model reveal that early post-orogenic sediments of the foreland basin should drape and seal structures of the thrust wedge. This trend is explained by a continuation of highly eroded sediment flux from the range and a diminution of accommodation space in the foreland basin because of reduction and cessation of lithospheric flexure. The northern Aquitaine retro-foreland basin shows similar evidence with Early to Middle Miocene sediments draping the Sub-Pyrenean Zone and North Pyrenean Thrust Belt. Alluvial cover of the thrust-wedge during the post-orogenic stage in combination with low lithosphere elastic thickness and the presence of resistant lithologies have important implications for topographic survival. With this three conditions, landscape evolution models allow long post-orogenic persistence of topography and relief. Our model results suggest also that higher sediment flux should be recorded in surrounding continental margin depocenters during the post-orogenic stage. The Pyrenean system confirms again this trend with an increase of sediment accumulation in the Bay of Biscay.

Overall, this multi-disciplinary study brings new constraints on how the landscape of an orogenic system evolves during the post-orogenic decay stage. We highlight multiple interactions and coupled dynamic from the mountain range toward surrounding foreland basin and continental margin.

ACKNOWLEDGEMENT

I would particularly like to express my gratitude to my main supervisor, Hugh Sinclair, for his support, advice and encouragements. He has always been available when needed without being intrusive in my works. I would like also to express my gratitude to Mary Ford for continued assistance throughout the PhD.

I have greatly benefited from different persons for their helps and allow me to publish papers during this thesis. First, Frédéric Christophoul gives me insightful knowledge on the geology of the Aquitaine Basin. I also thank Mark Naylor for his suggestions about numerical modelling. I thank Simon Mudd for his expertise on topographic analyses. Finally, I thank Boris Gailleton for his help with the software LSDTopoTools and with some python coding.

I would like to offer my special thanks to Symeon Makris for his help during fieldwork and really appreciate our time in the Spanish and French Pyrenees. He is a really strong man and can carry by himself down the mountain, four bag of samples each weighing 5 to 7 kilograms.

There is several others persons who help me during this PhD and need acknowledgements. First, thanks to Kerry Gallagher who have always answered very rapidly to my questions about thermochronology and more particularly about the QTQt software. I would like also to thank Philippe Steer for very interesting discussions which initiate some important works in my thesis. Thanks go also to Linda Kirstein, Odlin Nicholas, Jürgen Schleppi and Chrystiann Lavarini for assistance during mineral separation process at the University of Edinburgh. I thank Charlotte Fillon and Arnaud Vacherat for discussion and ideas about low-temperature thermochronology of the Pyrenees. I want to thank also Paul Angrand for discussion on the dynamic of the Aquitaine Basin. Thanks go to Laura Quick for introducing me about grain size distribution sieve analysis. I thank Peter van der Beek for discussion and precious time spend on the field to find the best samples. Finally, I would like to offer my gratitude to David Shuster for laboratory

technical assistance with $^{4}He/^{3}He$ thermochronology.

I would like to show my greatest appreciation to all the persons of the Orogen team. That includes too many names to be listed but presentations and discussions during workshops, conferences or summer schools help me to improve my works.

Finally, I want to thank also all the person of Land Surface Dynamic team of The University of Edinburgh. Except for those already thanked above, that includes Mikael Attal, Fiona Clubb, Elizabeth Dingle, Emma Graf, Guillaume Goodwin, Callum Strong, Justine Domingo, Louis Kinnear, Marina Ruiz Sanche-Oro and Noorzalianee Ghazali. Again discussion, particularly during "Friday Lunch Talk" were the best opportunities to present my works, have feedback and improve my works.

TABLE OF CONTENTS

Chapter I

GENERAL INTRODUCTION

I.1 Scientific Background

I.1.1 Thesis framework: The Orogen research project

This thesis is part of the Orogen research project resulting from the collaboration between the INSA (French National Geosciences Institute), the BRGM (French Geological Survey) and TOTAL. Main challenges of the project is to understand orogenic processes through the different evolutional stages of mountain belts: 1) Reactivation of oceanic and rift inheritances during subduction and pre-collision orogeny; 2) Collision stage and foreland basin emplacement and 3) Post-orogenic mountain dismantling and lithospheric readjustment. The Orogen research themes are focused on the Iberia area and employ a multi-approach methodology to answer problems with field geology, thermochronology, plate kinematic restoration, lithosphere and basin scale passive seismic images, geochemistry, seismic interpretation and numerical modelling. This project focuses on the late to post-orogenic evolution of the Pyrenees and its associated retro-foreland basin, the Aquitaine basin in terms of exhumation history, topographic evolution and sedimentary fluxes.

I.1.2 Thesis context

Evolution of mountain systems, including surrounding foreland basins, results from the long-term competition between tectonics and surface processes linked to climate (Beaumont et al., 2000; D. Davis et al., 1983). It has long been recognised that the topographic evolution of active mountain ranges reflects the multiple interactions and feedback between tectonics, surface processes and topography (Champagnac et al., 2012).

Numerous studies have investigated these interactions between tectonics, climate and erosion on mountain ranges such as the Andes (Lamb & Davis, 2003; Montgomery & Brandon, 2002), New Zealand (Koons, 1990; Norris et al., 1990) or Taiwan (Deffontaines et al., 1994; Suppe, 1981) where strong climate condition are present and tectonic active.

However most of the mountain ranges in the world appear to be in various stages of post-orogenic decay, such as the European Alps, Urals, Caledonides, Appalachians and Pyrenees. The landscape evolution of these decaying mountains that evolve from localised fault-controlled rock uplifted to more regional isostatic controls, should appear simple with progressive and relatively uniform erosion resulting in a general lowering of both elevation and topographic relief (Baldwin et al., 2003). However, in a number of examples, post-orogenic systems suggest complex interactions with their associated foreland basins (Tucker & van der Beek, 2013).

Sediment production on Earth is dominated by the erosion of active mountain ranges, therefore, orogenesis should correlate with maximum sediment flux to continental margin deltas. However, foreland basins located on both sides of the range act as traps for the erosional efflux. Model predictions indicate that the majority of sediment is released as shortening decelerates, leading to post-orogenic rebound of the foreland basin. The erosional products of the mountain range are combined with the sediment eroded from the foreland basins to generate increased sediment flux to continental margins.

Underpinning the transition to a post-orogenic state is the competition between erosion and crustal thickening; the balance of these processes determines the timing and magnitude of isostatic rebound and hence subsidence versus uplift of the foreland basin. It is expected that any change in the parameters controlling the balance versus crustal thickening will impact the topographic evolution and sediment flux from mountain ranges and foreland basins to surrounding continental margins.

I.1.3 Thesis chart

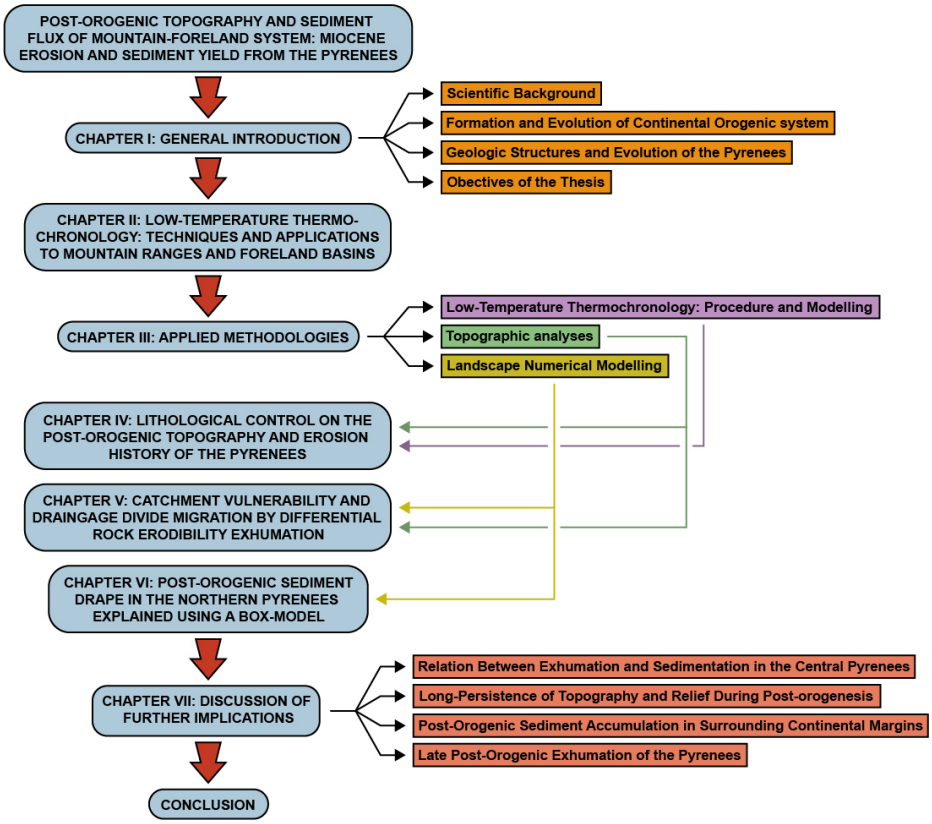

Figure I.1: Thesis chart

I.2 Formation and Evolution of Continental Orogenic System

I.2.1 Thrust wedge mechanism

The development and formation of small mountain ranges by plate convergence and continental collision have been approximated by the Critical Coulomb wedge model that allows an explanation of the first order features of "thrust wedge" (Chapple, 1978; D. Davis et al., 1983). Tapered wedge geometry can be defined as the gentle dip of a basal detachment of a mountain range into its interior, combined with the mean topographic slope dipping in the opposite direction. Thrust wedges of continental crust are considered mechanically similar to oceanic accretionary wedges. It can be compared to the development of a pile of sand pushed along by a bulldozer. Elliott, (1976) firstly proposed that an orogenic prism which develop as a wedge with a regional surface slope is the main factor controlling the gravitational forces of a thrust belt. The regional average shear stress τ of a thrust sheet of thickness H is equal to the down-surface slope stress $\rho g H$ plus the regional deviatoric stresses induced through tectonics. This statement differs from the accepted mechanism of moving thrust by "gravity gliding" where 1) thrusts move entirely under the influence of gravity, 2) at the time of motion, thrust planes dipped downhill in the direction of motion, and 3) that at their trailing edge the thrusts cut upsection towards the surface.

Chapple, (1978) proposed a new model which can be applied to a variety of tectonic situations. The theory of this model is based on three fundamental basis: 1) the basal layer of this treatment has plastic material rather than frictional behaviour. 2) The basal layer is chosen to be considerably weaker than the overlying section. 3) The model treats explicitly the wedge shape of the sedimentary prism and the observed shortening of this wedge.

Following this framework, Davis et al., (1983) and Dahlen, (1984, 1990) introduce the concept of the tapered thrust wedge, where the plastically deforming rock mass with a Coulomb yield stress slides over an undeformed lower boundary. The material within the wedge deforms until a critical taper is attained, after which it slides stably and continues to grow at constant taper as material is added to the system (Davis et al., 1983). Taper angle can be reduced at any time by erosion and sediment transport away from the surface of the thrust wedge or though extension on the wedge. The

entire system can be view as a wedge of deforming rock on the verge of failure which counteracts the impact of frontal accretion and erosion by internal thickening in order to maintain a stable taper. Deformation of rocks is assumed to follow a Coulomb criterion which link the normal and shear stresses. The Coulomb criterion for shear traction at failure is:

$$\tau = S_0 + \mu(\sigma_n - p_f) \tag{I.1}$$

where τ is the shear traction; S_0 is the cohesion; μ is the coefficient of internal friction $\mu = tan\phi$; σ_n is the normal stress; and p_f is the fluid pressure. The taper angle of a thrust sheet is the combination of the mean surface slope α and the dip angle of the basal detachment β. Through the wedge act three main forces which determine the critical taper: the gravitational body force F_g, the compressive traction F_s and the surface force on the base F_b (Figure I.2). By balancing these three forces, the approximate critical taper equation for a dry sand wedge in front of a bulldozer is (Dahlen, 1990):

$$\alpha + \beta = \left(\frac{1 - sin\phi}{1 + sin\phi}\right)(\beta + tan\phi_b) \tag{I.2}$$

Where α is the mean topographic slope; β is the basal slope; ϕ is the internal angle of friction of the thrust wedge; and ϕ_b is the friction angle for the lower detachment surface. Equation 2 allows a determination of a combination of different $\alpha$and β angles and to define different domains. Where the wedge is characterised as sub-critical, internally thickening occurs before sliding on the detachment. Where the wedge is characterised as internally stable, the wedge slides on the basal detachment. Where the wedge is characterized as critical, sliding occurs and the wedge propagates.

I.2.2 Doubly vergent thrust wedges

The major assumption for the Critical Coulomb tapered wedge model where, simply, a pile of sand is pushing by a bulldozer is that the height and character of the rear of the wedge is defined by a rigid backstop. In natural settings, an orogenic wedge is built from the subduction and collision of two plates and causes the development of a doubly vergent thrust wedges where two critically tapered wedges back-to-back to one another is simulating a small mountain range. The polarity of subduction of the mountain belt will determined and differentiate the two opposing thrust wedges. The wedge and associated foreland basin situated above the subducting plate are referred

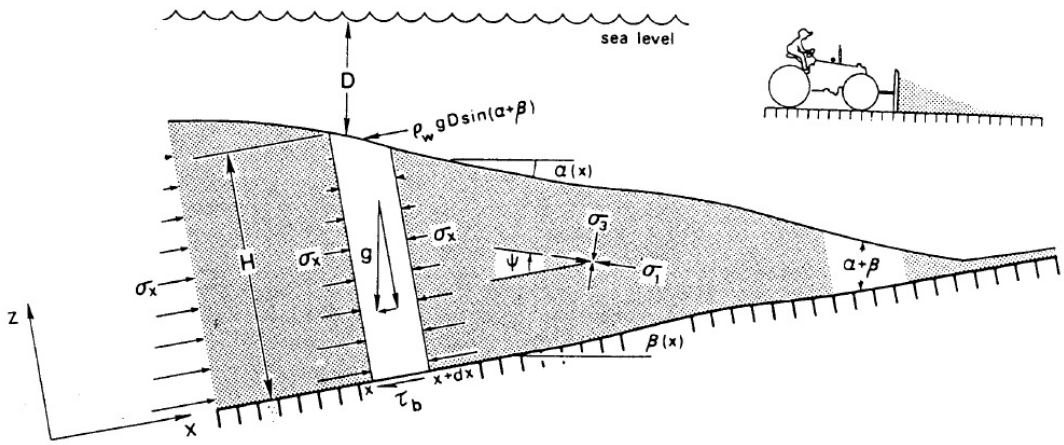

Figure I.2: Schematic diagram of the forces acting on a wedge subject to compression on the verge of Coulomb failure throughout from Davis et al., (1983).

as the retro-wedge and retro-foreland basin while those above the overlying plate are referred as pro-wedge and pro-foreland basin (Figure I.3).

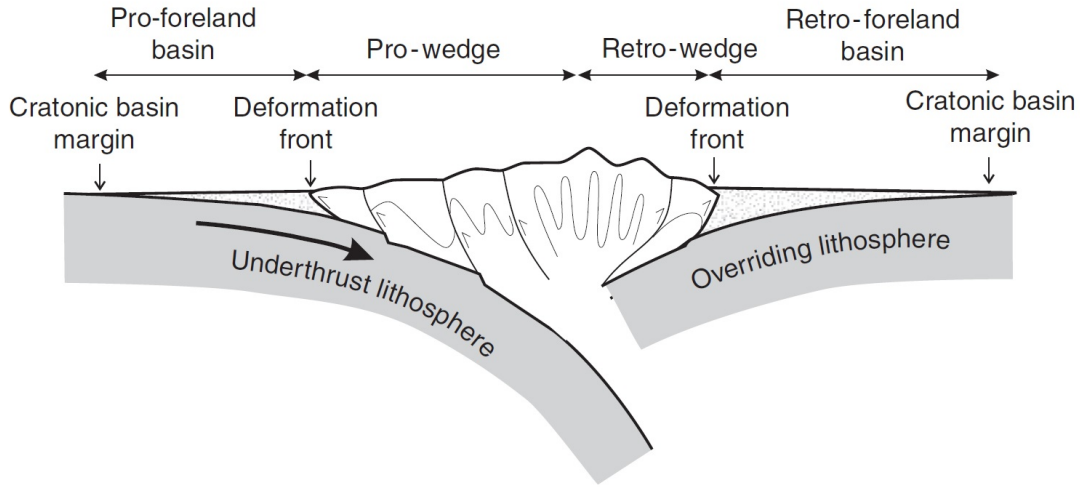

Figure I.3: Schematic representation of a doubly-vergent orogen at steady-state showing the different subdivision of foreland basins and wedges from Naylor and Sinclair, (2008). The pro-foreland basin and pro-wedge are situated over the subducting slab and the retro-foreland basin and retro-wedge are situated on the over-ridding slab.

Modelling of a doubly-vergent wedge was first performed by Willett et al., (1993). The position where the subducting plate meets the overlying plate is the interpolate convergence point, singularity or S-point (Willett et al., 1993). Modelling shows that a Coulomb crustal layer subject to basal velocity boundary conditions passed through

three stages of orogenic growth (Figure I.4) (Willett et al., 1993): 1) block uplift bounded by step-up shear zones rooted at the singularity point. 2) Development of a low-taper wedge over the underthrusting mantle plate and defining the pro-wedge. 3) Development of a low-taper wedge overlying the overthrusting mantle plate and verging in the opposite direction. General direction of material moving associated to these different stages implies that the majority of material is accreted into the pro-wedge with little accretion in the retro-wedge. This lead to a general flux of material coming from the pro-side to the retro-side and forming an important asymmetry in the system. The pro-wedge exhibit a minimal critical tapered angle and the retro-wedge present a maximal critical tapered angle (Dahlen, 1984; Willett et al., 1993). These differences between the pro- and retro-side of the orogen will have an importance for the different foreland basins. The basin overlying the subducting plate will have a different history than the basin overlying the opposite plate.

The asymmetry inferred from numerical modelling (Willett et al., 1993; Willett et al., 2001) for mountain range with a frontal accretion component is consistent with natural mountain ranges. Mountain ranges around the world such as Taiwan, Southern Alp of New Zealand, and the Pyrenees exhibit a notable asymmetry in their geomorphology. The main drainage divide of mountain ranges provides generally a strong first order boundary which divides the pro- and retro-wedge side of the range. Drainage divides in doubly vergent mountain ranges are rarely stationary, but migrate through time depending on the controlling forces of tectonics, climate and underlying geology. General evolutionary models coupling tectonics and surface processes predict the development of a roughly straight drainage divide generally parallel with the mountain front and tracking the thickest part of a doubly-vergent wedge located above the S-point (Koons, 1990). The exact location of the drainage divide during orogenesis fluctuates according to the relative proportions of frontal accretion and underplating (Willett et al., 2001). Frontal accretion will tend to push the drainage divide toward the retro-side of the orogen. Tectonics play an important role in determining the position of the drainage divide but studies show that the climate can also alter this position, either by enhancing or acting against the tectonic signals (Koons, 1989; Willett, 1992).

The different states in the evolution of an orogen have been defined by Jamieson and Beaumont, (1988) based on the relative rates of mass loss and mass addition. These states are monitored by foreland basins and their sedimentary record. The first stage

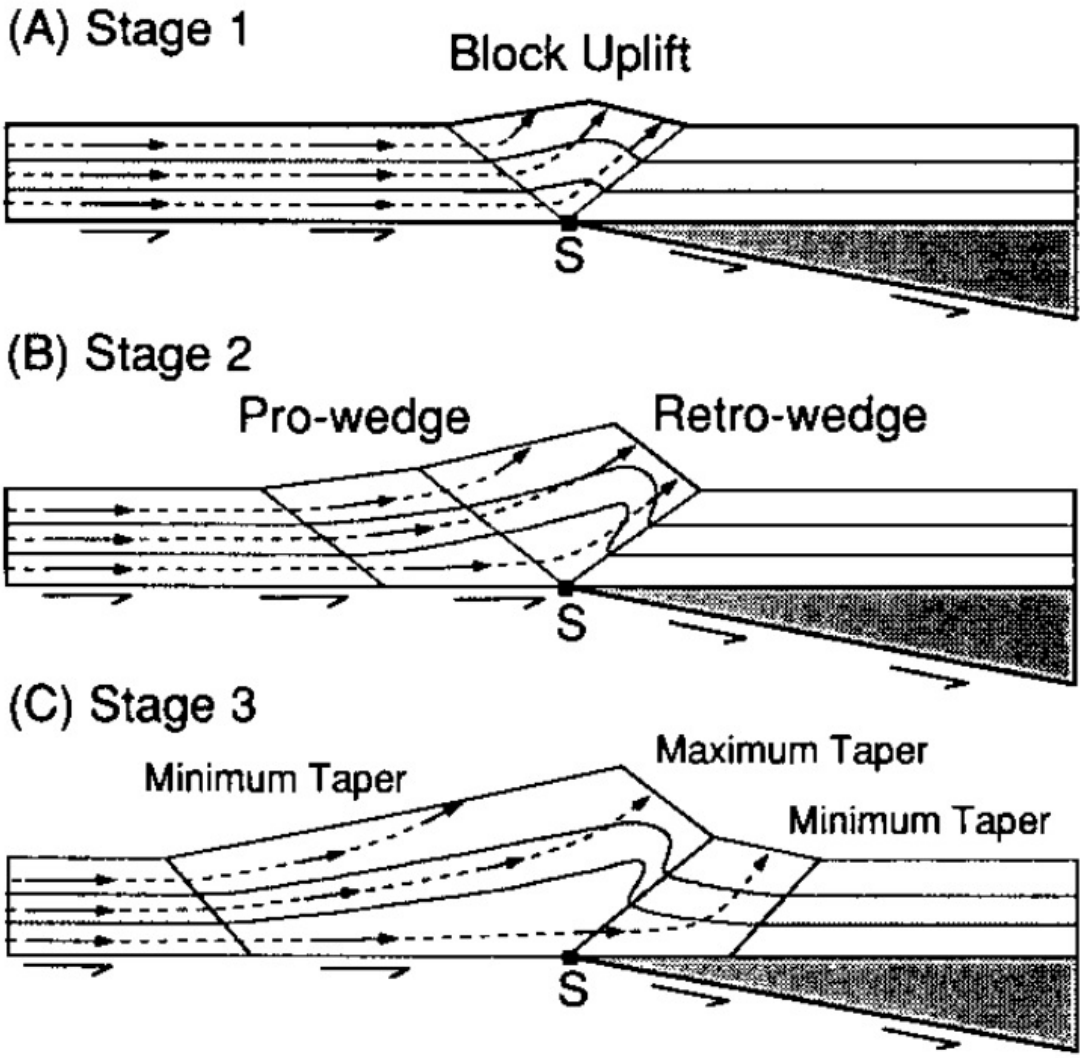

Figure I.4: Model showing the different stages of development in the evolution of a simple doubly-vergent wedge by (Willett et al., 1993): (A) Block uplift bounded by step-up shear zones. (B) Development of a low taper wedge over underthrusting plate. (C) Development of a low taper wedge over overthrusting plate and verging in opposite direction. S = Singularity point.

corresponds to a "constructive state" where mass addition is greater than mass loss (accretion rate is superior to erosion rate). During this phase, the overthrust wedge thickens, surface elevation increases, the deformation front advances rapidly and flexural isostatic adjustment of the orogen increases the depth of the foreland basin (Jamieson & Beaumont, 1988; Stockmal & Beaumont, 1987; Stockmal et al., 1986). The second stage is referred as "steady state" and corresponds to a stage of equilibrium where the mass removed by erosion balances the mass added by accretion. Internal deformation is active and allows the critical topography to be maintained at the same rate as erosion reduces topography. As the mass of the orogen stays constant, the retro-foreland basin remains in equilibrium and sediments eroded form the orogen bypass the basin because of no longer subsidence. For the pro-foreland basin, subsidence continue due to ongoing convergence. The "destructive state" is characterized by greater mass loss due to erosion than mass addition due to crustal thickening. During the destructive phase the topographic load of the orogen decreases and isostatic uplift results in erosion of the foreland basin (Cederbom et al., 2004). The orogenic destructive state can combine erosion and crustal extension. If erosion is the dominant process, exhumation of the orogen will equal the amount of predicted from the uplift of the foreland basin. However, if extensional tectonics is the dominant process, the orogen will record less erosion than predicted from the uplift of the foreland basin (Jamieson & Beaumont, 1988).

I.2.3 Foreland basins

Foreland basins correspond to sedimentary basins located on the continental lithosphere at the outer edge of the mountain range and formed synchronous to the wedge development (Dickinson, 1974). Formation of foreland basins result from the increasing load apply to the underlying lithosphere because of crustal thickening in the range. Regional isostatic compensation by lithospheric flexure creates a flexural depression that is deepest at the termination of the wedge. Their dimensions perpendicular to the mountain front range from 100 to 300 km. The shape of foreland basin is controlled by topography, internal density variation, flexural parameters of the lithosphere and other bending forces (Beaumont, 1981; Jordan, 1981). The most important parameter for the lithospheric flexure is the elastic flexural rigidity D (Karner & Watts, 1983; Watts, 2001):

$$D = \frac{ET_e^3}{(12(1-v^3)} \tag{I.3}$$

Where D is the flexural parameter (Nm); T_e is the equivalent elastic thickness of the lithosphere (km); E is the Young's module and v is the Poisson module. On the above equation, T_e is the main parameter which controls the flexure of the lithosphere and the shape of the basin. For example, if T_e is high, the rigidity of the lithosphere will be important leading to the development of a wide and shallow basin, as in the Appalachians where T_e 100 km (Watts, 2001). Inversely, if T_e is low, the basin will be deep and narrow, as in the southern Pyrenees, where T_e of the Iberian plate is 20 km (Zoetemeijer et al., 1990). However it's still unclear whether the long-term evolution of the lithosphere is better approximated by a visco-elastic, temperature dependent rheology (Beaumont, 1981) or by a simple elastic case. Present-day plate rigidities vary spatially along-strike of individual foreland basins as estimated from gravity data (Stewart & Watts, 1997). Spatial variability in rigidity has been recorded from a number of basins resulting in along strike variations in basin subsidence. An example of along-strike subsidence variability is the Bermejo retro-arc foreland basin of Argentina (Cardozo & Jordan, 2001). Foreland basins develop over continental lithospheres, which evolve through time with associated variation of flexural rigidities through time. Flexural rigidities variability though time have been interpreted for the Chaco foreland basin of Bolivia (Prezzi et al., 2009).

Foreland basins are classically subdivided into "peripheral" foreland basins that correspond to basins located on either side of a collisional mountain range and "retro-arc" foreland basin located behind a magmatic arc fed by oceanic subduction (Dickinson, 1974). Peripheral foreland basins located from the different sides of the range at the outboard of the pro- or retro-wedge may evolve differently. Johnson and Beaumont, (1995) used the term "pro-foreland basin" and retro-foreland basin" to differentiate the two foreland basins situated on either side of the doubly vergent thrust wedge. Using a coupled tectonic and surface process numerical model, they explore the effect of asymmetric precipitation across the range. Naylor and Sinclair, (2008) demonstrate the important difference of stratigraphic architecture, chronostratigraphy, and subsidence rate between the pro- and retro-foreland basins. Subsidence in the pro-foreland basin is principally controlled by the subduction of the lithosphere regardless of the growth of the pro-wedge which contrast with the retro-foreland basin where it is a function of the growth of the retro-wedge. This mean that the duration of preserved stratigraphy in the pro-foreland basin is determined by the width of the basin divided by its subduction

velocity. The result is that the undeformed stratigraphic infill of the pro-foreland basin is usually only a fraction of the history of the orogenesis (Figure I.5) (Naylor & Sinclair, 2008; Sinclair, 2012). In contrast, retro-foreland basins record the full history of orogenesis with a complete record of the constructive state and a condensed record of the steady-state (Figure I.5). An example of a pro-foreland basin is the Gangetic foreland basin (Lyon-Caen & Molnar, 1985) where the oldest sediments preserved have an age of 16 Ma. Another example is the Ebro pro-foreland basin of the Pyrenees which records only Eocene stratigraphy (deformed older and younger stratigraphy are preserved in the wedge top basin) (Vergés et al., 1998). In contrast, retro-foreland basins experience a different history. The Aquitaine retro-foreland basin north of the Pyrenees records a full sedimentary record of orogenesis from early Maastrichtian times to Miocene succession (Ford et al., 2016).

Subsidence has been widely constrained from foreland basins across the world. Foreland basin subsidence is mainly driven by the flexure of the continental lithosphere in response to topographic and subsurface loads formed during mountain building (Beaumont, 1981; Jordan, 1981; Karner and Watts, 1983). Additionally, subduction of the underthrust continental contributes to basin subsidence by advecting the basin down the flexure profile (Jordan, 1981; Naylor & Sinclair, 2008; Allen et al., 1986). Studies have demonstrated that the tectonic subsidence of foreland basins tend to accelerate through time (P. A. Allen & Allen, 2005; Angevine et al., 1990; DeCelles & Giles, 1996; Xie & Heller, 2009). Basin subsidence accelerations are then used to indicate the onset of orogenesis (Burgess & Gayer, 2000) and to indicate the initiation of the foreland basin. Sinclair and Naylor, (2012) performed a compilation of subsidence rate of foreland basins (Figure I.6). Convex-upward subsidence curve patterns of accelerated subsidence (Ebro and Carpathian basins) are the generally accepted model for pro-foreland basins. They demonstrate that these basins record rapid (>0.5 km/Ma), short-lived (<20 Ma) subsidence such as western Taiwan, South Wales or Carpathian. In contrast, other basins record a slower subsidence (<0.5 km/Ma) with more punctuated histories lasting from 40 to about 80 Myrs such as the Alberta, Aquitaine or North Balkan basins. Tectonic subsidence in retro-foreland basins increase during the constructive orogenic phase and become constant during the steady orogenic state. The transition from the constructive to steady state phase during orogenesis can then be recorded by a flattening of the tectonic subsidence curves (Sinclair & Naylor, 2012). For the majority of foreland

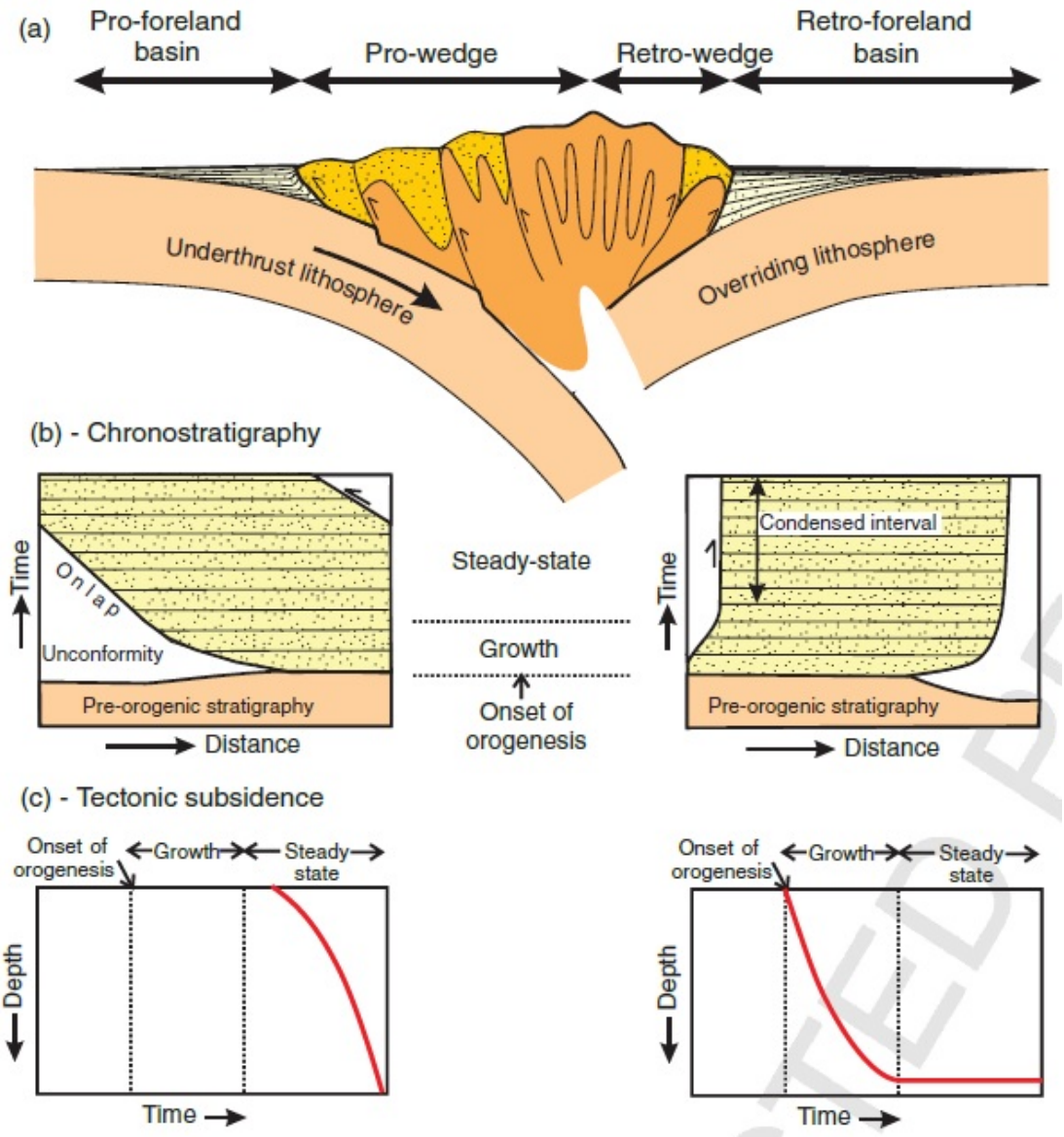

Figure I.5: Diagram figure showing contrasting characteristics of pro-foreland and retro-foreland basins from Sinclair, (2012). (a) Schematic representation of a doubly-vergent orogen and associated foreland basins. (b) Chronostratigraphy preservation into pro- versus retro- foreland basins. The pro-foreland basin records relatively limited chronostratigraphic interval relative to the retro-foreland basin. (c) Theoretical curves of the tectonic subsidence for pro- versus retro- foreland basins.

basins, the load of the topography of the mountain range and of the sediments are responsible for the flexural profile of the associated basin (Karner & Watts, 1983). In some cases, the topographic load is insufficient to explain the flexure. Other processes that can enhanced flexure of the lithosphere are: (i) retreat or "rolling back" of the underlying plate as in the Apennines or Carpathians (Royden, 1993; Royden & Karner, 1984); (ii) in-plane stress (Peper et al., 1992); (iii) negative dynamic topography induced by mantle flow forced by oceanic plate subduction (Burgess et al., 1997; Mitrovica et al., 1989).

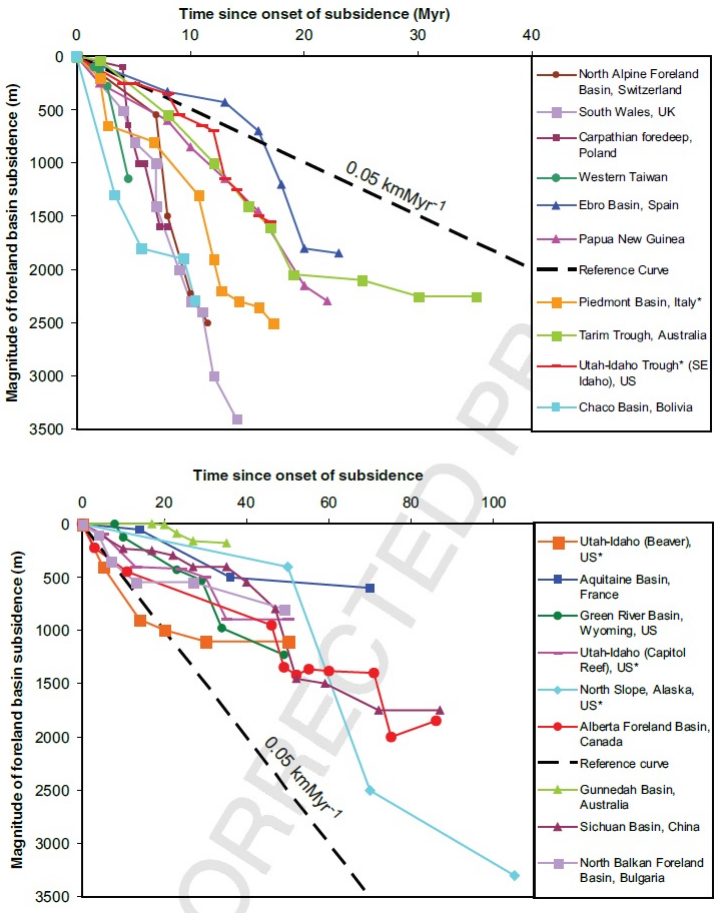

Figure I.6: Compilation of subsidence histories for different worldwide foreland basins from Sinclair, (2012). Top panel correspond mostly to pro-foreland basins characterized by rapid subsidence and lower panel correspond mostly to retro-foreland basins characterized by slow subsidence.

I.2.4 Tectonic, surface process and climate interaction.

The topography of mountain ranges result from the balance between tectonic rock uplift, crustal strength and surface processes which depend on climate, lithology and other factors. Understanding how tectonics and surface processes affect the geomorphologic and topographic evolution of mountain ranges is a great challenge because of the important and multiple interactions and feedbacks between these parameters (Champagnac et al., 2012) (Figure I.7). Tectonics, climate and erosion conditions dictate the landscape evolution of mountain area. How and when these conditions are imposed on the system, and how they change through time are important. Two traditional strategies have been used in order to understand the influence of tectonics and climate (Champagnac et al., 2012). First, consist to quantify landscape change through time and relate this evolution to possible change in either tectonic or climate. Second, involves the comparison of regions with different tectonic or climate conditions.

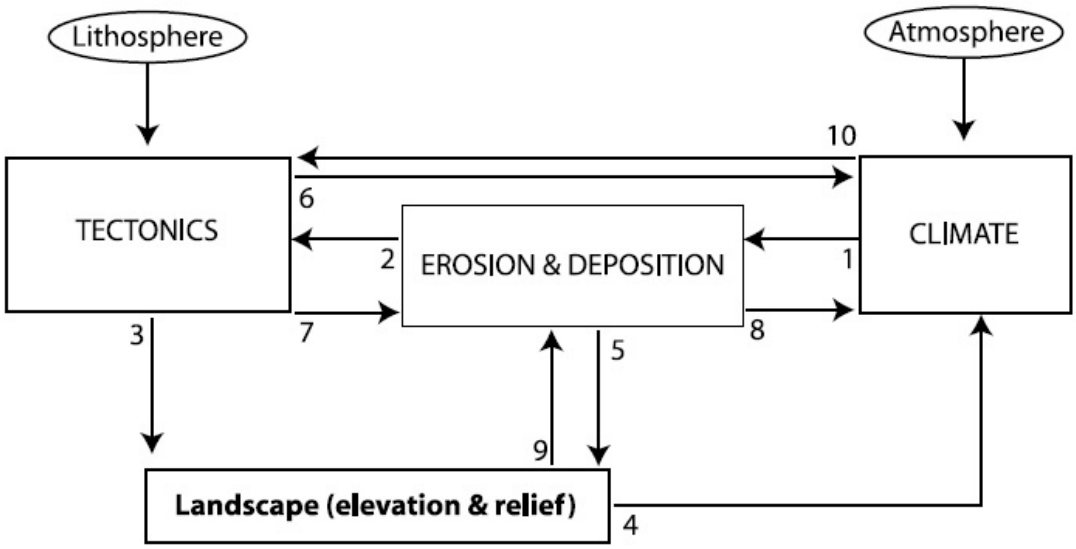

Figure I.7: Schematic sketch showing links between the lithosphere and atmosphere and resulting feedbacks between tectonics, climate and surface processes on the landscape from Champagnac et al., (2012).

Tectonics and climate coupling exist through various mechanism in mountain ranges and affect each other resulting in numerous feedbacks. Tectonics affect local and regional climate by elevating high mountain or plateau leading to orographic enhancement of precipitation (Beaumont et al., 2001; Koons, 1990; Roe et al., 2003; Willett, 1999). In another way, climate affects tectonics by increasing erosion of tectonic structures altering

the gravitational stress and internal structure (Beaumont et al., 2001; Beaumont et al., 1992; Dahlen, 1990; Willett, 1999). Erosion and sedimentation are no longer passive responses to tectonic forcing but may enhance or reduce structural activity in deforming thrust wedges and even determine their overall dimensions (Stolar et al., 2006) and exhumation patterns (Willett, 1999). Numerous numerical models coupling tectonic and surface process have explored the effect of surface processes on thrust wedges. Feedbacks between tectonics and erosion rates have been included in numerical models that couple plane-strain finite element models (Batt & Braun, 1997; Beaumont et al., 2001; Willett, 1999). Linkages between critical wedge theory and erosional processes have been explored in models which couple critical taper angle, mean elevation profile and one-dimensional hillslope-fluvial channel profile (Hilley & Strecker, 2004; Roe et al., 2006; Stolar et al., 2006; Whipple & Meade, 2004).

The Southern Alps of New Zealand has been extensively studied as it is an example of a young and tectonically active mountain range which has perturbed regional atmospheric circulation. Precipitation on the west side of the range is about ten times greater than on the east side. The resulting pattern results in rocks being more rapidly exhumed from a much larger depth on the western side of the range (Beaumont et al., 1996; Koons, 1990). Southern Alps of New Zealand is an example where the distribution of metamorphic rocks, geometry and structures results from the climatic pattern.

Another mountain range with an overall geomorphology and history having been influenced by surface process is the Eastern Andes (Strecker et al., 2007). Long-term aridity in the interior of the southern central Andes has enhanced the formation of the Puna-Altiplano plateau. As the plateau reached a stable elevation, deformation propagated eastward into the foreland basin. This resulted in further aridification of the interior due to orographic enhancement at the margins of the eastern Cordillera. The Andes also presents a strong morphologic latitudinal variation due to the global climatic pattern (Montgomery et al., 2001). The Northern Andes are characterized by a narrow mountain range maintained by high precipitation rate and fluvial erosion. In the Central Andes, tectonic dominance coupled with limited erosion except in major river valleys, lead to the formation of a mechanically limited plateau. It is suggested that the lake of erosion play an important role in mass accumulation in the mountain belt because of crustal thickening by tectonic wedge propagation. Finally in the Southern Andes, dominance of glacial erosion have preferentially eroded the highest topography resulting

in an excess of elevation at the glacial limit and a decline in maximum elevation. The large scale distribution of crustal mass in a mountain belt is therefore not only controlled by tectonic shortening but also by the type and intensity of erosional processes.

I.2.5 Post-orogenic system

Numerous studies have been carried out on young and active mountain ranges in order to investigate the important interaction between tectonics, surface processes and climate such as Southern Alps of New Zealand, Andes or Taiwan. In comparison, less work has examined the post-orogenic evolution of mountain ranges which represent the majority of the world mountains such as the European Alps, Urals, Caledonides, Appalachians, Rocky Mountains and Pyrenees. However, these systems may also record complex interactions linked to the evolution of the foreland basin (Tucker & van der Beek, 2013). The persistence of their remnant topography over millions years after cessation of orogenesis remains unclear, particularly in examples such as the Appalachian Mountains (Pazzaglia & Brandon, 1996). Studies have proposed that the persistence of topography results simply from the isostatic compensation of crustal roots (Stephenson, 1984).

Early quantitative studies estimate the decay time of orogenesis by dividing the mean elevation of mountain ranges by the average denudation rate. Estimation of time needed to reduce a mountainous topography to a base level, based on this method, range between 10 and 25 Myrs (Gilluly, 1955; Judson & Ritter, 1964; Schumm, 1963). For example, Gilluly, (1955) estimated a period time for topographic persistence of 10 Myrs for the continental United States with a spatially averaged erosion and no isostatic compensation and. If erosion is concentrated on mountainous area and isostatic compensation of crustal roots are integrated, this period time increase to 33 Myrs. Later, studies found a correlation between denudation rate and elevation suggesting an exponential decline in mean elevation with time. For example, Pazzaglia & Brandon, (1996), find a global average decay timescale of 69 Myrs including effect of isostatic compensation which can be applicable to the present day Appalachian. Others geomorphologic explanations can be take in consideration for the persistence of topography. Evidences based on suspended sediments loads suggest that old orogens have a lower effective erosion rates than young orogens (Pinet & Souriau, 1988) and can result in longer preservation of topography for old orogen. The geological parameters considered as important for the evolution of post-orogenic system are tectonics, climate and lithology (Pazzaglia &

Brandon, 1996).

The reason for the survival of mountain topography in ancient mountain ranges has been investigated by Baldwin et al., (2003). Using numerical modelling of fluvial erosion processes applied to post-orogenic topographic decay, the study demonstrated that a number of factors can inhibit erosion and encourage the presence of residual topography for hundreds of million years. The model incorporated the effect of isostatic rebound of the crustal root, a transition to transport-limited condition during topographic decline, a stochastic distribution of flood discharge and a critical shear stress for channel bed erosion. With a detachment-limited system model, the decay time is fast, typically 1 to 10 Myrs. By incorporating isostatic rebound model of a thick orogenic root in the model, the decay time is increase by a factor of 6 (10 – 30 Myrs). The transition to transported-limited condition implying protection of channel bed by alluvial cover increase the response time by a factor of 2-3 (36-90 Myrs). Finally including a stochastic distribution flood and critical shear stress for channel bed erosion increases the response time by a factor of 20 depending on climate and the critical shear stress required for erosion.

Mountain ranges approach a post-orogenic state because convergence rate decreases and frontal accretion slows down. As erosional fluxes are sustained in the system and can be greater in terms of their mass flux than the accretion fluxes, a reduction in total size is predicted for a doubly vergent thrust wedge (Stolar et al., 2006). As long as the stress state of the wedge determines that it is a failure, then the model is forced to contract self-similarly (Sinclair, 2012). This leads to the abandonment of the outer part of the wedge, which can then be draped with sediment as it was proposed for the Pliocene of the Alps (Willett et al., 2006). During active tectonics, shortening dominated by thrusting, crustal thickening and mountain building causes asymmetric subsidence in foreland basins. Subsidence is considerably more important close to the range and deposition occurs in the proximal parts of the foreland basins (Flemings & Jordan, 1989; Flemings & Jordan, 1990; Heller et al., 1988). Subsidence inhibits the propagation of transverse fans across the foreland. Rivers respond equally with transverse rivers restricted to the proximal parts and longitudinal or axial rivers located along the medial part of the foreland near the fan toes (Burbank, 1992). During a reduction of size of an active mountain range because of a slow down in accretionary fluxes, the topographic load is reduced and the foreland basin records an uplift because of upward isostatic

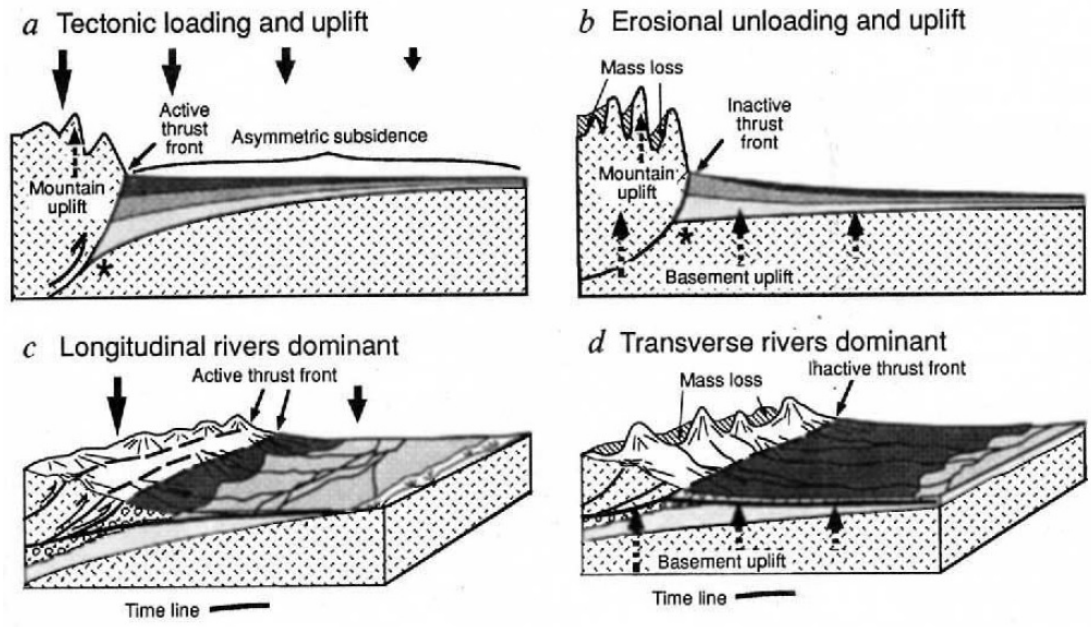

Figure I.8: Schematic representation of contrasts in subsidence and depositional patterns in foreland basins in syn-orogenic or post-orogenic settings from Burbank, (1992). (a) Asymmetric subsidence in foreland basin because of tectonic loading of the range during syn-orogenesis. (b) Tabular sedimentary deposits in response to erosional unloading during post-orogenesis. (c) Depositional patterns during active thrust loading characterized by short transverse rivers and dominant longitudinal rivers. (d) Dominant transverse rivers and gravel spreading across the foreland during uplift rebound of the basin.

rebound of the lithosphere. Rebound of the basin implies fluvial incision, erosion and widespread dispersal of sediment away from the mountain range (Heller et al., 1988). Redistribution of the sediment load within the basin causes both a shift of the center of the load away from the hinterland (Flemings & Jordan, 1990) and increases of the foreland basin width. The progressive shift from subsidence toward uplift in foreland basin with a more important uplift in the proximal part of the basin cause also transvers fans to expand and longitudinal rivers to be displaced toward the distal basin (Burbank, 1992). During erosional unloading of the range, the foreland basin become dominated by transverse rivers and gravel sediments are spreading across the foreland (Figure I.8). Sediment production from the mountain range where erosion is still active even during post-orogenesis are combined with the sediment eroded from the rebound basin to increase sediment dispersal to the surrounding continental margin. Cederbom et al., (2004) demonstrate that the North Alpine Foreland Basin of Switzerland experienced rebound and erosion caused by erosional unroofing of the mountain range which have been regionally compensated by flexural uplift of the underlying plates. Simultaneous than basin rebound, mass reduction of the Alps was enhanced by a wetter climate induced by the intensification of the Gulf Stream at 4.6 Ma.

I.2.6 Numerical modelling of thrust-wedges and foreland basins

The long-term growth of mountain ranges and foreland basins have been investigated by numerical modelling. Early models explored the geometry of foreland basins in relation to the development of thrust belts because of crustal thickening along major thrust faults. These models allowed the links between rheology, thrust history, flexural response and sedimentary basin development to be analysed (Beaumont, 1981; Jordan, 1981; Karner & Watts, 1983; Royden & Karner, 1984). These models have been restricted to the overall basin geometry but not the geometry of stratigraphic infill. Development of new numerical models resolved mass redistribution through erosion in the wedge and deposition in the basin approximated by diffusive processes:

$$\frac{dh}{dt} = \kappa \frac{d^2h}{dx^2} \tag{I.4}$$

Where t is the time, h is elevation, x is horizontal position and κ is a transport coefficient. These models allow the simulation of the progressive infilling of foreland basins and predict complex stratigraphic time line architectures as well as facies evolution in relation

to thrust belt deformation (Flemings & Jordan, 1989; Sinclair et al., 1991) (Figure I.9). An important implication of these models is the prediction of underfilled versus overfilled basin. In underfilled condition, sediments are trapped within the flexure and the forebulge. In contrast, during an overfilled condition, sediments overflow the uplift of the forebulge which is buried by sediment.

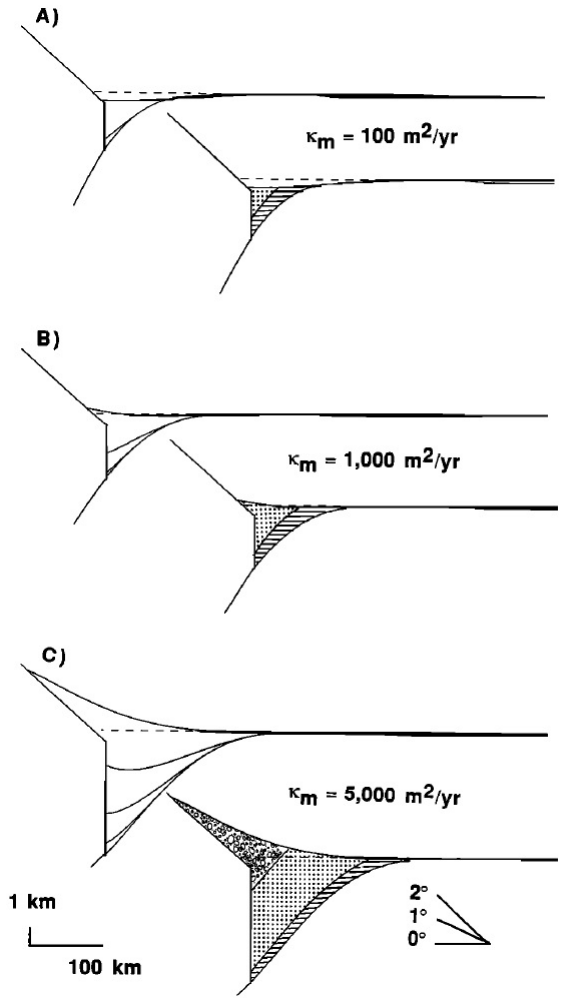

Figure I.9: Diffusion model from Flemings and Jordan, (1989) predicting strata geometry and different energy facies for different erosional transport coefficients (κ) of 100, 1,000 and 5,000 m^2.yr$^-$1. In this experience, the sediment transport coefficient is 5000 m^2.yr$^-$1, the flexural rigidity is 1 x 1050 dyne cm and the thrust velocity is 10 mm.yr$^-$1.

Finite element model have been applied to thrust wedge systems and provide a better insight into the dynamics and controls of these systems. Willett, (1992) applied the critical wedge theory into a finite element model to investigate the response of the wedge to a change in basal friction. They demonstrated that in order to maintain the

wedge taper, deformation oscillates between internal thickening and frontal accretion. These type of models have also better investigation about complex feedback and coupling between processes as erosion, isostasy and temperature-dependent rheology.

Discrete element methods simulating motions and effects of small particles have been applied to thrust-wedge systems. Elements of the model can represent either discrete objects, such as individual grains or bulk materials. In the case of an application to thrust-wedge system, each elements represent some mass of rocks. In discrete element method, particle sizes define the resolution of structures in the model and can be applied to sandbox problems. Particles interact through a linear elastic spring dashpot in the normal direction and fail through a Coulomb failure criteria in the tangential direction. It allows also to explore the spatial organization of structures through time. Naylor et al., (2005) used this method to explore controls on the structural, kinematic and macro-geomorphic development of mountain belts where fault displacements are approximated in the wedge. They demonstrated advection of materials from the pro-side to the retro-side, the topographic ridge oscillate around a point above the singularity and a gradual advection of the topographic ridge towards the retro-side. Mountain ranges are dominated by punctuated thrust activity. Naylor and Sinclair, (2007) provide a model that dictates the frequency and timing of thrust activity in the context of the growth of a doubly vergent wedge. They demonstrate that the rate of surface uplift, frontal accretion and exhumation should be punctuated on a time scales linked to thrust sheet geometry and convergence rates.

Multiple interactions between surface processes, thrust activity and flexural isostasy govern evolution of mountain and foreland basin systems. In a finite element model integrating fully dynamic and coupled fold-thrust deformation, flexural-isostatic compensation and surface mass transport, Simpson, (2006) explored interactions between deforming fold-thrust belts and progressive infilling of basins (Figure I.10). Modelling demonstrated that increasing the rate of surface mass transport results in a shallower, more filled foreland basin and lower amount of sedimentation on top of the deforming wedge. Evolution of the grain size and strata geometry in stratigraphic record is strongly controlled by changes of tectonics and climate (Armitage et al., 2011). More complex models incorporate the dynamics of three-dimensional landscape in order to simulate full fluvial networks (Braun & Willett, 2013; Garcia-Castellanos et al., 2002; Garcia-Castellanos, 2002). Recent modelling method (Yuan, Braun, Guerit, Rouby,

et al., 2019) explore how the topography of an uplifted relief and the stratigraphy of a foreland basin are controlled by the efficiency of river erosion and the efficiency of sediment transport by rivers.

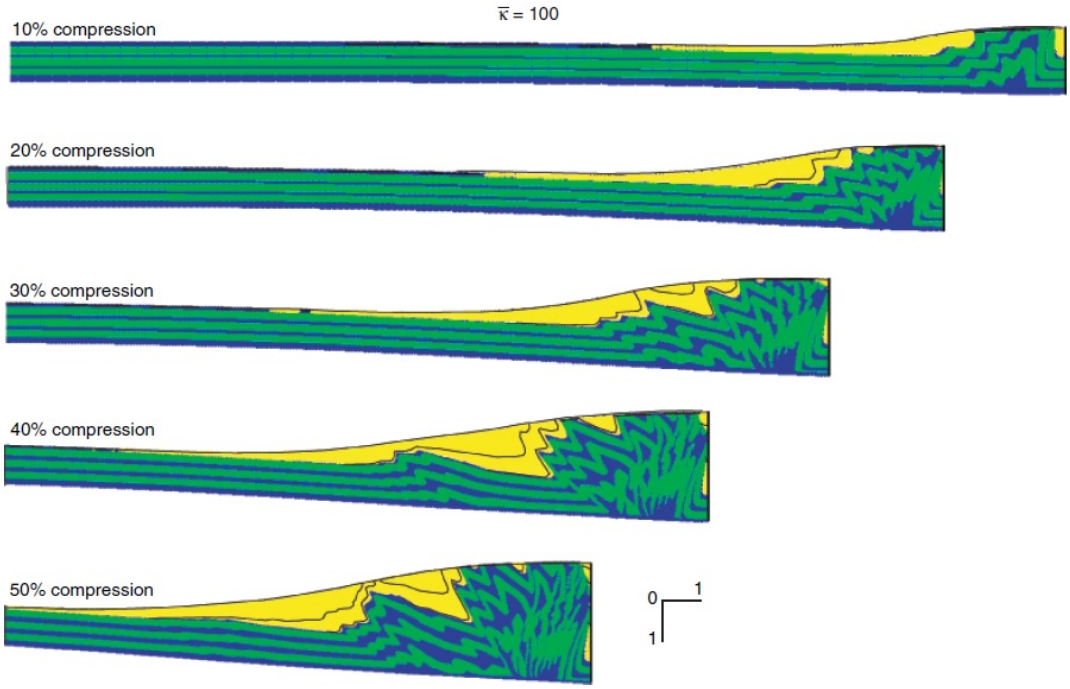

Figure I.10: Sequential development of fold-thrust belt and piggyback basins for relatively inefficient surface processes from Simpson, (2006). Grey and Blue layers correspond to passive markers of the finite deformation of the initial sequence. Yellow unit corresponds to sediment deposition from erosion of the thrust-wedge with lines indicating chronostratigraphic times.

I.3 Geologic Structure and Evolution of the Pyrenees

The Pyrenean orogen forms a 450 km topographic barrier from the Mediterranean Sea (Cap de Creus) to the Bay of Biscay (Cap Higuer) but extend on about 1000 km toward the Cantabrian platform in Northern Spain. The central width is about 150 km and separates the Iberian Peninsula from the European continent. The Pyrenees extend as a general linear east-north-east, west-north-west trend with a strong climatic asymmetry on both sides of the ranges. The Northern Pyrenees is characterized by a relatively precipitous flank compared to the semi-arid southern flank. The Pyrenean Mountain constitute the westernmost segment of the long Alpine-Himalayan belt caused by the

closure of the Tethys Ocean. The formation of the Pyrenean mountains result from the convergence, collision and partial subduction of the Iberian micro paleo-continent beneath the European plate from late Cretaceous to Early Miocene time (Roest & Srivastava, 1991). The geodynamical expression of this convergence is the formation of a doubly-vergent collisional orogen, which accommodates at least about 165 km of shortening leading to upper crustal thickening (Beaumont et al., 2000; Muñoz, 1992). The Pyrenees are characterised by an asymmetric landscape with a narrow northern retro-wedge and a wider southern pro-wedge. Because of the relatively small-sized of the orogen, good quality of exposure and large volume of geophysical data, the Pyrenees provide a good natural example to study the processes of orogenesis.

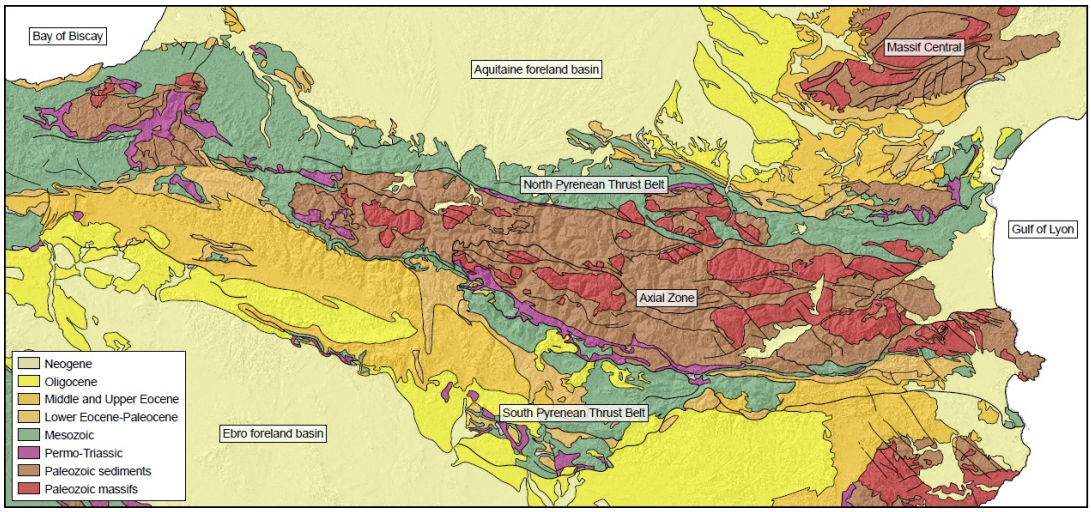

Figure I.11: Geologic map of the Pyrenees in colours from the 1:1000000 BRGM geological map of France draped on a hillslope map from a SRTM with a resolution of 30 m highlighting the main structures of the Pyrenees (Aquitaine foreland basin, North Pyrenean Thrust Belt, Axial Zone, South Pyrenean Thrust Belt and Ebro foreland basin).

I.3.1 Structure of the Pyrenees

The Central Pyrenean system can be divided into different series of structural units from tectonic and sedimentological standards. From south to north, six units define the Pyrenean system (Figures I.11 and I.12) (Muñoz, 1992; Vergés et al., 1995):

1. The Ebro Pro-Foreland Basin

2. The South Pyrenean Thrust Belt

3. A basement core: The Axial Zone

4. The North Pyrenean Fault Zone

5. The North Pyrenean Thrust Belt

6. The Aquitaine Retro-Foreland basin

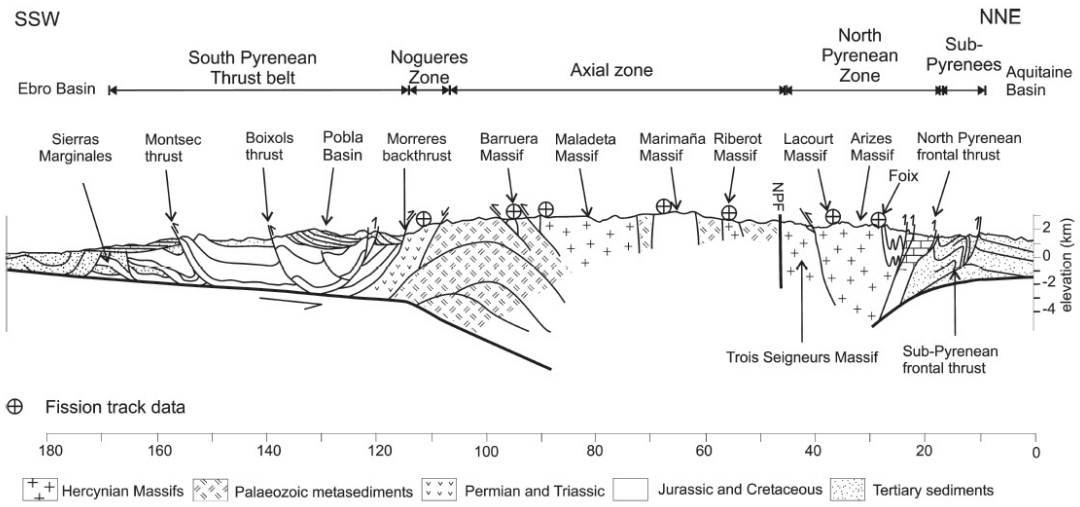

Figure I.12: Geological cross section of the Central Pyrenees from Sinclair et al., (2005) showing the main tectonic structures and massifs.

The Ebro Pro-Foreland Basin

The Ebro basin constitutes the southern foreland basin of the Pyrenees and is characterized by a triangular shape. It is surrounded by three mountain ranges: the Pyrenees to the north, the Iberian Ranges to the south-west and the Catalan Coastal range to the south-east. The formation of the Ebro foreland basin began during the Paleocene by flexural subsidence related to the growth of the Pyrenees, Catalan Coastal Range and Iberian Range respectively (Garcia-Castellanos et al., 2003). During the Palaeocene and early Eocene, the continuous convergence and partially synchronous tectonic shortening of the Pyrenees and the Iberian Range led to the closure of the western connection of the Ebro basin toward the Atlantic Ocean (Garcia-Castellanos et al., 2003). The Ebro basin started a long period of endorheic regime at about 36 Ma (Costa et al., 2010; Vergés et al., 1998) associated with a long period of lacustrine deposition through the

Oligocene and most of the Miocene. Sedimentation during Cenozoic time is mainly concentrated to the north of the basin with the deposition of up to 3 km of coarse sands and conglomerates (Brunet, 1986) leading to the backfilling of the basin and draping of the southern flanks of the Pyrenees (Coney et al., 1996).

During late-middle Miocene time, the Ebro River cut through the Catalan Coastal Ranges leading to the onset of the connection of the Ebro River to the Mediterranean Sea (Gaspar-Escribano et al., 2001). From this point, the sedimentary fill of the Ebro Basin is progressively eroded and discharged to the Ebro Delta in the Valencia Trough. The timing and origin of this major drainage change have been largely debated and is still not completely constrained. Frequent eustatic sea level changes during Miocene and Pliocene have been suggested (Calvo et al., 1992). Garcia-Castellanos et al., (2003) proposed that the opening of the Ebro Basin is a combined result of lake capture (piracy) and sediment overfilling of the basin.

The South Pyrenean Thrust Belt

The south Pyrenean Thrust Belt comprises thrusted and faulted Mesozoic and Palaeogene rocks (Muñoz, 1992). It can be described as the succession of three main thrust sheets named from south to north: Sierras Marginales, Montsec and Boixols which have been southwardly transported and imbricated across autochthonous Palaeogene and Mesozoic cover rocks of the Ebro basement (Figure I.13).

The Sierras Marginales thrust sheet is separated at the north by the Montsec thrust and to the south by the South Pyrenean Main Thrust from the Ebro Basin (Pocoví, 1978). Initial emplacement of the Sierras Marginales thrust sheet occurred between Early Eocene and Late Eocene times followed by later deformation during the Upper Eocene-Lower Oligocene times (Verges & Munoz, 1990). They consist of several small imbricate units characterized by a thin Mesozoic sequence which become thicker and more complete to the North (Pocoví, 1978). A Lower Eocene succession overlies the Mesozoic series. The upper Eocene-Lower Oligocene conglomerates, sandstones and gypsums unconformably overlie the Lower Eocene Alveolina limestones.

The Montsec thrust sheet is situated between the Sierras Marginales to the north and the Boixols thrust sheet to the south. The Montsec thrust consists broadly to a Mesozoic and Cenozoic sequence. The Mesozoic sequence is about 2000 m thick, mainly Upper Cretaceous limestones. The Cenozoic sequence is represented by Palaeocene

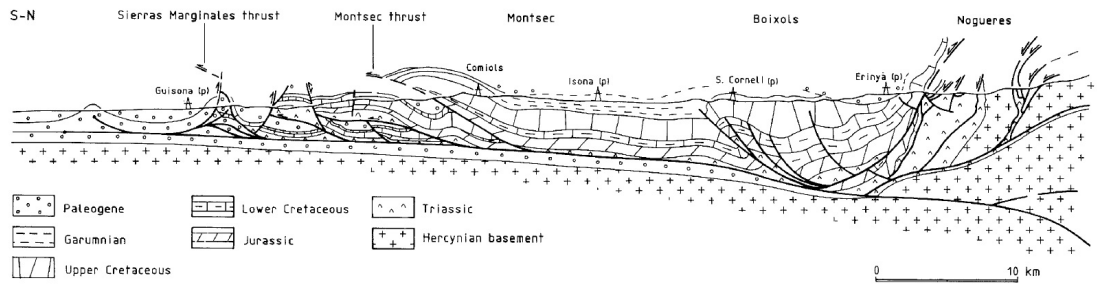

Figure I.13: Geologic cross-section of the cover thrust sheets of the South Pyrenean Thrust Belt from Vergés and Muñoz, (1990).

and Lower to Middle Eocene clastic rocks in the Tremp-Graus basin (Muñoz, 1992). The structure of the Montsec thrust is simple and consists of a broad syncline which supports the Tremp-Graus basin. The Montsec thrust emplacement occurred during Ypresian times.

Finally the Boixols thrust sheet, the most northerly of the South Pyrenean Thrust Sheet series, is bound to the north by the south-dipping Morreres Backthrust. This thrust sheet consists of a thick (over 5000 m) Mesozoic series mainly Lower Cretaceous in age (Vergés and Muñoz, 1990).

The axial Zone

The Central Pyrenean Axial Zone is bounded by the North Pyrenean Fault Zone to the North and by the South Pyrenean Thrust Belt to the south. The Axial Zone is mainly constituted of Paleozoic sediments intrude by granitic massifs (Zwart, 1986) during Ordovician times (Barbey et al., 2001) and following by deformations and intrusions from Upper Carboniferous to Lower Permian times (Denèle et al., 2012). The Axial Zone display mountain belt-scale thrusting acquired during Pyrenean crustal shortening (Choukroune, 1989). This structure is dominated by thrusting, Alpine cleavages and folds being very subordinate.

The Axial Zone is characterized by a large spatial variation in its Paleozoic stratigraphy. However, the Central Pyrenees Axial Zone can be summarised as follow: Orthogneiss massifs (Canigou, Aston-Hospitalet) present in the east interpreted as Precambrian basement and intrusive Cambro-Ordovician granites (Zwart, 1986). The Silurian epoch is represented by black carbonaceous shales which are overlain by highly variable and fossiliferous Devonian limestones, dolomites, shales and quartzites (Zwart,

1986). Carboniferous sub-facies include nodular limestones, cherts, greywackes and conglomerates. Several large and elongated, E-W oriented granitoid bodies intrude into the Paleozoic stratigraphy. Finally the post-Variscan succession is largely represented in the southernmost part of the Axial Zone. Upper Carboniferous deposit correspond principally to fluvial and lacustrine environment. Overlying it are Permian and Triassic strata dominated by red sandstones and mudstones (Zwart, 1986).

The Central Axial Zone, at a large scale, corresponds of a stacked of Hercynian basement thrust sheets with localized deformed Permian and Triassic cover rocks. From south to north these thrust sheets are named: Nogueres, Rialp and Orri units. The uppermost of these thrust sheets is the Nogueres Zone where thrusts affect basement and Triassic cover rocks. Two units are differentiated: The Upper and Lower Nogueres Units. The Upper Nogueres consists of Silurian, Devonian and Lower Carboniferous series followed by an unconformity and the Triassic red beds. This series is affected by Hercynian thrusts and constitute the main structural features (Muñoz, 1992). The Lower Nogueres unit is constituted of several small thrust sheets with a hectometric to kilometric displacement to the south. The Lower Nogueres are differentiated from the Upper Nogueres by the presence of thick Stephano-Permian sequences below the Triassic strata and the nature of the Hercynian facies. Northward along the axial zone and below the Nogueres Zone is the Rialp Thrust. This Unit is composed of Cambro-Ordovician, Silurian and Devonian rocks which outcrop through a complex tectonic window along the Noguera Pallaresa valley (Muñoz, 1992). Finally the Orri thrust sheet exposure form much more of the southern central Axial Zone and in particular the broad anticlinal Orri Dome (Zwart, 1986).

The North Pyrenean Fault Zone

The North Pyrenean fault bound the north of the Axial Zone and the south of the North Pyrenean Thrust Belt. The location of this fault is well defined in the east and center of the orogen between the Axial Zone and North Pyrenean Zone. However, at the west, the fault contact is not very well defined. This fault and the related others form a narrow belt characterized by the presence of Jurassic and Lower Cretaceous rocks which have been affected by thermal metamorphism of high temperature and low pressure and a strong deformation during Middle Cretaceous time.

The North Pyrenean Fault developed during the sinistral displacement of Iberia

and played an important role during the Lower Cretaceous extension accommodating the opening of the Bay of Biscay and several pull-apart flysch basins (Manatschal & Bernoulli, 1999). The age of this displacement correspond to the age of the flysch basin formed synchronously with the strike-slip movement along the North Pyrenean Fault. Datation of both metamorphic and magmatic minerals yield an ages of Middle Albian to Middle Cenomanian. However its role during the Cenozoic continental collision seems limited in contrast to Hercynian structure like the fault of "Toulouse" and "Pamplone" (Chevrot et al., 2014).

Seismic refraction and teleseismic data indicate a vertical offset of the Moho discontinuity of approximately 15 km beneath the North Pyrenean Thrust Zone (Choukroune, 1989). This Moho discontinuity step would be the result of differential thickness of the Iberian crust with a normal thickness and the thinned European crust. This evidence allows us to consider the North Pyrenean Thrust Zone as the axis or suture zone of the mountain belt and present the boundary between the European and Iberian plates (Choukroune, 1989).

The North Pyrenean Thrust Belt

The North Pyrenean Thrust Belt is delimited to the south by the North Pyrenean Thrust Zone from the Axial Zone and to the north by the Sub-Pyrenean Thrust from the Aquitaine basin. The North Pyrenean Zone of the Central Pyrenees consists of folded and northward imbricated thrusts involving mainly Mesozoic basins in contact with numerous windows into Hercynian basement culmination which formed the so-called "North Pyrenean Massifs" (Arise and Trois-Seigneurs along the ECORS profile, Agly, Saint-Barthélémy, Castillon, Milhas and Barousse) (Fischer, 1984). In contrast to the North-Pyrenean Thrust Zone, the Upper Cretaceous flysch series unconformably overlie the Hercynian massifs with a non-metamorphosed and weakly deformed pattern (Muñoz, 1992).

The Arize massif is defined as a basement pop-up structure because it is observed in cross-section to overthrust Upper Cretaceous turbidites at both its northern and southern extremes. Southward, the Trois-Seigneurs massifs and its unconformable strata share a sub-vertical south-vergent thrust contact with the heavily deformed Mesozoic metamorphic terrane to the south (Vielzeuf & Kornprobst, 1984). In the same way the St-Barthélémy massif to the East is situated in the hangingwall of the same

north-vergent thrust (Deramond et al., 1993; Fischer, 1984). Northwards of the Arize massif, is located the Camarade basin constituted of Cenomanian breccias and turbiditic series of several thousands of meter thick as the result of the sinistral displacement of Iberia (Muñoz, 1992). The northern fault boundary of the Camarade basin controlled the location of the North Pyrenean frontal thrust.

Lying between the North Pyrenean Zone and Aquitaine basin are the Sub-Pyrenees which consist of a narrow zone of thin skinned accretion of Cenozoic foreland basin strata and are bound to the north by the Sub-Pyrenean Thrust and to the south by the North Pyrenean Frontal Thrust (Deramond et al., 1993).

The Aquitaine Basin

The Aquitaine Basin corresponds to the northern retro-foreland basin of the Pyrenees. It is delimited to the south by the North Pyrenean Frontal Thrust, to the north by the Armorican Massif and to the east by the Central Massif. The Aquitaine retro-foreland basin evolved by flexure of the upper plate in response to the load of the North Pyrenean thrust sheets (Brunet, 1986; Desegaulx et al., 1990). The sedimentary infill of the basin is abundant and is composed of Late Cretaceous to Eocene sandy-calcareous flysch sequences, becoming more siliciclastic during Eocene to Miocene times as the majority of the south and east of the basin became dominated by continental sedimentation (Bourrouilh et al., 1995). More precisely this sedimentation start with the deposition of Late Cretaceous turbidites in the Nalzen Basin (Deramond et al., 1993). The Paleocene red beds are ovr by Early Eocene shelfal platform carbonate deposition. Continental deposits occurring during Ypresian to Bartonian age are alluvial and fluvial deposits and up to 4750 m thick. These deposits are named “Poudingues de Palasou” and consist of three depositional sequences separated by angular unconformities. They result from the erosion of the belt continental collision as the formation from Miocene time of the Lannemezan alluvial cone (Babault & Van Den Driessche, 2005).

The development of the Aquitaine basin was strongly influenced by pre-existing Hercynian structural lineaments (Bourrouilh et al., 1995) leading to the inversion of mid Cretaceous pull-apart basins during the compressive deformation related to the growth of the Pyrenees.

I.3.2 Deep structures of the Pyrenees

First studies in the years 1980 on deep structures of the Pyrenees used geophysical seismic data in order to observe the main tectonic structures of the Pyrenees and the crust thickness. The Iberian crustal thickness under the Axial Zone is 40-50 km whereas the European crustal thickness under the North Pyrenean Zone is only 30 km indicated vertical shift of about 15 km (Daignieres et al., 1982). This Moho step in the Pyrenees is sharp and recorded between the Axial Zone and North Pyrenean Zone indicating the importance of the North Pyrenean Fault as a limit boundary between the Iberian and European plates. Crustal thickness in the western and eastern part of the Pyrenees decrease because of the influence of the opening of the Bay of Biscay in the Atlantic Ocean and the Gulf of Lyon in the Mediterranean Sea. For example, seismic data have shown that the Moho in the western part of the Axial Zone is situated at a depth of 26 km (Daignieres et al., 1982).

The ECORS-Pyrenees profile, a Spanish and French organisation, cross the entire orogen in the Central Pyrenees and have allowed to obtain important information about the orogen architecture (Choukroune, 1989; Choukroune et al., 1990; Daignieres et al., 1982; Muñoz, 1992; Roure et al., 1989; Vergés et al., 1995). These data allow to confirm that the Iberian crust is thicker than the European crust with a thickness of about 50 km south of the North Pyrenean Fault. The Pyrenees shows an asymmetric structures with a south vergence of the crustal units. Beneath the North Pyrenean Thrust Fault, the Iberian crust underlies the southern edge of the European crust (Choukroune, 1989) but the extension of the Iberian crust is less than 20 km north of the North Pyrenean Fault (Daignieres et al., 1982; Torné et al., 1989).

Gravimetric (Casas et al., 1997; Pedreira et al., 2007; Torné et al., 1989; Vacher & Souriau, 2001) and seismic tomography (Chevrot et al., 2014; Sibuet et al., 2004; A. Souriau et al., 2008; A. Souriau & Granet, 1995; Wang et al., 2016) have allowed to obtain a more precise comprehension of the deep structures of the Pyrenees. The gravimetric study of Torné et al., (1989) reveals that the downward flexural subduction of the Iberian Moho reach a maximum depth of 65 km under the Axial Zone whereas a depth of 35 km is found for the European Moho.

Gravimetric anomalies have revealed the presence of dense bodies in the Pyrenees. Positive gravimetric anomalies under the Labourd massif and around Saint-Gaudens area have been interpreted as dense intracrustal mantle slices or lower crustal sheets

incorporated during the formation of the orogenic prism (Torné et al., 1989; Casas et al., 1997). Recent work from the PYROPE and IBEARRAY (Chevrot et al., 2014) projects proposed that the anomaly below Mauléon basin is the result of an exhumed mantle inherited from the pre-compressional hyperextended Pyrenean rift system. The study of Chevrot et al., (2014) show that the absence of a pronounced fast anomaly along the whole Pyrenean range prohibit the subduction of an oceanic domain under the European plates. However, the Pyrenean lithosphere is segmented by Variscan structures (Pamplona and Toulouse faults).

I.3.3 Pre-collisional geodynamic history

Variscan orogeny

Remnants of the Variscan orogeny are preserved in the Axial Zone of the Pyrenees. These relics correspond to the collision between several plates and Gondwana causing subduction of the Paleo-Tethys and Rheic Ocean to form the Pangea supercontinent. The collision cause important deformation and led to the creation of the Ibero-Armorican arc during late Paleozoic and up to Permian time (500-250 Ma). Following evolution during Permian to Early Triassic corresponds to a first phase of rifting associated to the opening of the Neo-Tethys Ocean and the first dismantling of the Variscan orogen. This phase is associated with the formation of graben and deposition of detrital sediments which are observed in discordance with Variscan metamorphic bedrock (Lucas, 1985). The Variscan belt is subsequently broken up by the opening of the Atlantic Ocean during Late Triassic and Early Jurassic time.

Mesozoic history

Evaporitic sedimentation occurs during Late Triassic and cause important salt tectonics in the North Pyrenean Zone, southern and western part of the Aquitaine basin (Biteau et al., 2006; Rougier et al., 2016). Jurassic and Early Cretaceous time are dominated by carbonate sedimentation. The Mesozoic geodynamic especially during Albian and Cenomanian time with the major phase of rifting and opening of Bay of Biscay is still debated in terms of plate kinematics; several models have been proposed to reconstruct the Iberian plate movement relatively to the European plate based on fieldwork data, seafloor magnetic anomalies or geomagnetic pole rotation (Jammes et al., 2009; Olivet, 1996; Sibuet et al., 2004; Srivastava et al., 1990; Vissers & Meijer, 2012). Common

features between these different models are an anticlockwise rotation of Iberia of about 35° or the presence of a major left-lateral strike slip movement. The position, rotation pole, quantities of extension, timing and amounts of shortening varies following the different models:

A first model, principally based on geological observations imply an extensive component of dextral strike-slip rifting along the North Pyrenean Fault during Albian and Cenomanian time. This model interprets the northern Pyrenean basins as pull-apart basins (Choukroune & Mattauer, 1978; Olivet, 1996; Savostin et al., 1986). However this model does not respect magnetic anomalies data, mantle exhumation and crustal thinning.

The scissor opening model proposes an opening of the Bay of Biscay by a 35° rotation of the Iberian plate during Albian time (Sibuet et al., 2004; Sibuet et al., 2007; Srivastava et al., 2000; Vissers & Meijer, 2012). This model implies that the opening of the Bay of Biscay is synchronous with a convergence phase associated to the subduction of the Neo-Tethys Ocean under the Pyrenean domain with a north vergence. Following this evolution, the Pyrenean domain has a back-arc position and basins of the Northern Pyrenean zone are considered as back-arc basins.

Jammes et al., (2009) proposed an intermediate model with a dextral strike-slip extensiional phase starting during Late Jurassic time and ending during Late Albian. This phase was followed by the opening of the Bay of Biscay by a scissor movement during Aptian and Albian times. This phase allow the anti-clockwise rotation of the Iberian block relative to the European block.

The convergence between the Iberian and European plate began at the start of the Cretaceous Normal Superchron (geomagnetic polarity which last from about 120 to 83 Ma) for Srivastava et al., (2000) whereas Olivet et al., (1996) suggest an onset of convergence at the end of the Cretaceous Normal Superchron (83 Ma). Both interpretations imply that convergence was active at around 83 Ma and is consistent with the end of oceanic accretion in the Bay of Biscay. However, the resulting total plate convergence differs and ranges from 100 km (Olivet, 1996) to up to 400 km (Rosenbaum et al., 2002; Srivastava et al., 2000; Vissers & Meijer, 2012). Shortening across the Pyrenees have been estimated from balanced geological cross sections. Apparent consensus for the total amount of shortening of the Iberian plate indicate about 180 km of convergence (Olivet, 1996; Rosenbaum et al., 2002; Sibuet et al., 2004) and decreasing from west

to east (Vergés et al., 2002). However in the Central Pyrenees, different amounts of shortening have been proposed to interpret the current geological structures. Beaumont et al., (2000) estimate an important shortening of 160 km compare to Roure et al., (1989) or Mouthereau et al., (2014) which indicate respectively 100 and 92 km of shortening across the Central Pyrenees. Machiavelli et al., (2017) proposed an N-S shortening of 125 km.

Estimation of shortening rates vary also in the Central Pyrenees. Mouthereau et al., (2014) indicate that the most rapid shortening rates happened during the onset of convergence at 80-60 Ma (3.5 mm/yr) followed by a period of constant shortening rate of 2.0 mm/yr. In contrast, Beaumont et al., (2000) modelled an initial shortening rate of convergence from late Cretaceous to Eocene time of 2.0 mm/yr followed by an increase of shortening rate of 4.5 mm/yr during Oligocene time. Machiavelli et al., (2017) proposed a more complex shortening rate history but in better agreement with the model of Beaumont et al., (2000) for the Cenozoic part.

I.3.4 Exhumation of the Central Pyrenees from thermochronology

In order to investigate the latter stages of evolution and exhumation of the Pyrenean system during Cenozoic time, low-temperature thermochronologic systems have been massively employed. Granitoid rocks located on the Hercynian plutonic massif through the Pyrenees constitute perfect target for zircon fission track, apatite fission track and apatite helium analyses.

Individual elevation sampling strategy in the Central Pyrenees

Initial researches implying low-temperature thermochronology techniques involve single-elevation samples through the Pyrenees. Yelland, (1990) performed a multitude of single apatite fission track analyses from independent basement and granitic massifs across the central and eastern Pyrenees. This method allows coverage of a large area with a minimum number of samples and to obtain a large pattern of the timing and relative rates of regional exhumation within the Pyrenean orogen. Long mean track lengths (13.3-14.6 μm) and low standard deviations (0.9-1.7 μm) in the northern axial zone are observed and compared to the short mean track lengths (11.3-13.9 μm) and high standard deviations (1.3-3.2 μm) of the south. This contrast between the south and north of the mean track length was interpreted as an initial period of rapid

Palaeocene-Eocene uplift in the northern Pyrenees followed by a protracted period of less rapid uplift in the southern Pyrenees.

Morris et al., (1998) performed a subsequent modelling based on the low-temperature thermochronological dataset of Yelland, (1990). Modelling allows to evaluate the spatial and temporal variability in the magnitude of the cooling histories associated to each samples from the central and eastern Pyrenees (Figure I.14). Exhumation and erosional denudation are inferred from the cooling histories in order to build a map of denudation and to calculate sediment discharge to the neighbour foreland basins through time. With a modern geothermal gradient, Morris et al., (1998) calculated an exhumation rate ranging from 0.034 to 0.061 km.Ma^{-1} during the period from 40 to 10 Ma with a maximum rate of 0.24 km.Ma^{-1} in the region of the Querigut-Millas massif during the interval 35-30 Ma. The comparison of sediment discharge between the Ebro and Aquitaine basins shows a discharge 1.5 to 2.8 times greater to the south than to the north.

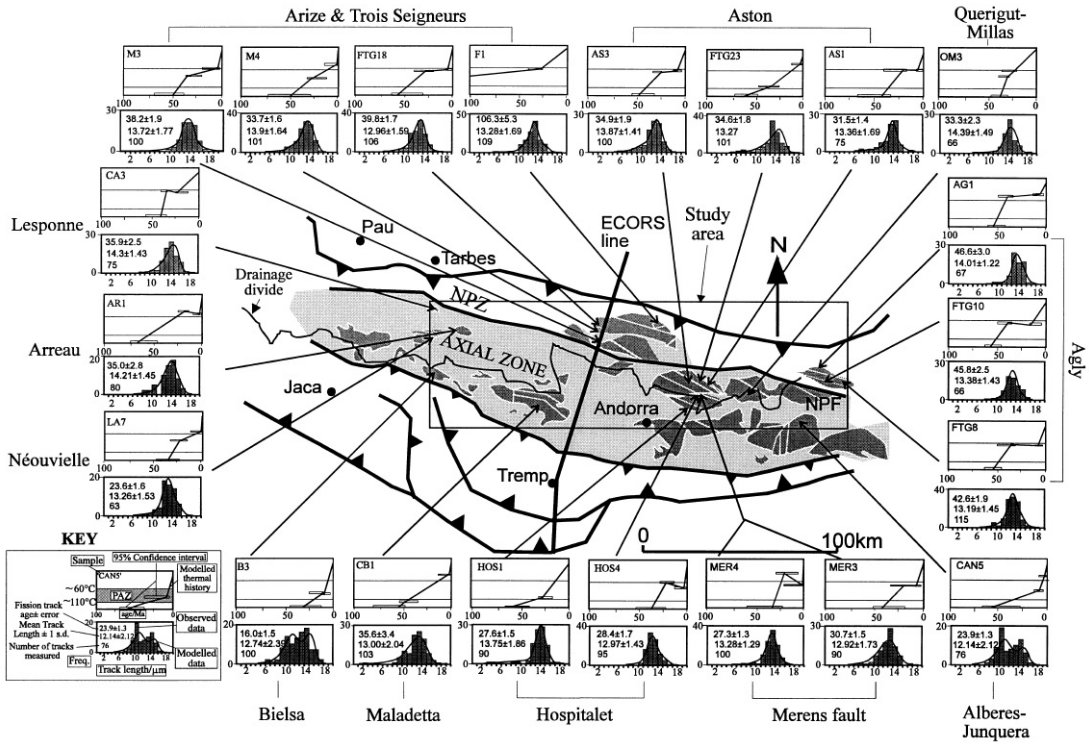

Figure I.14: Set of thermal histories modelled from single elevation samples taken from granitoid massifs of the Axial Zone and North Pyrenean Thrust Belt of the Pyrenean orogen from Morris et al., (2001).

Vertical profiles sampling strategy in the Central Pyrenees

The first study to perform low-temperature thermochronology in the Pyrenees with a vertical profiles sampling strategy is the one of (Fitzgerald et al., 1999). By using multiple vertical profiles from granitic massifs in the Pyrenees, the study highlights temporal and spatial variation in rates of exhumation through Palaeogene times (Figure I.15). The vertical profiles form a transect in the Axial Zone and the North Pyrenean Thrust Belt of the Central Pyrenees. From north to south the three sub-vertical profiles are: Lacourt, Riberot and Maladeta. Results show an asymmetric exhumation with AFT ages younging from north to south across the Pyrenees. More precisely the northern profile, Lacourt, is interpreted as the base of an exhumed partial annealing zone and records the onset of an episode of rapid cooling. Interpretation is based in the distinction of two parts in the profile from the track length distribution and the ages ranging between 55±3 to 37±1 Ma. Upper samples show slightly shorter mean track lengths ($\leq$13.7 μm) and larger standard deviations ($\geq$1.7 μm) indicative of more annealing in the partial annealing zone. Lower samples show mean track lengths $\geq$13.9 μm and standard deviations $\leq$1.7 μm indicative of rapid exhumation. The break in slope representing the base of the exhumed PAZ at 50 Ma and 1 km. Riberot profile yield apatite fission track ages ranging from 44 to 36 Ma, mean track lengths of $\geq$14 μm and standard deviations of $\leq$1.2 μm indicative of rapid cooling. The AFT ages-elevation slope indicates an average exhumation rate of 173±80 m.Ma^{-1}. The Maladeta profile, southern profile, yields apatite fission tracks ages from 34±4 to 21±3 Ma and records an abrupt transition in the age-elevation slope at 30 Ma. The upper part of the profile records an extremely rapid exhumation because of consistent ages of 32-30 Ma and high mean track lengths ($\geq$14 μm). The vertical slope of the upper part is considered as a rapid exhumation at a rate of 2-4 km.Ma^{-1}. The lower part of the profiles reflects a paleo-partial annealing zone developed during thermal and tectonic stability during post-orogenic period. This is characterized by a relatively low mean track length ($\leq$13.6 μm) and an important age transition from 31±3 to 21±3 Ma. The change in slope on the Maladeta profile at 32-30 Ma marks an abrupt transition from a period of rapid exhumation to a period of relatively thermal and tectonic stability.

Sinclair et al., (2005) present new apatite and zircon fission track data along vertical profiles of the Nogueres Zone, Barruera, Maladeta and Marimaña massifs. These new dataset are integrated with the data from Fitzgerald et al., (1999), Morris et al., (1998)

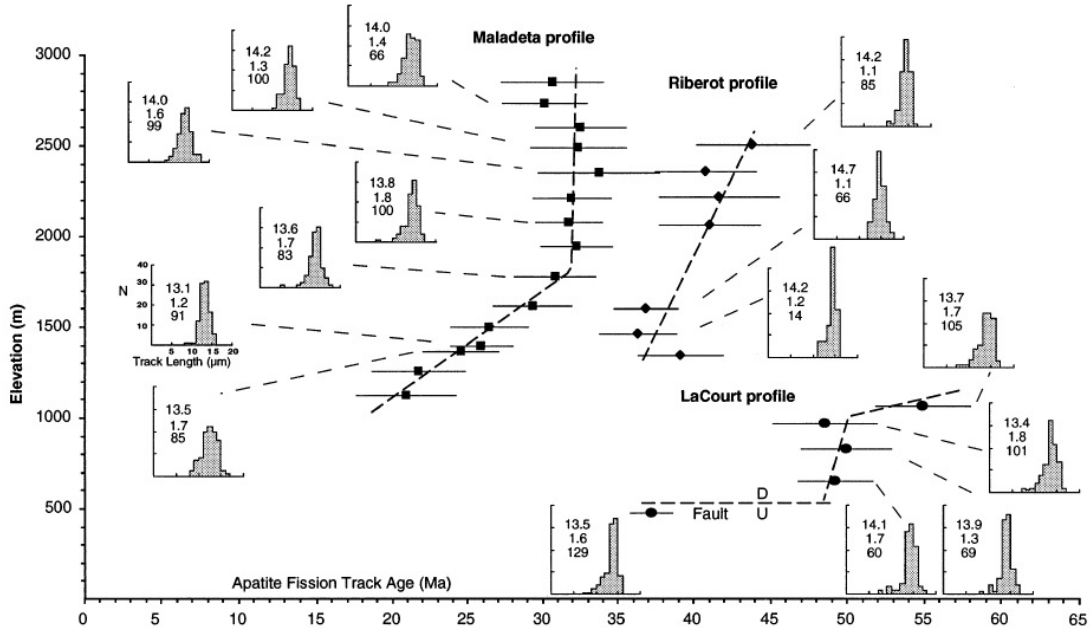

Figure I.15: Apatite fission track ages versus elevation profiles for Maladeta, Riberot and Lacourt massifs in the Central Pyrenees from Fitzgerald et al., (1999) with multiple sampling along sub-vertical profiles (generally along valley). Application of the annealing zone concept and multiple vertical sampling allow to determine the timing, amount and rate of exhumation.

and Yelland et al., (1990). The study highlights a broad unroofing from 60 to 40 Ma. The core of the Axial Zone is characterised by the greatest depth of exhumation followed by a progressive southward shift with a period of highest erosion rate associated to the growth of the antiformal stacks from 36 to 20 Ma. The ZFT ages (50 Ma) for the Maladeta and Marimaña massifs indicate approximately 6 to 9.5 km of erosion over the core of the Axial Zone during maximum rates of frontal accretion and retro-ward advection of rock particles. Data from Maladeta and Marimaña indicate also that exhumation of the northern antiformal stack decelerate after 32 Ma while the southern antiformal stack around the Nogueres Zone continued to erode after 26 Ma. The youngest AFT ages of 35 to 20 Ma record the growth of the antiformal stacks.

Following the paper of Sinclair et al., (2005), Gibson et al., (2007) performed and present new apatite (U+Th+Sm)/He thermochronometric ages from four sub-vertical profiles of Hercynian massifs: Barruera, Maladeta, Arties and Marimaña massifs and new apatite fission track data from Nogueres and Arties profiles combined with pre-existing apatite fission track data from Maladeta, Marimaña and Nogueres (Sinclair et al., 2005). Maladeta profile situated at the south of the modern drainage divide records an accelerated exhumation from 31 to 29 Ma at 1.5 km.Ma^{-1} following by a slow exhumation from 29 Ma to present day of 0.3 km. Ma-1. Similar exhumation histories are reported for northern profiles (Arties and Marimaña) but with a rate ¿1.5 km. Ma-1 at 30 Ma followed by a slower passage to the surface with a rate of ¡0.03 km.Ma^{-1}. Barruera profile situated at the southern axis of the Axial Zone records the youngest evidence for accelerated differential exhumation at 20 Ma. The study concludes that the transition from syn- to post-orogenic exhumation is diachronous across the mountain belt.

Exhumation of the northern central Pyrenees have also been recorded in a study by (Vacherat et al., 2016). Thirteen bedrock samples have been collected from Trois-Seigneurs, Lacourt and Foix plutons for apatite and zircon fission track analyses and apatite and zircon (U+Th+Sm)/He analyses. AHe and AFT ages range from 31.1±2.5 Ma to 55.8±4.5 Ma and 35.4±2.4 to 46.5±4.7 Ma respectively and are consistent with syn-orogenic ages. Lacourt massif samples record AFT ages of 43.9±2.1 Ma to 38.5±1.8 Ma and AHe ages from 37.9 to 27.7±2.2 Ma. Finally AHe ages of Foix massif range from 34.5±2.8 Ma to 55.4±4.4 Ma and younger than an AFT age of 74.9±1.2 Ma. Modelling of the dataset from Trois-Seigneurs, Lacourt and Foix show that the area

record a monotonic cooling phase starting at 50 Ma and lasting until 35 Ma.

Most of the low-temperature thermochronological analyses in the Pyrenees have been performed on granitic massifs. In the study of (Fillon et al., 2013), the evolution of the South Pyrenean thrust belt have been tested using apatite fission-track and apatite (U+Th+Sm)/He detrital samples from the Boixols, Montsec and Sierras Marginales thrust belt. Modelling predicts burial from the Late Cretaceous to the Miocene-Pliocene with a temperature increase up to 70-95°C equivalent to 0.7-1.6 km of late Eocene-Oligocene overburden. This phase was followed by an onset of exhumation ranging from 20 to 5 Ma with an exhumation rate of 0.13-0.5 km.Ma^{-1}. This is interpreted to have been caused by the onset of the Ebro Basin incision following opening of the Mediterranean Sea through the Catalan Coastal ranges.

Exhumation in the eastern and western Pyrenees

Exhumation of the Néouvielle, Bordère-Lourdon and Bielsa massifs are determined from a combined work of Jolivet et al., (2007) using apatite fission track and biotite /K-feldspar ^{40}Ar/^{39}Ar ages and tectonic data. The granite massifs were exhumed by tectonic activity at 35 Ma and at 32 Ma for the Bordère-Lourdon massif in relation to thrusting on the Gavarnie thrust. Exhumation of the Bielsa massif is younger at 19 Ma because of the out-of-sequence movements of the Bielsa thrust. Modelling indicate also a last cooling event starting around 5 Ma and certainly related to the Pliocene reexcavation of the southern and northern flank of the Pyrenees. Exhumation of the westernmost part of the Pyrenean Axial Zone have been inferred by (Bosch, Teixell, et al., 2016) using apatite fission track and apatite and zircon helium data. Modelling of the dataset shows cooling signal between 50 and 26 Ma in the Chaînons Béarnais consistent with the onset of thrust-related cooling in the neighbouring Mauléon basin. Footwall of the Lakora thrust records a cooling pulse during Late Eocene to Oligocene time associated to the activity of the Gavarnie thrust. Activity of the Lakora thrust caused cooling from Early Eocene time of the Lakora thrust hanging wall. Finally, modelling of samples from Eaux-Chaudes and Balaitous-Panticosa granitic plutons indicate fast cooling between 20 and 30 Ma associated to the motion of the Guarga thrust. AHe data indicates a renewed erosion post-tectonic signal at 8-9 Ma.

On the eastern part of the Pyrenees, exhumation histories of Canigou and Mont-Louis massifs have been investigated (Maurel et al., 2008). AFT ages from the Canigou

massif range from 21.6±2 Ma to 26.1±1 Ma and with ZFT ages from 30.9±2.5 Ma to 33.8±3.1 Ma. Mont-louis massif records AFT ages between 32.3±2.4 and 36.4±2.0 Ma with a ZFT age of 41.6±3.1 Ma. AHe ages range from 17.8±0.9 to 25.0±1.2 Ma for the Canigou massif and an individual age of 29.7±1.5 Ma for Mont-Louis massif. This dataset suggest two exhumation stages of the Canigou and Mont-Louis massif during Early Oligocene and Late Burdigalian time. Gunnell et al., (2009) performed apatite fission track and apatite helium data on multiple basements of the Eastern Pyrenees. Result show that AFT ages mainly range between 30 and 40 Ma and associated with mean track lengths ≥14 μm indicative of a rapid cooling. AFT data record also a quiescence during the post-30 Ma interval.

I.3.5 Tectonic-Sedimentary relation and evolution in the Central Pyrenees

Southern Pyrenees

Thrust geometries and related sedimentation in the south-central Pyrenean thrust belt is mainly associated to the inversion of the three main thrusts: Boixols, Montsec and Sierras Marginales (Figure I.16 and I.18). Thrusting in the South Central Pyrenees began during Late-Cretaceous with the inversion of the Boixols fault (Puigdefàbregas & Souquet, 1986). Sediment was dispersed toward a west-north-west direction with an open connection to the Atlantic Ocean (Puigdefàbregas and Souquet, 1986).

The first syn-orogenic sediments of the South-Pyrenean Foreland basin consist of late Santonian-Campanian turbidites (Vallcarga formation) deposited during the inversion of the Early Cretaceous extensional faults (Boixols thrust). These Upper Cretaceous sediments were deposited synchronously along the Boixols Thrust front.

The foredeep deposits correspond to the Aren shallow marine sandstones following by the Garumnian fluvial sandstones in response to the emergence of the inner part of the chain in the eastern Pyrenees (Puigdefàbregas et al., 1986). A subsequent stage of the South Pyrenean Foreland Basin resulted from thrust propagation into the foreland during Paleocene-Early Eocene. As a consequence, the Aren and Garumnian formation were detached and carried piggy-back style as part of the Montsec and Sierras Marginales thrust sheets owing to the sequential migration of the thrust front (Puigdefàbregas and Souquet, 1986, Muñoz, 1992). The Tremp and Ager wedge-top basin developed on top of the Montsec thrust and initially under marine condition. The

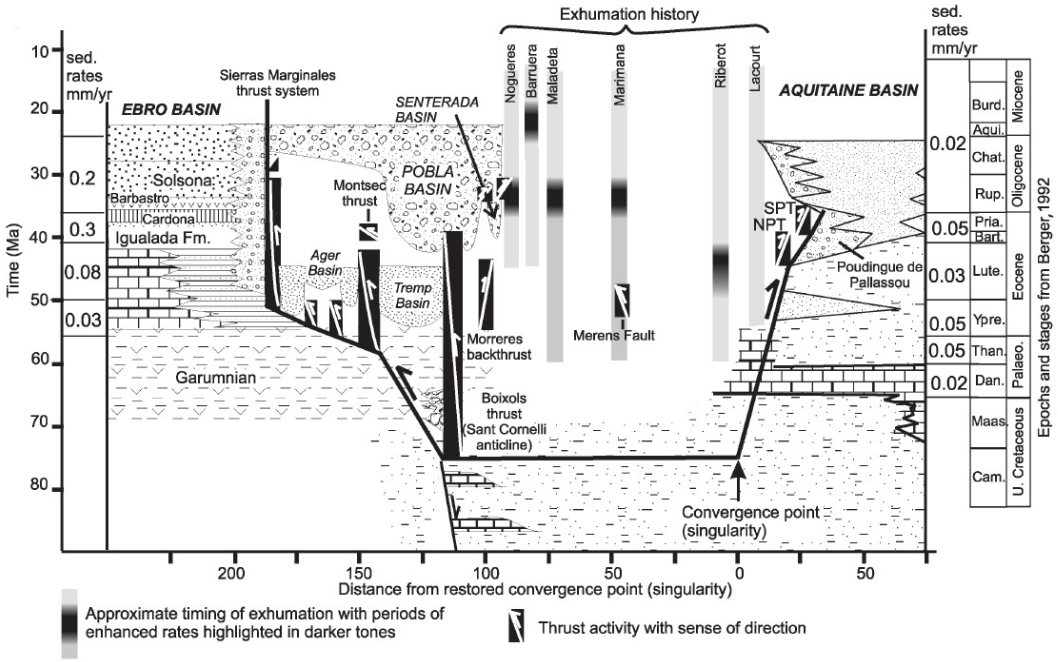

Figure I.16: Chronostratigraphic relation between the timing of thrust shortening, timing of erosional exhumation in the core of the mountain and timing of preserved stratigraphic record in the Ebro pro-foreland basin and Aquitaine retro-foreland basin in the Central Pyrenees from Sinclair et al., (2005).

stratigraphy of the Tremp basin is characterised by the Ilerdian Alveolina Limestone, a transgressive unit at the bottom of the Eocene succession (López-Blanco et al., 2003). Sedimentation continued with the deltaic/tidal Roda and Baronia systems, with a south-southwestward progradation toward the open Atlantic Ocean (López-Blanco et al., 2003). The depositional environment within the wedge-top basins shallowed during middle Eocene with deposition of the Corsa and Castissent fluvial sandstones. The two systems exhibit some interconnection between the Ager and Tremp basins, with a dominant orogen-parallel transport direction, connecting to the Ainsa and marine Jaca basin in the west (Nijman, 1998).

Development of the Pobla and Senterada basins occurred during early Eocene and Oligocene time because of out-of-sequence thrusting recorded by the re-activation of the Boixols thrust and Morreres Backthrust. The fluvial and alluvial deposition within these basins records the transition between orogen-parallel and orogen-transverse sediment dispersal at this time (Whitchurch et al., 2011). The Morreres backthrust partitioned the intramontane basin into two sub-basins: La Pobla de Segur Basin in its hanging-wall and Senterada Basin in its footwall (Mellere, 1994). La Pobla de Segur Conglomerates have a poorly age constrained. However, the formation has an estimated age of Late Eocene to Oligocene time and considered as a post-orogenic infill of an intramontane basin which has not suffered any major tectonic activity. The Pessonada allogroup consist of a proximal-medial alluvial-fan assemblage, generally prograding south-southwestwards (Mellere, 1994). During the middle Eocene, The Pobla Basin developed as underfilled and lacustrine (Ermita formation; Mellere, 1994). Prograding alluvial units of the Montsor and Senterada formations record the progressive northward expansion of drainage catchments during the late Eocene to Oligocene (Beamud et al., 2011; Mellere, 1994). The Montsor and Senterada composition indicates a Nogueres Zone and Axial Zone origin with high grade metamorphic rocks and a variety of Paleozoic clasts (Mellere, 1994).

The Antist Group constitutes the youngest formation of La Pobla de Segur conglomerate and mark the transition to a fully transverse deposition during Oligocene time. Clast lithologies of this formation indicate an Axial Zone origin with diverse Paleozoic metamorphic rocks, Paleozoic and Mesozoic limestones and Triassic sandstones. It has been argued that these Upper Eocene to Lower Miocene continental sediments have draped the entire southern thrust belt flank of the Pyrenees (Coney

et al., 1996) although these deposits are preserved only in isolated locations. The remnant includes the Antist Formation within the Senterada and Pobla basins (Mellere, 1994), the Collegats formation at the top of the Sis paleovalley (Mellere, 1994; Vincent, 2001), The Claramunt conglomerates in the Tremp basin, and the Oliana and Huesca Fan conglomerate units exposed at the Sierras Marginales thrust front, within the Ebro basin (Burbank & Verges, 1994; Burbank et al., 1992; Meigs et al., 1996).

Northern Pyrenees

As predicted by model evolution of foreland basin (Naylor and Sinclair, 2008; Sinclair, 2012), the Aquitaine retro-foreland basin preserves the full stratigraphic record of the Pyrenean growth (Figure I.17). initial sedimentation in the northern Pyrenees was associated with the rifting phase between the Iberian and European plates from Lower Triassic with Lower and Middle Triassic fluvial sandstones and conglomerates (Red Sandstones Group) (Rougier et al., 2016). The Lower-Middle Triassic sediments are overlain by Upper Triassic sediments comprising evaporite to shallow marine deposits (Keuper Group) (Rougier et al., 2016). Sedimentation continued during Jurassic to Early Albian with carbonates, marls and dolomites subdivided into different groups: Black dolomite (Jurassic), Miranda (Berriasan-Barremian) and Pierrelys Groups (Aptian-Albian). Late Albian to Turonian marine clastic Black Flysch Group are characterized by sedimentary breccias rich in clasts of Paleozoic, Black Dolomite and Pierrelys Groups and concentrated in the immediate hanging wall of the NPFT (Rougier et al., 2016) and reach thickness of up to 3.5 km in the NPZ.

The Grey Flysch Group (Middle Cenomanian to end-Santonian) was deposited over a wide area from the Axial Zone to the Aquitaine Platform (Ford et al., 2016) and can reach thickness of more than 1,500 m and unconformably overlies tilted Black Flysch Group strata and external basement in the NPZ (Monod et al., 2014). The Grey Flysch Group is very heterogeneous and is interpreted as turbiditic with reworked platform and slope failure. This unit is considered to record post-rift thermal subsidence (Monod et al., 2014).

Following deposits are only observed north of the North Pyrenean Frontal Thrust. The Petites Pyrénés Group, also known as the Senonian Flysch consists mainly of marine calcareous shales and carbonates and records the first phase of foreland subsidence. This group is confined mainly to the SPZ and thins very rapidly north of the SPT. Eastward

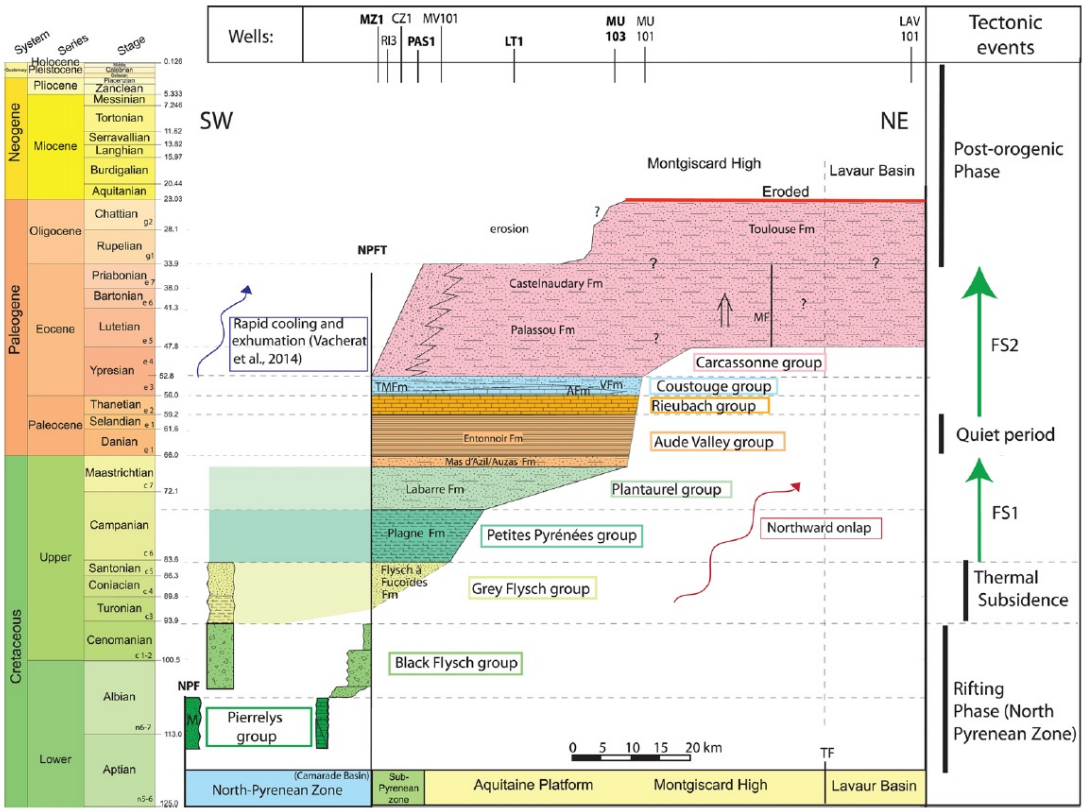

Figure I.17: Chronostratigraphy of the North Pyrenean Zone and Aquitaine Basin along the Ariège ECORS line in the Central-Eastern Northern Pyrenees from Ford et al., (2016).

of the Toulouse Fault is recorded the Plantaurel Group and is characterized by quartzitic sandstones and conglomerates rich in fossilized plant debris deposited in tidal to fluvial environment (Ford et al., 2016). The Aude Valley Group with a formation age of Late Maastrichtian to Thanetian is characterized by continental clastic facies and records low-energy fluvial, palustrine and lacustrine conditions (Rougier et al., 2016). This group can be equated to the Garumnian facies of the Eastern Pyrenees. This succession from early Campanian to end-Maastrichtian marks a first phase of relatively important tectonic subsidence (Fig 2.2.7). The upper Aude Valley Group deposited across the northern foreland with low sedimentation rate and no basin migration indicates a quiet period of tectonic subsidence from Danian to end-Selandian (Ford et al., 2016).

The Rieubash Group is characterized by marine deposits of Danian to Thanetian and is laterally equivalent to, and interfingers with, the upper Valley Group. The Early Ypresian Coustouge Group records a marine transgression that penetrated across the foreland basin to its easternmost closure (Rougier et al., 2016) and comprises limestones, marls and sandstones (Ford et al., 2016). At the end of the Ilerdian, sedimentation became predominantly continental with the deposition of the Carcassonne Group. The lower Carcassonne Group (Upper Ypresian to Priabonian) comprises a continental, mainly clastic succession. On the East, the Palassou Formation consists of mudstones and marls with variable volume of conglomerates, sandstones and limestones (Figure I.16 and I.17). Conglomerates occur mainly in the Sub-Pyrenean Zone, adjacent to the thrust front. Thanetian to Oligocene time in the Northern Pyrenees corresponded to a second phase of subsidence. The early phase is characterised by accelerated tectonic subsidence and increased sedimentation rate and remain high in the second phase (Ford et al., 2016).

The upper Carcassonne Group is dominated by the Toulouse Formation comprising micaschists and quartz pebbles and cobble conglomerates, mica-rich sandstones, siltstones, dolomites and limestones and was deposited across the whole Aquitaine platform with constant high thickness. It onlaps and seals the structures of the Northern Sub-Pyrenean Zone (Rougier et al., 2016) and corresponds to the post-orogenic phase of the Pyrenees.

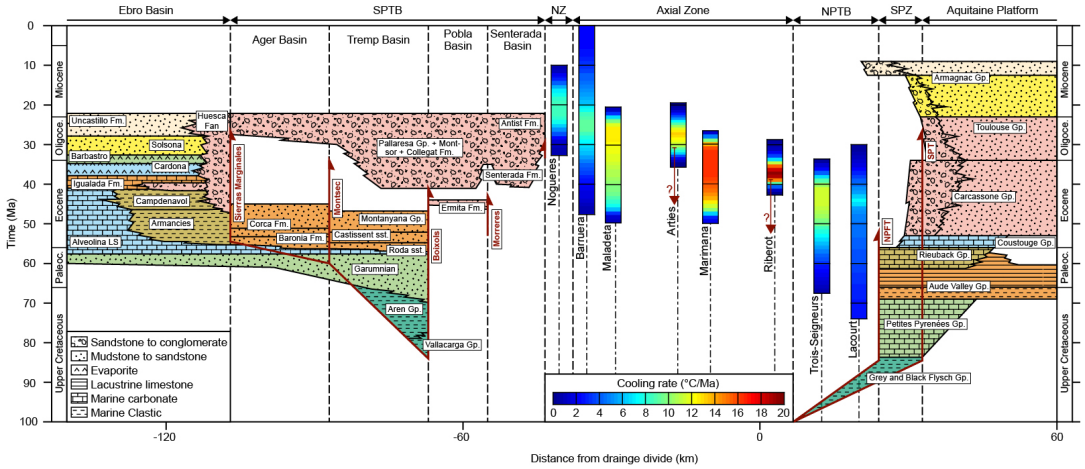

Figure I.18: Chronostratigraphic schema showing relation between exhumation in the Pyrenean range and sedimentation in the north retro-foreland Aquitaine basin and south pro-foreland Ebro basin from Upper Cretaceous to Miocene time. Cooling rate in the Axial Zone and North Pyrenean Zone are plotted in colour (red: high cooling rate; blue: low cooling rate). Stratigraphy of the Aquitaine basin is adapted from Ford et al., (2016) and Rougier et al., (2016). Stratigraphy of the South Pyrenean Thrust Belt and Ebro basin are adapted from Mutti et al., (1998), Vergés (1999), Vergés et al., (2002). SPTB: South Pyrenean Thrust Belt. NZ: Nogueres Zone. NPTB: North Pyrenean Thrust Belt, SPZ: South Pyrenean Zone. NPFT: North Pyrenean Frontal Thrust. SPT: Sub-Pyrenean Thrust.

I.3.6 Geomorphology of the Pyrenees

High elevated and low-gradient surfaces

An important feature of the Pyrenean geomorphology is the presence at high elevation of low-relief erosional surfaces (Figure I.19). These surfaces are considered as the remnance of a single composite planation recently dissected by erosive processes (Babault, Van Den Driessche, et al., 2005; Calvet, 1996) but their formation remains a subject of debate. This planation surface is in discordance with the Pyrenean tectonic structures and is locally overlapped by Upper Miocene continental deposits providing limits ages for their formation (Carbrera et al., 1988; Ortuño et al., 2013; Roca, 1996). Occurrence of these surfaces are on both side of the range and form smooth reliefs at elevation up to 2800 m in the Axial Zone of the Pyrenees (Bosch et al., 2016). The low-gradient surfaces are more or less disrupted by glacial erosion depending on their altitudes (Bosch et al., 2016).

Low-relief surfaces have been considered as the peneplanation near sea level by long-term erosional processes of earlier reliefs such as mountain belt (W. M. Davis, 1899). Therefore, low-relief surfaces situated at high elevation at the Earth surfaces are interpreted because of surface uplift (W. M. Davis, 1899; Farías et al., 2008; Hetzel et al., 2011). For the Eastern Pyrenees, a similar interpretation involving a near 2000 m of uplift has been proposed for the occurrence of low-relief surfaces at high altitudes (Figure I.20) (Calvet, 1996; Calvet & Gunnell, 2008; Gunnell et al., 2009). The most widely accepted conditions for rocks or surfaces uplift are crustal thickening, thinning or heating of the lithosphere, mantle delamination or melting. Uplift by crustal thickening should induce important faulting and folding which is not in agreement with the preservation of relatively flat surfaces. Moreover, exhumaion in the eastern Pyrenees was definitively interrupted after 30 Ma based on thermochronological data. For Calvet and Gunnel (2008), surfaces are all post-collisional, formed by middle Miocene times at 1 km above paleo-sea level and latter uplifted at 1.5 km higher altitude. The uplift event is explained by mantle processes (i.e. crustal root detachment of the Eastern Pyrenees).

Another explanation for the occurrence of low-relief surfaces, in contradiction with the Davis's theory, implies an original formation at high elevation by inhibition of erosion by the drainage system because of piedmont aggradation of detrital sediment (Figure I.19) (Babault, Van Den Driessche, et al., 2005; Bosch, Van Den Driessche, et al., 2016).

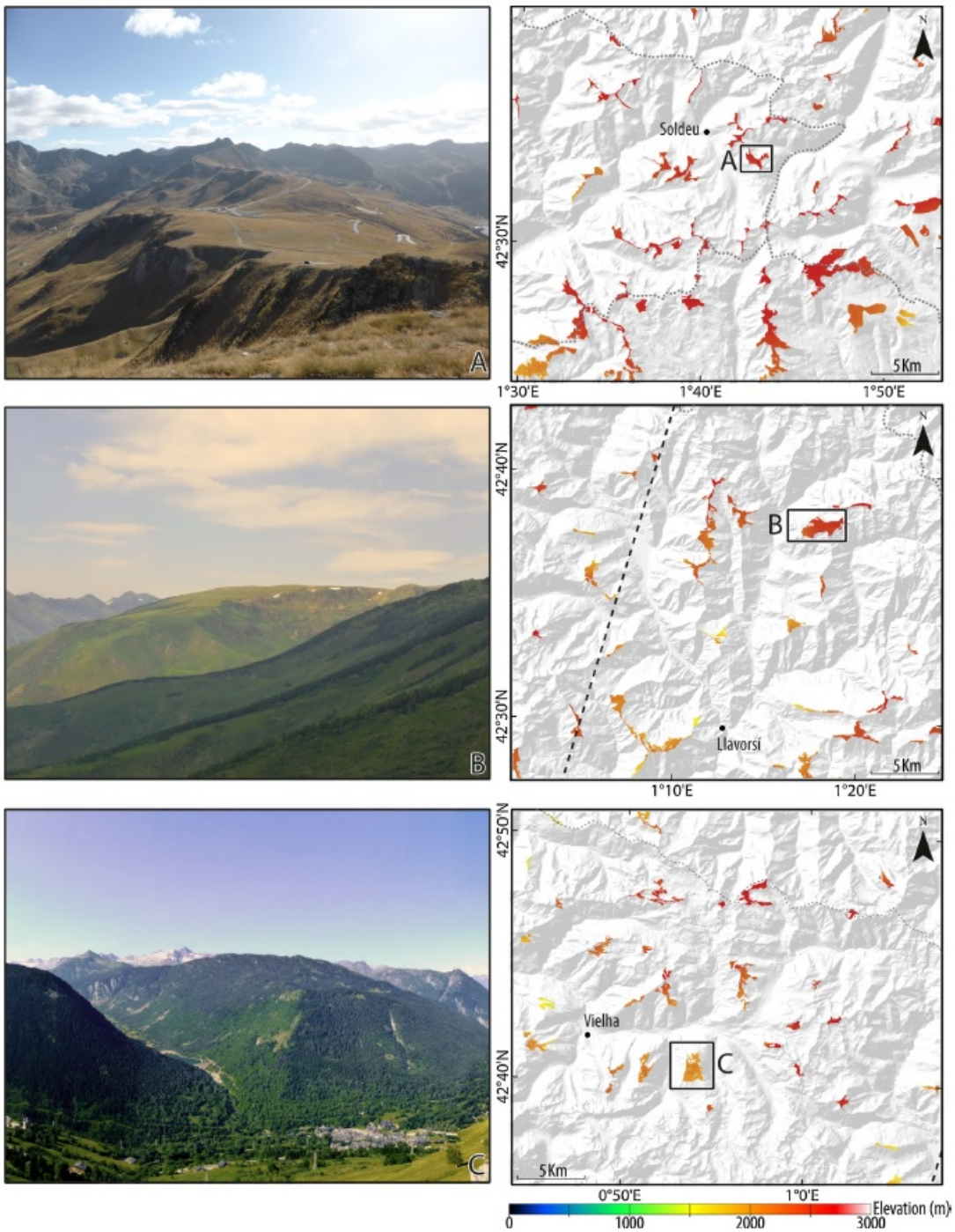

Figure I.19: Example of high-elevation, low-gradient surfaces in the Axial Zone of the Pyrenees from Bosch et al., (2016). Field photos of surfaces (left) and corresponding geographic and topographic location on DEM (right). Top: Pla d'Envalira; middle: Pla de Boldis; bottom: Pla de Prüedo.

This process is well documented for the southern Pyrenees where important discharge of continental detrital sediments, especially conglomerates filled the paleovalleys (i.e. Sis valley, Spain) and rising the base level (Babault, Van Den Driessche, et al., 2005; Coney et al., 1996; Fillon & van der Beek, 2012). Increase of the base level for the southern Pyrenees was enhanced because of the closure of the Ebro foreland basin (Garcia-Castellanos, 2003). A major difference for the northern Pyrenees is the fact that the basin drainage remains external. Coarse sediment on northern side of the Pyrenees are not observed at high elevation as for the southern Pyrenees. Miocene deposit reach elevation of 600-700 m on the northern piedmont. Geologic evidences for the northern side are not as supportive as the southern side of the Pyrenees for this hypothesis. In the Central Pyrenees, the presence of a well documented crustal root (Chevrot et al., 2014) and that actual elevation of the belt is compensated by isostasy agree with surfaces formed at high elevation. On the eastern Pyrenees, crust thinning results rather from the Upper-Oligocene to Lower-Miocene extensional tectonics related to the opening of the gulf of Lyon (L. Jolivet et al., 2015).

Some of the flat surfaces located at high elevation in the Pyrenees are developed over significantly weathered granitic and gneissic rocks (Monod et al., 2016). Weathered profiles exhibit common organization of successive weathered profiles and are characterized by unconsolidated quartz alterites, fissured granites and normal faults cross-cut. Surfaces on Aston massif (i.e. eastern Pyrenees) are deformed by normal faulting (Monod et al., 2016) which are consistent with post-Miocene extension in the Pyrenees. Association between flat surfaces, weathering profiles and normal faulting indicates that surface formation are post-orogenic and may have been developed between the Eocene-Oligocene and Late-Miocene. Subsequently, they are abandoned and incised with step features suggesting an increase of the local relief and recent normal faulting (Monod et al., 2016).

Glacial geomorphology

Predominant erosive agents of the modern Pyrenees are mainly dominated by fluvial erosion. However, the landscape of the Pyrenees highlight different geomorphologic features characteristic of glacial erosion. Main glacial features observed in the Pyrenees are deep U-shaped valleys, cirques and hanging valley types in high mountains.

The majority of present day glacier in the Pyrenees are located in a north or

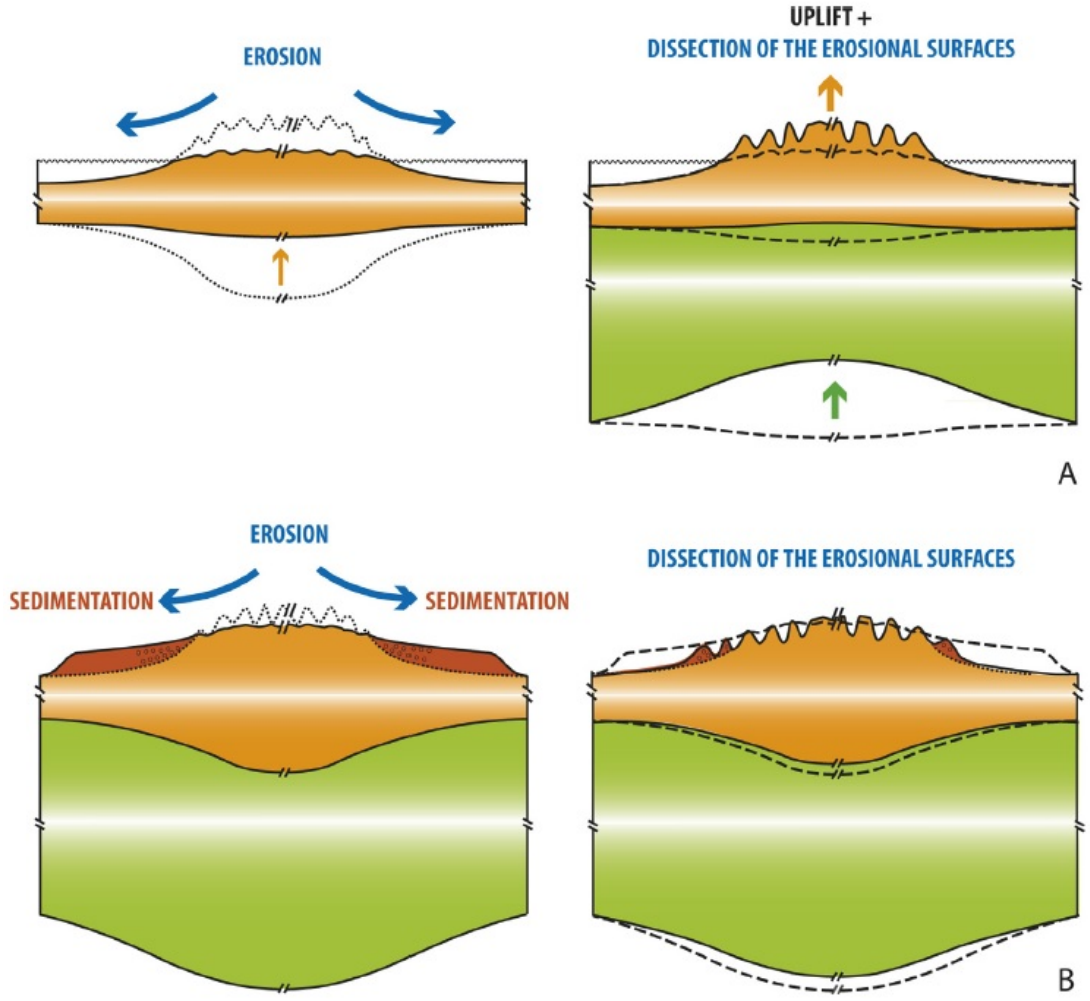

Figure I.20: Two conceptual models for the explanation of low gradient surfaces at high elevation in the Pyrenees. Model A implies that these surfaces are peneplains form near sea level and latter elevated by uplift events (Calvet and Gunnel, 2008). Model B implies that these surfaces are originally formed at high elevation due to erosion inhibition enhanced by thick piedmont sedimentation. Crustal root is conserved for model A at contrary to model B.

north-eastern facing cirques (Taillefer, 1969) with a modern equilibrium line altitude of 3100 m. The Pyrenees comprises a present surface area of glaciers of 8.1 to 12 km2 with only forty-one individual glaciers (Knight, 1999). In contrast, the Quaternary glaciation of the Pyrenees was extensive (Taillefer, 1967; Taillefer, 1957). Evidence of glacial features in the Pyrenees (Jiménez-Sánchez et al., 2013) suggest that a series of glaciation with advances and retreats participate in the shaping of the observed landscape. Maximum glacier advance on the Northern Pyrenees was prior to 38.4 Ka (Andrieu-Ponel et al., 1988) while in the southern Pyrenees maximum glacial extension for Cinca and Gallego valleys occurs at 60 and 85 Ka respectively (Lewis et al., 2009). A glacial asymmetry exist within the Pyrenees with glacier extending to lower elevation and further in the foreland in the northern part than in the southern part of the Pyrenees. This asymmetry is mainly due to the orographic effect with higher precipitation in the northern side and therefore enhanced glacial erosion.

I.4 Objectives of the Thesis

This thesis has the following objectives:

i) Quantify the late syn-orogenic pattern of exhumation of the Central Pyrenees and determine a timing for the termination of active crustal thickening. This first objective is explored with analyses of thermal histories from low-temperature thermochronological data (apatite and zircon fission tracks and apatite helium data) from key plutonic massifs of the Central Pyrenees. the timing of the deceleration in exhumation from thermochronological datasets are discussed in combination with other data on thrust activity, stratigraphic architecture and clast lithology in order to clarify the timing for the late syn- to post-orogenic transition.

ii) Explore the potential effect of different rock types on the landscapes of the Pyrenees. This question is addressed by: 1) determining the rock strength of the different main lithologies of the Pyrenees using Schmidt hammer measurements; 2) performing topographic analyses of the river channel steepnesses along rivers of the main catchments of the Pyrenees. The relationship between rock strength and topographic index are investigated in order to characterise how variations in rock types have affected the topographic development of the Pyrenees.

iii) Investigate the effect of the exhumation of rocks with variable rock strength through time and space on mountainous landscape. We particularly explore the response of rivers along different catchments when exhuming harder rocks and the resulting drainage divide migration. This is achieved by continuous channel steepness calculations during landscape evolution model.

iv) Characterise the response of a mountain range and foreland basin system to the late syn- to post-orogenic in term of topography and sediment flux. Application of a "box-model" to the Northern Pyrenees using inverse modelling and combined with stratigraphic data from the Aquitaine basin provide a mechanism for the formation of post-orogenic sediment drape on the proximal portion of the thrust-wedge. We discuss these results and their effect on the long-term persistence of topography and the formation of low-relief and high elevated surfaces during post-orogenesis.

v) Determine late to post-orogenic exhumation signals in the Pyrenean range related to possible base level change, climate change or intensification of glaciation using very low-temperature thermochronology: $^{4}He/^{3}He$ thermochronology. Because of laboratory problems during $^{4}He/^{3}He$ analyses and the Covid-19 situation during the late stage of this PhD, $^{4}He/^{3}He$ dataset are not presented in this thesis.

Chapter II

LOW-TEMPERATURE THERMOCHRONOLOGY: TECHNIQUES AND APPLICATIONS TO MOUNTAIN RANGES AND FORELAND BASINS

Since the presentation of Ernest Rutherford in 1905 about U-He radioisotopic dating to determine the age of mineral, different thermochronometric systems have been studied and developed. Application of isotopic systems sensible at low and very low-temperature allow the quantification of rock time-temperature (t-T path) evolution and the geological processes which affect their evolution at the surface and in the uppermost part of the crust. The principle which governs this method and most of thermochronometric systems is based on two physical processes: Accumulation of a daughter isotope product by natural radioactive decay of an unstable parent isotope and loss of these daughter isotopes out of the system by thermally processes such as diffusion. Thermochronology exploit then the fact that most dating methods do not provide an age that reflect the time when the rock was formed but provide an indication of the time (thermochronology) when the rock was at a particular temperature, or within a given temperature range (thermochronology). The temperature is using as a proxy of depth and with cooling/heating histories (t-T path) of a sample or a suite of samples, allow to estimate displacement of the rock from depth to surface. Different isotope dating systems show different temperature sensitivities ranging from 900 to 20 °C. The temperature in the crust increase in function of the geothermal gradient ranging generally from 20 to 30 °C. Bedrock exhumation is in most case is explained by faulting

or by erosion, possibly driven by uplift and/or climate change. For our problem involving exhumation of the upper few km of the Earth's crust in mountain-basin domain we need radiometric dating systems sensitive to relatively low-temperatures (<200-250 °C).

This chapter will highlight the basic principle behind three different radiometric systems sensible at different low-temperature and resolution: fission track thermochronometer (zircon and apatite), apatite (U-Th)/He thermochronometer and apatite $^{4}He/^{3}He$ thermochronometer.

Recent effort have been done in order to interpret low-temperature thermochronological data. This chapter will discuss also the development of sampling strategies, interpretation and limitation of low-temperature thermochronological data.

II.1 Fission track thermochronology

Fission track analyses is one of the most developed and used method throughout the geological community to reconstruct thermal histories of rocks in the upper part crust of the Earth. Fission track analyses has been applied to resolve a large number of geological problems as sedimentary provenance, thermal histories of sedimentary basin, structural evolution of mountain range and long-term continental denudation. Fission tracks are damages features cause by the travel of a charged nuclear particles through insulating solids and reflect intense damage on the atomic scale. Natural or spontaneous track in geologic samples are principally produce by the spontaneous fission of the ^{238}U isotope into two positively charged fission fragments that are propelled from each other's. Others heavy isotopes as ^{235}U or ^{232}Th which are potential candidate for spontaneous fissions have a too long half-lives to produce a significant number of tracks. The most accepted model for the formation of fission track is the one of Fleischer et al., (1975) called the ion spike explosion model. This model is summarized in Figure II.1 and consist of three steps: (i) the rapidly moving two positively charged particles along a linear trajectory. (ii) The resulting clusters of positive ions are displaced from their original lattice sites as a result of Coulomb repulsion. (iii) The stressed region relaxes elastically (Fleischer et al., 1975).

II.1.1 Determining a fission track age

As natural fission track can be easily observe optically under a high magnification (x1200) and occurs at a statistically constant rate lead that it is possible to use fission track as a dating method. Fission track dating is based on the same equation than radioactive scheme. To calculate an age, it requires a relative abundance of the amount of radiogenic decay or daughter compare to the original parent isotope product per unit volume. The daughter quantity can be directly quantify by counting the number of spontaneous fission tracks. The parent product cannot be directly know as an amount of ^{238}U have been disintegrating through geological time. To determine the ^{238}U abundance, a similar track-counting approach is used. The sample is irradiated with low-energy thermal neutron in order to induce fission in ^{235}U. A higher thermal neutron would produce an unwanted fission from ^{232}Th and ^{238}U. New fissions (induced tracks) are indicative of the amount of ^{235}U, and, as the ratio ^{238}U/^{235}U is constant in nature, we can estimate the abundance of ^{238}U. Two major techniques are used by scientific community to determine an analytical age: the population detector method and the external detector method.

The population detector method consist on measuring the spontaneous and induced tracks densities on two different aliquots from the same sample. This method implies that (i) the uranium distribution is uniform and (ii) neglects the distribution of crystal ages. The external detector method is the most widely accepted method of dating mineral grain at this time. Figure II.2 summarize the different procedures of this method. The method depends on the measurement of three track densities: ρ_s, ρ_i and ρ_d. Spontaneous fission track (ρ_s) are etched and revealed on an internal polished surface of a mineral grain, whereas induced fission track (ρ_i) are recorded on an external detector.

The external detector method allow (i) to avoid assumption of uniform uranium in population of different grains and uncertainties concerning thermal flux and fission decay constants (Gleadow & Duddy, 1981; Green & Hurford, 1984; Hurford & Green, 1982). (ii) This method is in accord with the International Union of Geological Sciences Working Group's recommended approach (Hurford, 1990). (iii) The possibilities to dated individual grains or crystals. The fission track age for each crystal is then calculated

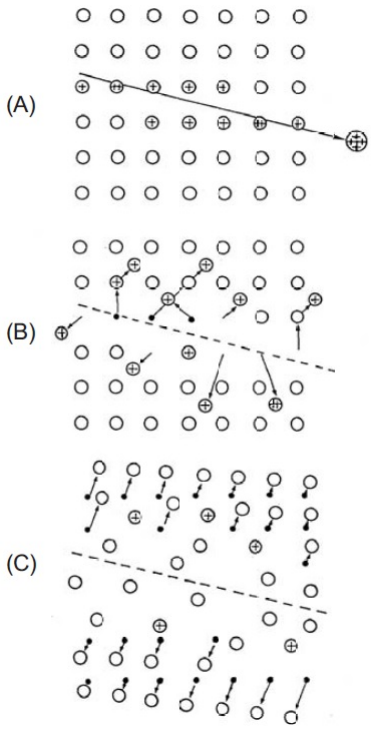

Figure II.1: Schematic representation from Tagami and O'Sullivan, (2005) of the ion spike representation model from (Fleisher et al., 1975) in three steps. (A) The rapidly moving two positively charged particles along a linear trajectory. (B) The resulting clusters of positive ions are displaced from their original lattice sites as a result of Coulomb repulsion. (C) The stressed region relaxes elastically.

using a modified form of the radioactive decay equation:

$$t = \frac{1}{\lambda_d} Ln \left(\lambda_d \frac{\rho_s}{\rho_i} \rho_d \xi g + 1 \right) \tag{II.1}$$

Where t is the age; ρ_s, ρ_i and ρ_d are respectively the spontaneous track density, the induced track density and the track density in a dosimeter; λ_d is the λ decay constant of ^{238}U; g is the geometry factor and ξ is a constant of proportionality which is personal to each analyst (Hurford & Green, 1982). Generally the fission track age is reported as a sort of average of different individual singles grain ages (between 20 and 40). Three different "mean" age are used: the mean, pooled, and central ages. The pooled age is simply the sum of spontaneous count divided by the sum of induced count. The mean age is the arithmetic mean of the individual ratio of spontaneous to induced tracks. The central ages is a more recent development (Galbraith & Laslett, 1993) which compare to others age and represent the weighted mean of the log normal distribution of single grain ages.

II.1.2 Fission track lengths

Fission track dimensions is an important features of the fission track method. Fission tracks have a longer of 10 to 20 μm depending on the material properties of the crystal lattice and a wide ranging from 25-50 Å. However all newly-formed fission tracks display a characteristic track length. Bhandari et al., (1971), suggest that induced tracks in apatites had roughly the same mean length of 15.3 μm. However Green et al., (1981) claimed that induced fission tracks can have a length ranging from 15.3 to 17.2 μm compare to 15.8 to 16.6 μm for the study of Gleadow et al., (1986). This range of length difference between newly-formed tracks and actually observed track is because they are metastable and fade or anneal, which lead to shortening of individual tracks. Track formed in a randomly orientation in three-dimensional space. An important point report by Laslett et al., (1984; 1982) concerning track length annealing is the different probability of tracks of different length to intersect a surface and the consequence on the measurement of track density used in age determination is based on a two-dimensional sample of tracks intersecting an internal surface. The basic idea is the following: The probability for a long track to intersect a surface is greater than for a shorter track. Therefore, as the fission age is determined by counting the surface tracks, it is expected to obtain an older age for a sample with long tracks. A sample which undergo annealing

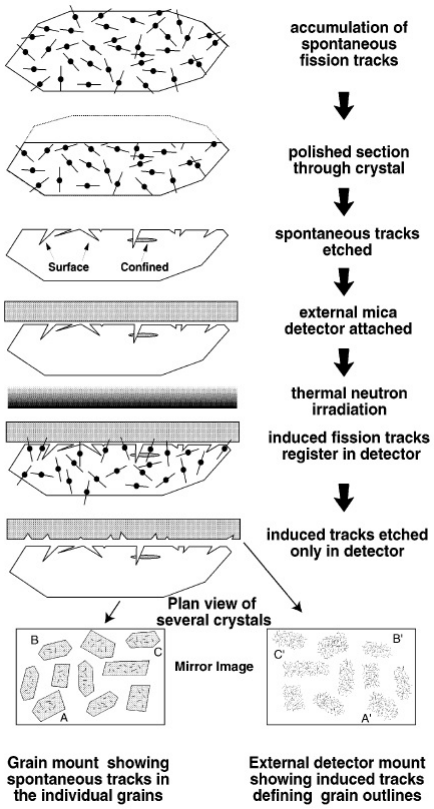

Figure II.2: The external detector from Gallagher et al., (1998) after Hurford and Carter, (1991). The surface of a mineral is polished and etched in order to reveal spontaneous tracks (surface) which are intersecting the mineral surface. Tracks (confined) below the surface can also be revealed by pathway from the surface to the confined track (surface track, cleavage, fracture). A detector is sealed against the grain surface and sent to a nuclear reactor to irradiate the sample with low-energy thermal neutrons, which induces fission in ^{235}U. By counting the number of spontaneous track in the mineral, we estimate the concentration of the daughter product, and by counting the number of induced track on the detector, we estimate the concentration of parent in the mineral.

will result in a lower apparent track density and therefore, an age relatively younger. Experimental works (Ahrens et al., 1970; Tagami et al., 1990) have been done on the control of geochemical-geophysical factors that may cause annealing in crystal as apatites or zircons. These parameters include temperature, time, chemical solution, pressure and ionizing radiation. From all these parameters, temperature combined with time is the most important used commonly in geological applications and leads to an Arrhenious-type relationship for track length evolution after initial formation (Gallagher et al., 1998).

II.1.3 Confined versus Projected track lengths

Track length measurement are described as confined or projected. Projected tracks are those that do intersect the surface of the polished surface of the grain mount. The length of the remaining track or the length projected vertically up to the surface can be truly measure except that we cannot determine how much of the length have been truncated by the surface. Only the showing part of the track can be measured and consequently their lengths cannot be accurately determined (Gleadow et al., 1986). Wagner, (1988) and Wagner and Hejl, (1991) have argued qualitatively that the projected track length distribution contain detailed information. However it have been supported by mathematical calculation, by Galbraith et al., (1990) and Laslett et al., (1994) that the amount of thermal history retrievable from projected track length distribution is limited. Confined tracks are those that are completely below the polished surface and highlight by etchant from pathway using projected tracks, fractures or cleavages. The confined track provide the more robust and reproducible of the true track length distribution (Gleadow et al., 1986; Green et al., 1989). Only horizontal (or track within 15° of horizontal) confined tracks are measured. These tracks can be identified by a distinctive appearance in reflected light with a more or less simultaneous strong backscattered image all along the total length.

It is important to have a clear understanding of the fission track length distribution in order to fully understand the signification of the track age. More, the combination of these two type of data: the fission track age and the track length distribution can provide important information to reconstruct the thermal histories of a sample (Gallagher et al., 1998).

II.1.4 Track length distribution

The amount of annealing recorded in the track length distribution provides a strong indicator of the thermal history it has experienced (Gallagher et al., 1998; Ketcham et al., 2003). Examples of different confined track length distribution are given in Figure II.3. The undisturbed volcanic track length distribution is characterized by a thermal history with a rapid cooling through the PAZ and no prolonged residence between this temperature (60-110 °C) and with no subsequently heating. The mean track length indicative of this history lie between 14 and 15.7 μm with the standard deviation of the distribution range between 0.8 and 1.3 μm with most of them between 0.8 and 1 μm (Gleadow et al., 1986). This distribution characteristic referred as "undisturbed volcanic-type" will not necessarily only be found in volcanic type rock, but only on those which have experienced rapid cooling through the PAZ following by residence at low temperature. This distribution can also be found in non-volcanic rocks like crystalline basement rocks which is diagnostic of a rapid cooling. The undisturbed basement distribution is characterized by shorter mean track length and larger standard deviation and suggest a monotonic cooling from high temperature where tracks are not retained to surface temperature where tracks are retained. This distribution has shorter mean track length and larger standard deviation due by a longer time duration into the PAZ with a mean track length distribution in the range of 12 and 14 μm and a standard deviation between 12 and 14 μm (Gleadow et al., 1986; Green et al., 1986). The third type of distribution correspond to mixed track lengths with a special case for the bimodal distribution when the two components become more separated and well resolved. This distribution is formed by a more complicated thermal history implying at least two history stages. The first track length component is formed by partially thermally annealed tracks and the second component is formed by subsequent later cooling. The shorter component correspond to tracks formed during the first cooling event which have been subsequently returned to the PAZ and partially annealed while the longer track represent those formed during the latter cooling event towards low temperatures. Mixed and bimodal distribution are characterized by a mean track length below 13 μm and a standard deviation above 2 μm (Gleadow et al., 1986).

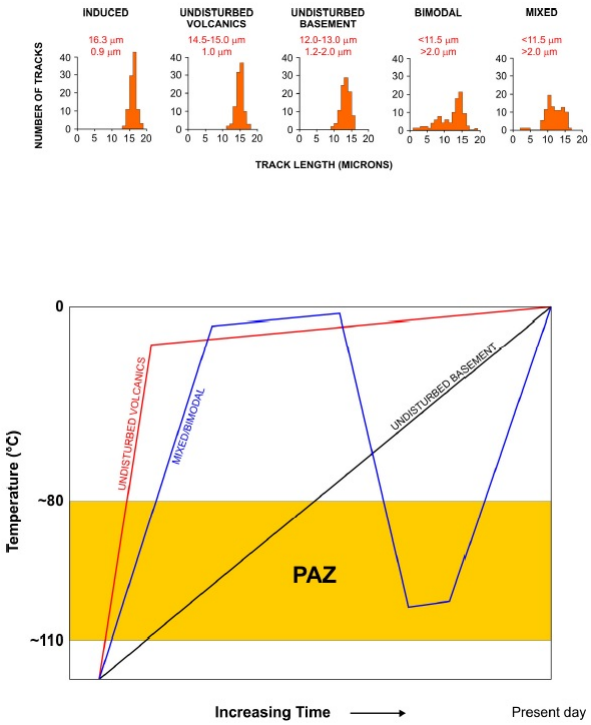

Figure II.3: Set of possible confined track length distribution and their associated possible thermal histories from Lynn, (2005) modified after Gleadow et al., (1986). Values in red on track length distributions graph correspond to the mean track lengths and standard deviations.

II.1.5 Fission track annealing and AFT partial annealing zone (PAZ)

Fission track in apatite shorten or anneal irreversibly and instantaneously over geological time at elevated temperature because of thermally activated diffusion processes. The temperature range over which annealing occurs varies for different crystals and depends of the heating rate. As crystals used for this study for fission track thermochronology are apatites and zircons and they correspond to the most commonly analysed crystals we will focus on the annealing characteristics of these two minerals.

The concept of closure temperature introduce by Dodson, (1973), defined as its temperature at the time corresponding to its apparent age. For thermally activated diffusion it is given by

$$T_c = R/[Eln(A\tau D_0/\alpha^2)] \tag{II.2}$$

Where R is the gas constant; E the activation energy; τ the time constant with which the diffusion coefficient D diminishes; α is a characteristic diffusion size; and A is a numerical constant depending on geometry and decay constant of parent. The time constant τ is related to cooling rate by:

$$\tau = R/\frac{EdT^{-1}}{dt} \tag{II.3}$$

This concept is generally an oversimplification. For example, 110±10 °C is accepted as the closure temperature for apatite fission track method. However, significant annealing occurs at temperature between this closure temperature and 60 °C (Gleadow, 1981). This temperature range where fission tracks suffer an amount of annealing but not enough to be completely anneal is referred as the partial retention zone (PAZ) (Fitzgerald et al., 1995; M. Wagner et al., 1992). The actual comprehension and knowledge of the annealing process of fission track for the application of these data to geological problem derived from an extensive set of well-controlled laboratory annealing data experiments. The results from these numerous annealing experiments have previously been summarized by Fleischer et al., (1975) and Wagner et al., (1992). Some of the major results inferred from these experiment are summarized below:

1. The crystallographic orientation of the fission tracks have an effect on the track annealing rate dr/dt .For example fission tracks with a parallel orientation to the crystal c-axis anneal at a slower rate than fission tracks with a perpendicular

orientation for both apatite (Donelick & Miller, 1991; Green et al., 1986) and zircon (Tagami et al., 1990).

2. Annealing rate depends upon the chemical composition of a mineral. For example, because apatites can accommodate a variety of anions in its crystalline structure especially with fluorine (F), chlorine (CL) and Hydroxyl (OH), the relative proportion of these elements may be an important control on annealing rate. Based on geological observations, it has been know that apatites rich in Cl content relative to F seem to be more resistant to annealing compare to apatites rich in F content compare to Cl (Donelick, 1991; Gleadow, 1981; Green et al., 1986; O'Sullivan & Parrish, 1995). Laslett and Galbraith, (1996) using laboratory annealing experiments extrapolate a new model which is consistent with the general observation that F-apatite is expected to anneal more easily than the Durango apatite.

3. Difference of track annealing rate can rise from the use of different etchants. An etched figure represents the geometrical figure formed by the intersection of an etched pit (a fission track or other crystallographic imperfection) and the c-axis parallel polished and etched apatite surface. In order to quantity this effect a parameter known as Dpar is used and correspond to the arithmetic mean fission track etch figure diameter parallel to the crystallographic c-axis (Donelick, 2005). Apatite grains with relatively low values of Dpar ($\leq$1.75 μm for apatite grains etched for 20 s in 5.5 M HNO3 at 21°C) anneal rapidly and can be generally considered fast-annealing. Apatite grains with relatively high values of Dpar (>1.75 μm for apatite grains etched for 20 s in 5.5 M HNO3 at 21°C) usually anneal more slowly.

4. Accumulation of radiation damage in crystal such as zircon and sphene may have a control on the annealing rate. Experimental laboratory data suggest that fission tracks in zircon which have experience more radiation damage (i.e. older zircons) anneal slower than those which have experience less radiation damage (i.e. younger zircons) (Kasuya & Naeser, 1988; Rahn et al., 2004; R. Yamada et al., 1998).

5. The annealing rate depends on pressure (Wendt et al., 2002). Donelick, (2005) performed a limited range of variable pressure experiments in Durango apatites but did not observed a significant effect up to 1 kbar. Others experiments show no such dependence on the annealing rate on zircon (Brix et al., 2002; Fleischer et al.,

1975; K. Yamada et al., 2003). However similar studies report conflict results in term of a pressure influence (Kohn et al., 2003; Wendt et al., 2002).

6. Laboratory experiments performed under isothermal and variable temperature conditions have been used to construct an empirical mathematical description of the annealing process expressed in terms of the reduction in track lengths for a given temperature over a particular time interval. Numerical FT annealing model have been investigated and improved for both apatite (Carlson, 1990; K. d. Crowley et al., 1991; Ketcham et al., 2007; Ketcham et al., 1999; Laslett & Galbraith, 1996; Laslett et al., 1987) and zircon (Galbraith & Laslett, 1997; Tagami et al., 1998; R. Yamada et al., 2007; R. Yamada et al., 1995) (Figure II.4). The first robust apatite fission track annealing model formulate as an Arrhenius-type model is given by Laslett et al., (1987). The most used track annealing model actually is the multikinetic model of Ketcham et al., (2007) which allow to take into account effect of c-axis projection, composition, etch-figure dimension and unit-cell parameters. The last fission track annealing model for zircon is the one of Yamada et al., (2007). From this study two type of models are constructed. The first one consist of a hybrid-linear model (fanning-linear model at high temperature and parallel-linear model at low temperature connected with a transitional temperature zone) which should be used for thermal history problem of short-time phenomena. The second one consist of a parallel-curvilinear model for thermal history problems with time range longer than several hours.

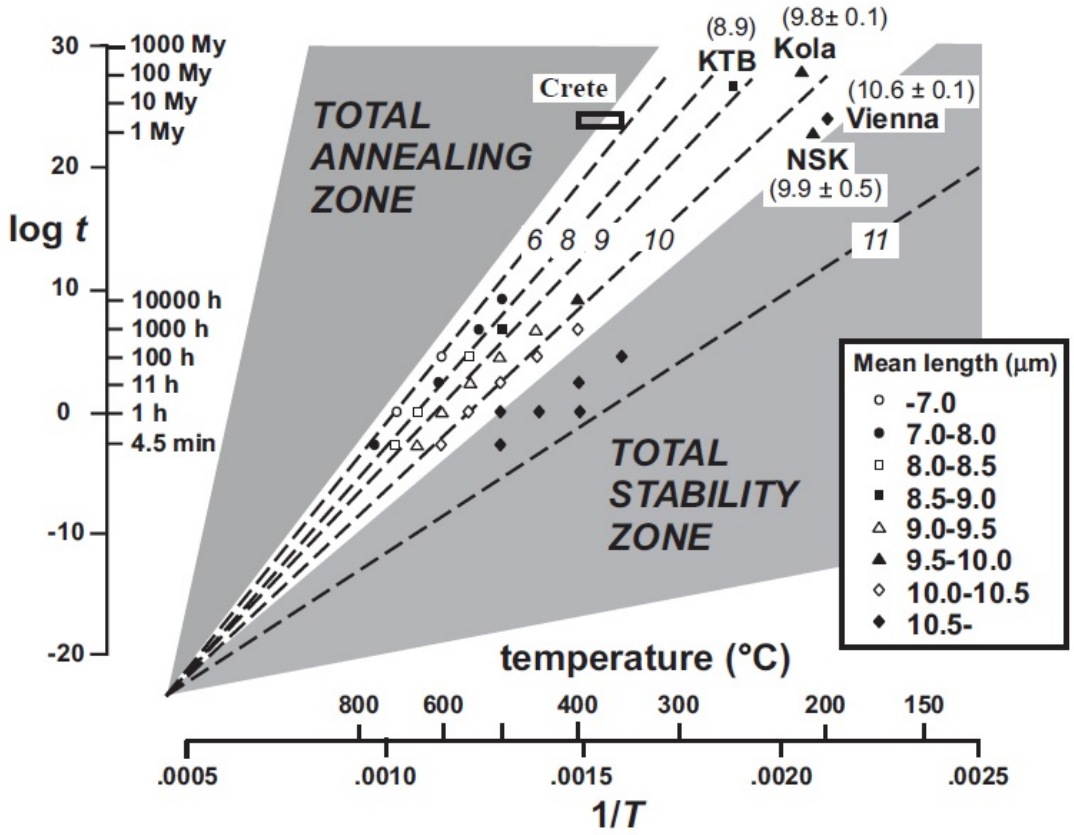

Figure II.4: Arrhenious plot showing the design points of the laboratory annealing experiments of spontaneous fission tracks in zircons as well as contour lines for the fitted fanning model extrapolated to geological time scale (Tagami et al., 1998; R. Yamada et al., 1995; model after Galbraith and Laslett, 1997). Three temperature zone can be defined as first-order approximation of fission track annealing: the total annealing zone (TAZ) where tracks are unstable and instantaneously faded after their formation; the total stability zone (TSZ) where tracks are considered as thermally stable and allow an increase of tracks through time; the partial annealing zone (PAZ) where track are partially stable leading to partially annealing and shortening.

II.2 Apatite (U+Th+Sm)/He thermochronology

The decay of uranium and thorium and the production of helium as the final disintegration product has been known since the discovery of radioactivity (Rutherford, 1905). If the rate of the production of helium by radium is known, by measuring the observed volume of helium stored and the amount of radium present it is possible to estimate the age of the mineral giving rise to the development of an absolute geological time scale (Rutherford, 1905; Strutt, 1905). However, following these initial studies, it was recognized that measuring helium concentration was not reliable and often lead to unreasonably young ages (Hurley, 1954). This idea was supported by diffusive loss of helium possibly associated with radiation damage or to the ejection of high energy alpha particles from the phased being dated (Hurley, 1954). Moreover, with the development in the year 1950 of the K-Ar system and other methods, lead (U+Th)/He to being seen as a suspect method and relegated it to abandonment and non-development during several decades (Zeitler et al., 1987). Renew interest of the method was performed by Zeitler et al., (1987) and show that for the case of apatites, apatite helium (AHe) ages can interpret cooling through very low-temperature with a closure temperature of 100 °C. This study shown that for the case of a rapid cooling, apatites from Durango fluorapatite (Young et al., 1969) had retained ^{4}He during a time consistent than those derived by other techniques (K-Ar and apatite fission track methods, Zeitler et al., 1987). Frequently observed too young ages can be explain by the fact that U-Th-He record a much later phase of the thermal history of a sample (Zeitler et al., 1987). Subsequent studies have confirmed this low closure temperature (Lippolt et al., 1994; Warnock et al., 1997; Wolf et al., 1996) and high-precision stepped-heating diffusion experiments record the time when a sample passed through 68±5 °C (Farley, 2000). At higher temperatures diffusive processes remove He as fast as it is produced by radioactive decay. Apatite helium dating provide an important tools for investigated the latest stages of cooling in the uppermost part of the crust.

Like apatite fission track thermochronology, apatite helium dating have been used to study geologic process (generally tectonism) that cause rock uplift. Because of the lower temperature closure of the AHe system, it is possible to detect and quantify lower magnitude of cooling with a better resolution (Armstrong et al., 2003). As AHe system is sensible at low temperature, AHe ages are strongly sensible to perturbation

of the geothermal gradient and most notably isotherms which become more and more influenced by the surface topography as we get closer to the surface. Sensitivity of AHe can then be used to infer the evolution of topography and interaction between topography and exhumation (Braun, 2002; House et al., 1998). Topographic evolution may be caused by tectonism as faulting but is also the cause of interaction between tectonics, climate and erosion. In this regard AHe system may provide an important tool to understand the different interplay between surface processes as river incision or glacial erosion which controls the time-temperature of the uppermost part of the crust, erosion by tectonic uplift and the long-term evolution of landscape.

II.2.1 Principles of (U+Th)/He thermochronology

(U-Th)/He dating is based on the production of alpha particles (i.e. nuclei of 4He) during the natural radioactive decay of elements ^{238}U, ^{235}U and ^{232}Th (Farley, 2002) to stable isotopes ^{206}Pb, ^{207}Pb and ^{208}Pb. Another source for ^{4}He production, generally considered as insignificant, is the decay of ^{147}Sm to ^{143}Nd (Reiners et al., 2002). The quantity of radiogenic 4He, assuming no extraneous sources of He or subsequent He loss is expressed by the following equation:

$$^{4}He = 8x^{238}U(e^{\lambda_{238}t-1}) + 7x^{235}U(e^{\lambda_{235}t-1}) +^{232} Th(e^{\lambda_{232}t-1}) \qquad \text{(II.4)}$$

Where ^{4}He, ^{238}U, ^{235}U and ^{232}Th are the present day atoms, t is the time since He accumulation commenced or the AHe age and λ are the decay constants of the respective decay series (Farley, 2002; Ehlers and Farley, 2003). Measurement of parent and daughter isotopes define the time since closure. This equation assume no initial 4He present in the sample before the accumulation. This assumption is generally valid because concentration of helium in the atmosphere is very low (5ppm compare to 1% for 40Ar where a substantial fraction of Ar is frequently taken in account for K/Ar or Ar/Ar dating). Selective picking of apatite crystal free of fluid or minerals which may hosting 4He is to be avoid. There is no fundamental assumption on the range of accessible age as AHe ages can range from few hundred kyr to 4.56 Ga.

The most widely accepted procedure and use in laboratories today for 4He analyse involves in vacuo extraction of He by heating in a furnace (Lippolt et al., 1994; Wolf et al., 1996; Zeitler et al., 1987) or with a laser (House et al., 2000; Reiners et al., 2002). The released gas is purified, a 3He spike is added, and the resulting mixture analysed in

most cases by a quadrupole mass spectrometer. After removal from the vacuum system, the apatites are dissolved and U and Th analysed, usually by inductively coupled plasma mass spectrometry (ICP-MS).

α ejection

During radiogenic decay of U and Th, α particles are produced and emit with sufficient kinetic energy to travel significant distance through the crystal before coming to rest (Farley et al., 1996). As a consequence, α particles may be ejected from crystal edges or injected from surrounding crystal and introduce a segregation between parent and daughter. Alpha ejection effect can be considered as negligible at the rock scale but may become substantial at the scale of a crystal (Farley et al., 1996). If α ejection effect is not corrected, this can cause too old or too young ages in some crystal areas and a total errors of up to 10% in He ages. Figure II.5 show an approximate factor by which the measured age have to be multiplied in function of the prism cross section. Alpha-ejection correction factor range from 1.2 to 1.5 for apatite with a prism cross-section ranging from 175 to 75 μm. It is also show the uncertainties associated to the α-ejection factor which increase as the α-ejection factor increase. For grains superior to about 125 μm in cross-section the uncertainty is about $\pm$2% which is comparable to the analytical error in isotopic measurement and goes up to about $\pm$10% for apatites with very small prism cross-section.

Every α decay within the U, Th and Sm series has a characteristic kinetic energy and so a characteristic travel distance (Ziegler, 1977), within a specific crystal. These distances range from a minimum of 11 μm to a maximum of 34 μm. For most common minerals, density is the strongest control on the alpha stopping distance for a given energy. For examples, increase of density for the common datable mineral: apatite (3.2 g.cm^{-3}), titanite (3.6 g.cm^{-3}) to zircon (4.4 g.cm^{-3}), the average α stopping distance in the 238U series drop respectively from 19.7, 17.8 to 16.6 μm (Farley et al., 1996). For apatite the approximate stopping distance is taken as 20 μm. However, knowing the concentration of U, Th and Sm, it is possible to calculate a more precise α stopping distance in the apatite crystal from this equation:

$$\alpha_{ejection} = SD_{238}R_{238} + SD_{235}R_{235} + SD_{232}R_{232} + SD_{147}R_{147} \qquad \text{(II.5)}$$

Where SD corresponds to the α stopping distance of , ^{238}U, ^{235}U, ^{238}Th and ^{238}Sm

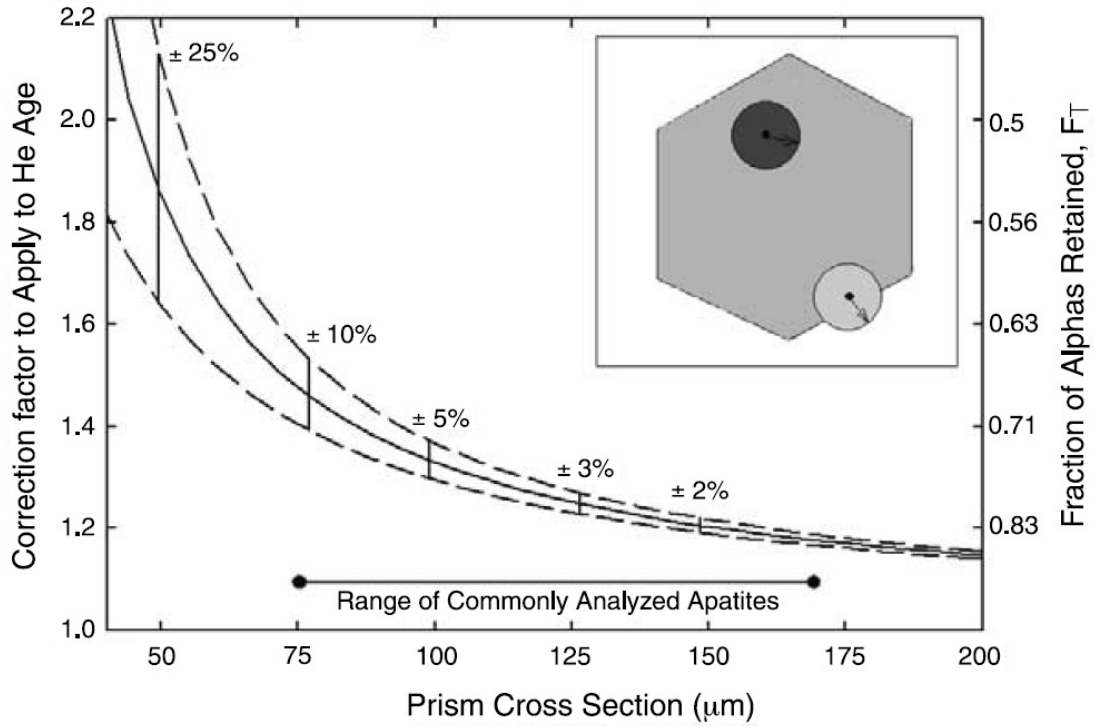

Figure II.5: The effect of α ejection on apatite He ages from Ehlers and Farley, (2003). Inside figure is a schematic model which show the possible travel of He atoms inside the host apatite according to parent nucleus position. For parent nuclei more than 20 μm from the crystal edge, all He are retained inside the crystal (black circle). For parent nuclei less than 20 μm from the crystal edge, a fraction of He particles is ejected from the crystal (light circle). The curves highlight approximately the correction factor depending the crystal prism cross section to apply to the He ages in order to take into account alpha ejection.

with:

$$R_{238} = \frac{8}{4.47}\frac{[U]}{concsum}0.9927432 \tag{II.6}$$

$$R_{235} = \frac{7}{0.704}\frac{[U]}{concsum}0.007252268 \tag{II.7}$$

$$R_{232} = \frac{6}{14.05}\frac{[Th]}{concsum} \tag{II.8}$$

$$R_{147} = \frac{0.1499}{106}\frac{[Sm]}{concsum} \tag{II.9}$$

Where U, Th, Sm are respectively the concentration of uranium, thorium and samarium with:

$$concsum = [U]\left(8\frac{0.99274732}{4.47} + 7\frac{0.007252268}{0.704}\right) + [Th]\frac{6}{14.05} + [Sm]\frac{0.1499}{106} \tag{II.10}$$

Depending on the parent nucleus position different scenarios can occurred and are represented in Figure II.5. If a parent nucleus is in a position greater than the α stopping distance from the edge of the crystal then whatever the α vector is, it will always been retained within the crystal. A second scenario is if the parent nucleus is located between the edges of the crystal and the α stopping distance, then there is a chance than the α particles was ejected from the crystal depending of the α vectors. This probability for the α particles to be ejected rise to 50% if the nucleus radius is located on the crystal edge. The last scenario implies an implementation of α particles to the crystal from a parent nucleus which lie outside of the crystal.

If the last scenario is neglected, then the distribution of α particles along a crystal cross-section is display in Figure II.6, complete retention of α particles is recorded in the core of the crystal decreasing up to 50% from 20 μm from the edge. This phenomenon is then restricted to the outermost 20 μm of the crystal. A solution to resolve this problem is to remove chemically or mechanically the surface of the grain to eliminate the effect (Farley, 2002). However, for the case of apatite helium dating, the He diffusion domain correspond to the grain itself (Bahr et al., 1994; Farley, 2000; Reiners & Farley, 1999) and because the crystal edge correspond generally to the site of diffusional helium loss, it is expected to have a lower concentration of He. Removal of this section of the crystal will tend then to implement a bias in the age estimation. As this effect is a function of the thermal histories of the samples, removal approach for large crystals (diffusion gradient is on a same longer length-scale than α-ejection) or for crystals which have experienced a fast cooling, may be appropriate. However, surface removal will implicate in general erroneous ages.

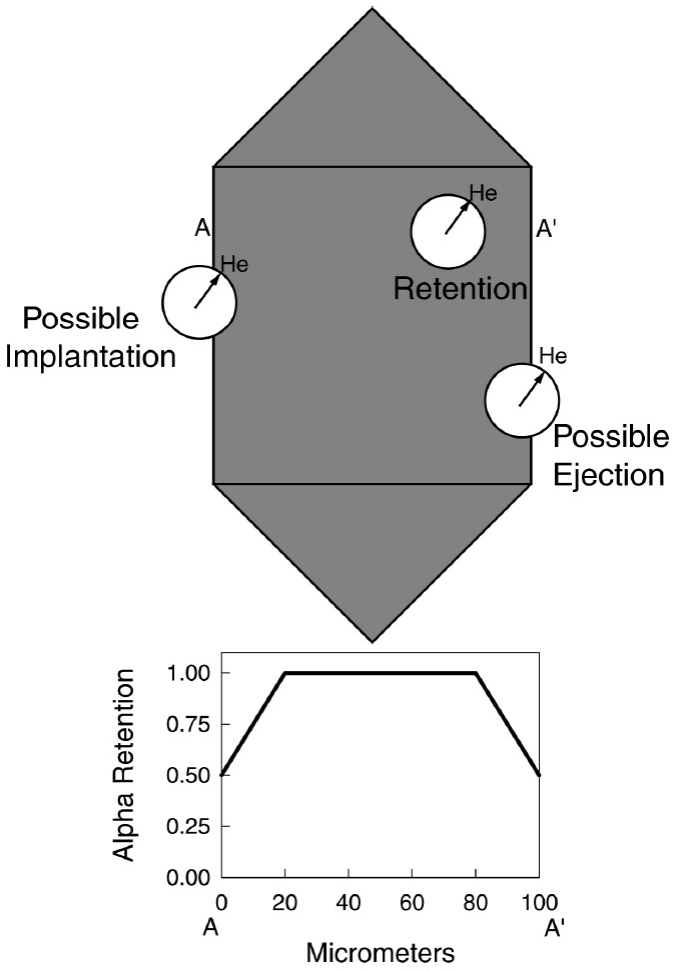

Figure II.6: The effect of α stopping distance on the He retention along an apatite cross-section from Farley, (2002). The upper figure show three different scenarios depending on the location of the nucleus parent within the crystal. 1) α retention, 2) possible α retention and 3) possible α implementation. The center of each circles correspond to the location of the U, Th or Sm nuclide and the edges of each circles correspond to the maximum distance where the α product may rest. Arrays from the circle centers to the edges show a possible trajectories. Lower figure display schematically how α retention changes along apatite c-axis perpendicular cross-section.

In order to take account of the α ejection effect, a mathematical frameworks have been developed in order to modelled the fraction α retained (F_t)in crystals of various dimensions and to correct AHe ages. As surface-to-volume ratio and the distribution of parent atoms relative to the surface control the magnitude of α ejection, the dimensions of the crystal must be accurately determined. Several assumptions are required:

1) Implantation from the surrounding matrix is insignificant in order to only consider α ejection. In most datable mineral suitable for He dating, the concentration of parent nuclides (U, Th and Sm) contrast largely between the mineral being dated and the host rock. Implementation of α particles from the host rock is very few compare to the concentration of parent nuclides and in-situ production of He (Farley, 2002).

2) The distribution of U and Th in the crystal being dated must be specified (Farley, 2002). In general case, the α ejection is calculated assuming a homogeneous spatial distribution of U and Th, which is not always correct. Alpha ejection can be calculated for zoned crystal (Farley et al., 1996; Meesters & Dunai, 2002). However it is generally not possible to date grains in which zonation has already been measured. Homogeneity is then assumed or zonation is characterized from a selection of different crystals from the same sample.

Solutions for the α-ejection, in accord with intuition, show that the two most important parameters controlling the total fraction of α particles in a crystal are the surface to volume ratio (β) of the crystal and the α stopping distance. The geometry that most closely describes natural apatite is an isotropic, symmetrical, hexagonal prism. This have been modelled by Farley (2002) to be:

$$F_t = 1 + \alpha_1\beta + \alpha_2\beta^2 \tag{II.11}$$

Where, $\beta = (2.31L + 2R)/(RL)$ and correspond to the surface to volume ratio for a hexagonal prism R is the half distance between opposing apices, L is the length) and α_1 and α_2 are coefficients obtained through iterative modelling (Farley et al., 1996; Farley, 2002). As mentioned above the magnitude of the α-ejection correction F_t depends on the surface to volume ratio, the distribution of parent elements and the α stopping distance. To obtain an α-ejection-corrected age, the measured age have to be divided by the α-ejection correction factor as:

$$He_{corrected-age} = \frac{He_{non-corrected-age}}{F_t} \tag{II.12}$$

Resulting from α-ejection effect, crystals with relatively small values of β (large prism

widths) affected by α-ejection required a small FT correction, whereas those with larger β values (small prism widths) which have a greater percentage area affected by α-ejection will require a large F_t correction. In order to calculate a F_t correction, the width and length of an apatite crystal must be accurately measured. The nature of apatite termination are also noted (flat/parallel, good pyramidal or irregular). Figure II.7 illustrate the α-ejection correction factor F_t in function of the crystal geometry (apatite hexagonal prism width, surface to volume ratio and equivalent radius).

II.2.2 Diffusion behaviour of helium in apatite

Knowledge of the He-retention and diffusion characteristics of the apatite is a critical parameter for correct interpretation of (U+Th)/He data. It is moreover important as actually the application of the apatite (U-Th)/He method is the assessment of cooling histories. As often with low-temperature thermochronological system, the transition from loss to retention of helium in apatites occurs over a range of temperatures. This transitional region is known as the Partial Retention Zone (PRZ) and can be defined as the range of temperatures where the age fall between 90% to 10% of the holding time, i.e. the temperature range where He age changes most rapidly with temperature (Wolf et al., 1998). For the case of apatite, at high temperature $< 265°C$ no helium is retained and is diffuse out of the system over geological time (Farley, 2000; Wolf et al., 1996). In order to use the apatite (U+Th)/He dating system the diffusion behaviour have to be accurately quantify to establish the temperature range over the system is sensitive. Several studies have documented the temperature control of He diffusion in apatites through step heating experiments (Farley, 2000; Lippolt et al., 1994; Reiners & Farley, 1999; Warnock et al., 1997; Wolf et al., 1996; Zeitler et al., 1987). At temperature ¡265°C, He diffusion plots on an extremely linear Arrhenius array (Farley, 2000) suggesting that thermally-activated process is the controlling parameter on He loss from the crystal lattice (Farley, 2000). Under these condition, the expression of diffusivity in function of temperature is defined by the following relationship:

$$\frac{D}{\alpha^2} = \frac{D_0}{\alpha^2} exp(-E_a/RT) \tag{II.13}$$

Where D is the diffusivity; D_0 the diffusivity at infinite temperature; E_a the activation energy; R the gas constant; T the temperature; and α is the diffusion domain radius (Fechtig & Kalbitzer, 1966). In Durango apatite, the quantity D/α^2 varies with grain

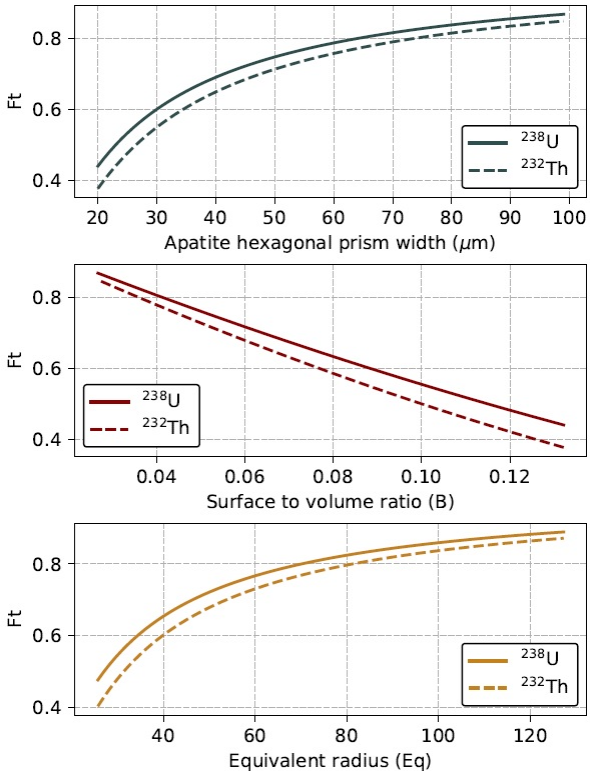

Figure II.7: The effect of α-ejection on He retention in an apatite hexagonal prism. Ft is the total fraction of alphas retained within the crystal, assumed here to have a length/width ratio of 3. The upper plot show the α-ejection correction in function of the apatite hexagonal prism width in μm. The middle plot show the α-ejection correction in function of the surface to volume ratio (B). The lower plot show the α-ejection correction in function of the equivalent radius (Eq). The ^{238}U and ^{232}Th different curves are due to the difference in stopping α-ejection distances for ^{238}U and ^{235}U. ^{235}U curve should be between ^{238}U and ^{232}Th curves while ^{147}Sm curve should be below the ^{238}U curve. The different curve are calculated from equation and coefficient presented in Farley et al., (1996) and Farley, (2002).

size in the manner expected if the diffusion domain is the grain itself (Farley, 2002). The relevant dimension for diffusion is thus the prism radius, as this is the shortest pathway for He loss and with prism length being of secondary importance (Farley, 2000, 2002). Laboratory measurements indicate that radiogenic He is retained in apatite under mean Earth surface conditions, but is lost by diffusion at only slightly higher temperatures (Lippolt et al., 1994; Wolf et al., 1996; Zeitler et al., 1987). First estimation of the closure temperature of the apatite (U+Th)/He is at low temperatures (¡100°C) by Zeitler et al., (1987). Based on laboratory diffusivities, the He closure temperature in apatite, assuming a cooling rate of 10 °C/Ma is estimated of about 75±5°C by Wolf et al., (1996). Other laboratory experiments involving Durango apatites estimate an activation energy for He diffusion of 33±0.5 kcal/mol which implies a He closure temperature for a grain of 100 μm radius of 68°C/Ma assuming again a cooling rate of 10 °C/Ma (Farley, 2000). This closure temperature varies by ±5°C for grains ranging from 50 to 150 μm (Farley, 2000). Wolf et al., (1998) demonstrates also with the analytical solution of the He production-diffusion equation and published diffusivity data that the He partial retention zone in apatite is ranging between 40°C and 85°C. Calibration studies were also performed using samples from boreholes where the geothermal gradient is established. Warnock et al., (1997) present U-Th/He age from quickly cooled plutonic rocks which show good helium retention and U-Th/He ages from borehole in Germany younger than or equal to that for the apatite fission track method. That indicate a closure temperature less or equal to that for AFT method. Other studies from boreholes samples are performed in the Otway Basin, Australia (House et al., 1999) or in the White Mountains, California (Stockli et al., 2000).

II.2.3 Natural radiation damage

(U+Th)/He ages is based on alpha production from natural radioactive decay of U and Th, and on ejection and diffusion of these alpha particles. These naturally occurring radioactivity can alter the mineral's structures by introducing isolated defects and vacancies (Ewing et al., 1995). Several authors (Green & Duddy, 2006; Shuster et al., 2006) have proposed that α-recoil damage in apatite is correlated with changes in He diffusivity. In fact during uranium or thorium decay and alpha emission associated, the helium particles itself does not induce important crystal damage. However energetic recoil of U and Th particles can induce a large level of disorder in the crystalline structure

of the apatite. Then, more the concentration of U and Th is important (referenced as eU, with $eU = [U] + 0.24[Th]$ more the quantity of damage link to the disintegration of U and Th particles is important and more the 4He retention increase. Sites of radiation damage can act as traps for He particles as the activation energy (Ea) needed for He particles to move out of a trap is greater than the activation energy needed to move into an undamaged crystal (Shuster et al., 2006). The presence of isolated sites of radiation damage can then decrease the net rate of helium mobility and therefore increase helium retention at a given temperature. This effect have been called as "Trapping model" (Shuster et al., 2006). Green et al., (2006) showed this effect by comparing FT and (U+Th)/He data. They demonstrated that mismatch between FT and (U+Th)/He age scale with the density of radioactive decay. This change in He kinetics could explain the "too old" AHe ages, especially in case of slowly-cooled basement where α-recoil damage would be important. An important parameter not considering in the model of Shuster et al., (2006) is the annealing of these damage through time by heating or by a slow cooling of the sample. Characteristic effect is first effacing of damage radiation cancelling their trap effect and second diffusion of helium already trap in the annealing damage. Effective fission-track density, rather than He concentration, as the proxy for the volume fraction of radiation damage appears to be a better proxy.

Flowers et al., (2009) developed the RDAAM (Radiation Damage Accumulation and Annealing Model) model which tracks the evolution of He retentivity in apatite by accounting for both the accumulation and the annealing of radiation damage. This model differs from the "Trapping model" model developed by Shuster et al., (2006) which uses effective fission track-track density, rather than He concentration, as the proxy for the volume fraction of radiation damage (Flowers et al., 2009). RDAAM model have been incorporate into HeFTy modelling software (Ketcham, 2005) to assess the implication for the interpretation of apatite (U+Th)/He data on thermal histories. Important consequence of RDAAM model on thermal histories implies: i) effective closure temperature that increase with decreasing cooling rate, ii) a HePRZ that continuously evolves to higher temperatures, iii) burial and reheating scenarios that yield a several hundred Ma.

In the same time Gautheron et al., (2009) developed a similar model in order to take account of damage annealing. This one have been introduced into a full Monte Carlo simulation of He production/ejection/diffusion (Gautheron & Tassan-Got, 2010)

in which the effect of irradiation damage and annealing is incorporated through the time/temperature dependence of the diffusion coefficient.

Following the idea that radiation damage can correlate with He retention in apatite, Guenthner et al., (2013) document the same process on zircons. They show that at low damage or low eU concentration, (inferior at 1000 ppm) damage accumulation in zircon cause decrease in He diffusivity. However, at high eU concentration (superior to 1000 ppm) helium diffusivity increase drastically resulting from the damage zone interconnection.

II.3 Apatite 4He/3He thermochronology

^{4}He/^{3}He thermochronometry is a recently developed variant of the conventional (U+Th) /He method. Description of the technique has been largely presented in complementary papers: Shuster and Farley, (2004) and Shuster et al., (2004) and more recently as a general review of the system, in Shuster and Farley, (Shuster & Farley, 2005). Contrary to thermochronology which most often involves the determination of a cooling age from parent and daughter concentration within a single crystal or a population of crystal, complementary information can be use from the spatial concentration distribution of the daughter production in a single crystal. Combining these two types of information: a bulk cooling age and a daughter distribution (C(x,y,z)) from the same single crystal, it is possible to obtain information on the time-temperature (t-T) path of the sample. We will focus this description of this type of analyses to the (U+Th)/He system on apatite crystals because of its very low-temperature sensibility. 4He diffusive mobility occurs at temperature just above than those of the Earth's surface. Fundamental overview of ^{4}He/^{3}He thermochronometry will be presented and how the determination of the diffusion helium kinetics and the 4He distribution in a same crystal can provide limits on the sample's t-T path.

II.3.1 4He distribution

Like others thermochronometers, (U+Th)/He is based on two physical processes: accumulation of a daughter product (4He) and loss of this daughter by thermally processes as diffusion. The basis of ^{4}He/^{3}He thermochronometer is based on these processes in which result a spatial distribution of radiogenic 4He. The following schematic equation

summarize the process and resulting distribution applies to an individual crystal:

$$\int_{t_0}^{today} [Production(x,y,z,t) - Removal(x,y,z,t)]dt = Distribution(x,y,z,t) \quad \text{(II.14)}$$

where production is the radiogenic production function of ^{4}He dependant to time, Removal is the loss function of ^{4}He dependant of time and temperature, Distribution is the spatial concentration function of ^{4}He within the sample today and t_0 is the time when ^{4}He accumulation initiate. Knowing the different functions of production, removal and distribution from the above schematic equation provide a relationship between measurable entities and t-T path of the sample.

The clearest way to characterize the relationship between time, temperature and spatial distribution of a noble radiogenic gas within a solid matrix is to consider the crystal geometry as a spherical diffusion domain of equivalent surface area to volume ratio. Within a spherical diffusion domain (0 < r < a), diffusion substance having an initial radius concentration $C_0(r)$, the concentration at a later time is (Jaeger & Carslaw, 1959):

$$C(r,\tau) = \frac{2}{ar}\sum_{k=1}^{\infty} e^{-k^2\pi^2\tau} sin\frac{k\pi r}{a}\int_0^a r' C_0(r') sin\frac{k\pi r'}{a} dr' \quad \text{(II.15)}$$

If its mobility follows thermally activated volume diffusion and $C_0(a) = 0$ for all t. In this case we use the non-dimensional diffusion time:

$$\tau(T,t) = \int_0^{\tau} \frac{D(T,t'}{a^2} dt' \quad \text{(II.16)}$$

By discretization of τ_i to be a piecewise linear quantity over the course of an experiment:

$$\tau_i = \sum_i \tau(T_i t_i) \quad \text{(II.17)}$$

The radial distribution after a discrete step of duration t_i at T_i is given by:

$$C_i(r) = C(r,\tau_i) \quad \text{(II.18)}$$

This expression allow to predict the evolution of a radial ^{4}He profile within a spherical diffusion domain over geologic time. With knowledge of a sample's helium diffusion kinetics, model ^{4}He distributions can be calculating according to any arbitrary t-T path. Alternatively, if the natural 4He spatial distribution within a sample can be constrained with a He age, then a finite set of t-T paths can be identified.

II.3.2 Proton irradiation: uniform 3He distribution

Major difference of 4He distribution in a single crystal induced by different t-T paths are situated in the outermost most few percent of the domain. Typical accessory minerals using for $^4He/^3He$ thermochronometry as apatites have a dimension of only 100 μ4m and obligate a 4He profile detection with a spatial resolution of better than a few microns. Actual techniques as nuclear reaction analyses, secondary ionization or laser microprobe mass spectrometry lack sufficient sensivity and or spatial resolution and cannot directly measure a ^4He distribution in a single crystal at this resolution. Because of this technical problem, another method is used to indirectly measure it. This method consist to use a stepwise degassing approach which allow to obtain both essential information needed: the ^4He concentration profile and the helium diffusion kinetics of the same sample. Again, with only one single isotope: ^4He, it is impossible to de-convolve a non-uniform ^4He distribution and unknown helium diffusivity from a set of helium release fractions. A solution is to produce a uniform 3He distribution throughout the crystal. This method shows that the presence of a uniformly distributed second isotope synthetically generated, Ar for example (^{37}Ar or ^{39}Ar) combining with a stepwise degassing Ar data can be used to directly invert for the 40Ar distribution. Laboratory-induced uniform ^3He distribution coupled with an isotope ration step-heating experiment can be then used to determine He diffusivities in any mineral by using the 3He release fractions and an unknown natural 4He distribution using the evolution of the $^4He/^3He$ ration over the course of sequential degassing.

Shuster et al., (2003), show that it is possible to produces sufficient spallation ^3He via energetic proton irradiation, more specifically by bombarding samples with a 150 MeV proton beam. Spallation ^3He is dominantly produced by a process known as charged particle evaporation. The principle of this process is that the target nucleus can get in an excited state because of their interaction with the incident proton. By de-excitation to a new ground state, the residual target nucleus have a probability to release a ^3He nucleus as show by this equation:

$$^{28}Si(p,p)^{28}Si* \rightarrow^{25} Mg +^3 He \tag{II.19}$$

As ^3He emit by this reaction follow a stochastic trajectories and within the solid 1 to 50 μm surrounding each target atoms in the mineral, the final ^3He distribution within the crystal should be crystallographically random and similar to ^4He after nuclear ejection.

The experiment of Shuster et al., (2004) show also that (i) lattice damage associated with proton irradiation does not affect the helium diffusion properties of at least apatite and titanite. (ii) The proton-induced distribution of ^{3}He is uniform. An evidence of this statement is the use cycled heating schedule including both prograde and retrograde steps. (iii) 3He diffuses at an equivalent rate as or a rate quantitatively relatable to ^{4}He. Durango apatite experiment by Shuster et al., (2004) show that proton-induced ^{3}He and radiogenic 4He have nearly equivalent diffusivity in that material with a ^{4}He potential diffusivity slightly faster than ^{3}He. (iv) The sample is heated by less than a few °C during irradiation, so helium diffusion during the process is negligible. From the experiment, the proton beam energy exiting the target stack is 115 MeV, depositing 35 MeV in the stack. At 4.0 nA and assuming that all the 35 MeV deposited in the target as kinetic energy appearing as heat, this energy deposition translate to 0.15 W from witch its correspond to a maximum temperature increase during irradiation of 1-2 °C above ambient. For apatite and olivine there is no indication of diffusive rounding imply by this temperature increase.

II.3.3 The 4He/3He ratio evolution diagram

Proton-induced ^{3}He provides a means to interrogate the natural ^{4}He distribution within a crystal by sequentially measuring 4He/3He ratio during a stepwise degassing. During a degassing experiment, the 4He/3He release spectrum or ratio evolution diagram is a sensitive function of the natural spatial distribution of 4He (Shuster and Farley, 2004). For a given kinetic, $D(T)/a^2$, it is possible to predict the piecewise evolution of the radical distribution after discrete steps of duration t_i at T_i of a simulated degassing experiment for any arbitrary initial profile, $C_0(r)$. By integrating profiles and taking their differences between each step, a set of simulated helium release fractions is calculated for any arbitrary heating schedules. As we know the relative diffusivity between the two helium it is possible to calculate isotope ratios for the concurrent release of uniformly distributed isotope (^{3}He) and an isotope with an arbitrary natural distribution (^{4}He).

II.3.4 Constraining thermal histories.

Specifics t-T paths result of specific 4He concentration profiles. The absolute He concentration depends on the U and Th concentrations, but the distribution profile of the ^{4}He depends only on thermal histories and alpha ejection. Figure II.8a illustrates a

geologic problem where a cooling event is assumed to be from 50 °C to 0 °C. Six cooling paths are represented with different rate and initiation of cooling. Application of the conventional (U+Th)/He will allow to obtain an age of 5 Ma on an apatite with a = 65 μm. However, it will not be possible to determine between these different t-T paths with this sample because all six cooling histories in Figure II.8a would result in a 5 Ma bulk He age. However, each different t-T path would result in a distinct ^{4}He/^{3}He ratio (Figure II.8b). Thermal histories with earlier cooling event show a higher ^{4}He/^{3}He ratio associated in the first step to zero ^{4}He/^{3}He ration for very recent cooling rate up to a limit of 0.55 for this case of cooling at 5 Ma and because of alpha ejection. Note that the alpha ejection phenomenon is not a problem for the technique but needed to be considered.

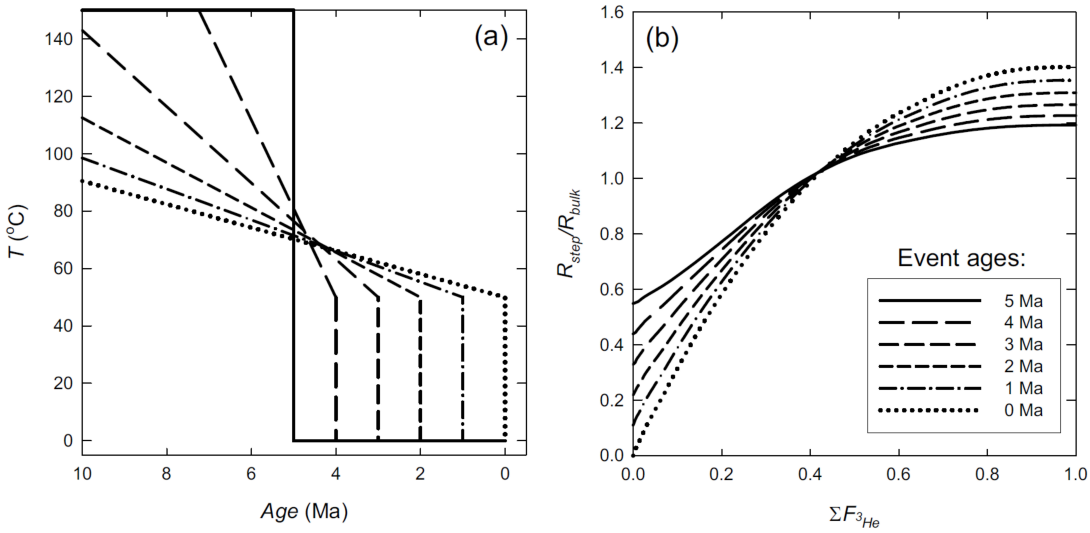

Figure II.8: Effect of different cooling event on the ^{4}He profile from Shuster and Farley, (2005). a) Six different t-T paths which each result in a same bulk He age of 5 Ma. b) Corresponding ^{4}He profiles express here as simulated ratio evolution spectra shown.

Figure II.9 present another example of step-heating simulation for a diffusion domain where a = 65 μm. In Figure II.9a,b,d,e, concentration profile (Figure II.9a,b) and corresponding step-heating ratio evolution diagram (Figure II.9d,e) are calculated according to thermal histories recording constant cooling rate (0.1, 1, 10, 100 °C/Ma) from 125 °C to 25°C. Profiles are calculated excluding (Figure II.9a,d) or including (Figure II.9b,e) alpha ejection. Figure II.9d show distinct ration evolution according to the different t-T path. Thermal histories with faster cooling rate produce less rounded

concentration profile (more ^{4}He in the edge of the crystal) and steeper trajectories on the ratio evolution diagram with a pronounce effect in the first 10-20% of gas released. Effect of alpha ejection on the concentration profile and ratio diagram evolution are shown in Figure II.9b,e. Effect of alpha ejection is predominant in the 30% of gas released with a more pronounced linear shape of the ratio evolution plot. Also as the alpha ejection is independent of temperature, his influence dominate ratio evolution plot associated with fast cooling rate and become less significant for slow cooling rate. Figure II.9c,f presents similar concentration profile and ratio evolution diagram but according to a thermal history witch record a constant cooling rate (0.1, 1, 10 and 100 °C/Ma) from 125 °C to 25°C but following by 5 Ma of isotherm holding at 25°C. Difference in the ratio evolution diagram between Figure II.9d and Figure II.9f illustrate that low-temperature isothermal holding cause a profile more "square" and lead to greater retention of gas toward the domain edge.

II.3.5 Assumption and potential complication.

A first potential complication concern mineral surfaces. As most of the difference of the ^{4}He distribution in a single crystal is recorded toward the grain edges it is important to analyse samples with intact and original surfaces. Incorporate broken crystal will generate misleading results in the stepwise degassing as a broken crystal will expose a steeper concentration gradient than expected in a complete crystal.

Major assumption of this method is the used of the spherical diffusion domain to characterise the diffusion model of crystal. This model is an oversimplification because domains for ^{4}He diffusion in many crystal is govern by euhedral (non-spherical) domain (Farley, 2000; Reiners & Farley, 1999; Reiners et al., 2002).

Another assumption is the statement of a uniform distribution of the parent nuclides (U and Th) throughout the diffusion domain in order to simplify calculation of the concentration profile and the ratio diagram evolution. It is totally feasible to consider a strongly heterogeneous distribution of parent nuclides witch could influence the final spatial distribution of ^{4}He within a single crystal. If an accurate distribution of U and Th nuclide is known, it is possible to incorporate it into the ^{4}He/^{3}He method by simply allowing for spatial variability in the ^{4}He production function.

Complication unique to (U+Th)/He system are introduced by the fact that alpha particles (helium) produce by the disintegration of uranium and thorium are emit with

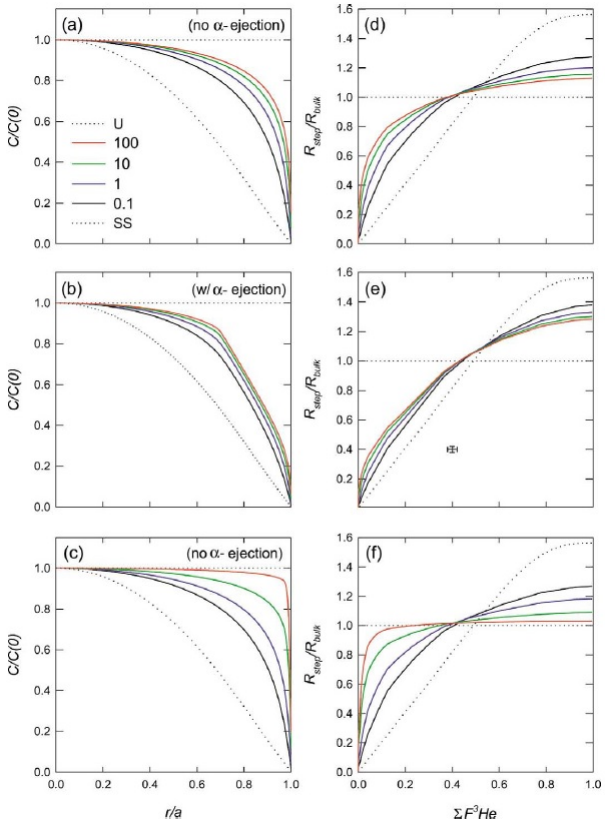

Figure II.9: Step-heating simulation of profiles resulting from different monotonic cooling from Shuster et al., (2005). Each curves of different colors correspond to a particular monotonic cooling with a cooling rate from 125 to 25 °C. a-c) Concentration profiles. d-f) Evolution diagram of the step-heating simulation. The result are show without α-ejection in panel a) and d) and with α-ejection in panel b) and e). Panel c) and f) correspond to panel a) and d) but with a t-T simulation which reach 25 °C and following by 5 Ma of isotherm holding at 5 Ma.

sufficient kinetic energy to travel 20 μm from the site of decay and some fraction are ejected from grain surfaces (Farley et al., 1996). This effect exerts a strong and predictable effect on the ^{4}He production function that is independent of diffusion (Farley et al., 1996), particularly in smaller grains. Although alpha ejection influences the ^{4}He distribution, experiments of Shuster and Farley, (2004) demonstrated that if the effect is incorporated into the modelling it does not significantly diminish the sensivity of ^{4}He/^{3}He thermochronometry.

II.4 Application of thermochronology to geologic problems

The main application of low-temperature thermochronology is to record the cooling of rock through time associated to their exhumation (displacement of a rock column toward the Earth's surface). Other applications exist but in this section we will present the ones focusing in understanding the evolution of mountain range. Rocks are generally exhumed by tectonics processes, by erosion or by the interplay of the two. In compressive context, rock exhumation is due by the erosion of the hanging wall because of the uplift associated to the movement of inverse faults or thrusts. In extensive context, exhumation of rocks can be purely tectonic because rocks from the footwall are exhumed along the fault plan or associated with the erosion of the footwall. Thermochronology is generally apply to two distinct geologic objects: crystalline massifs (in-situ analyses) and sedimentary basins (detrital analyses). Continental convergence is accommodated in orogenic belts by crustal thickening, lateral and radial expulsion, and erosion. Orogenic belts are often characterized by the presence of crystalline massif in the center of the orogenic prism. In-situ analyses are made on this crustal massifs in order to quantify surface uplift over crustal length scales during orogeny as the fundamental displacement to be measured. First use of low-temperature thermochronology have been made using different radiometric techniques on cogenetic minerals from a single sample (often include zircon fission tracks, apatite fission track and apatite helium analyses) (Hurford, 1986; Zeitler, 1985; Zeitler et al., 1982). Even if this method does not reveal the processes responsible for unroofing a sampling, it provides valuable information on the time when cooling start and the rate at which cooling proceeds. The single age approach allows derivation of cooling time across a large area. However this method lack precision

in determining the thermal and exhumation history through time. To resolve this problem, research focused on sub-vertical profile sampling strategy within valleys. This method emerged from thermochronological research in Antarctica and Alaskan ranges (Fitzgerald, 1992; Fitzgerald et al., 1995; Fitzgerald & Stump, 1997) and more recently, has involved the development of modelling strategies for multiples samples (Gallagher, 2005). Sampling over significant relief and limited horizontal distance in mountain belts yield ages that exhibit a positive correlation with sample elevation (G. A. Wagner & Reimer, 1972). This spatial (vertical) frame is used to establish an age-altitude profile and allow to estimate the rate and initiation of exhumation. This method is based on the principle that sample exhume with a vertical motion and that during the exhumation, samples keep their same vertical distribution. By plotting the thermochronological age in function of the elevation associated to each samples, it is then possible to estimate the exhumation rate (Figure II.10). Moreover it is possible to estimate the initiation of exhumation when the age-altitude profile display a break in slope (Fitzgerald et al., 1995). This feature is explained because some of the samples are situated in the PAZ and others below the PAZ before the exhumation. Samples above the break with old ages and low mean track lengths correspond to colder samples which undergone important annealing within the PAZ before the onset of rapid cooling. Sample below the break with younger ages and high mean track lengths correspond to hotter samples below the PAZ which undergone no annealing before the onset of rapid cooling and low annealing during the rapid cooling. The break in slope is interpreted as the base of a fossil PAZ.

Another major application in order to characterize the formation and evolution of mountain range and provenance information is the datation of detrital rocks in sedimentary basins. Sedimentary basin that surround orogenic belts contain an easily accessible and long-term orogenic record (Garver et al., 1999). Consequently fission track of common detrital uranium-bearing minerals such as apatite, zircon and sphene have been used in order to i) trace the provenance of sediments, ii) studying the long-term exhumation history of convergent mountain belts and iii) date low-temperature thermal events. Detrital ages are generally distributed and can be evaluated in several different ways but the goal in each approach is to discriminate population of cooling ages. When the goal is to determine an average exhumation rates it is common to calculate the mean age of the distribution. Minerals which have not been partially or totally reset

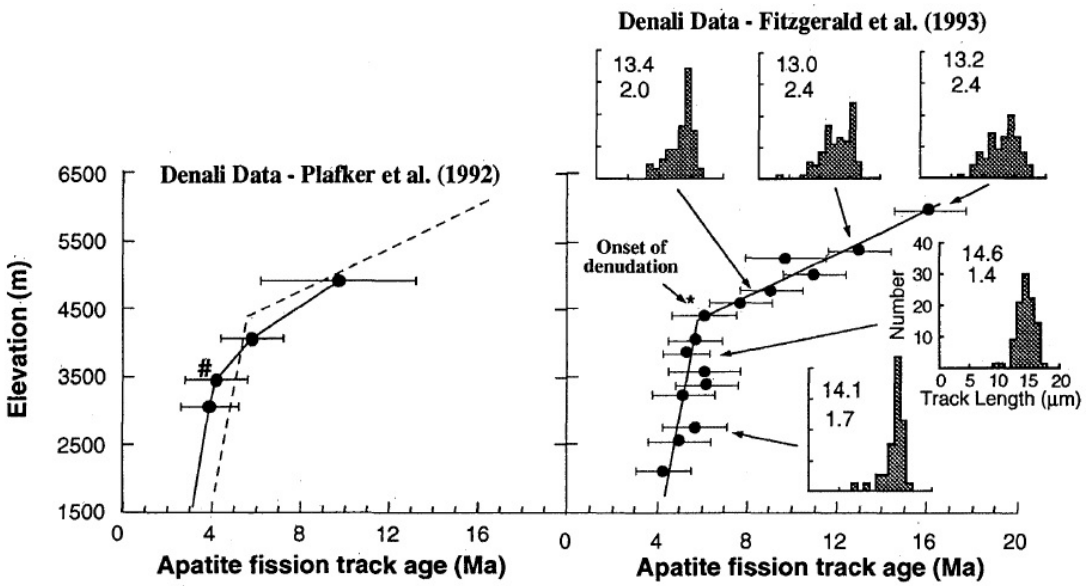

Figure II.10: Example of apatite age-elevation profiles from Plafker et al., (1992) and Fitzgerald et al., (1993; 1995). Samples were collected on the west flank of Denali in Central Alaskan range. Plot of apatite ages in function of their elevations highlight different rate of exhumations through time and the break in slope indicates an onset of rapid cooling.

after deposition in the sedimentary detritus can be related to past thermal events in the source terrain. Then cooling ages provide a direct link to uplift and exhumation of source rocks. In order to quantify the evolution of the source rock through time a "lag-time" is determined in sedimentary layers of different ages (Bernet & Garver, 2005). In this case, the lag-time is defined as the difference between the peak age and the depositional age (Bernet et al., 2001; Garver & Brandon, 1994; Garver et al., 1999) and represent the difference between closure of the system in the source area and deposition in the adjacent basin (Figure II.11). The lag-time represents then the time required for the rock to be exhumed to the surface, eroded and then deposited and is a function of exhumation rate in the source area. Evolution of the lag-time through time or toward sedimentary layers can highlight variation of the exhumation rate. Three different trends can be expected from a sedimentary sequence (Bernet & Garver, 2005) (Figure II.12). The first one is a decrease of the lag-time through time which corresponds to an acceleration of the exhumation rate. The second one is an increase of the lag-time through time, which indicates a slowing of exhumation rate. Finally, the last trend is a constant lag-time (peak ages young at the same rate as for the depositional age). This

type of lag-time indicates a constant exhumation rate.

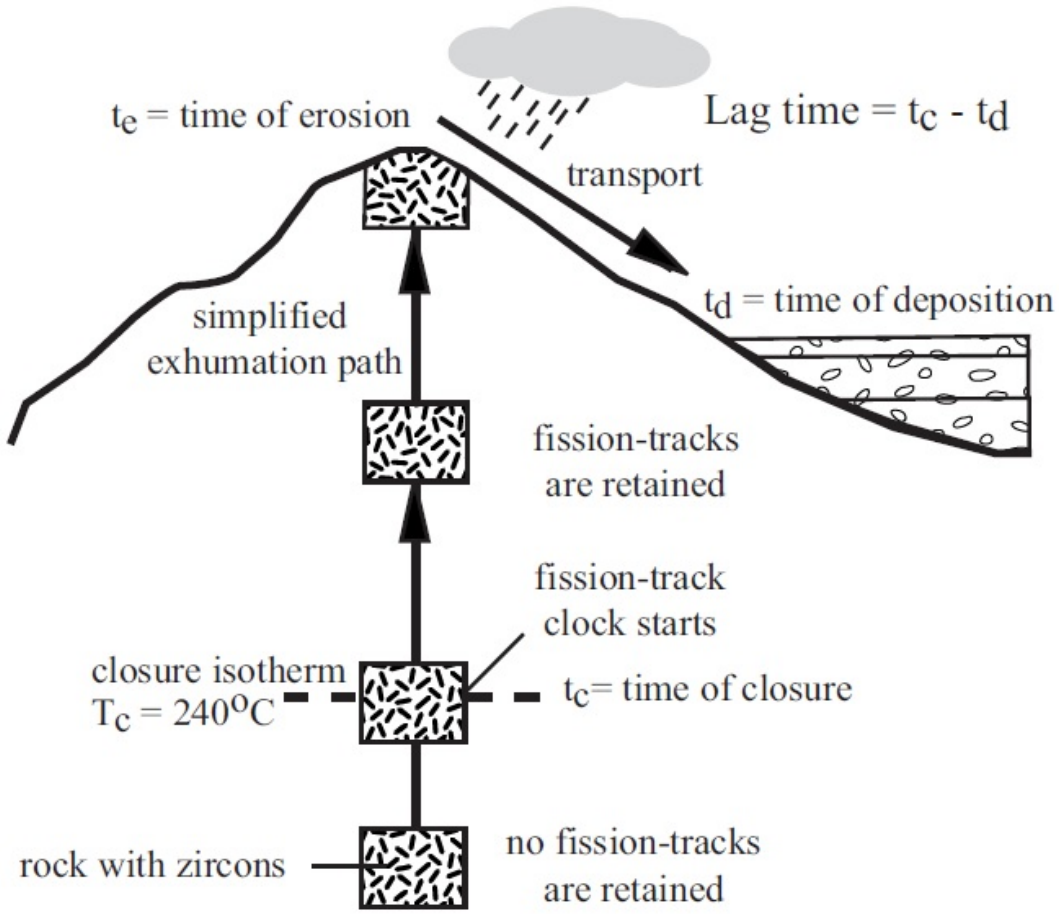

Figure II.11: Schematic representation of the lag-time principle from Bernet and Garver, (2005). The lag-time of a sample is the time required for the sample to cool, get exhumed to the surface and get deposited in the surrounding basin. The lag-time correspond then to the difference between the thermochronological age and the sedimentary age of the sample.

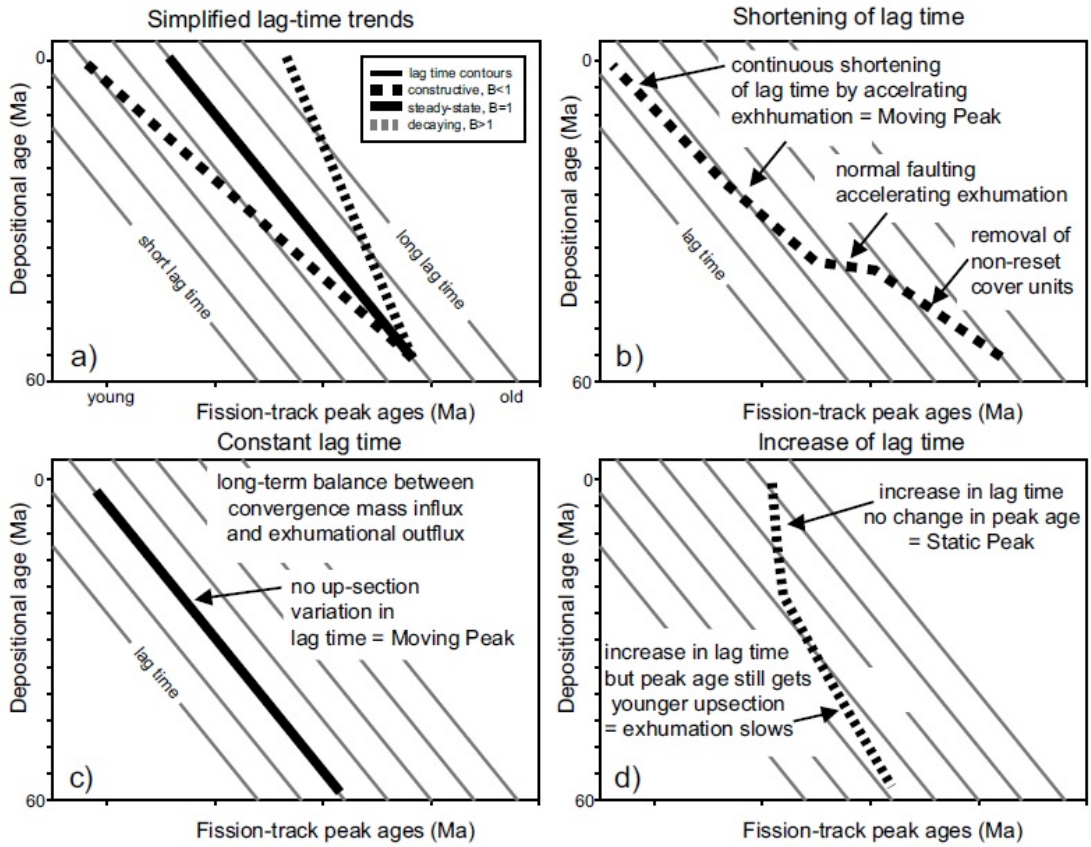

Figure II.12: Representation of the lag-time on a fission-track ages and depositional ages plot from Bernet and Garver, (2005). Evolution of the lag-time indicate the exhumation rate state. If lag-time increase, then the exhumation rate decrease and at contrary, if the lag-time decrease, then the exhumation rate increase. Lag-time can also be view as an indication on the orogenic evolution (Bernet and Garver, 2005). A decrease lag-time or increase exhumation rate indicate an orogen in a constructive phase. A constant lag-time or constant exhumation rate indicate an orogen in a steady-state phase. An increase lag-time or decrease exhumation rate indicate an orogen in decaying way.

II.5 Limitations of low-temperature thermochronological dataset.

The main limitation associated to the interpretation of low-temperature thermochronological dataset for geological problems is the estimation of a geothermal gradient. Modelling of low-temperature thermochronological dataset allow generally to obtain an evolution of rock temperature through time and to calculate a cooling rate. In order to infer an exhumation rate from the cooling rate a geothermal gradient is needed. A geothermal gradient value between 15 and 45 °C/km is generally accepted, however taking into account geothermal gradient is important as the use of different ones will directly impact the interpretation of exhumation rate from an age-altitude profile or a multi-thermochronometric dataset for example. Surface heat flow at surface which correspond to the expression of geothermal process at depth show a high range of variability though the earth surface (Pollack et al., 1993). Geothermal gradient vary in function of space according to the geological context but also in function of time. In this part we will see different process which can perturb the geothermal gradient or the interpretation of low-temperature thermochronological dataset.

II.5.1 Erosion and sedimentation

Landscape evolution results in the redistribution of mass through time through the processes of erosion and sedimentation. This redistribution of mass gone with an associated redistribution of heat. Erosion process remove material from the Earth's surface resulting in the upward movement of warmer rocks. This upward movement of rocks causes a net increase in temperatures at any given depth relatively to the initial temperature prior to erosion. For example after 5, 10 and 15 Ma at an erosion rate of 1 mm/yr, temperature at 4 km depth increase from 100 °C to 140, 170 and 195 °C respectively (Ehlers, 2005) (Figure II.13a). Moreover erosion causes an increase in thermal gradient as the isotherm get closer from each other's. At an erosion rate of 10 mm/yr, after 105 years the thermal gradient double from 25 to 50 °C/km (Ehlers, 2005) (Figure II.13b). Sedimentation have an inverse impact on the temperature and geothermal gradient of the upper crust. During sedimentation, cooler materials are moving downward, causing a net decrease of temperature at any given depth below the surface relative to temperature prior to sedimentation. For example after 5, 10 and 15 Ma

of sedimentation at a rate of 1mm/yr, the temperature at 4 km depth decrease from 100 °C to 70, 55 and 46 °C (Ehlers, 2005) (Figure II.14a). Again, at the contrary to erosion, sedimentation can cause a decrease in the thermal gradient as the isotherm get further from each other's. After 106 and 107 years of sedimentation at the same rate the thermal gradient of 25 °C/km will decrease to 20 and 12 °C/km respectively (Ehlers, 2005) (Figure II.14b). Depending on the rate and also the duration, erosion and sedimentation have to be taken in account when dealing with low-temperature thermochronological datasets. If erosion or sedimentation are estimated from other geological constraints to be ¡1 mm/yr for a duration on order 10 Ma or less, then the disturbance of the thermal field will be less than 10%. However if rate and duration is estimated higher, then the perturbation of the thermal field can be greater and could impose further investigation in order to interpret the low-temperature thermochronological dataset (Ehlers, 2005).

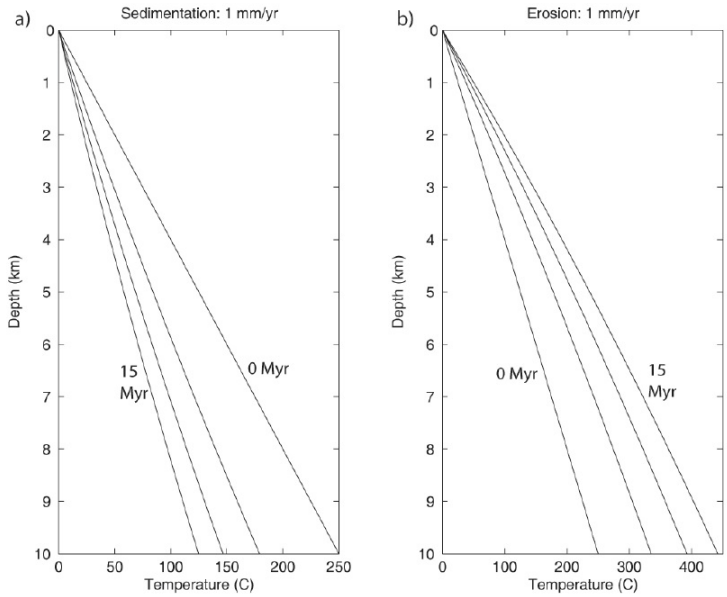

Figure II.13: Geotherms calculated with erosion and sedimentation at a rate of 1 mm/yr after 5, 10 and 15 Ma from an initial thermal gradient of 25 °C/km and a thermal diffusivity of 32 km^2/Ma at 0 Ma from Ehlers, (2005). a) Influence of sedimentation on geotherms. b) Influence of erosion on geotherms.

II.5.2 Topography

In order to interpret thermochronometer dataset along vertical profiles, several studies have plotted sample ages versus the elevation. This approach have been used because

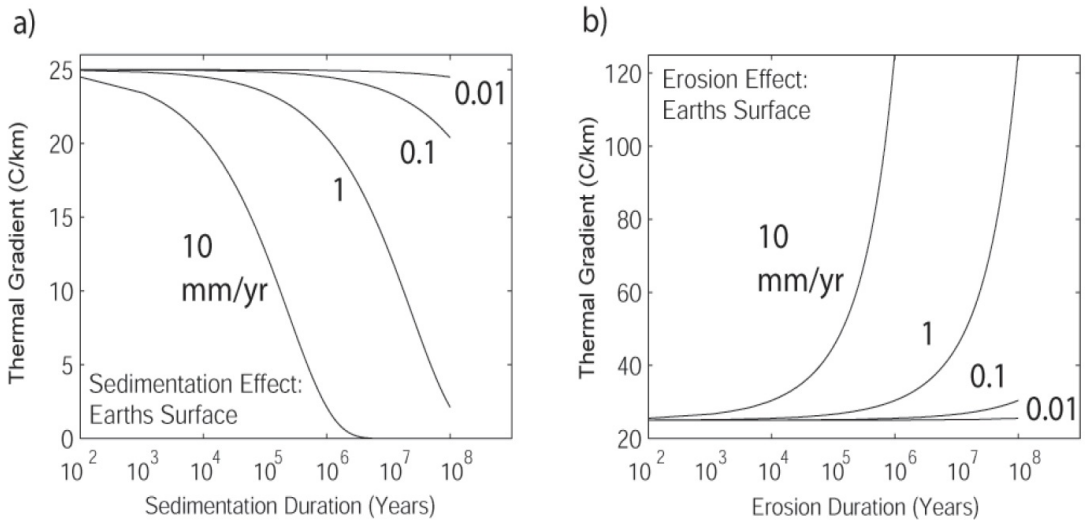

Figure II.14: Effect of erosion and sedimentation rate and duration on the thermal gradient at the Earth's surface for an initial thermal gradient of 25 °C and a thermal diffusivity of 32 km^2/Ma from Ehlers, (2005). a) Effect of sedimentation on the thermal gradient. b) Effect of erosion on the thermal gradient.

the slope of the best-fitting line through the age data in function of elevation allow to infer easily the cooling/exhumation rate history of the vertical profile through time. This method lies mainly on the assumption that all the samples have cross through the closure temperature at the same elevation. However it have been shown that the topography can perturb the position of the different isotherm through space under the surface (Braun, 2002; Ehlers & Farley, 2003). This pattern can control the apparent cooling rate from an age-elevation profile (Ehlers, 2005). For example, closure isotherms can mimic the topography resulting that the different samples don't cross closure isotherms at the same elevation. Moreover, cooler isotherms will be more deformed by the topography than warmer isotherms as the thermal perturbation caused by a finite surface topography decrease exponentially with depth (Figure II.15a). The cooling rate infer from an age-elevation profile will appear more important for a thermochronometer of low-temperature compared to a thermochronometer of high-temperature (Figure II.15b).

Another assumption on which lie the age-elevation relation is that the relief stay constant through time. In the case of a constant relief, a certain slope can be determine from the age-elevation can be determined. However in the case of an increasing relief through time, the slope of the age-elevation profile will decrease. In the case of a

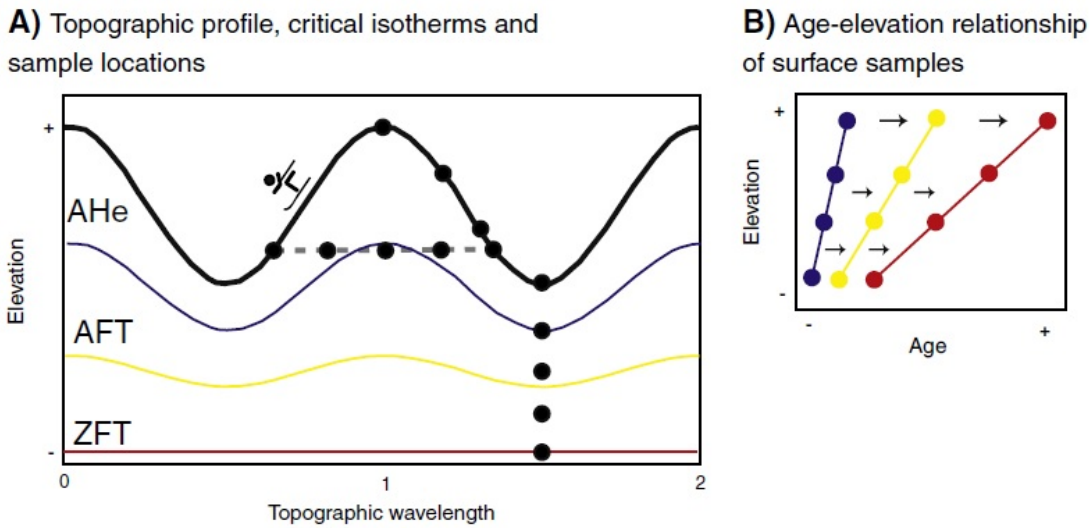

Figure II.15: Schematic representation of the relation between surface topography, isotherms and age elevation plot from (Braun et al., 2012). A) Topographic profile with resulting closure-temperature isotherms for the AHe, AFT and ZFT thermochronometers. B) Age-elevation profile of the AHe, AFT and ZFT data. Slope of the AHe and AFT age-elevation relation are overestimate due to the perturbation of the closure isotherm of these two systems. The ZFT data yield the correct exhumation as the closure isotherm of this system is horizontal.

decreasing relief through time, the slope of the age-elevation will increase up to be inverted (Braun, 2002) (Figure II.16).

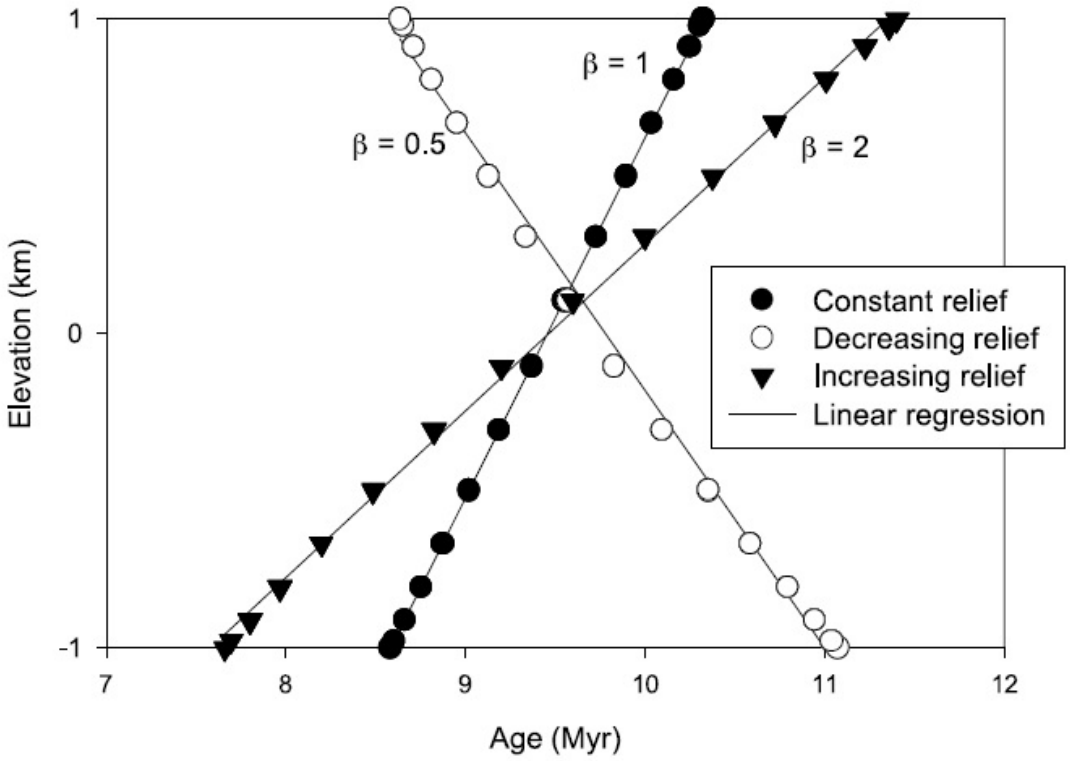

Figure II.16: AHe ages-elevation relation predict for different topographic relief evolution scenarios (constant, decrease and increase) from Braun, (2002).

II.5.3 Tectonic events

Fault activity is a common feature in orogenic belts. The rate and timing of motion associated to faults have been characterised by thermochronometry. However tectonic movements can also perturb the thermochronometer data. The main disturbance of the thermal field associated to the activity of faults is the transport of mass from erosion and sedimentation from one side of the fault to the other. The different important thermal consequences to the redistribution of mass along faults are (Ehlers, 2005): 1) the rate of erosion and sedimentation in each side of the fault can cause important change in the geothermal gradient 2) The juxtaposition of enhanced and depressed thermal field can cause a curvature of the closure isotherms across the fault. 3) Lateral heat flow across the fault.

II.5.4 Rock erodibility

Geologic settings are characterised by rocks of contrasting erodibilities. It is particularly common in orogenic belt to find generally softer sedimentary rocks overlying igneous and metamorphic basement rocks that are generally harder.

Flowers and Ehlers, (2018) evaluate the role of rock erodibility variations on the interpretation of thermochronologic dataset and thermal histories. The numerical modelling result of the study explore the influence of different rock layers of different erodibility eroded through time on the thermochronological ages (AFT and AHe) and on thermal histories. They demonstrate that the rock erodibility variations from different lithologies can have a substantial to negligible effect on the thermochronologic record depending on ordering of rock types, erodibility contrast, erosion rate, layer thickness and cumulative erosion magnitude (Flowers and Ehlers, 2018). The modelling suggest that even a relatively low rock erodibility contrast (2-10x) can have important influence of the thermochronometric ages and thermal histories if the rock layers implied are relatively thick ($\geq$ 2 km) and the cumulative erosion magnitude important (at least 4 km for AHe data and 6-8 km for AFT data) (Figure II.17). These results implies that in a geological context where sedimentary rocks covered hardest rock as crystalline basement rock now at the outcrop, the thermochronometric ages can be perturbed by the difference of rock erodibility eroded through time. An important shift in the cooling rate of thermal histories can be the result of this pattern and not only and simplistically a change of rock uplift rate by tectonics.

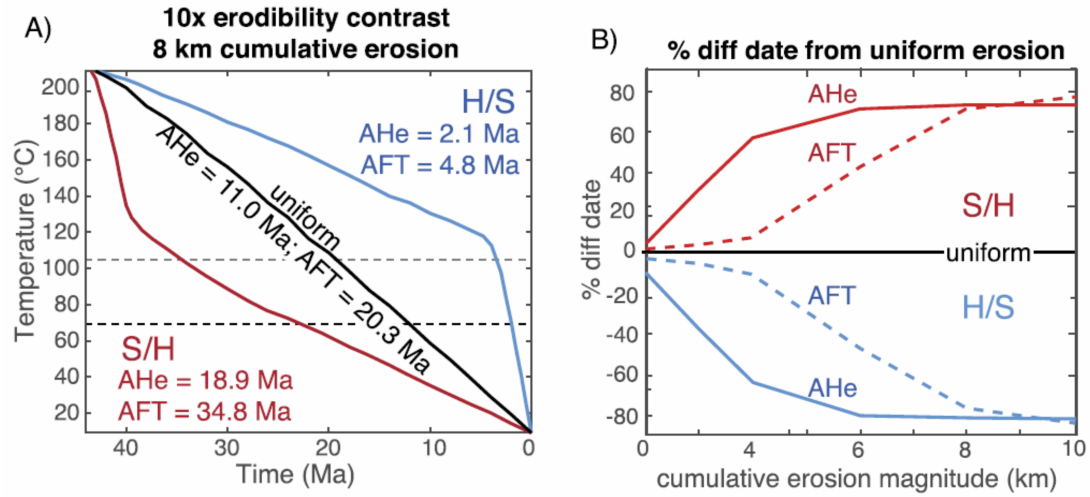

Figure II.17: Influence of rock erodibility on thermochronological ages and thermal histories from Flowers and Ehlers, (2018). A) Thermal histories predicted for soft/hard rock succession, uniform and hard/soft rock succession simulations for a cumulative erosion magnitude of 8 km and 10x erodibility contrast between the soft and hard rocks. B) Difference in % for the AFT and AHe date between layered and uniform models for a fixed erodibility contrast of 10x and fixed erosion rate of 0.1 mm/yr.

Chapter III

APPLIED METHODOLOGIES

As mentioned earlier, a mountain belt-foreland basin system is complex in which multiple processes and interactions occur. Therefore, in order to have a global comprehension of the system, we use a multi-methodological approach. It will allow us to explore the exhumation pattern in the mountain range and style of deposition in the basin and their effects on the geomorphology. Methodologies will evolve with: i) Rock and mineral procedures and interpretation of low-temperature thermochronological data by numerical modelling to produce cooling histories in order to reconstruct pattern of late exhumation in the Central Pyrenees and the timing or transition toward post-orogenesis; ii) Topographic analyses from digital elevation models (DEM) in order to explore the landscape response to changes in forcing; iii) Landscape numerical models in order to predict topographic and landscape shape evolution. The first one introduced is a "Box-model" which is used with geological evidence of the Northern Pyrenees in order to predict paleo-topographic evolution of the Aquitaine basin relative to the Pyrenees. The second model "Fastscape" is used in combination with topographic analyses in order to constrain the landscape response to change of conditions through time.

III.1 Low-Temperature Thermochronology Procedure and Modelling

III.1.1 Rock sampling and mineral procedure for 4He/3He

Rock sampling

We sampled three sub-vertical profiles from granodioritic massifs with Hercynian ages within the Axial Zone of the Central Pyrenees (Bielsa, Maladeta and Neouvielle massif).

All samples are from fresh and unweathered granitic blocks with no evidence of proximal faulting, shear structures or hydrothermal veins. For all sub-vertical profiles, localities were chosen in order to sample the lowest elevation of the granitic massif with an important vertical topographic relief and minimal horizontal displacement between the different samples. The southern sub-vertical profiles from the Bielsa massif consist of two samples along the Barrosa River northward of Bielsa village at elevation of 1108 and 1410 m. Maladeta sub-vertical profile is located in the south part of the Maladeta massif north to the Flamicell River and consists of four samples at 1788, 2138, 2412 and 2651 m. Neouvielle sub-vertical profile is also located in the southern part of the Neouvielle massif and consist of four samples. Samples are located at the base of the Lac d'Orédon and along the Ruisseau de Cap de Long with elevation of 1852, 2193, 2544 and 2804 m. Bielsa and Maladeta sub-vertical profiles are located southward of the drainage divide whereas Neouvielle sub-vertical profiles is located northward of the drainage divide of the Pyrenees.

Mineral separation process

In order to perform the $^{4}He/^{3}He$ thermochronology procedure, a separate of heavy minerals with a good percentage of apatite are required. Each samples have an initial weight of about 5.5 to 7.5 kg. The mineral separation has been performed using facilities at the Institute of Geology in The University of Edinburgh. The first step of the procedure involve the crushing of the rock samples. The rock samples are first broken down and reduce to centimetric cubes by using a hydraulic presses with two metal blades. Normal jaw crusher is secondly used to transform the centimetric rock samples to sand-sized grains in order to liberate target mineral grains. We choose to not use ring mill in the crushing process to avoid breaking the apatite crystals. Theses sand-sizes samples are then sieved through different sieves to obtain samples with the specific grainsizes: 63 to 125 μm, 125 to 250 μm and 250 to 500 μm. It appeared at the end of the process that the best grainsizes for apatite separation is 63 to 125 μm. The 125 to 250 μm grainsizes contain almost no apatites and completely no apatites for the 250 to 500 μm grainsizes.

The second step of the procedure involve gravity separation using water with a Wilfley Table. The idea of this method is to use both the vibration and slope of the table for reducing sample composition to mineral of interest. The heavy mineral component of

the sample resist the flow of the water and move along the uppermost part of the table. The majority of minerals of interest for thermochronology including apatite are found in the heavy fraction. Lighter mineral are normally entrained with the water flow in the lower portion of the table. At the start, grains of the samples are placed continually in a small funnel and collected at the end into different buckets depending of the density. Efficiency of the process depends of the setting of the Wilfley Table. Parameters which impact the gravity separation are the vibration rate and the slope (inclination and rotation) of the table. However the Wifley Table at the University of Edinburgh don't allow to change the water flow and the disposition of the different buckets leading to difficulty in setting a perfect separation. After processing, the samples are dried under normal conditions and packed up for further separation.

The third step of the process consist to use the magnetic properties of minerals. Using a Frantz Magnetic Separator (FMS), mineral concentrate can be refine by removing mineral with varying degrees of magnetic susceptibility. Initially, samples are run through a hand magnet in order to remove mineral with high magnetic susceptibility (magnetite). This step is important because magnetite can obstruct the conduit of the FMS and perturb the magnetic separation. Samples are then separated with the FMS several times with different magnetic susceptibility: 0.4, 0.8 and 1.5 ampere. Each time the magnetic separate is removed and the non-magnetic separate is run over with a higher magnetic susceptibility as described earlier. The final product is a non-magnetic sample which contain apatites.

The final step of the mineral separation process is gravity separation using heavy liquids. Different types of heavy liquids exist and can be used in function of the density of the target minerals. In our case to extract a maximum concentration of apatites we use Lithium Heterotungstate (LST) Fastfloat. LST is a high density liquid for laboratory density separations with a density of 2.82 g/mL but with a density saturation of 2.95 g/mL at 25 °C. LST present numerous advantages compared to other products such as Tetrabromoethane (TBE). The first one is the low toxicity of the product which allow to manipulate it without fume cupboards. Secondly, LST is a low viscosity water based product which allow fast separation. Finally it is a stable product at high temperature which allows it to recover easily washing dilute by heating. Samples are mixed with LST in a separating funnel, sink grain are collected and consist of the heavy mineral part with a density superior of 2.8. Float grains consist of the light mineral. The heavy

mineral part is clean with distilled water, dried, packed and ready for further analyses.

4He/3He analyses

Heavy mineral separates have been sent to the Berkeley Geochronology Center for the measurement of $^4He/^3He$ data under the direction of David Shuster. A small portion of the heavy mineral separates are irradiated at the Francis H. Burr Proton Therapy Center at the Massachusetts General Hospital (Shuster et al., 2014) in order to produce a uniform 3He distribution within samples. Apatite crystals from the samples were exposed to $4.6x10^{15}$ protons/cm^2 with incident energy of 220 MeV over a continuous period of 8 hours. After cooling and for each irradiated sample, we selected euhedral apatite grains with perfect crystal faces and placed into a Pt-Ir packet for degassing experiment. The crystals were sequentially heated at different temperatures in multiple steps under ultra-high vacuum while in contact with a type-C thermocouple using a feedback-controlled 70 W diode laser in the Noble Gas thermochronology Lab of Berkeley Geochronology Center. The ^3He abundance and the $^4He/^3He$ ratio were measured for each heating step using conventional sector-field mass spectrometry and corrected for blank contributions to ^3He and ^4He.

Initial irradiation and degassing steps gave good quality results and following dataset will coming (Shuster, pers. comm.). However, as stated in the objectives sections, final steps have been delayed because of technical instrument problems and the Covid-19 situation.

III.1.2 Pre-Existing low-temperature thermochronological dataset of the Central Pyrenees

The Pyrenees is a mountainous domain where low-temperature thermochronologic technique has been largely applied from the first study of Yelland et al., (1991) and up to recent time (Vacherat et al., 2016). This large number of studies has been facilitated by the presence of plutonic massifs dispersed in the Pyrenean Mountain and strongly suitable for the presence of key minerals (apatite, zircon, etc...). Thermochronological datasets are available in various locations along the strike of the Pyrenees (East to West direction) but also transversally (North to South). In this study, we compiled available low-temperature thermochronological data of the Central Pyrenees. Datasets correspond to a compilation of thermochronological ages mainly situated along sub-vertical profiles

from the north to south of the Central Pyrenees. Sub-vertical profiles take the form of a series of samples from valleys and up to the ridges of different massifs of the Central Pyrenees. Different isotopic systems are also combined with Zircon fission track (ZFT) apatite fission track (AFT) and AFT mean track length (MTL) and apatite helium (AHe) systems. A combination of different isotopic system with different temperature sensibility (205-240 °C, 60-110 °C for AFT and 40-75°C for AHe) at different elevations allow a record of the lower temperature cooling history of the target massifs to be constructed.

In this section, we present a pre-existing dataset (Figure III.1 and III.2) from the central Pyrenees used in this study. Identification of the different vertical profiles uses the name of the massifs. Except one profile, all sampling took place in Variscan plutonic massifs that correspond broadly to granodioritic lithologic compositions. From south to north, the profiles are Nogueres, Barruera, Maladeta, Arties, Marimaña, Riberot, Trois-Seigneurs, Lacourt and Foix (only one sample).

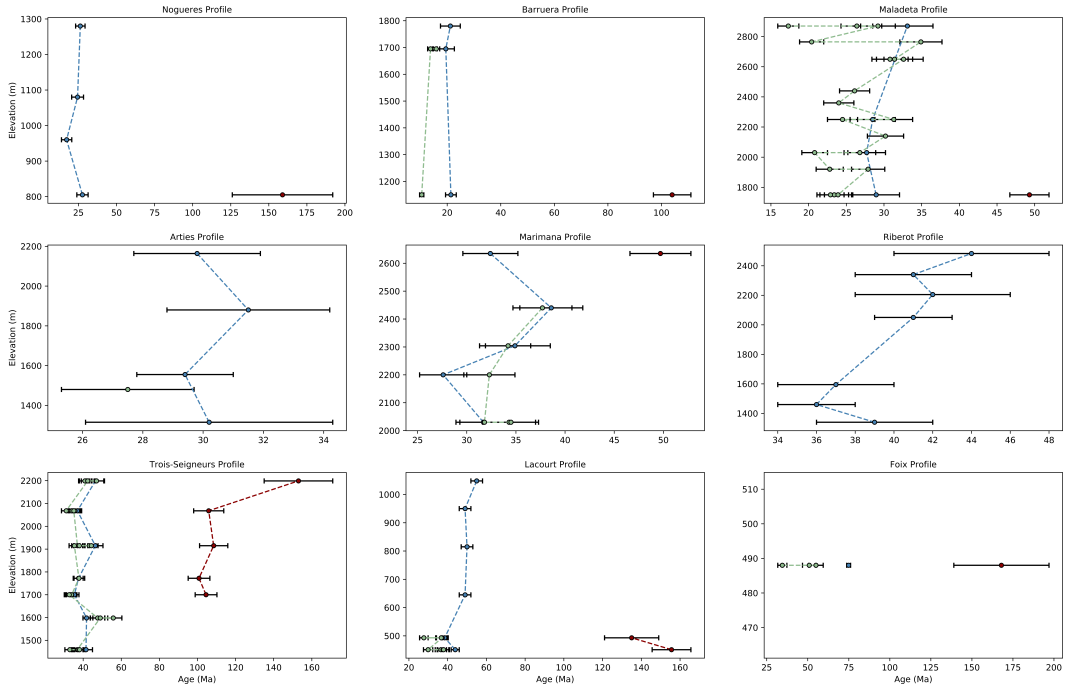

Figure III.1: Age versus elevation plot of the different isotopic cooling ages for the different profiles. Red, blue and green dots correspond respectively to ZFT, AFT and AHe ages.

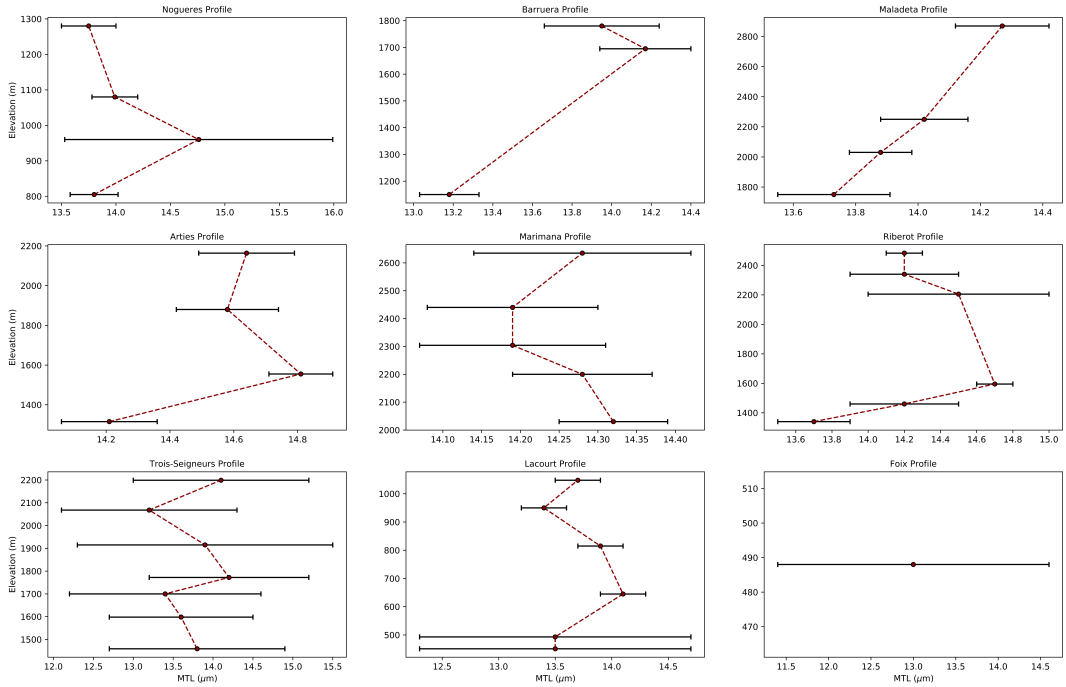

Figure III.2: Apatite fission track mean track length versus elevation plot for the different profiles.

Nogueres Profile

The Nogueres sub-vertical profiles corresponds to four samples (Sinclair et al., 2005) extracted from volcanoclastic and pyroclastic deposits of the Permo-Carboniferous Erill-Castell succession (Soriano et al., 1996) south of Montardit village. Elevation of the lowest and uppermost samples are respectively 805 and 1280 m. ZFT cooling ages of the lowest sample is 159±33 Ma. AFT cooling ages for the four samples range from 17.2±3.4 Ma to 26.3±3.1 Ma with MTL ranging from 13.75±0.21 μm (standard deviation of 2.23 μm) to 14.76±1.23 μm (standard deviation of 2.76 μm).

Barruera Profile

The Barruera sub-vertical profile is situated on the south-eastern flank of Corona del Pinar (2053) within the small Barruera massif. The massif is situated to the south west of the Maladeta profile and closer to the southern structures of the Axial Zone.The elevation range of the profile is 630 m with the lowest sample situated at 1150 m and the uppermost sample at 1780 m. The Barruera profile comprises AFT, ZFT and AHe data (Sinclair et al., 2005; Gibson et al., 2007). ZFT cooling ages for the lowest samples

(1150 m) is 104±7 Ma. AFT cooling ages range from 19.5±3.2 Ma to 21.4±2.0 Ma. Track lengths of the different samples are relatively long with a MTL ranging from 13.18±0.15 μm (standard deviation of 1.69 μm) to 14.47±0.23 μm (standard deviation of 1.45 μm). AHe data range from 10.5±0.8 Ma to 15.9 Ma.

Maladeta Profile

Northward of the Barruera massif is the Maladeta massif, which correspond to a structural block bound in the north and the south by Alpine-age faults. The Maladeta massif is also crossed by the main drainage divide with an east-west direction. The Maladeta profile is however situated southward of the drainage divide at the head of the Flamisell valley draining southward into to the Ebro basin. The Maladeta profile sampled in the Estany Gento region exhibit the greater elevation range of 1110 m with the highest sample at 2889 m (Summit of Pala Pedregos) and the lowest sample at 1760 m (Panta de Sallente). As with the Barruera profile, the Maladeta profile comprise age from three different isotopic system (ZFT, AFT and AHe) (Sinclair et al., 2005; Gibson et al., 2007). ZFT cooling age from the lowest sample has a Lower Eocene age of 49.3±2.6 Ma and contrast with older ZFT age from Barruera and Nogueres profile. AFT ages range from 27.7±2.5 Ma to 33.1±3.4 Ma with a MTL ranging from 13.73±0.18 (standard deviation of 1.33 μm) to 14.27±0.15 μm (standard deviation of 1.7 μm). Finally AHe cooling age range from 17.3 Ma to 3.9 Ma.

Arties Profile

The Arties profiles is situated in the northern Pyrenees in the Val d'Aran. The valley of the vertical profile is a Tributary of the Garonne River, which reach the Atlantic Ocean in the Bay of Biscay. The vertical profile is constituted by four samples with a vertical range of 849 m ranging from the bottom of the valley at 1315 m to the top of the ridge at 2164 m (Gibson et al., 2007). AFT data of Arties profile are characterized by a narrow age distribution, long mean track length and low standard deviation suggesting a rapid exhumation around 30 Ma. AFT cooling ages range from 29.4±1.6 Ma and 31.5±2.7 Ma with a MTL ranging from 14.21±0.15 μm (standard deviation of 1.63 μm) to 14.81±0.10 (standard deviation of 1.12). AHe measurement are available for one sample and give an age of 27.5±2.2 Ma.

Marimaña Profile

The Marimaña profile comprises five samples and is located immediately to the west of the ECORS line. Samples are taken from the summit of the Tuc de Baciver to down the south-western flank of the mountain. The Marimaña massif is also crossed by the modern drainage divide with a north-south direction and is bounded to the south and north-west by large sub-vertical faults. The lowest and uppermost samples are situated at an elevation of 2030 and 2635 m. ZFT, AFT and AHe cooling age measurements are available for the Marimaña profile (Sinclair et al., 2005; Gibson et al., 2007). The ZFT cooling ages of the uppermost sample is 49.7±3.1 Ma and is in the same order than the one of Maladeta profile. AFT cooling ages range from 27.6±2.4 Ma to 36.6±3.2 Ma with a MTL ranging from 14.32±0.07 μm (standard deviation of 1.37 μm) to 14.32±0.07 μm (standard deviation of 1.0 μm). AHe cooling ages for four samples range from 31.8±2.5 to 37.7±3.0 Ma.

Riberot Profile

The Riberot profile is located northward of the modern drainage divide and extends from 1340 m to 2483 m spanning a vertical range of 1143 m. Only AFT data are available for this profile. AFT cooling ages range from 36±2 to 44±4 Ma with a MTL ranging from 13.4±0.2 μm to 14.1±0.2 μm (Fitzgerald et al., 1999).

Trois-Seigneurs Profile

The Trois-Seigneurs profile is situated on the south central side of a Paleozoic crystalline basement (Arize and Trois-Seigneurs massif) and comprises seven samples incorporating ZFT, AFT and AHe data (Vacherat et al., 2016). The Arize massif is broadly delimited to the north by the Camarade basin by the North Pyrenean Frontal Thrust and to the south with the St-Girons/Aulus basin by the North Pyrenean Fault. ZFT cooling ages for the Trois-Seigneurs massif range from 100.8 to 153.0 Ma and greatly contrast with the younger ZFT age of the Axial Zone (Maladeta and Marimaña massif). AFT ages range from 35.4 Ma to 46.5 Ma with a mean track length ranging from 13.2 μm (standard deviation of 1.8 μm) to 14.2 μm (standard deviation of 2.0 μm). Finally, AHe ages range from 31.1 to 55.8 Ma.

Lacourt Profile

The Lacourt profile is situated on the same Paleozoic crystalline basement as the Trois-Seigneurs profile. More exactly, the Lacourt profile is located on the eastern side of the Arize massif. The Lacourt profile combines two different datasets from Fitzgerald et al., (1999) and Vacherat et al., (2016). Data from Fitzgerald et al., (1999) comprise measurement of AFT ages and mean track length on five samples. However, we use only four samples as the lower one is separated by a fault and exhibit a lower ages compare to other samples of the profile. AFT cooling ages range from 49±2 to 55±3 Ma with a mean track length ranging from 13.4 μm (standard deviation of 1.8 μm) to 14.1 μm (standard deviation of 1.7 μm). Dataset of Vacherat et al., (2016) is constituted of two samples with ZFT, AFT and AHe. ZFT cooling ages yield pre-orogenic ages ranging from 135.0±14.0 to 155.6±10.0 Ma. AFT cooling ages range from 38.5±1.8 to 43.9±2.1 Ma with a mean track length of 13.5±1.2 μm. Finally AHe cooling ages are younger than AFT ages and range from 27.7±2.2 to 37.9±3.0 Ma.

Foix Sample

The Foix location constitutes the northernmost location of the different profiles along the Central Pyrenees and has only one sample. ZFT measurement record a pre-orogenic age of 168.0±29.0 Ma. The AFT cooling age is 74.9±1.2 Ma and the AHe cooling age is slightly younger with measurements ranging from 27.7±2.2 to 37.9±3.0 Ma. AFT mean track length is 13.5±1.2 μm.

III.1.3 Inverse modelling procedure

Thermochronological data from various radiometric systems are often used to define a cooling path of the host rock assuming that the measured age represents the time at which the rock cooled through a particular range ofclosure range temperature. As mentioned before, different low-temperature thermochronological system have been developed as noble gases (argon in feldspar, helium in apatite and zircon) and fission track analyses (apatite and zircon) to provide important constraints on the evolution of the upper crust (1-3 km). Applications have been used in various geological context from regional cooling in orogenic belt, landscape evolution to resource exploration in sedimentary basin. However, a thermochronological age does not generally reflect a discrete event. For example, AFT systems can give more information than a simple

cooling age by analysing the mean track length distribution. Furthermore, it become more and more traditional to use several thermochronometers in a same study in order to have a complete record of the thermal histories according to the closure temperature of each systems. A major advance to understanding low-temperature radiometric systems has been the development of quantitative models for the temperature dependence of kinetic diffusion in minerals (Ketcham et al., (2007) for apatite fission tracks; Yamada et al., (2007) for zircon fission tracks; Farley, (2000) for apatite helium as examples). Considering multiple parameters of diffusion domains and multiple cooling ages from different thermochronometers, it is difficult to extract all the information from a simple interpretation of cooling ages. Extraction of thermal histories from inverse modelling become necessary given the complex coupling of different parameters and dataset through a single thermal history. A number of computer programs have been developed to deal thermochronological data in order to estimate thermal histories (Corrigan, 1991; K. D. Crowley, 1993; Gallagher, 2012; Ketcham et al., 2003; Lutz & Omar, 1991) (Figure III.3).

QTQt

QTQt is a modelling software used to infer thermal histories from low-temperature thermochronological data (Gallagher, 2012). This software allows forward and inverse modelling but thermal history information are best treated as an inverse problem. The different thermochronological systems implemented in QTQt comprise apatite and zircon fission tracks, apatite and zircon (U+Th)/He data, $^{4}He/^{4}He$, $^{40}Ar/^{39}Ar$ age spectra and vitrinite reflectance but also allow to enter any kinetics for any mineral/isotope system combination. QTQt is specifically designed to model several samples from a same sub-vertical profile. This method enables the reduction of over-interpretation, noise and the definition of a better models for the profile (Gallagher et al., 2009). In order to deal with apatite fission track data, QTQt uses the multicompositional algorithms of Ketcham et al., (1999, 2007) and the original apatite-based algorithm of Laslett et al., (1987) and the algorithms of Tagami et al., (1998) and Yamada (2007) for zircon. For predicting He diffusion, QTQt uses standard diffusion equation and include radiation damage models of Gautheron et al., (2009); Flower et al., (2009) for apatite and Guenthner et al., (2013) for zircon.

Inverse modelling schemes performed in QTQt are based on the Bayesian Markov

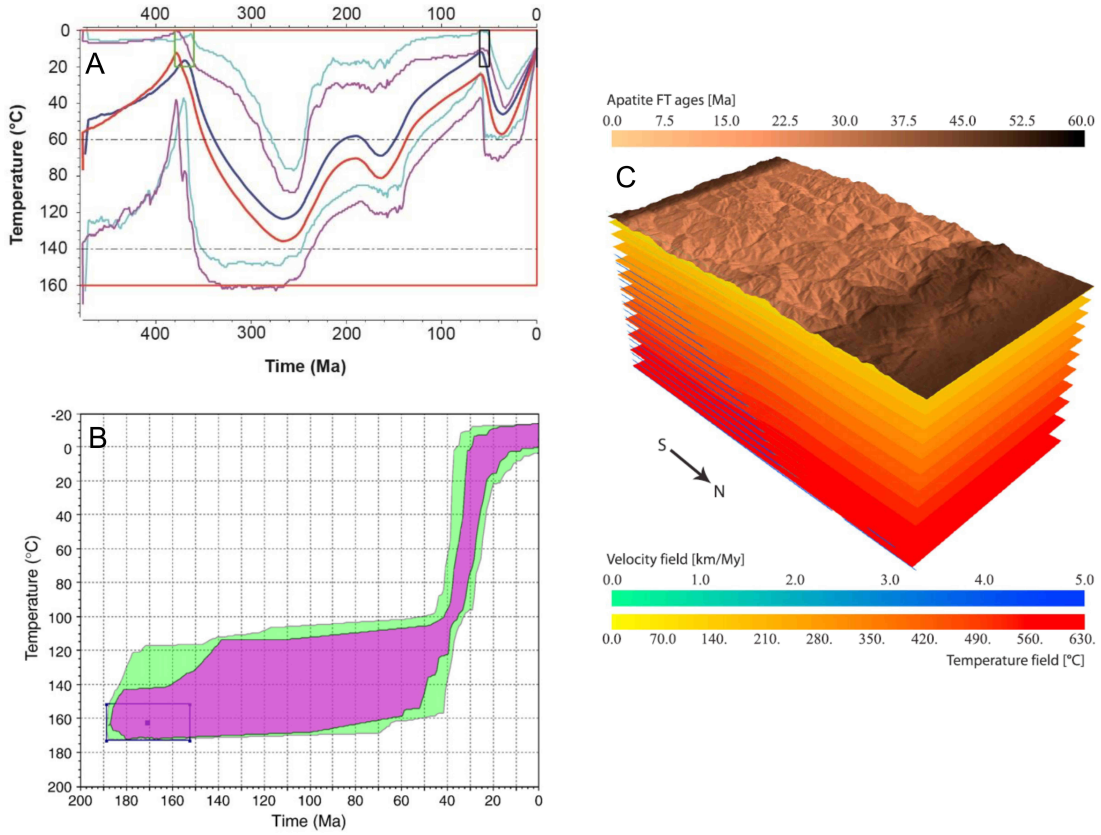

Figure III.3: Set of results from three different software specializing in the inverse modelling of low-temperature thermochronological data. A. Thermal history obtained with QTQt from (Bernard et al., 2016). Red and blue curves correspond to the hottest (lowest elevation) and coldest (highest elevation) sample respectively in case of a vertical profile modelling. Magenta and cyan curves are 95% credible intervals for the red and blue curves. B. Thermal history obtained with HeFTy from (Ketcham et al., 2009). Green and Purple area correspond respectively to accepted path with a $\sigma 1$ precision and good path with a $\sigma 2$ precision. C. 3D diagram obtained with PECUBE from (Erdös et al., 2014). Distribution of AFT ages are represented in color at the surface of the model in relation with the topography, speed fields and thermal fields.

chain Monte Carlo (MCMC) (Denison et al., 2002; Gallagher et al., 2009; Gilks et al., 1996) in order to search the range of possible solutions in function of the unknown model parameters and data. The purpose of the Bayesian approach is to construct the probability distribution of the model parameter values given the data. This relies on the Bayes rule and can be written as:

$$p(m \parallel d) = p(m)p(d \parallel m) \tag{III.1}$$

Where $p(m \parallel d)$ is the posterior probability density function (PDF) of the model parameters, m, given the data, d. $p(m)$ is the prior PDF on the model and $p(d \parallel m)$ ids the likelihood function which quantifies the probability of obtaining the data, d, given the model, m.

MCMC is an iterative sampling approach in which the first part of the series (burn-in) represents an initial exploration of the model space. The second part (post-burn-in) is used to approximate the posterior distribution for the model parameters. QTQt works with two models at each iteration: current model (mc) and proposal model (mp). The latter is generated by random modification of the first model. At each iteration, it either accepts the proposed model and replaces the actual model or rejects it and keeps the actual model. To decide if the proposed model is accepted, the software analyses if the proposed model fits better the data compared to the actual model. To produce the proposed model, a series of possible transformations on the current model is proposed: (1) move a time point; (2) move a temperature point; (3) move an offset value; (4) remove a time-temperature-offset point (death); (5) add a time-temperature-offset point (birth); (6) move the kinetic parameter for an individual sample; (7) move an observed data value for an individual sample. For each of the iterations, a single transformation is chosen randomly from a probability pi where the sum of the probability of the possible transformation is equal to one ($sump_i = 1$). Determination of a change, for each transformation involving a movement (temperature-time-offset-kinetic change), is again randomly chosen between a pre-defined change amplitude and applied to the current model to produce the proposed model. Definition of the perfect amplitude of change is important. If the amplitude defined in the model is too small, model perturbation is also small, and then the proposed model is very similar to the current model. Almost every proposed model are accepted but models change too slowly. In contrast, if the amplitude is too high, model perturbation is also high and too many proposed models are rejected. A way to calibrate this amplitude is by looking to the acceptance rate. As

a general guide, acceptance rate have to be between around 20 and 50%. Acceptance rate for transformation implying birth or death tend to be much lower: 0.1-10%.

This method allows, after a number of iterations, an extraction of the optimal thermal history compared to the data. It is estimated at 200,000 (Gallagher, pers. com.) the number of iteration needed at least in order to produce a good and robust thermal histories. It is possible to add some time-temperature constraints in order to force the general thermal history to pass through it. Note that adding manual constraints is against the spirit of transdimentional MCMC. One advantage of QTQt is the possibility to have a summary model predictions that allow visualizing how good are the prediction of the model compared to the data. This feature correspond to a simple plot of the observed data versus the predicted data (fission track ages, fission track mean track length and AHe ages) for all the samples of the profiles.

Modelling strategy

Modelling of the different datasets used in this study have already been performed but with different techniques and software causing difficulties when comparing the results . In this section, we present the modelling strategy to produce thermal histories which are presented and analysed in the chapter paper: "Lithological control on the post-orogenic topography and erosion history of the Pyrenees". The main principle is to produce thermal histories using the same methodology and QTQt software. We model all available thermochronological data from the different samples of sub-vertical profiles in order to take full advantage of the multi-sample inversion approach. It allows a reduction of the potential of both over interpretation and introduction of artefacts and noises in the inferred thermal history (Gallagher et al., 2005).

In order to build the thermal histories, we integrate through QTQt the following dataset:(i) Apatite and zircon fission track ages and apatite helium ages; (ii) Mean track length and standard deviation as well as the full apatite fission track length distributions; (iii) grain dimensions for apatite helium data. For some profiles, the complete fission track length distribution was not available. For these cases, we built a set of artificial individual track lengths which have the same statistic (and track length and standard deviation). We use the following kinematic models: (i) the multicompositional algorithms of Ketcham et al., (2007) for AFT data; (ii) the kinematic model of Yamada et al., (2007) for ZFT data; (iii) the annealing and apatite radiation damage of Flowers

et al., (2009) and Gautheron et al., (2009). For all vertical profiles, we setup for the inverse modelling parameter a geothermal gradient of 30±15 °C.km^{-1} and present day temperatures of 10±10 °C. The range for general prior, which govern where the thermal history is resolved are let by default. We have decided to not incorporated constrain through the modelling. Thermal histories are obtained after at least 200,000 iterations if the acceptance rate results present a good range of values. We check after each modelling the likelihood chain and the summary model predictions to access the goodness of the inverse modelling.

Result outputs

The modelling produces different outputs. Here, we present the most used outputs to interpret the low-temperature thermochronological data.The first output is the likelihood chain which allows us to access the performance and outcome of the modelling (Figure III.4). This plot allows the visualisation of the likelihood chain as a function of post-burn-in sampling and reflects the goodness of the model results compared to the observed data through iterations. A higher likelihood value signifies a better model prediction. Normally, there should be no obvious trend in the likelihood plot meaning that the modelling cannot propose a better solution in comparison with the observed data. If the likelihood trend is increasing, it means that the number of iterations are not enough to produce the best model and subsequent modelling iterations have to be performed. Alongside the likelihood, the number of time-temperature points for the thermal histories are plotted. Noted that a higher number of time-temperature points does not mean a better model result.

The different thermal history models which can be examined are the maximum likelihood, maximum posterior, maximum mode and expected thermal histories. The maximum likelihood model (Figure III.5) corresponds to the thermal history which best fit the observed data. The maximum mode model often propose a too complex thermal history but allows an observation of the first order change of temperature through time. The expected model (Figure III.6) is the preferred thermal history as it provides features that are more realistic. This model allow also the calculation of uncertainty.

A generic profile comprise several samples at different elevations. Graphical representation of the expected thermal history is made along a time axis (x) and a temperature axis (y) and includes one time-temperature path for each samples of the profile. The

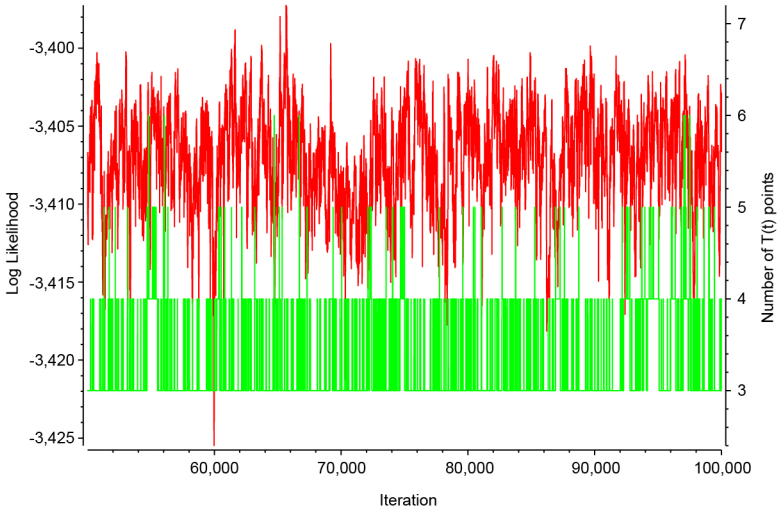

Figure III.4: Likelihood chain performance example from the Marimaña profile inverse modelling. Red line corresponds to the likelihood chain evolution through iteration showing no major trend. Green line corresponds to the number of time-temperature point through iterations.

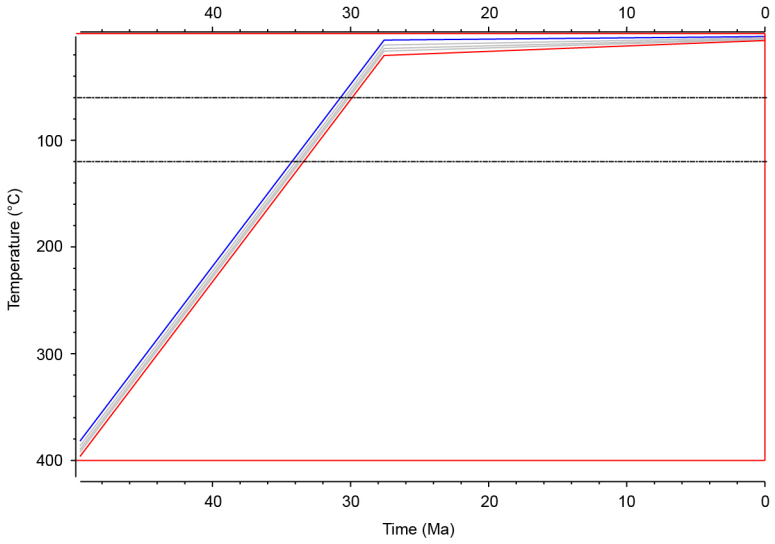

Figure III.5: Likelihood thermal history model example of the Marimaña profile.

uppermost sample is represented by a blue line while the lowermost sample is represented by a red line. Intermediate samples are represented by grey lines. The difference between the thermal histories for the highest and lowest samples is defined as the temperature offset parameter and is estimated assuming a range in geothermal gradients imposed on the model. Thermal histories of intermediate samples are calculated by linear interpolation between the highest and lowest elevation samples. Cyan lines and magenta lines correspond respectively to the 95% credible intervals for the uppermost and lowermost samples. Credible intervals reflect the combined uncertainty in the inferred thermal histories and offset parameters. Black boxes are constraints imposed on models. Finally, the red box corresponds to the prior range on the time-temperature values for the highest elevation sample.

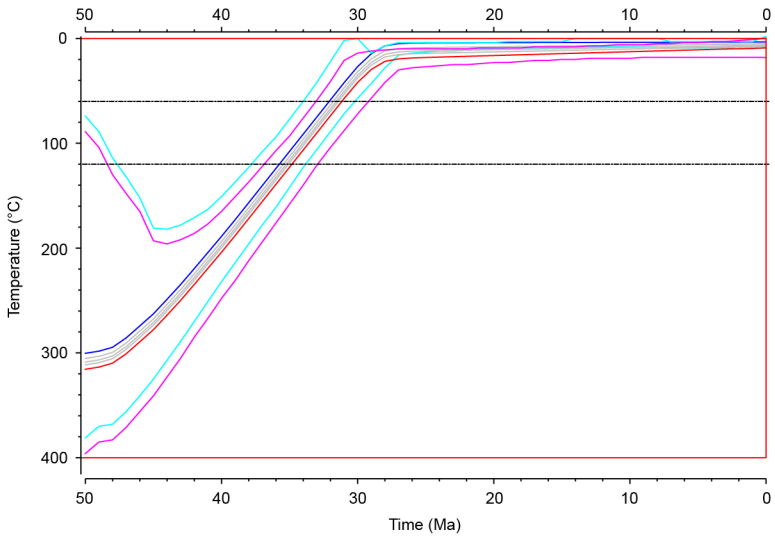

Figure III.6: Expected thermal history model example for the Marimaña profile.

The final outputs is the summary model predictions (Figure III.7) which allows a comparison between the predicted data generated by the thermal history model results versus the observed data as a function of elevation. This plot allows to observe if the model predict well the input data for each samples of the profile. For thermal histories inferred from ZFT, AFT and AHe datasets, the summary model predictions can be described as follow. Normal green triangles, blue circles and red diamonds are respectively AHe ages, FT ages and MTL observed. Error bars on AHe ages, FT and MTL are included and are represented by green, blue and horizontal lines. Inverse green triangles, blue verticals lines and red vertical lines are the predicted AHe ages, FT ages

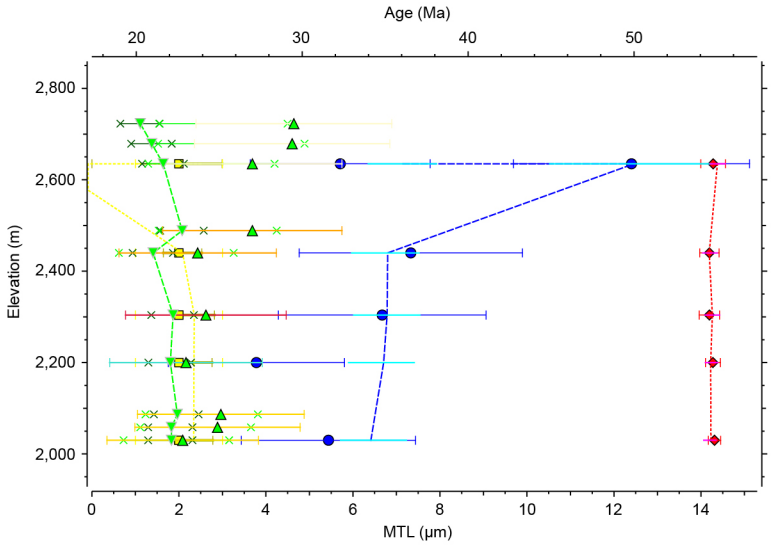

Figure III.7: Summary model prediction example for the Marimaña profile.

and MTL respectively. The cyan, magenta and green horizontal lines are the mean and 95% credible range for the predictions on FT ages, MTL and AHe ages respectively. Green cross correspond to the helium prediction range for accepted models. Yellow squares and yellow horizontal lines are the prior kinetic parameters and error bars (multi-composition model of Ketcham et al., 2007 for AFT data, Yamada et al., 2007 for ZFT data, and Gautheron et al., 2009 for helium data) used as inputs for the inverse modelling. Yellow vertical lines are the predicted kinetic parameters while the modelled 95% credible range is show as light yellow horizontal lines.

III.2 Topographic Analyses

III.2.1 Fluvial erosion

Incision of river channels record the topographic evolution of a landscape. The evolution of river profiles can be classified based on the dynamic state that governs the rate of channel incision. Two main systems describe incision of river systems. Incision for transport-limited condition is set by the downstream divergence of sediment transport capacity (Whipple, 2002). Incision occurs only if the local transport capacity of the stream is greater than the sediment load supply from upstream (Howard, 1980; Howard & Kerby, 1983). The rate of incision in detachment-limited conditions is determined by the stream's ability to erode the bed by a combination of abrasion and plucking

processes (Hancock et al., 1998; Whipple & Tucker, 1999). Hybrid systems are defined for rivers where both transport capacity and detachment control channel incision (Sklar & Dietrich, 1998; Tucker & Whipple, 2002).

River channel incision can be related with the river slope and drainage area by the stream power law:

$$E = KA^m S^n \tag{III.2}$$

Where E is the erosion rate of river channel, A is the drainage area as a proxy for water discharge, S is the local slope, K is an erodibility coefficient of the channel which take in account the influence of climate, lithology and other factors and m and n are empirical coefficient conditions. Equation 5.1 is often applied to detachment-limited models to simulate landscape evolution. The topographic evolution of a channel river experiencing uplift and erosion driven by the stream power can then be stated by the following equation:

$$\frac{dz}{dt} = U - E = U(x,t) - K(x,t)A^m \left(\frac{dz}{dx}\right)^n \tag{III.3}$$

Where U is the uplift rate, z is the elevation of the river, x is a longitudinal coordinate along the river and t is time (Howard and Kerby, 1983; Whipple and Tucker, 1999). Parameters U and K can be a function of time and space and parameter K can be also function of sediment supply (Hobley et al., 2011; Sklar & Dietrich, 2004). Considering a steady-state system where U and K stay constant through time and uplift is compensated by erosion, equation 5.2 can be simplified as follow:

$$S = k_s n A^{-\theta} \tag{III.4}$$

Where $k_{sn} = (E/K)^{1/n}$ is the steepness of the profile and $\theta = m/n$ represents the concavity of the channel profile (Flint, 1974; Hack, 1973; Sklar & Dietrich, 2001; Whipple & Tucker, 1999; Wobus et al., 2006). The channel steepness (k_{sn}) is sensitive to the rock uplift rate, climate and lithology of the eroded bedrock (Kirby & Whipple, 2012; Wobus et al., 2006). The concavity index is sensitive to temporal and spatial variations of these factors through the system. For example, a river channel with a higher uplift in the upstream part will show a higher concavity index and vice versa (Kirby & Whipple, 2001). More important precipitation in a non-uplifted area can produce a more concave river profile (Zaprowski et al., 2005). Equation 5.3 predicts a power-law relationship between the slope and drainage area of a river profile which is

often represented on a logarithmic scale (Figure III.8). The steepness and concavity can be extracted from this type of plot where the y-intercept and is the gradient of a line through the data. Studies using these relations are generally strongly based on DEM analyses. One of the main limitations is the noise associated with the creation of the DEM because of sediment transport processes, bed roughness or from the data processing which can influence interpretations. The noise is amplified by the derivation of the topographic surface to obtain parameters of the channel gradient (Perron & Royden, 2013). The noise is reverberated by significant scatter on the plot which makes extraction of process changes such as lithology, climate or uplift from the log-log trend difficult to achieve.

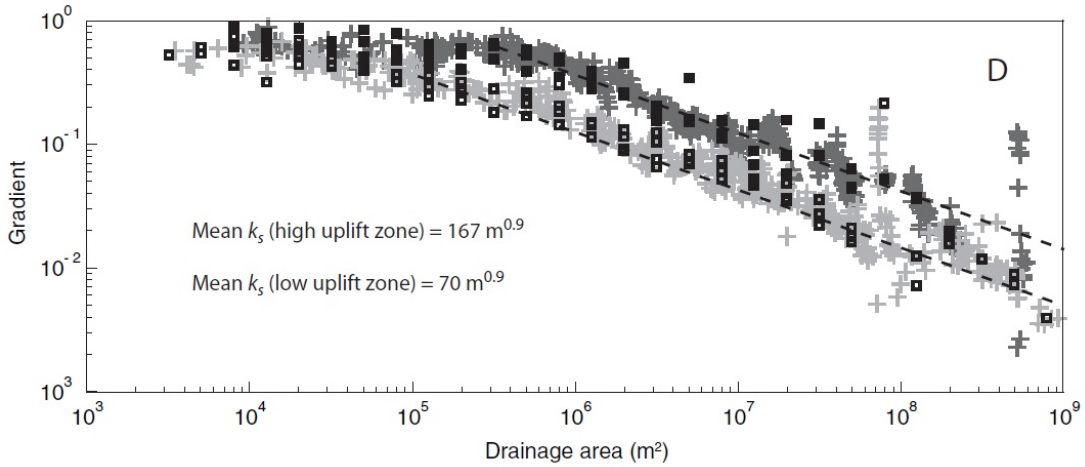

Figure III.8: Composite slope versus drainage area plot from six rivers of the San Gabriel Mountains east of Los Angeles, California from a SRTM with a resolution of 10 m from Wobus et al., (2006). Parameters $k_s n$ is the y-intercept and θ is the gradient of a best-fit linear regression through the data in log-log space.

III.2.2 Integrated approach for river profile transformation

An alternative approach to eliminate noise associated with the DEM is to integrate the drainage area along the channel length (Harkins et al., 2007; Mudd et al., 2014; Perron & Royden, 2013). The integral method allows a comparison of basins of different size and only requires extraction of elevation and drainage area from DEM and therefore less subject to topographic noise then slope-drainage area. The rational of this method can be seen by integrating equation 5.3, because the topographic gradient, S, is the

derivate of elevation, z, with respect to downstream distance x. Integration results is:

$$z(x) = z(x_b) + \left(\frac{U}{K}\right)^{1/n} \int_{x_b}^{x} \frac{dx}{A(x)^{m/n}} \tag{III.5}$$

With an integration performed from a base level reference (x_b) to a specific point of the river channel (x). To create transformed river profiles with units of length on both axis, a reference drainage area (A_0) is introduce to ensure that the integrand is dimensionless:

$$z(x) = z(x_b) + \left(\frac{U}{KA_0^m}\right)^{1/n} \chi \tag{III.6}$$

with:

$$\chi = \int_{x_b}^{x} \left(\frac{A_0}{A_x}\right)^{m/n} dx \tag{III.7}$$

The transformed coordinate χ has dimension of length and the elevation $z(x)$ is a linear function of χ. A channel represented in a chi versus elevation plot with constant U and K in space and time will appear as a straight line with the slope being a function of the uplift to erodibility ratio (U/K raised to the power $1/n$ (Perron and Royden 2013. Mudd et al., 2014). The integral approach has several advantage (Perron and Royden, 2013): (i) the reduced scatter relative to slope-area plots provide better constraints on stream power parameters estimated from topographic data. (ii) Removing the effect of drainage area through this coordinate transformation makes it possible to compare river profiles from different drainage area size. (iii) River profiles transformed with the integrated approach allow us to explore transient river profile evolution. Studies have started to use the integrated approach to determine the dynamic state of river channels, especially at the drainage divide between two basins (Willett et al., 2014). The parameter χ characterizes the river network topology and geometry and gives a metric quantification for the steady-state elevation of a channel at a specific distance x. Therefore, within an area with constant tectonic forcing and homogenous physical properties conditions, difference in χ across a divide implies a disequilibrium of the system and motion of the divide towards a higher χ (Figure III.9).

III.2.3 River channel steepness

Royden and Perron (2013) demonstrate that chi plots can be used for channels with constant and uniform uplift and erodibility condition through space and time. However, they argued further that the integrated method can also be used for transient river

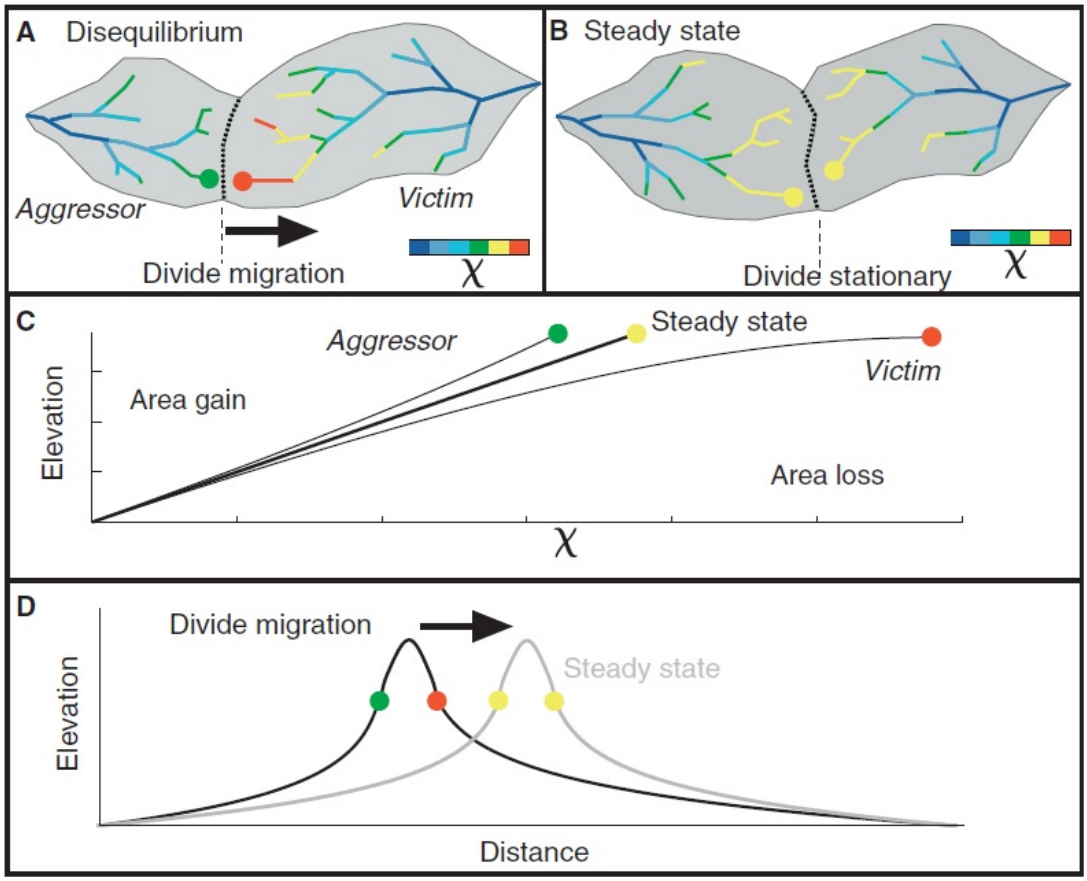

Figure III.9: Schematic representation of river channel in equilibrium and disequilibrium from Willet et al., (2014). A, B) Change in size and shape of two catchments that share a common drainage divide from a disequilibrium state (A) toward an equilibrium state (B). C, D) Modification of elevation distribution of a drainage divide network by incision, deposition and divide migration to reach steady-state configuration. The steady-state condition is performed with a symmetric distribution of χ parameter across the drainage divide.

channels characterised by the presence of "patches" or segment of constant slope in the χ-elevation space. These segments can be described by:

$$z(x) = B_\chi + \left(\frac{E}{K(A_0)^m}\right)^{1/n} \chi \tag{III.8}$$

Equation III.6 is a linear equation with a slope corresponding to the gradient in χ-elevation space (Mudd et al., 2014):

$$M_\chi = \left(\frac{U}{K(A_0)^m}\right)^{1/n} \tag{III.9}$$

The χ-elevation plot gradient or M_χ is closely related to the normalized channel steepness ($k_s n$) which is the steepness index (k_s) calculated with a reference concavity θ (Hodges et al., 2004; Kirby & Whipple, 2012). It has been demonstrated that changes of M_χ can be the result of varying erosion rate along the river profile. Change of M_χ may be the result from factors as uplift or channel erodibility (Figure III.10).

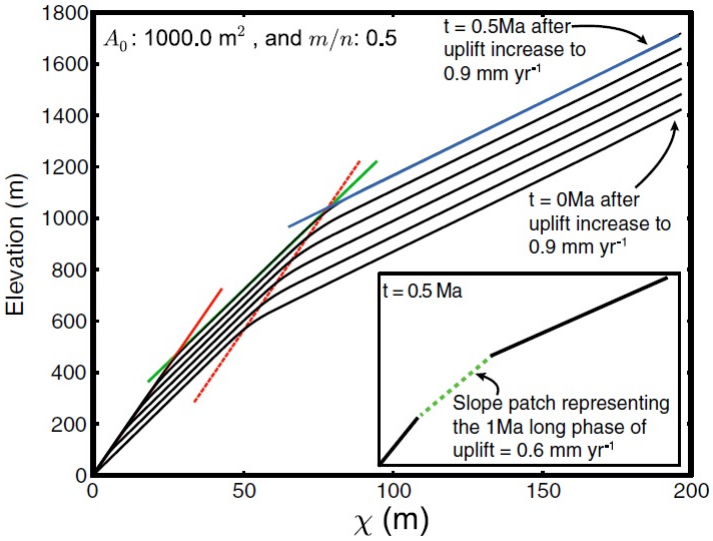

Figure III.10: Illustration of upstream migration of channel segment in χ-elevation space from a channel river originally in steady state with an uplift rate of 0.3 mm.yr^{-1} experienced two consecutive step increase in uplift rate 1 Ma apart to 0.6 and 0.9 mm.yr^{-1} from Mudd et al., (2014).

An important parameter for the χ or M_χ coordinate determination is the concavity index (m/n ratio). The concavity index is not an *a priori* known parameter. However, a general value of 0.45-0.5 is generally used because it represents a theoretical value that river channels should achieve if erosion rates are proportional to the specific stream

power (Wobus et al., 2006). Perron and Royden (2013) demonstrated that the most likely m/n ratio can be determined because all individual tributaries should be linear and co-linear in χ-elevation space. Therefore, the best fitting concavity index is extracted by selecting the θ_{ref} that results in the most co-linear trunk stream/tributary profile in χ–elevation space. In the case of transient channels , Mudd et al., (2014) developed a method to determine the best concavity index which best-fits a series of linear segments. In a recent study, (Mudd et al., 2018) test different methods to determine the best concavity index from both slope-drainage analyses and the integrated method. Best results for the concavity index evolution is found in χ-elevation space using a bootstrap or disorder methods (Figure III.11).

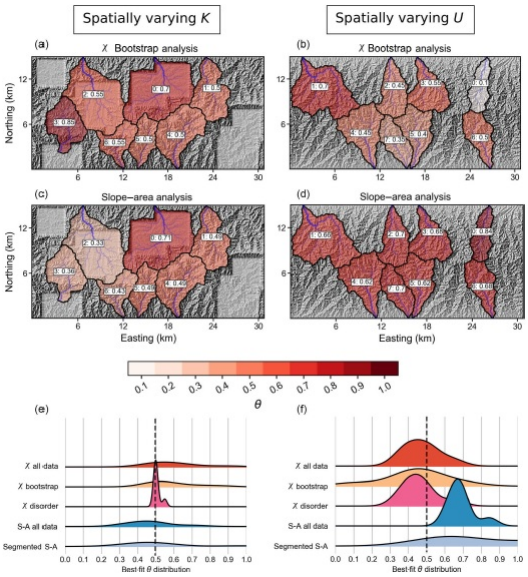

Figure III.11: Results of the determination of the best concavity index from different methods in catchments with spatially varying erodibility and uplift from Mudd et al., (2018). Panel a-d) spatial pattern of predicted θ from the χ bootstrap and slope-area analyses. Panel e and f) density plots of the distribution of θ for each method, where the dashed line marks the correct $\theta = 0.5$.

III.2.4 Topographic analyses of the Pyrenees

Topographic analysis for the Pyrenees have been performed using Shuttle Radar Topography Mission (SRTM) data. SRTM data are derived from both X and C band radar and corresponds to a snapshot of the Earth's surface in early 2000. We use the version 3 of SRTM data which have a resolution of 1 arcsecond (i.e. 30 m) available on the USGS

EarthExplorer websites (http://earthexplorer.usgs.gov/). Topographic analyses for the Pyrenean system are situated between 40°N and 45°N and between 3°W and 3°E and performed using LSDTopoTools (https://lsdtopotools.github.io/) packages software.

We first analyse the χ index in order to predict major drainage divide migration using ocean water as a base level (Figure III.12). However because of high climate and lithology difference between the northern and southern Pyrenees and between catchments it is difficult to rigorously predict divide migration at the scale of the orogen. The channel steepness index (i.e. M_χ or k_{sn}) is calculate along the river channels of the Pyrenees (Figure III.13). We use the channel steepness index on the main catchment of the Pyrenees in order to constrain the influence of resistant lithologies on the topography of the Pyrenees. Calculation of channel steepness is also combined with landscape evolution model (see following section) in order to provide a mechanism for the migration of drainage divide caused by the exhumation of harder lithologies.

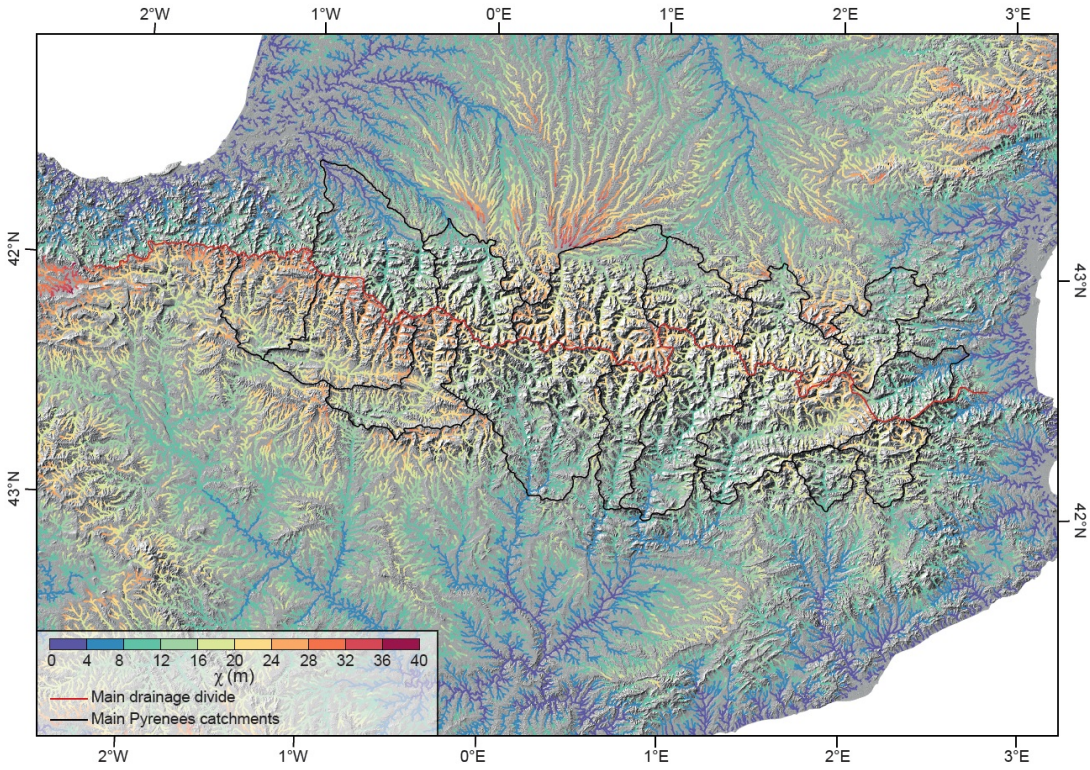

Figure III.12: Result of the χ topographic index for the Pyrenean system. The χ parameter is represented by a succession of points along river channels with colors from purple (low value) to red (high value). Red line indicates the main drainage divide and black lines indicate main catchment of the Pyrenees.

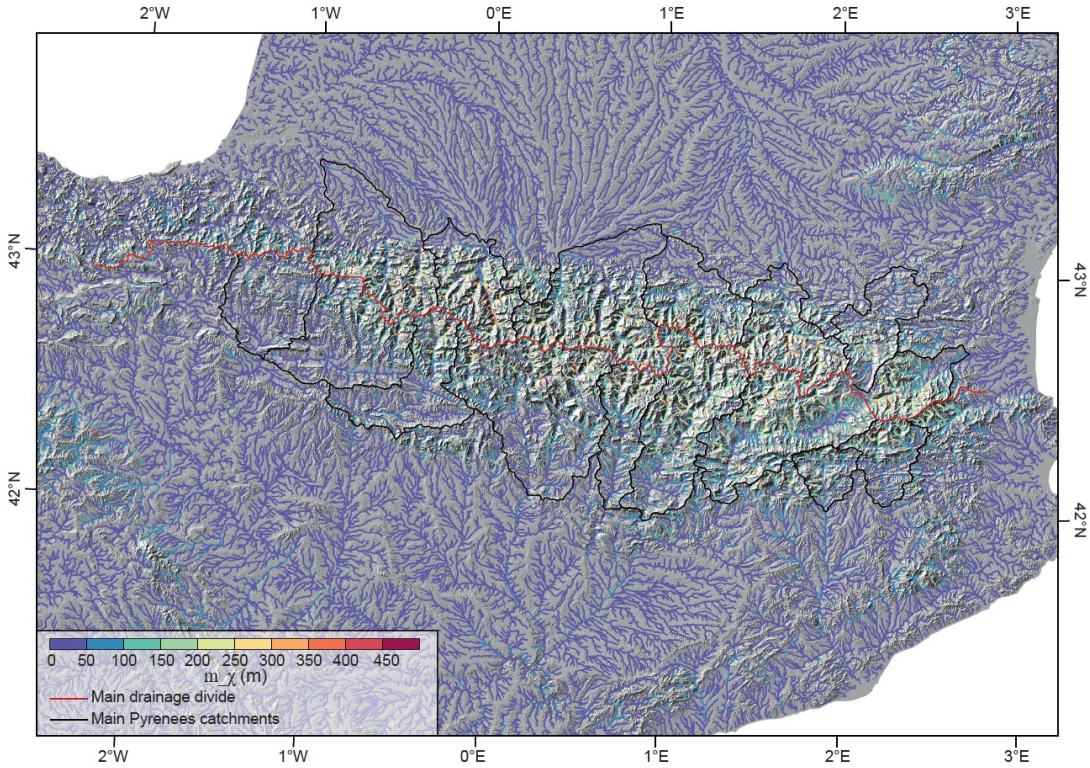

Figure III.13: Result of the M_χ topographic index for the Pyrenean system. The M_χ parameter is represented by a succession of points along river channels with colors from purple (low value) to red (high value). Red line indicates the main drainage divide and black lines indicate main catchment of the Pyrenees.

III.3 Landscape Numerical Modelling

III.3.1 "Box-model" landscape model

The "Box-model" developed by Tucker and van der Beek, (2013) is a model that simulates the evolution of a single thrust-wedge and foreland basin through time. The model treats the problem with two boxes (i.e. one for the range and another one for the basin) which exchange mass with their surroundings by sediment transport, crustal thickening and tectonic accretion. Mass exchanges through the model follow two principles: 1) mass conservation, which means that all material that exits a box has to be redistributed to their surrounding and 2) a correlation between topographic relief and sediment flux. The range is defined as a column of rock which is locally thicker by an amount η_r and with a length L_r. Likewise, the basin is defined as a box with length L_b and average thickness η_b. The model is coupled with lithospheric flexural isostasy, which predicts the average deflection beneath the range w_r and basin w_b In this way the range topography can be defined by $H_r = \eta_r - w_r$ and the basin topography by $H_r = \eta_r - w_r$ .Changes in topographic elevation of the range and basin relative to a base level (Figure III.14) are then defined with the following equations:

$$\frac{dH_r}{dt} = (1 - \psi_r)\left(\frac{F_c + F_a - F_r}{\rho_r L_r}\right) \tag{III.10}$$

$$\frac{dH_b}{dt} = \frac{F_r + -_a - F_b}{\rho_b L_b} - \psi_b \frac{d\eta_r}{dt} \tag{III.11}$$

where F_c corresponds to the accretionary flux of crustal rocks into the thrust wedge in response to plate convergence and underplating; F_a is the accretionary flux of basin sediments through frontal thrusting. F_r and F_b are respectively the sediment flux out of the range and sediment flux out of the basin; ρ_r and ρ_b are material density for the range and basin respectively; and ψ_r and ψ_b are flexural isostatic parameters for the range and basin respectively.

The accretionary flux (F_c) is expressed with the following equation:

$$F_c = V_c T_c \rho_r \tag{III.12}$$

where V_c is the total convergence velocity, T_c is the thickness of the accreted rock. The accretionary flux (F_a) is expressed with the following equation:

$$F_a = \rho_b f V_c \eta_b \tag{III.13}$$

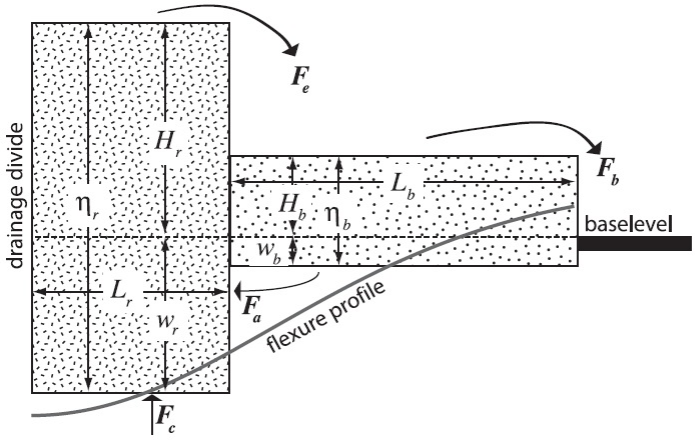

Figure III.14: Schematic illustration of the "Box-model" from Tucker and van der Beek, (2013).

where f correspond to a fraction of basin fill that is brought into the orogen by frontal accretion or underplating. The sediment flux from the range to the basin (F_r) and the sediment flux from the foreland basin (F_b) to the outer depocentre are defined as follow:

$$\frac{F_r}{\rho_r L_r} = \frac{1}{\tau_r}(H_r - H_b) \tag{III.14}$$

$$\frac{F_b}{\rho_b L_b} = \frac{1}{\tau_b} H_b \tag{III.15}$$

where τ_r and τ_b are the range and basin response times respectively. Finally, The average deflection beneath the range (ψ_r) and basin (ψ_b) are given by the following equation (Watts, 2001):

$$\psi_r = \frac{\rho_r}{\rho_m - \rho_b} \frac{e^{-2\lambda Lr}(e^{2\lambda Lr}(-1 + 4\lambda L_r) + cos(2\lambda L_r) - sin(2\lambda L_r))}{4\lambda L_r} \tag{III.16}$$

$$\psi_b = \frac{\rho_r}{\rho_m - \rho_b} \frac{1}{3\pi - 4\lambda L_r} 2e^{-2\lambda Lr - 3\pi/4}(\sqrt{2}e^{\lambda Lr}(-1 + e^{2\lambda Lr})cos(\lambda Lr) + e^{3\pi/4}(e^{2\lambda Lr} - cos(2\lambda Lr) + sin(2\lambda Lr))) \tag{III.17}$$

with ρ_m is mantle density and λ is the inverse flexural parameter.

III.3.2 "Fastscape" landscape model

The "Fastscape" algorithm is a landscape evolution model which allows us to simulate various geomorphologic processes of erosion, transport and deposition in both continental and marine domain (Figure III.15) (Braun & Willett, 2013; Yuan, Braun, Guerit,

Rouby, et al., 2019; Yuan, Braun, Guerit, Simon, et al., 2019). We use a recent version of "Fastscape" available through the python Xarray-Simlab package (Bovy, 2020). Continental erosion is simulated by river channel incision and hillslope processes with the stream power incision model and linear diffusion law respectively:

$$E = K_f A^m S^n + K_c \nabla^2 h \tag{III.18}$$

where E is erosion; A is drainage area; S is slope; m and n are area and slope exponent coefficient respectively; h is elevation; K_f is the erodibility and K_c is a transport coefficient. Transport and sediment deposition in continental domain are included in the model with the following condition:

$$D = \frac{G}{A} \int_A \left(U - \frac{dh}{dt} \right) dA \tag{III.19}$$

where D is deposition; G is a coefficient for deposition and t is time. In marine domain, sediment transport are simulated through a diffusion equation:

$$\frac{dh}{dt} K_m \nabla^2 h + Q_s \tag{III.20}$$

where K_m is the marine sediment transport coefficient; Q_s is the sediment flux coming from the continental model of the model.

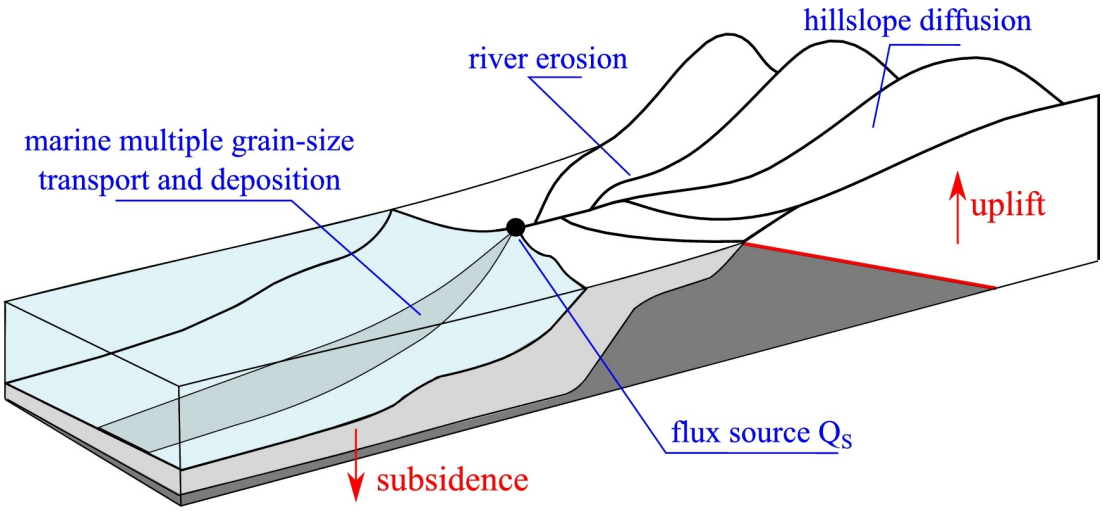

Figure III.15: Schematic illustration of the model combining erosion, transport and deposition in both continental and marine domain from Yuan et al., (2019).

III.3.3 Application of landscape numerical modelling

Through this thesis, we apply both models ("Box-model" and "Fastscape") for the comprehension of mountain belt/foreland basin systems. We particularly explored the

topographic and sediment flux evolution of the Pyrenees and modelled the Northern Pyrenean system as a thrust-wedge and foreland basin coupled with isostatic flexure during the late syn- and post-orogenic phase.

We use the "Box-model" in order to approximate the Pyrenean system while keeping physical processes that governs a thrust-wedge and foreland basin system. First, we perform generic experiments with the "Box-model" to access first-order topographic and sediment flux signals related to the switch from active convergence to cessation of convergence. Equations encompassed in the "Box-model" are relatively simple and allow fast topographic and sediment flux calculation over large period of time (i.e. several million years). We use this advantage, in a second step, in order to perform inverse modelling which allow to approximate the Northern Pyrenean system. Multiple iterations allow to replicate first-order characteristic features of the Northern Pyrenees and to obtain robust signal associated to the late syn- to post-orogenic transition in term of topographic and sediment flux evolution.

The "Fastscape" algorithm allow to resolve erosion in both continental and marine domains. We adapted the model in order to predict topographic evolution of a mountainous landscape during change of condition. We particularly explore effect of variable erodibility coefficients through time and space which can simulate change of rocks lithologies exhumed through time. We combine our landscape evolution model with topographic analyses (described in the previous section) to analyse the landscape transience associated to these changes. The "Fastscape" model can resolve erosion but also transport and deposition laws in both continental and marine domains. This allow us also to model the evolution of a foreland basin evolving through under-filled (marine condition) to over-filled (continental condition) conditions. The foreland basin responds in term of flexural isostasy and sediment flux to the growth of an uplifted area (thrust-wedge domain) following by a progressive decay.

As a result, the landscape evolution model approach will allow us to resolve topographic and sediment flux responses of a coupled mountain range and foreland basin system to change of rock erodibility or change assosiated to the late syn- to post-orogenic transition.

Chapter IV

LITHOLOGICAL CONTROL ON THE POST-OROGENIC TOPOGRAPHY AND EROSION HISTORY OF THE PYRENEES

Accepted as an article in "Earth and Planetary Science Letters" journal.
Co-authors: Hugh D. Sinclair, Boris Gailleton, Simon M. Mudd and Mary Ford

IV.1 Abstract

Numerous studies on active mountain ranges have demonstrated the interaction between tectonics and climate in shaping topography. Here we explore how variations in rock types have affected the topographic development of the Pyrenees since cessation of orogenesis ca. 20 Ma. Our study is based on a multidisciplinary approach and integrates topographic analyses, rock strength measurements and thermal modelling of low-temperature thermochronological data published across the Central Pyrenees. Results indicate a strong influence of rock strength in determining the post-orogenic morphology of the Pyrenees. We observe a correlation between rock strength and the normalized channel steepness index (ksn) of the different lithologies. Moreover, the highest topography is dominated by the Variscan plutonic massifs which have highest rock strength. Consequently, the drainage divide appears to track the position of these massifs. Abrupt deceleration of exhumation recorded in inverse modelling of low-temperature thermochronologic data suggests that the exhumation of the Variscan massifs also played role in lowering in erosion rates over the massifs during orogenesis.

IV.2 Introduction

The topographic elevation and relief of active mountain ranges have long been recognised to reflect the long-term competition between tectonic and surface process linked to climate (Beaumont et al., 2001). The macro-geomorphic form of many active mountain chains such as the Southern Alps of New Zealand, the Andes and Taiwan have been reproduced through numerical modelling of tectonically forced rock trajectories countered by erosion (Koons, 1990). However, most of the mountain ranges in the world seem to be in various stages of post-orogenic decay such as the European Alps, Urals, Caledonides, Appalachians or Pyrenees (Baldwin et al., 2003; Tucker & van der Beek, 2013). Underpinning the transition to a post-orogenic state is the competition between erosion and crustal thickening.We consider post-orogenesis as the time at which erosion is dominant over crustal thickening and hence is characterised by regional isostatic rebound, and so during the early stages of post-orogenesis, structural deformation may continue. This definition avoids debate over the timing of cessation of fault movement in the range which may continue after net shortening has stopped. These processes do not include epeirogenic vertical motions forced by mantle flow (e.g. dynamic topography) although it is recognized that slab detachment and mantle processes can impact late stage orogenesis as interpreted in the south-eastern Carpathian (Maţenco, 2017). The landscape evolution of these decaying mountains, where the switch from localised fault-controlled rock uplift to more regional isostatic controls, should be relatively simple with progressive and relatively uniform erosion resulting in a general lowering of both elevation and topographic relief (Baldwin et al., 2003; Tucker and Van der Beek, 2013). In the absence of fault activity, this evolution may be perturbed by external erosional drivers or intrinsic characteristics such as base-level variations, drainage capture, dynamic topography, climate change or lithological variations (Flowers & Ehlers, 2018; Valla et al., 2012). The role of rock strength in moderating stress fields and erosion rates in active mountain ranges has been difficult to characterise (Koons et al., 2012). In contrast, in post-orogenic settings, the influence of rock strength can be more clearly isolated as proposed from the Cape Mountains of South Africa (Scharf et al., 2013) where low denudation rates and the maintenance of topography is primarily attributed to the presence of robust quartzites that constitute the backbone of the range.

Long-term erosion rates in active or inactive mountain ranges are largely limited by

the ability of rivers to erode into bedrock, which is governed by the processes of plucking and abrasion of the river bed (Whipple et al., 2000). The former is largely a function of fracture density, and the latter of tensile strength. Experimental studies demonstrate that lithologies with contrasting tensile strength influence the erosion rate along fluvial channels (Sklar & Dietrich, 2001). Several studies have used the stream power model to demonstrate that rock strength could cause variations in erosion rates by a factor of 3 to 5 depending on the range of lithologies (Sklar and Dietrich, 2001). Plucking is influenced by the presence and orientation of joints, beddings, faults, or foliation impacting the erodibility of rock (Whipple et al., 2000). Flowers and Ehlers (2018) show that thermochronological data and associated thermal histories can be strongly affected by changes of erosion rates caused by variations in the erodibility of rock, typically after removal of sedimentary cover and exposure of underlying crystalline basement. Glotzbach et al., (2011) show, for example, that decreases in exhumation rates at 6 $\pm$ 2 Ma in the Western Alps can be associated to a general decrease in convergence rates and/or extensive exposure of less erodible rock types.

Here, we explore the influence of rock strength on the modern topography of the Pyrenees at the border between France and Spain (Figure IV.1). The Pyrenees have been dominated by post-orogenic decay for the last ca. 20 Myr (Meigs et al., 1996; Sinclair et al., 2005). In this study we measure the tensile strength of the main lithologies across the range, and compare this to the normalised channel steepness (Wobus et al., 2006) derived from measurement of the χ parameter (Perron & Royden, 2013). We compare the rock strength to channel steepness, and determine the role of lithology in defining the modern drainage divide across the range. Finally, we explore the potential effect of unroofing lithologies with varying rock strengths on the evolution of the cooling/exhumation history during growth of the range. Our results demonstrate that lithology is a fundamental control on the topographic form and elevation of the modern Pyrenees, and that it may have played a key control on the history and distribution of erosion during orogenesis.

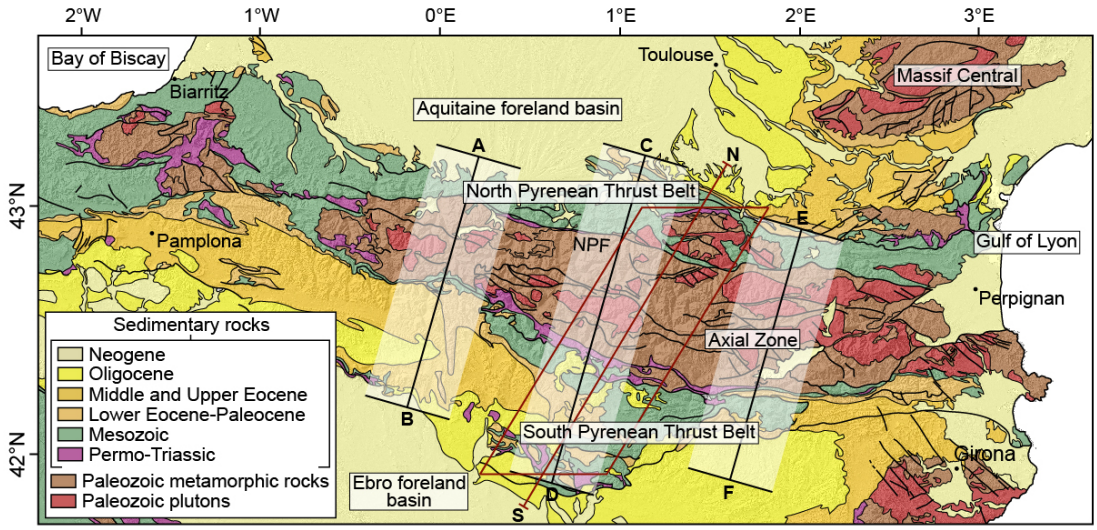

Figure IV.1: Geologic map of the Pyrenees from the 1:1000000 BRGM geological map of France draped on a hillslope map from a SRTM with a resolution of 30 m. Red rectangle highlights the area of Figure IV.7 and the red line indicates the approximate position of the geologic cross-section in Figure IV.4B. NPF: North Pyrenean Fault. Black lines and white transparent areas indicate locations of the different swath profiles of Figure IV.9. Cities are indicated by black dots.

IV.3 Geologic background

IV.3.1 Geology

The Pyrenees form a 450 km topographic long barrier that runs from the Mediterranean Sea (Cap de Creus) to the Bay of Biscay (Cap Higher) with a 150 km-wide central region that separates the Iberian Peninsula from the European continent (Figure. IV.1). The Pyrenees extend as a generally linear east-west orographic barrier with a climatic asymmetry across the range. The Northern Pyrenees are characterised by a relatively steep, wet flank compared to the broader semi-arid southern flank. This morphology has been inherited from the distinct growth of the southern side as an accretionary pro-wedge and the north as a retro-wedge (Beaumont et al., 2000; Sinclair et al., 2005). The formation of the Pyrenees resulted from the convergence and collision of the Iberian and European plates from late Cretaceous to early Miocene time (Roest & Srivastava, 1991). The geodynamical expression of this convergence is the formation of a doubly-vergent collisional orogen, which accommodates up to 165 km of shortening reflected in upper crustal thickening (Beaumont et al., 2000; Muñoz, 1992).

The Pyrenees can be divided into a series of five main tectonic units (Figure IV.1), which, from south to north, are: the Ebro pro-foreland basin, the South Pyrenean Thrust Belt, the Axial Zone, the North Pyrenean Thrust Belt and the Aquitaine retro-foreland basin (Muñoz, 1992; Vergés et al., 1995).

The Ebro foreland basin was initiated in Paleocene times and consists of marine successions of Paleocene to early Priabonian age, and continental successions of early Priabonian to mid- Oligocene age. The South Pyrenean Thrust Belt is made up mainly by a Mesozoic platform series and Palaeogene rocks (Muñoz, 1992) and in the Central Pyrenees consist of three main thrust sheets, named from south to north: Sierra Marginales, Montsec and Boixols.

The Axial zone is separated from the North Pyrenean Thrust Belt by the North Pyrenean fault zone, which corresponds to the present boundary between the Iberian and European continent (Verges & Munoz, 1990). The Axial zone is composed of three Variscan basement thrust sheets named from north to south, the Rialp, Orri and Nogueres thrust sheets (Muñoz, 1992). These units comprise thick Precambrian and Paleozoic metamorphosed sedimentary successions intruded by Variscan granitoid massifs.

The North Pyrenean Thrust Belt and Aquitaine Basin constitute the retro-wedge and retro-foreland basin of the Pyrenees respectively. The North Pyrenean Thrust System involves Variscan basement massifs (called the North Pyrenean Massifs such as the Trois-Seigneurs and Ariège massifs) and Mesozoic to lower Eocene sedimentary cover rock. The Aquitaine basin formed from Late Cretaceous to Miocene by flexure of the upper plate in response to the load the North Pyrenean Thrust Belt (Brunet, 1986).

IV.3.2 Exhumation history

The transition from syn-orogenic shortening to post-orogenic quiescence in the Pyrenees is associated with the last evidence of differential exhumation across thrust faults in the Axial Zone revealed by low temperature thermochronology at around 20 Ma (Gibson et al., 2007; M. Jolivet et al., 2007). Post-orogenic exhumation of the South Pyrenean Thrust Belt is recorded by apatite (U+Th)/He thermochronology (AHe) analysis at ca. 20 Ma to present time (Fillon et al., 2013). A late stage acceleration in exhumation around 9 Ma has been linked to the reconnection of the Ebro Basin to the Mediterranean Sea causing evacuation of a thick sedimentary succession that draped

the South Pyrenean Thrust Belt (Coney et al., 1996; Fillon & van der Beek, 2012).

Initial analyses of low-temperature thermochronology in the Pyrenees used single-elevation samples on basement and granitic massifs. Yelland, (1990) highlight a contrast in the apatite fission track ages (AFTA) and mean track length (MTL) between the south and north and interpret it as recording an initial period of rapid Palaeocene-Eocene exhumation in the northern Pyrenees followed by a protracted period of less rapid exhumation in the southern Pyrenees. Morris et al., (1998) performed subsequent modelling of the data from Yelland, (1990) to demonstrate a syn-orogenic sediment discharge that was 1.5 to 2.8 times greater to the south than to the north. By using multiple vertical profiles from granitic massifs in the Pyrenees (Maladeta, Riberot and Lacourt), Fitzgerald et al., (1999) showed an asymmetric exhumation with AFT ages younging from north to south across the Pyrenees. Sinclair et al. (2005) demonstrated that the core of the Axial Zone records the greatest depth of exhumation and that there was a progressive southward shift with highest exhumation rates associated to the growth of the antiformal stack from 36 to 20 Ma. Gibson et al., (2007) show the youngest evidence for accelerated differential exhumation at 20 Ma on the southern Axial Zone. Finally, exhumation of the northern central Pyrenees has also been recorded by (Vacherat et al., 2016) showing that the Trois-Seigneurs, Lacourt and Foix massifs record monotonic cooling starting at 50 Ma and lasting until 35 Ma.

IV.4 Methodology

Incision of river channels underpins the topographic evolution of landscapes. Moreover, river morphologies record information about external controlling factors such as vertical displacements of rock, climate and intrinsic characteristics such as lithology. The seminal work of Gilbert, (1877), suggested that erosion rates in bedrock rivers are proportional to a combination of channel gradient and water discharge. Gilbert, (1877) recognised that changing discharge will affect channel steepness, noting that if all else is equal, channels with more water will have gentler gradients. Authors began quantifying the relationship between channel gradients and drainage area (a proxy for discharge) in the middle of the 20th century and Morisawa, (1962) recognised that this relationship could be described by a power law. We can state this power law as:

$$S = k_s A^{-\theta} \tag{IV.1}$$

where S is the topographic slope (dimensionless), K_s is a steepness index ($m^{2\theta}$), A is the drainage area (m^2) and θ is called the "concavity index" (dimensionless). Numerous authors have found that the steepness index scales with erosion rate in rivers underlain by a homogenous lithology (see compilations in Kirby and Whipple, 2012 and Harel et al., 2016). Extraction of the steepness index from topographic data typically involves selecting a fixed value for the concavity index, called the reference concavity, and then extracting the "normalized" steepness index (k_{sn}) from slope-area data (e.g. Wobus et al., 2006; Kirby and Whipple, 2012). A drawback of this approach is that channel gradient data can be noisy and drainage areas tend to be discontinuous due to channel junctions, and so extraction of ksn from slope-area data requires a number of data smoothing techniques (e.g., Wobus et al., 2006).

An alternative approach, is to integrate drainage area along the channel length. The rationale for this can be seen by integrating equation (IV.1), because the topographic gradient, S, is the derivative of elevation, z, with respect to downstream distance, x: i.e. $S = dz/dx$. Integration results in:

$$z(x) = z(x_b) + \left(\frac{k_s}{A_0^\theta}\right) \int_{x_b}^{x} \left(\frac{A_0}{A_x}\right)^\theta dx \tag{IV.2}$$

where A_0 is a reference drainage area, introduced to nondimensionalise the term within the integral, and x_b is the location of an arbitrary base level. Based on equation (IV.2) we can define a longitudinal coordinate, χ, which has units of length (Perron & Royden, 2013):

$$\chi = \int_{x_b}^{x} \left(\frac{A_0}{A_x}\right)^\theta dx \tag{IV.3}$$

By defining χ in this way, equation (IV.2) then reduces to:

$$z(x) = z(x_b) + \left(\frac{k_s}{A_0^\theta}\right) \chi \tag{IV.4}$$

Using equations (IV.3) and (IV.4) we can then calculate k_s (or more precisely k_{sn}) because we must select a reference concavity index to perform the integration in equation (IV.3) by regressing the local value of the gradient along the χ-elevation profile and normalizing for A_0. Parameter A_0 is selected to be 1 m^2 in order for ks to correspond to the gradient k_sn in equation IV.4. This approach, called the integral method of channel analysis (or "chi" analysis) has been widely used in recent studies (e.g. Mudd et al., 2014; Mudd et al., 2018; Perron and Royden, 2013).

The values of the steepness index, k_{sn}, can adjust to changes in lithology, climate or rock uplift. We performed χ and k_{sn} analyses using the open-source algorithm from

Mudd et al. (2014), using reference concavities (θ) of 0.45 calculated using the method of Mudd et al. (2018), in a range of catchments which cover a large part (about 80%) of the Pyrenees. Some high elevation portions of catchments present widespread geomorphic evidence of glacial erosion (Calvet, 2004) which are also associated with low $k_s n$ values (Supplementary Figure IV.4) on glacial tributaries (e.g. MacGregor et al., 2000). For each catchment we define an elevation threshold that defines the altitude above which the majority of channels record evidence of glacial modification. Elevation threshold is defined by extracting an elevation threshold where the majority of breaks exist in the χ versus elevation long profile and associated low $k_s n$ values are observed (Supplementary Figure IV.1). Any $k_s n$ measurements above this altitude are removed from the dataset (Supplementary Figure IV.2) in order to exclude channels profiles influenced by glacial erosion. However, this method can also potentially remove channel upper parts which are not influenced by glacial erosion. Complementary analyses are performed in order to test if varying reference concavities (i.e. 0.2 to 0.7) influence the relative magnitude of channel steepness (Supplementary Figure IV.3). We use SRTM data with a resolution of 30 m from the USGS EarthExplorer (http://earthexplorer.usgs.gov/) to perform the analyses (Figure IV.3). Finally in order to compare the results of the topographic analyses with the effect of different lithologies we use a high resolution global lithological map (GLiM) (Hartmann & Moosdorf, 2012) (Figure IV.3). The GLiM dataset divides the Pyrenean geology into the following lithologies: unconsolidated sediments, siliciclastic sedimentary rocks, mixed sedimentary rocks, carbonate sedimentary rocks, metamorphic rocks, acid plutonic rocks, intermediate plutonic rocks, basic plutonic rocks, acid volcanic rocks, basic volcanic rocks and water bodies (Figure IV.3C and D). In order to simplify the lithological data, we combine the three plutonic lithologies (acid, plutonic, intermediate) into the single category of 'plutonic rock'. The acid and basic volcanic rocks and water bodies are removed from the analyses as they are not sufficiently represented compared to the other lithologies.

We also analyse the drainage divide of the Pyrenees in order to compare its position relative to the distribution of lithologies. We focus this analysis on the influence of plutonic massifs on the location of the main drainage divide that separates north- from south-flowing rivers. For this we compare the proportion of the drainage divide that intersects the plutonic massifs against random lines parallel to the range. Forty hypothetical drainage divides parallel to the range front and intersecting the plutonic

massif were taken. Hypothetical drainage divides are uniformly distributed in a box that covers the Pyrenees and encompassing all plutonic massifs (Figure IV.5). We then analyse the sinuosity index and the maximum lateral fluctuation of the main drainage divide from the Pyrenees and Western European Alps compared to active mountain ranges of Taiwan and Southern Alps of New Zealand. The sinuosity index corresponds to the ratio between the curvilinear length and the distance between the two extreme points of the drainage divide track. The maximum lateral fluctuation corresponds to the maximum perpendicular distance of the drainage divide from a hypothetical straight line going through the two extreme points of the drainage divide.

IV.4.1 Rock strength

In order to characterize the physical properties of each lithology we use the uniaxial compressive strength as a proxy for rock erodibility and approximate the durability of a rock to abrasion. Measurements of uniaxial compressive strength are carried out with a Schmidt hammer. The Schmidt hammer records the rebound velocity of a plunger that strikes the rock surface. Schmidt hammer measurements gained momentum in the 1960s and have been used in geomorphological research such as environmental controls of rock weathering. The Schmidt hammer uses a proprietary unit of compressive strength ranging from 10 to 100. The higher the rebound value, the higher the elastic strength of the rock.

Estimation of the uniaxial compressive strength from Schmidt hammers is susceptible to error because of the presence of fractures beneath the rock surface, moisture or local weathering at the surface of the rock. It is difficult to account for unseen fractures beneath the rock surface, but measurements are made at a minimum distance from visible fractures. Effects of surface weathering are mitigated by cleaning the rock surface and by performing several measurements on fresh fractured surfaces with no weathering. When dealing with metamorphic rocks characterized by foliation, rock compressive strength corresponds to the average of perpendicular and parallel measurements relative to the foliation. The suggested minimum sample size for Schmidt hammer dataset is 15 to 30 measurements on a single bedrock surface. We performed at least 30 measurements of bedrock surfaces at different locations for each different lithologies. The result is a compilation between 100 and 200 measurements for each of the main lithologies. Mean and median rebound values are then converted to compressive strength using conversion

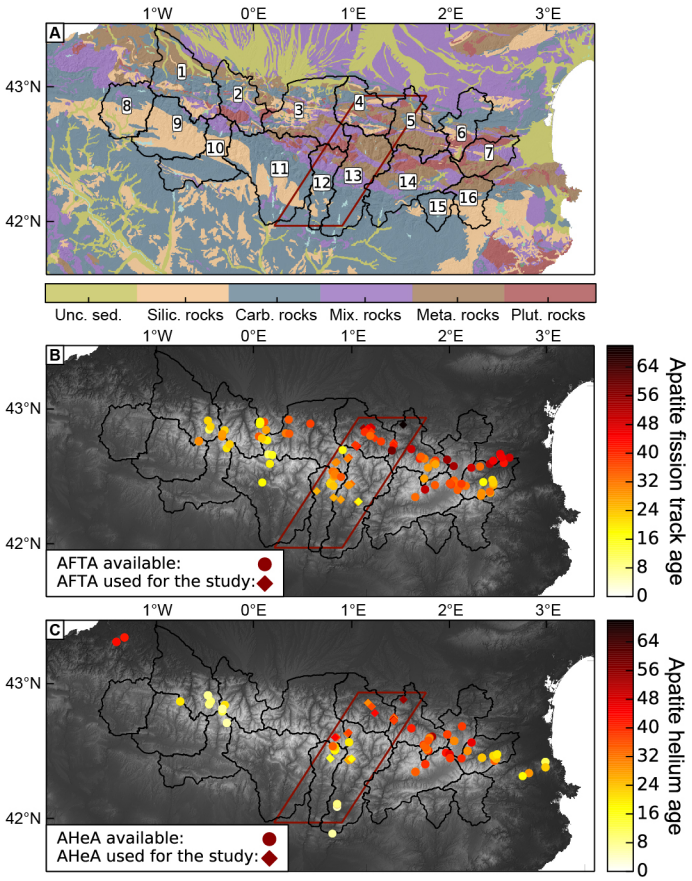

Figure IV.2: Maps of the Pyrenees from SRTM data with a resolution of 30 m. Black outlines represent main catchments and the red line corresponds to the area in the Figure IV.7. A) Lithologic map of the Pyrenean system from the geological map GLiM (Hartmann and Moosdorf, 2012) (Unc. Sed.: unconsolidated sediments; Silic. rocks: siliciclastic sedimentary rocks; Carb. rocks: carbonate sedimentary rocks; Mix. rocks: mixed sedimentary rocks; Meta. rocks: metamorphic rocks; Plut. rocks: plutonic rocks). The different catchments are labelled on the map as follows: (1) Saison, (2) Gave de Pau, (3) Garonne, (4) Salat, (5) Ariège, (6) Aude, (7) Tet, (8) Irati, (9) Aragon, (10) Gallego, (11) Cinca, (12) Noguera Ribagorzana, (13) Noguera Pallaresa, (14) Segre, (15) Llobegrat and (16) Ter. Garonne (3) and Noguera Pallaresa (13) catchments are used as examples in Figure IV.3. B) Compilation of apatite fission track ages represented by circles of white-yellow to red-black colors depending on age. C) Compilation of apatite helium ages represented by circle shape of white-yellow to red-black colors depending of the age. Thermochronological ages used in this study are represented by diamonds (Supplementary Tables IV.1 and IV.2).

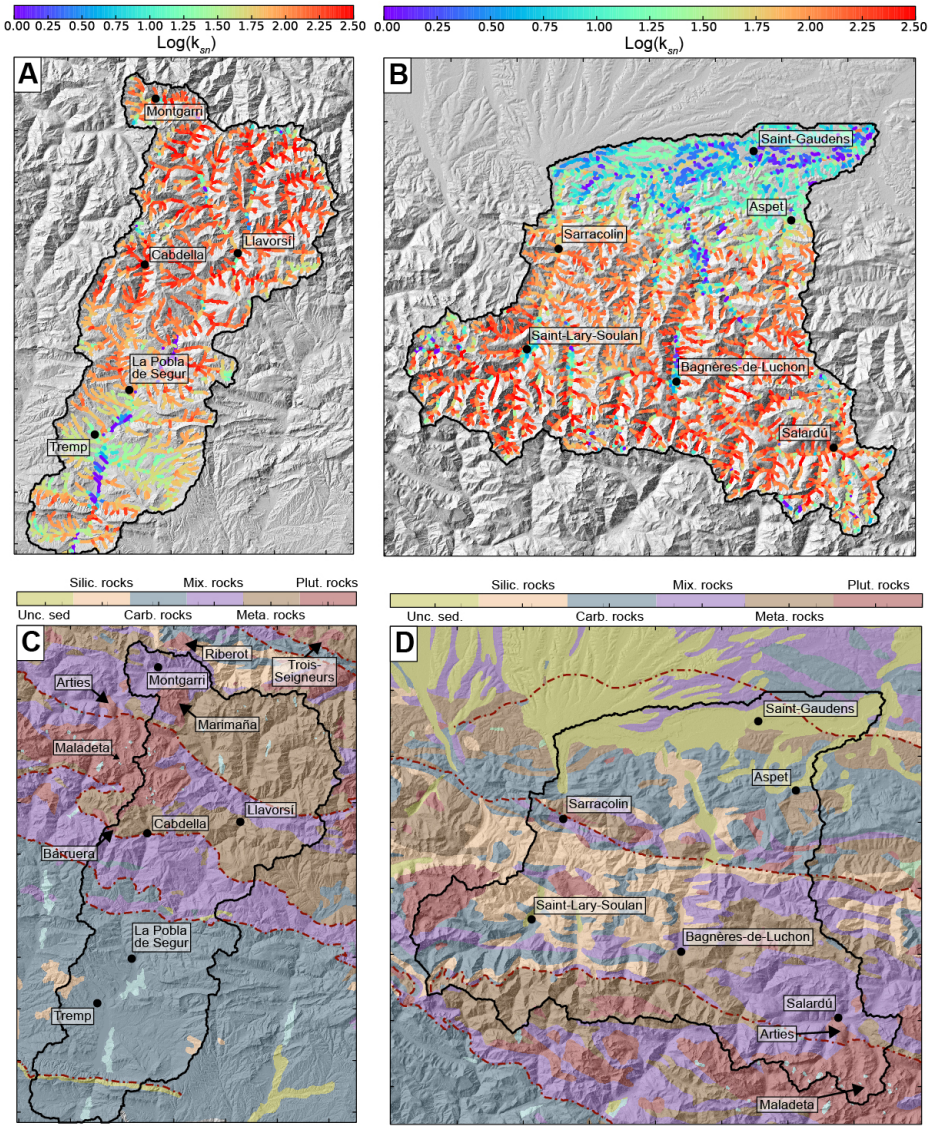

Figure IV.3: Relation between topography, lithology and k_sn in two catchment examples. Top panels are maps of k_sn for A) the Noguera Pallaresa catchment (south side prowedge) and B) the Garonne catchment (north side retrowedge). The Log(k_sn) parameter is represented by a succession of points along the river channel of the catchment with bright colors from purple (low values) to red (high value). The legend for the k_sn parameter is plotted above the panels. Lower panels (C and D) correspond to the same areas but with the lithology represented in colors. The legend of lithology corresponds with lithology colors in Figure IV.1A. Cities are represented by black dots and massifs by black arrows. Red dash lines correspond to the main faults.

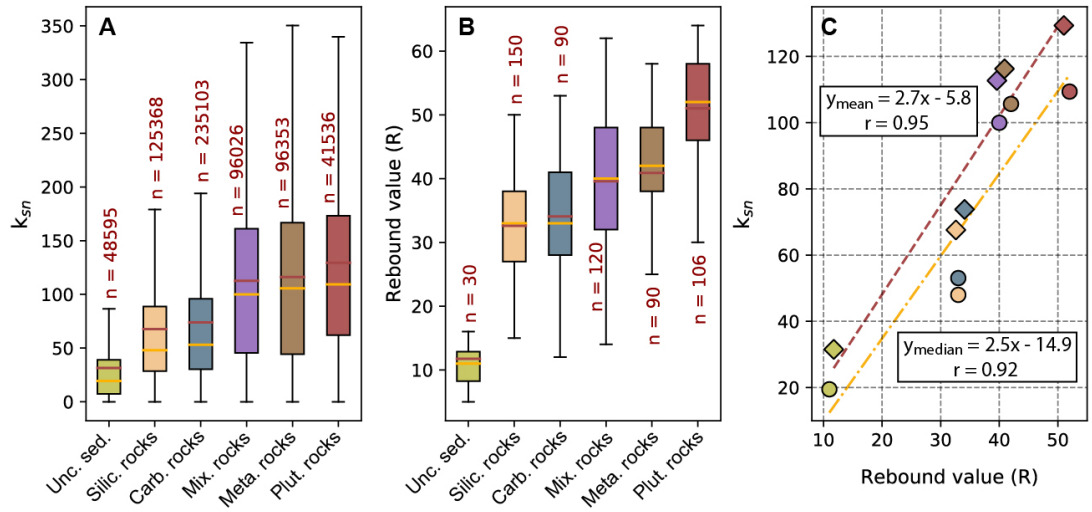

Figure IV.4: Channel steepness, rock strength and lithology correlations. Whisker and boxplot representation of A) k_sn and B) rebound value (R) plotted as a function of lithology. The number of values analysed associated to each lithology is displayed in red above or under the boxplot. Colors of boxplots and lithology abbreviations are in accord with Figure IV.3. Each box-and-whisker, in this figure, represents the minimal, 25th percentiles, 75th percentiles and maximal values in horizontal black lines while red and yellow horizontal lines represent respectively the mean and median values. C) Correlation between mean values (diamonds and red normal dashed line) and median values (rounds and yellow point dashed lines) of the channel steepness and rock strength. r is the correlation coefficient.

curves (determined from laboratory test) from manual of the Schmidt hammer model N used in the field.

IV.4.2 Thermochronological approach

We performed new analyses of published thermochronological datasets from elevation profiles across a north-south transect in the Central Pyrenees (Fitzgerald et al., 1999; Sinclair et al., 2005; Gibson et al., 2007; Vacherat et al., 2016) (Supplementary Table 1 and 2 and Figure IV.8B and C). All available datasets are included in the analyses. Where there are multiple elevation profiles for the same massif, we chose the one with the largest number of samples and thermochronometric systems used. The aim was to resolve the timing of the last phase of deceleration in exhumation across the range. Elevation profiles are mainly located on Variscan crystalline basement massifs (exact location in Figure IV.7 presented in the result section). The Nogueres profile is the southern-most profile and is situated on the Nogueres Zone (Sinclair et al., 2005, Gibson et al., 2007) which comprises Carboniferous volcanic rocks and has both apatite fission tracks (AFT) and zircon fission tracks (ZFT) data. Maladeta, Marimaña, Arties and Riberot profiles from south to north are located in the Axial Zone and correspond to high-relief Variscan granitoid massifs. The Maladeta and Marimaña massifs have apatite helium (AHe), AFT and ZFT data (Sinclair et al., 2005; Gibson et al., 2007) while Arties has AHe and AFT data (Gibson et al., 2007) and the Riberot profile only AFT data (Fitzgerald et al., 1999). The most northerly elevation profiles are the Trois-Seigneurs and Lacourt profiles corresponding also to granodioritic massifs and have AHe, AFT and ZFT data (Fitzgerald et al., 1999; Vacherat et al., 2016). The age ranges for AFT, AHe and ZFT, the mean track length for AFT system and the number of samples for each profiles are presented in Supplementary Tables IV1 and IV2.

In order to reconstruct accurate time-temperature histories we modelled the dataset using QTQt software (Gallagher, 2012), which inverts low-temperature thermochronological data. It uses the Bayesian Markov chain Monte Carlo methodology (Gallagher, 2012) and is specifically designed to model several samples from the same elevation profile. We use all samples in the profiles for modelling in order to take full advantage of the multi-sample inversion approach. This allows us to reduce the potential for both over interpretation and the introduction of artefacts in the inferred thermal histories (Gallagher, 2012). We use the latest kinetic model incorporated in the software with

the multicompositional algorithms of Ketcham et al., (2007) for AFT and those of Yamada et al., (2007) for ZFT. For AHe we use the annealing and apatite radiation damage model of Gautheron et al., (2009). To obtain robust thermal histories, at least 200,000 iterations are performed followed by a comparison between the observed data and the model predicted data (Supplementary Figure IV.4). The closure temperature of ZFT, AFT and AHe thermochronometers are unable to record post-orogenic events that occurred at temperatures below 40 °C. However, inverse modelling of this association of thermochronometer systems has the potential to record cooling deceleration for each thermal histories. The sensitivity of inverse modelling to accurately record deceleration is a function of model parameters (Gallagher, 2012; Gallagher, pers. comm.). The most influential parameters are: 1) the number and spatial coverage of samples along the vertical profiles; 2) the minimal elevation of the lower sample of the vertical profile; 3) the difference of cooling ages between the AFT and AHe system and its evolution along the vertical profile; 4) the distribution of apatite fission track lengths in samples along the vertical profile.

IV.5 Results

IV.5.1 Topographic and lithological analyses

Analyses of the ksn parameter are first performed for each major catchment of the Pyrenean system (Supplementary Figure IV.5 and IV.6). In order to compare analyses of the different catchments we use a constant concavity index of 0.45, as this was the median concavity derived using the method of Mudd et al., (2018). Examples of the output are presented in Figure IV.3 from the Noguera Pallaresa catchment (Figure IV.3A and C) located in the central southern Pyrenees, and the Garonne catchment (Figure IV.3B and D) located in the central northern Pyrenees. Channel steepness is plotted as a succession of points every 30 m along river channels (Figure IV.3A and B).

In order to quantify the impact of lithology on the landscape at the scale of an entire orogen we combine the results from the channel steepness analyses (Figure IV.3A and B and Supplementary Figure IV.7) from all of the non-glaciated catchments across the range (Figure IV.3). Figure IV.4A highlights this result by showing a box and whisker plot of ksn values associated with each of the main lithologies for the entire Pyrenees. The highest ksn values are for the Variscan plutonic rocks with a mean and a

median of 129 and 109 respectively. The metamorphic and mixed sedimentary rocks show notably lower mean and median ksn compared to Variscan plutonic rocks with values of 116 and 105, and 113 and 100 respectively. The second important decrease of ksn magnitude is observed with the carbonate and siliciclastic sedimentary rocks. Mean and median ksn values are 74 and 53 respectively for the carbonate and 68 and 48 respectively for the siliciclastic rocks. The final break in ksn magnitude corresponds to the unconsolidated sediment with a mean and median of 32 and 19 respectively.

IV.5.2 Rock strength measurement

Results for the rebound value, R, show a variable pattern for the different lithologies (Figure IV.4B). We convert the rebound value R to the rock compressive strength (MPa). Plutonic rocks record the maximum compressive strength with a mean value of 52 MPa. The rebound dataset of the plutonic rocks is also characterized by a quite narrow standard deviation of 8, which is due to the relative homogeneity of the plutonic rocks. Metamorphic and mixed sedimentary rocks are characterized by lower compressive strength values with a mean of 36 and 34 MPa respectively. Standard deviations of these two lithologies are also higher with a value of 11 MPa. These standard deviations highlight the heterogeneity in compressive strength of these two lithology group in which foliation and bedding play an important role. Carbonate and siliciclastic sedimentary rocks record a net rock strength reduction compared to the metamorphic and mixed sedimentary rocks. Mean rock compressive strengths are 26 and 24 MPa respectively for the carbonate sedimentary rocks and siliciclastic sedimentary rocks. Finally, the unconsolidated sedimentary rocks are characterized by a relatively low rock strength of 11 MPa.

IV.5.3 Drainage divide analyses

The proportion of the main drainage divides located within plutonic massifs through the Pyrenees is presented in Figure IV.5. The mean percentage intersection for the forty hypothetical linear drainage divides is 15%. The percentage intersection for the actual modern drainage divide is 32%. The analyses combined with a first order visual observation support a correlation between the position of the main drainage divide and the position of the plutonic massifs. Figure IV.6 shows results of the sinuosity index and maximum lateral fluctuation for the Pyrenees, Western Alps, Taiwan and New Zealand;

Taiwan and New Zealand are considered as example of actively accreting mountain ranges, and the Western Alps as an example of a range that has had approximately 5 Myr of isostatic rebound and post-orogenic decay (based on the definition outlined in the Introduction). The sinuosity index for these ranges is 1.47, 1.72, 1.29 and 1.12. Maximum and mean lateral fluctuation are respectively 30.1 and 14.2±5.3 km for the Pyrenees, 43.9 and 23.62±9.14 km for the Western Alps, 18.4 and 7.36±3.52 km for Taiwan and 18.0 and 8.13±3.64 for New-Zealand. These result show that the Pyrenees and Western Alps are characterised by a drainage divide with a high degree of sinuosity compare to Taiwan and New Zealand (Figure IV.6). Maximum lateral variations in the drainage divide differ also between the different ranges. Maximum lateral variation of the Pyrenees and Western Alps are almost twice as extensive as those observed for New Zealand or Taiwan (Figure IV.6).

IV.5.4 Thermal histories of the Central Pyrenees

Thermal histories are presented in Figures IV.7B-I for eight localities with elevation profiles in the Central Pyrenees (Figure IV.7A). For each thermal history built using QTQt we compared the predicted data, generated by multiple modelled thermal histories, to the observed data (Supplementary Figure IV.4). From these data we map the best-fit cooling rate along a north-south transect (Figure IV.8).

Figures IV.7 and IV.8 compare the time-temperature paths of each of the localities. The start of accelerated cooling is different for each elevation profile and youngs from north to south as has been reported previously (Fitzgerald et al., 1999; Sinclair et al., 2005). The time when cooling rates decreased varies from the different profiles with a systematic younging from north to south (supplementary Table 3). Deceleration of cooling is less evident for the Barruera profile but thermal histories appear to reach a constant cooling rate at about 7 Ma (Figure IV.8C). The general pattern of cooling along the Central Pyrenees is characterized by a diachronous onset and termination of rapid cooling.

The time of the decrease in the cooling rate, i.e. the time from the start of the decrease, to the end of the change in cooling rate defined from the inflexion point on the curve (Figure IV.8C), is variable between profiles (Supplementary Table 3). It corresponds to the time when the cooling rate goes from high values (yellow-red colours in Figure IV.8) to stable values (blue colours in Figure IV.8). By dividing the change of

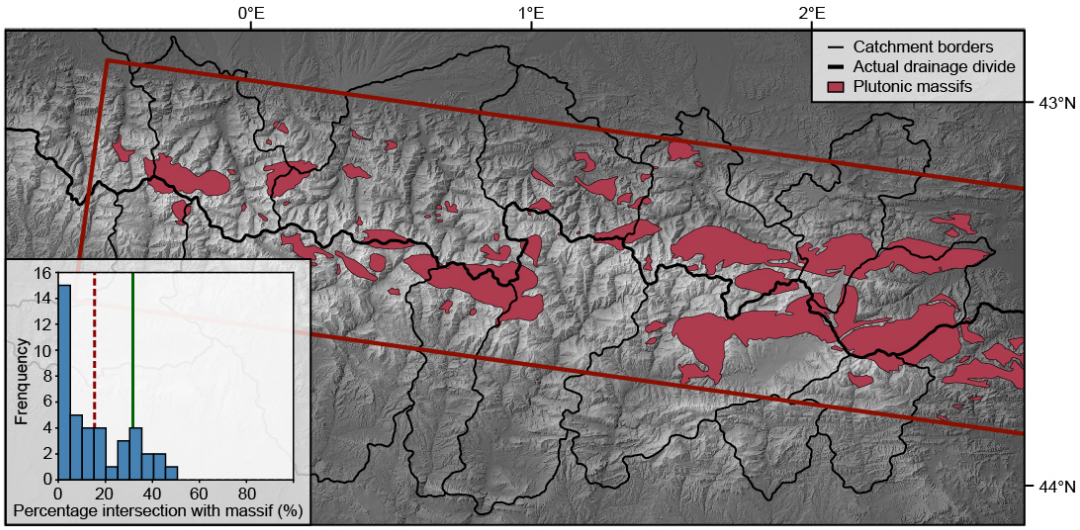

Figure IV.5: Topographic map of the Pyrenees from SRTM with a resolution of 30 m. The different Variscan plutonic massifs are plotted in red. The main and secondary drainage divide (associated to the delimitation of catchments) are represented respectively with a thick black line and with thin black lines (Based on Lynn, 2005). Frequency of the percentage intersection for random drainage with plutonic massifs is plotted in the lower left side. Forty hypothetical drainage divided parallel to the range have been analysed. For each linear drainage divide, the proportion of the line that intersected the plutonic massifs was calculated as a percentage. The mean percentage intersection with plutonic massifs from the forty hypothetical drainage divides is compared to the percentage intersection of the main drainage divide. The dashed vertical red line on the graph corresponds to the mean percentage of intersection of the random linear lines. The vertical green line corresponds to the percentage intersection of the modern drainage divide. The red box shows the area of the forty hypothetical drainage divides.

cooling rate during deceleration with the corresponding duration of deceleration, the rate of change of cooling (Supplementary Table 3) is revealed. The profiles located at the northern and southern edges of the mountain range (Lacourt, Barruera and Nogueres) record a slow deceleration in cooling rate. In contrast, profiles situated in the core of the mountain range such as Maladeta, Arties, Marimaña and Riberot record relatively rapid decelerations.

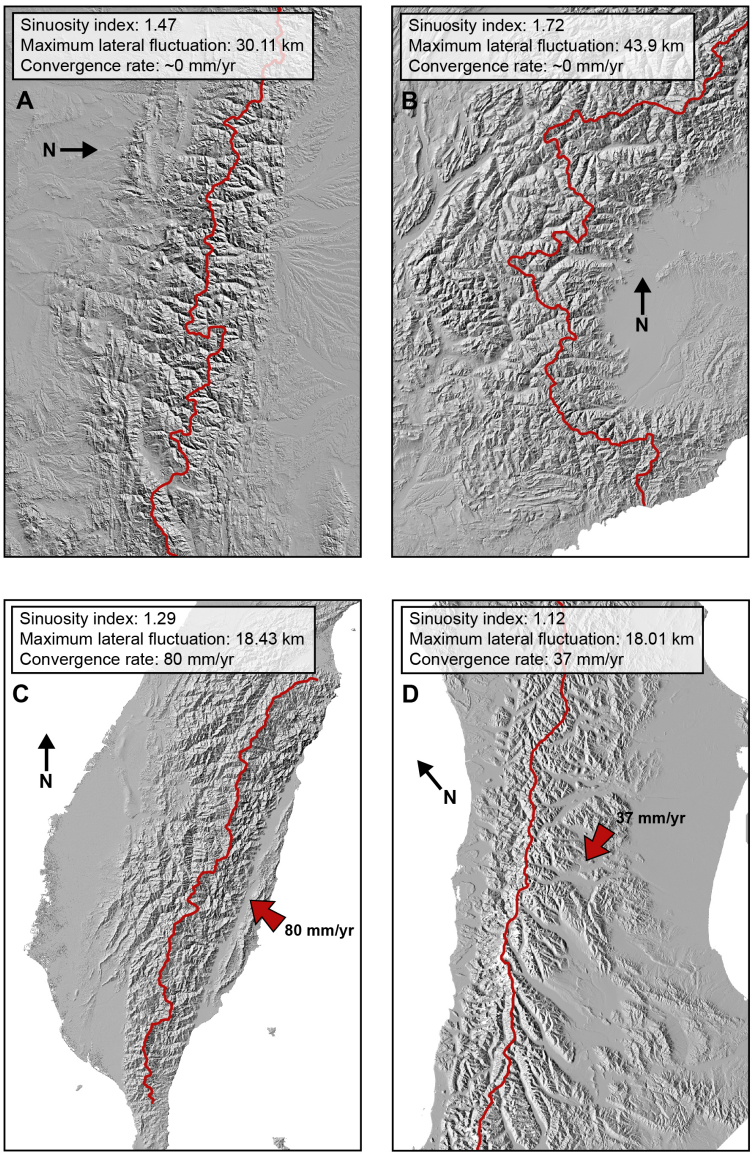

Figure IV.6: Comparison of the main actual drainage divide for mountain ranges shown at the same scale: A) Pyrenees, B) Western European Alps, C) Taiwan and D) Southern Alps of New Zealand, which all have similar dimensions. Red lines represent the main actual drainage divides and red arrows represent the rate and direction of convergence for the active systems of Southern Alps of the New Zealand and Taiwan.

IV.6 Discussion

IV.6.1 Lithological effect on river profiles

The topographic analyses for the entire Pyrenean orogen reveals a correlation between the channel steepness index ($k_s n$) and rock compressive strength associated with each lithology (Figure IV.4). Plutonic rocks are characterised by higher channel steepness and high rock compressive strength (Figure IV.4A and B). The metamorphic and mixed sedimentary rocks are associated with lower channel steepness and rock compressive strength compared to plutonic rocks. Finally, the two parameters are lower again for carbonate and siliciclastic sedimentary rocks. Figure IV.4C shows the direct correlation of the mean (correlation coefficient of 0.95) and median (correlation coefficient of 0.93) values between channel steepness and rock strength associated to each lithology. For both cases, there is a linear relationship between these two parameters indicating correlation between lithology, channel steepness and rock compressive strength. Elevation and lithology distribution seem also to be closely correlated. Swath profiles (Figure IV.9A, B and C) of the western, center and eastern Pyrenees (Figure IV.1) combined with a regional correlation between elevation and lithology (Figure IV.9D) indicate that plutonic and metamorphic rocks (high rock strength) consistently occupy the regions of higher elevation relative to the other lithologies.

Plucking during river erosion of mountain ranges is modulated mainly by the occurrence of joints, fractures and bedding (Whipple et al., 2000). Plutonic rocks tend to have the lowest density of fractures or joints compared to other rock types and are thus potentially more resistant to plucking (Whipple et al., 2000). Variation in rock strengths and especially high rock strength for the plutonic range are consistent with fracture and joint expectations.

The principal modern agent of erosion in the Pyrenees is fluvial erosion, although there is extensive evidence of glacial impact on channel profiles within the Pyrenees (Calvet, 2004). Glacial erosion tends to increase hillslope steepness by forming ridges and arêtes in the high-elevation part of the mountain and have the potential to lower channel gradients and their concavities (Brocklehurst & Whipple, 2002; MacGregor et al., 2000). Therefore, we would expect glacial erosion to have reduced channel gradients in the centre of the Pyrenean orogeny, which is where the harder plutonic and metamorphic rocks are mostly located (Figure IV.5A). Glaciation could then potentially impact the

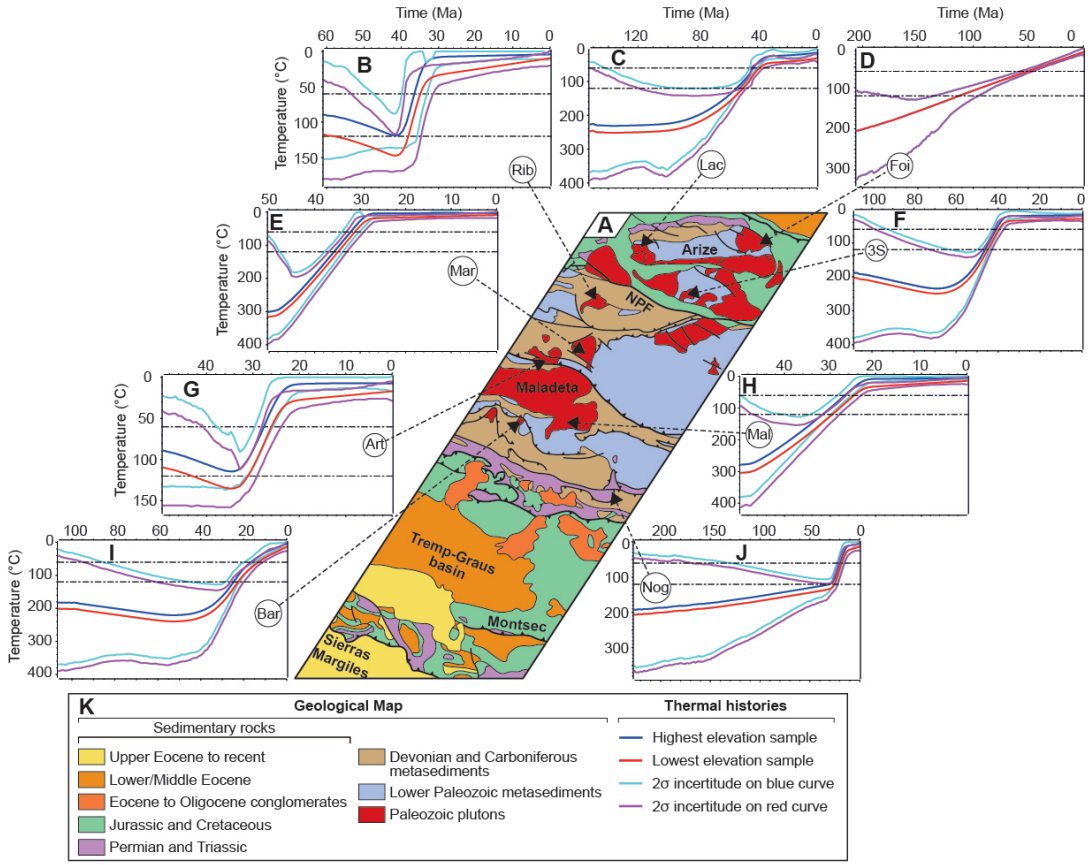

Figure IV.7: Complete set of thermal histories from the Central Pyrenees constructed from low-temperature thermochronology using QTQt. A) Detailed geological map of the Central Pyrenees around 1° with location of different profiles used in this study. B-J) Set of thermal histories from the Central Pyrenees (sources of data are provided in supplementary tables 1 and 2). Thermal histories are built with the annealing models of Yamada et al., (2007) for ZFT data, Ketcham et al., (2007) for the AFT data and Gautheron et al., (2009) for AHe data. Red and blue curves are thermal histories for hottest (lowest elevation) and coldest (highest elevation) samples respectively. Magenta and cyan curves are 95% credible intervals for the red and blue curves, respectively. The difference between the thermal histories for the highest and lowest elevation samples is defined as the temperature-offset parameter, and is estimated assuming a range in temperature gradient of 15 to 45 °C/km. The thermal histories of the intermediate elevation samples are calculated by linear interpolation between the highest and lowest elevation thermal histories. K) Legend of geologic map and thermal histories.

correlation between rock strength of different lithologies and channel steepness (Figure IV.4, Supplementary Figure IV.1 and IV.2). The mean altitude of the transition from fluvial to glacially-dominated long profiles varies between catchments. The transition for the Noguera Pallaresa (Supplementary Figure IV.1) ranges between 1900 and 2100 m. Transitions from different catchments seem to indicate a generally higher elevation for the southern basins compared to northern basins and can results from the more arid southern Pyrenees relatively to the northern side. The exclusion of k_sn values at elevations above the transition has an impact on the correlation between lithology and channel steepness with a general increase of the mean k_sn values for plutonic lithologies (Supplementary Figure IV.2A and B). Orographic enhancement of precipitation with greater precipitation in the northern Pyrenees than the south may result in increased discharge per unit area of catchment, and hence may lead to a decrease in k_sn from south to north, and may influence the degree of glacial impact. However, there is no evidence to suggest a significant difference in k_sn values between the northern and southern portions of the Pyrenees (Supplementary Figure IV.5, IV.6 and IV.7).

Other external forces such as spatially varying uplift rates induced by tectonic activity can impact channel steepness, however, given the ca. 20 Myrs since significant fault induced changes in exhumation rates, it is not considered a significant factor in the current case. Only the thermal history from the Barruera profile shows limited cooling that is associated to the late activity of the antiformal stack (Sinclair et al., 2005). Surface uplift of the eastern Pyrenees since middle Miocene times has been proposed related to opening of the Gulf of Lyon further East (Calvet & Gunnell, 2008) and could have caused recent differential uplift in the eastern side of the range. However, we don't observe any notable difference in the range of k_sn values for the eastern catchments compare to others (Supplementary Figure IV.5 and IV.6).

IV.6.2 Effect of lithology on the drainage divide

In a doubly-vergent mountain range such as the Pyrenees or Southern Alps of New Zealand, the main drainage divide provides a robust first order dividing line between the pro- and retro-sides of the mountain system. General evolutionary models coupling tectonics and surface processes indicate the development of a generally straight drainage divide roughly parallel with the mountain front and tracking the thickest part of a doubly-vergent wedge located above the S-point (Koons, 1989). The exact location of

the drainage divide during orogenesis fluctuates according to the relative proportions of frontal accretion and underplating (Willett et al., 2001) and is generally pushed toward the retro-side of the orogen. Tectonics play an important role in determining the position of the drainage divide but studies show that the climate can also alter this position, either by enhancing or acting against the tectonic signal (Koons, 1989; Willett, 1999).

The Pyrenees comprise an Axial Zone characterised by several Variscan granitoid massifs. (Figure IV.1 and IV.5) surrounded by sedimentary and low-grade metamorphic rocks. From a first visual observation, the drainage divide appears to approximately track the location of the plutonic massifs (Figure IV.5). Furthermore, the mean percentage of intersections with plutonic rocks from random linear lines (15%) is significantly lower than the one from the actual drainage divide (32%). The results suggest that plutonic massifs influence the current position of the Pyrenean drainage divide. The Pyrenees and Western European Alps present more irregular drainage divides relative to the Southern Alps of New Zealand and Taiwan which are similar in size to the Pyrenees, but are actively shortening (Figure IV.6). These active systems are characterized by relatively linear drainage divides with minor lateral fluctuation that split the pro- from the retro-wedges of the range indicating that they are primarily controlled by the advection of rock within the active doubly-vergent thrust wedges (Willett et al., 2001; Figure IV.6). The implication being that the switch from syn- to post-orogenic topography is characterised by a modification of the drainage divide, which becomes more strongly determined by rock strength as tectonic advection of rock ceases.

IV.6.3 Thermochronologic data and variation of rock type exposed through time

Changes in rates of rock exhumation in active mountain ranges are often interpreted in terms of the punctuated forcing of by thrust activity (e.g. Naylor and Sinclair, 2007) or changes in the erosive capacity of the climate (e.g. Thiede et al., 2004). The timing of deceleration in cooling rates (Figure IV.8) demonstrates that the transition from rapid to slow exhumation rates is diachronous from north to south across the Pyrenean mountain belt. The diachroneity in the decrease in exhumation rate can be explained by the diachronous termination of structural activity in the Axial Zone as predicted in modelling of active thrust wedges (Gibson et al., 2007; Naylor & Sinclair, 2007).

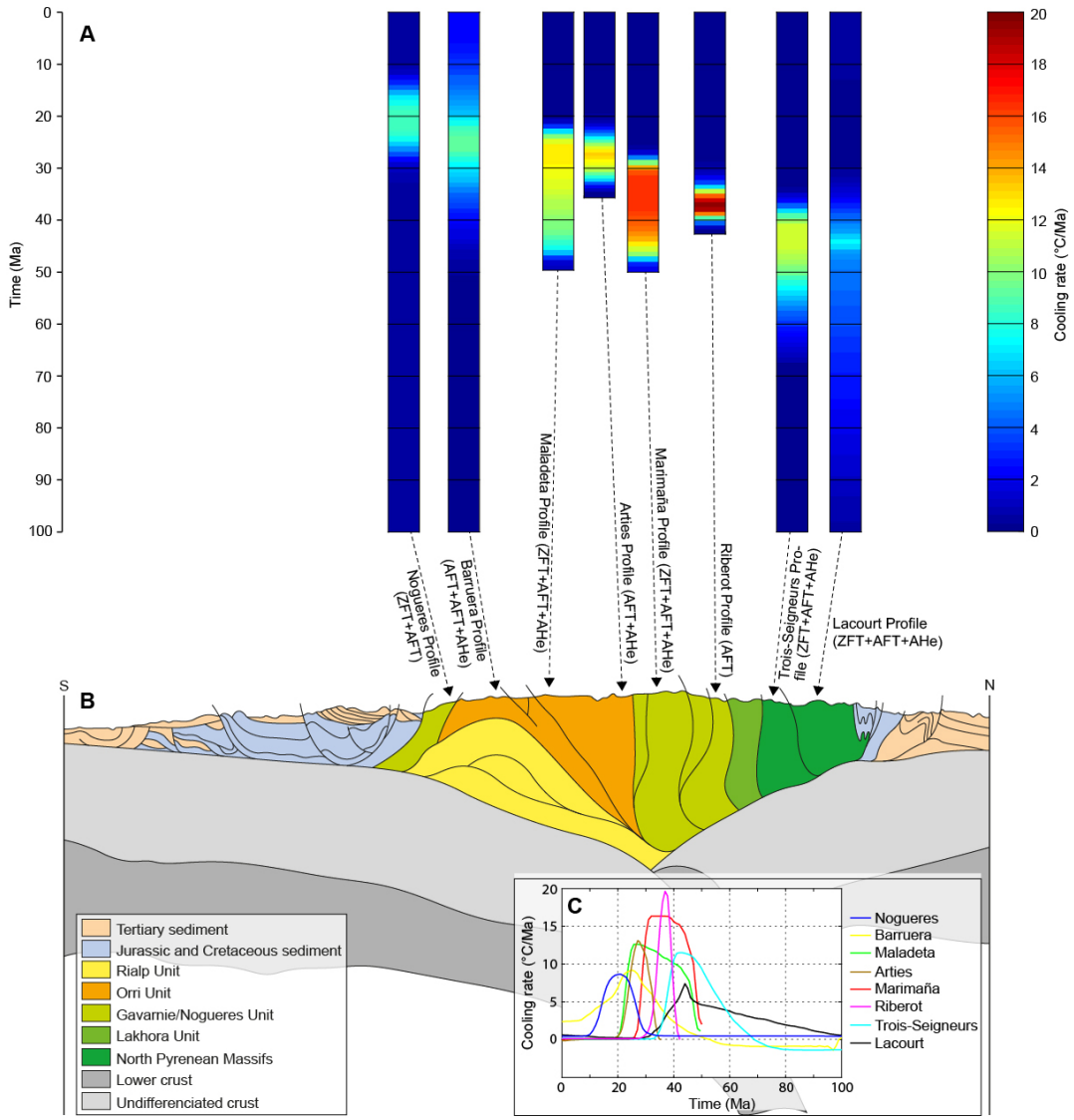

Figure IV.8: Cooling rate as a function of time along a north south transect in the Central Pyrenees. A) Colour representation of cooling rate build from the thermal histories as a function of time and according to the locality of each profile along the north south transect of the Central Pyrenees. Cooling rates are built from the QTQt thermal histories output. At each step-time (t_i ,about every 1 Myrs), cooling rate is defined as the difference of temperature ($T_{i-1} - T_{i+1}$) divided by the difference of time ($t_{i-1} - t_{i+1}$) Geological north south cross-section (Beaumont et al., 2000 and Sinclair et al., 2005) along the ECORS profile in the Central Pyrenees. C) Cooling rate curves as a function of time for each profile.

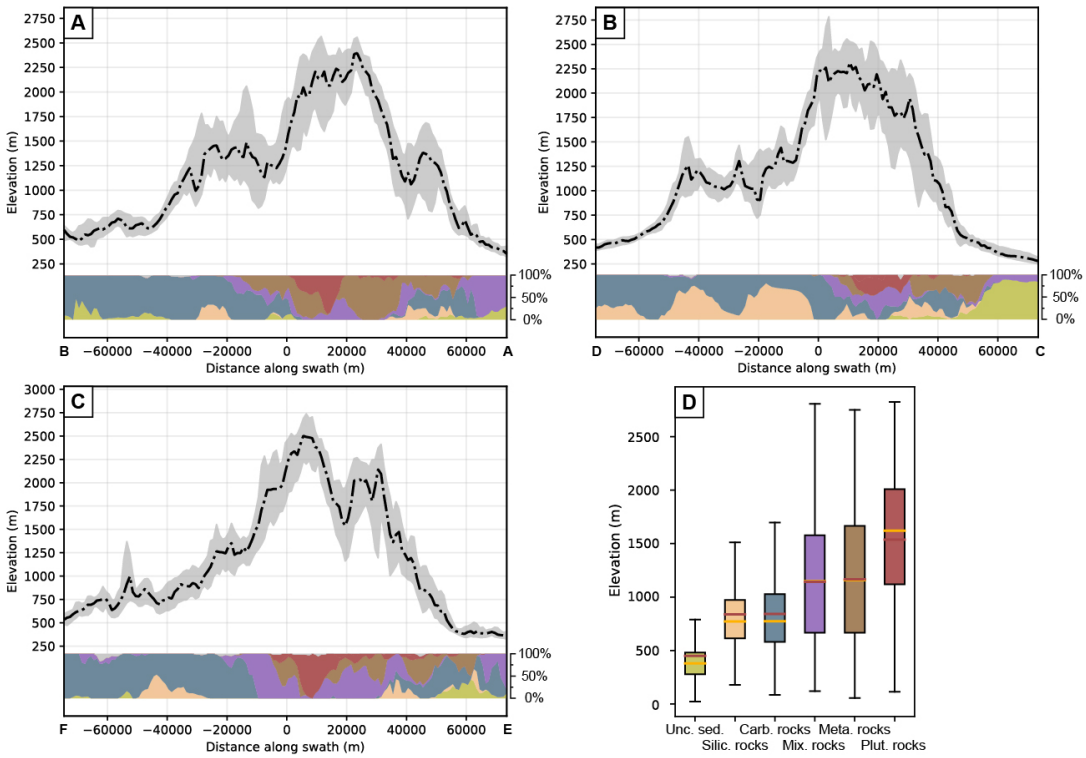

Figure IV.9: Topographic relation between elevation and lithology of the Pyrenees. A, B and C are transversal swath profiles of the Pyrenees (A) west; B) center; C) east). Dashed black line corresponds to the median elevation while the grey area corresponds to the elevation amplitude between the upper quartile elevation and lower quartile elevation. Color band below curve corresponds to the proportion of each lithology. Colors are the same as in panel D where the legend for lithology is indicated. D) Correlation between elevation and main lithology for the entire Pyrenees. Each box-and-whisker represent the minimal, 25th percentiles, 75th percentiles and maximal values in horizontal black lines while red and yellow horizontal lines represent respectively the mean and median values

Modelling results of Flowers and Ehlers (2018) suggest that even relatively low contrasts in the erodibility of bedrock (by factors of between two and ten) can influence thermal histories if the rock layers are relatively thick ($\geq$ 2 km) and the cumulative erosion magnitude is relatively high (at least 4 km for AHe data and 6-8 km for AFT data). These results suggest that in the geological scenario of a sedimentary cover overlying crystalline basement rock (i.e. Mesozoic and Palaeozoic cover of the Variscan Massifs in the Pyrenees), the reduction in exhumation rates due to lithology changes at the surface should be recorded in the thermochronometric ages; this is also suggested for the Tien Shan (Sobel et al., 2006) and the Western European Alps (Glotzbach et al., 2011). In the Pyrenees, with the exception of the Nogueres profile, thermal histories have been modelled from the Variscan crystalline basement massifs. These massifs were overlain by a succession of Upper Paleozoic and Mesozoic sedimentary strata according to structural reconstructions (e.g. Muñoz, 1992; Beaumont et al., 2000). The measured rock strengths in the granitoid massifs are 1.5 to 2 times higher than the surrounding and originally overlying successions. If fracture density and structural heterogeneities are also considered in evaluating bulk rock strength then the contrast between the erodibility of the granitoid basement and the Upper Paleozoic and Mesozoic sedimentary successions would likely be even greater. Therefore, it would be expected that there be some record of reduced exhumation rates in response to erosion through the sedimentary successions into the Variscan granitoid basement. Results from the thermal histories modelling (Figure IV.7) are consistent with this hypothesis. Indeed, thermal histories from Maladeta, Arties, Marimaña and Riberot characterised by large Variscan plutons and surrounded by Silurian to Cambrian meta-sedimentary rocks show a strong deceleration of the cooling (Figure IV.7A and B). In contrast, thermal histories from Nogueres, Barruera, Trois-Seigneurs or Lacourt record a gentler deceleration. However, the abrupt deceleration of some of the southern massifs may also be attributed to valley backfilling during the endorheic stage in the southern Ebro basin (Convey et al., 1996).

Evidence for the emergence of basement rocks during orogenesis may be recorded in the sedimentological record. Syn-tectonic sediment is well preserved in the South Pyrenean Thrust Belt where Mesozoic carbonates are overlain by syn-tectonic Paleogene siliciclastic sandstones and conglomerates (Meigs et al., 1996; Verges & Munoz, 1990). The Sis palaeovalley records long-term conglomerate accumulation and demonstrates that granitoid clasts were first present in small quantities (¡12%) in early Ypresian times

(ca. 54.5 Ma) until at least Rupelian/early Chattian times (ca. 27.8 Ma; Vincent, 2001). Granitic clasts make up about 4% of the mid-late Eocene Escanilla system of the central southern Pyrenees (Michael et al., 2014). The late Eocene and Oligocene conglomerates around Pobla de Segur are dominated by red Permian and Triassic sandstones and Palaeozoic metasedimentary rocks, with few clasts of granitoid lithologies (Mellere, 2009). The early Eocene to late Oligocene Carcassone Group of the proximal Aquitaine Basin comprises a series of conglomerates with occasional granitoid clasts. The presence of granitoid clasts in the syn-tectonic sedimentary successions of the Pyrenees demonstrates that the Variscan Massifs were being exposed throughout the evolution of the range from mid-Eocene onward. We conclude that the contrast in rock strength between the sedimentary cover and crystalline basement in the Pyrenees must be viewed as a probable control on the history of erosion and exhumation of the range.

IV.7 Conclusion

The post-orogenic topography of the Pyrenees is influenced by varying rock strength of the main lithological units, and we suggest this also impacted the syn-orogenic exhumation of the range. We quantify rock strength using elastic rebound measurements recorded using a Schmidt hammer, and demonstrate that the granitoid lithologies of the Variscan massifs have the greatest strength, with Palaeozoic metasediments, Mesozoic and Tertiary cover rocks recording progressively weaker lithologies. The strength of rock is also revealed by measurements of the steepness of river channels normalised to the upstream area; high, normalised channel steepness indices broadly correlate with areas of high rock strength across the range. The highest rock strengths also correlate to the highest elevation topography, with the main drainage divide preferentially tracking the Variscan granitoid massifs of the Axial Zone forming the spine of the range. By comparing the geometry of the drainage divide of the post-orogenic Pyrenees to similar-sized, tectonically active ranges, we suggest that, in the recent evolution of the Pyrenees, lithology plays a more dominant role than tectonics. Thermal modelling of thermochronological datasets from the Central Pyrenees reveal a southward migration and abrupt decelerations in cooling/erosion histories in granitic massifs; we suggest that exhumation of crystalline basement following removal of overlying sedimentary cover is also likely to have influenced the syn-tectonic erosional history of the syn-tectonic

history of the range.

IV.8 Supplementary Material

This supplementary material contains three tables about low-temperature thermochronological dataset used in this study and thermal history results. We present also height figures providing additional topographic analyses and inverse modelling information associated to this manuscript.

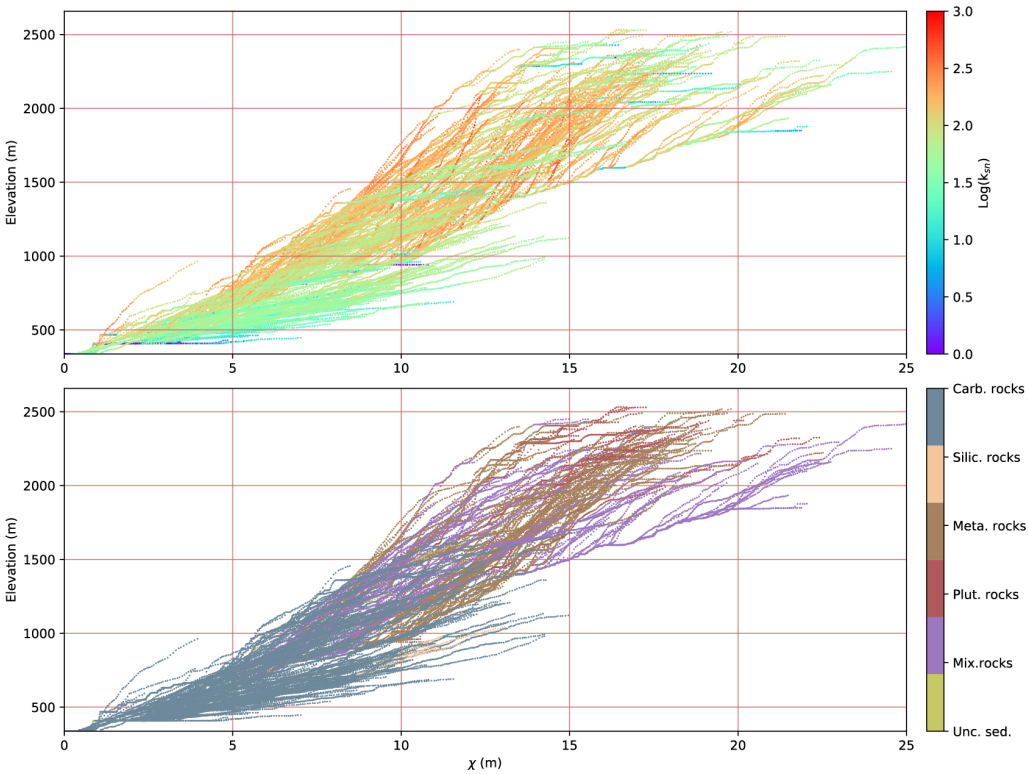

Supplementary Figure IV.1: Long profile χ-elevation plots for the Noguera Pallaresa catchment. Colors correspond to the log of $k_s n$ for the upper panel and to lithology for the lower panel. Plots highlight channels influenced by glacial erosion at high altitudes and characterized by a break in long profile and low $k_s n$ values. Low $k_s n$ values (blue colors) in lower panel suggest glacial influence becomes more pronounced above 1900 meters elevation. Metamorphic and plutonic rocks are the lithologies principally affected by glacial effect.

Sample	Location	Longitude	Latitude	Elevation	ZFTA	AFTA	AFTMTL	Reference
Mon-02/805	Nogueres	1,105	42,391	805	159±33	27.6±3.7	13.8±0.22	Sinclair et al., 2005
Mon-02/960	Nogueres	1,101	42,389	960	NaN	17.2±3.4	14.76±1.23	Sinclair et al., 2005
Mon-02/1085	Nogueres	1,097	42,388	1080	NaN	24.4±3.9	13.99±0.21	Sinclair et al., 2005
Mon-02/1280	Nogueres	1,092	42,386	1280	NaN	26.2±3.1	13.75±0.25	Sinclair et al., 2005
Bar-02/1150	Barruera	0,813	42,515	1150	104±7	21.4±2.0	13.18±0.15	Sinclair et al., 2005
Bar-02/1695	Barruera	0,808	42,52	1695	NaN	19.5±3.2	14.17±0.23	Sinclair et al., 2005
Bar-02/1780	Barruera	0,807	42,521	1780	Nan	21.2±3.7	13.95±0.29	Sinclair et al., 2005
Mal-00/1750	Maladeta	0,99	42,507	1750	49.3±2.6	28.9±3.1	13.73±0.18	Sinclair et al., 2005
Mal-00/2030	Maladeta	0,993	42,513	2030	NaN	27.7±2.5	13.88±0.10	Sinclair et al., 2005
Mal-00/2250	Maladeta	1,008	42,51	2250	NaN	28.5±3.0	14.02±0.14	Sinclair et al., 2005
Mal-00/2870	Maladeta	1,024	42,518	2870	NaN	33.1±3.4	14.27±0.15	Sinclair et al., 2005
ART/03/1315	Arties	0,872	42,677	1315	NaN	30.2±4.1	14.21±0.15	Gibson et al., 2007
ART/03/1555	Arties	0,867	42,675	1555	NaN	29.4±1.6	14.81±0.10	Gibson et al., 2007
ART/03/1880	Arties	0,862	42,675	1880	NaN	31.5±2.7	14.58±0.16	Gibson et al., 2007
ART/03/2164	Arties	8551	42,6728	2164	NaN	29.8±2.1	14.64±0.15	Gibson et al., 2007
Mar-00/2030	Marimana	0,976	42,705	2030	NaN	31.7±2.8	14.32±0.07	Sinclair et al., 2005
Mar-00/2200	Marimana	0,981	42,705	2200	NaN	27.6±2.4	14.28±0.09	Sinclair et al., 2005
Mar-00/2304	Marimana	0,983	42,706	2304	NaN	34.9±3.6	14.19±0.12	Sinclair et al., 2005
Mar-00/2440	Marimana	0,988	42,711	2440	NaN	36.6±3.2	14.19±0.11	Sinclair et al., 2005
Mar-00/2635	Marimana	0,993	42,714	2635	49.7±3.1	32.4±2.8	14.28±0.14	Sinclair et al., 2005
PY33	Riberot	1,05	42,806	1340	NaN	39±3	13.7±0.2	Fitzgerald et al., 1999
PY35	Riberot	1,052	42,808	1460	NaN	36±2	14.2±0.3	Fitzgerald et al., 1999
PY34	Riberot	1,0529	42,809	1595	NaN	37±2	14.7±0.1	Fitzgerald et al., 1999
PY39	Riberot	1,068	42,796	2050	NaN	41±3	NaN	Fitzgerald et al., 1999
PY38	Riberot	1,069	42,796	2205	NaN	42±4	14.5±0.5	Fitzgerald et al., 1999
PY37	Riberot	1,0725	42,797	2340	NaN	41±3	14.2±0.3	Fitzgerald et al., 1999
PY36	Riberot	1,0716	42,802	2483	NaN	44±4	14.2±0.1	Fitzgerald et al., 1999
3S-7	Trois-Seigneurs	1,441389	42,805278	1459	NaN	41.5±3.4	13.8±1.1	Vacherat et al., 2016
3S-6	Trois-Seigneurs	1,436944	42,812778	1598	NaN	41.8±1.9	13.6±0.9	Vacherat et al., 2016
3S-5	Trois-Seigneurs	1,435833	42,817778	1700	104.5±5.7	35.4±2.4	13.4±1.2	Vacherat et al., 2016
3S-4	Trois-Seigneurs	1,438611	42,820556	1772	100.8±5.7	37.6±2.4	14.2±1.0	Vacherat et al., 2016
3S-3	Trois-Seigneurs	1,440833	42,823611	1915	108.5±7.4	46.4±4.0	13.9±1.6	Vacherat et al., 2016
3S-2	Trois-Seigneurs	1,44	42,827222	2068	105.9±7.9	37.0±2.2	13.2±1.1	Vacherat et al., 2016
3S-1	Trois-Seigneurs	1,440278	42,830556	2199	153±18.0	46.5±4.7	14.1±1.1	Vacherat et al., 2016
Lac-1	Lacourt	1,176667	42,934167	451	155.6±10.0	43.9±2.1	13.5±1.2	Vacherat et al., 2016
Lac-2	Lacourt	1,213611	42,907778	493	135.0±14.0	38.5±1.8	13.5±1.2	Vacherat et al., 2016
PY6	Lacourt	1,215	42,94028	645	NaN	49±3	14.1±0.2	Fitzgerald et al., 1999
PY7	Lacourt	1,20222	42,9425	815	NaN	50±3	13.9±0.2	Fitzgerald et al., 1999
PY3	Lacourt	1,21417	42,93306	950	NaN	49±3	13.4±0.2	Fitzgerald et al., 1999
PY2	Lacourt	1,13306	42,93306	1048	NaN	55±3	13.7±0.2	Fitzgerald et al., 1999
Foi-1	Foix	1,532778	42,964444	488	168.0±29.0	74.9±1.2	13.0±1.6	Vacherat et al., 2016

Supplementary Table IV.1: List of apatite and zircon fission track analytical data in the Central Pyrenees used for this study. (i) Longitude and latitude are in degree decimal unit. (ii) ZFTA and AFTA correspond respectively to zircon fission track age and apatite fission track age. AFTMTL corresponds to apatite fission track mean track length.

Sample	Location	Longitude	Latitude	Elevation	AHeA	Reference
BAR/02/1150-2	Barruera	0,813	42,515	1150	10.5±0.8	Gibson et al., 2007
BAR/02/1695-2	Barruera	0,808	42,52	1695	13.8±1.1	Gibson et al., 2007
BAR/02/1150-3	Barruera	0,813	42,515	1695	15.9±1.3	Gibson et al., 2007
MAL/00/1750-1	Maladeta	0,99	42,507	1750	23.4±1.9	Gibson et al., 2007
MAL/00/1750-2	Maladeta	0,99	42,507	1750	22.9±1.8	Gibson et al., 2007
MAL/00/1750-3	Maladeta	0,99	42,507	1750	23.9±1.8	Gibson et al., 2007
MAL/00/1920-1	Maladeta	0,994	42,511	1920	27.9±2.2	Gibson et al., 2007
MAL/00/1920-2	Maladeta	0,994	42,511	1920	22.8±1.8	Gibson et al., 2007
MAL/00/2030-1	Maladeta	0,993	42,513	2030	20.8±1.7	Gibson et al., 2007
MAL/00/2030-2	Maladeta	0,993	42,513	2030	26.8±2.1	Gibson et al., 2007
MAL/00/2140-3	Maladeta	1,001	42,51	2140	30.2±2.4	Gibson et al., 2007
MAL/00/2250-1	Maladeta	1,008	42,51	2250	24.5±2.0	Gibson et al., 2007
MAL/00/2250-2	Maladeta	1,008	42,51	2250	31.3±2.5	Gibson et al., 2007
MAL/00/2360-1	Maladeta	1,013	42,512	2360	24.0±2.0	Gibson et al., 2007
MAL/00/2440-6	Maladeta	1,02	42,511	2440	26.1±2.0	Gibson et al., 2007
MAL/00/2650-3	Maladeta	1,025	42,513	2650	32.6±2.6	Gibson et al., 2007
MAL/00/2650-4	Maladeta	1,025	42,513	2650	30.8±2.4	Gibson et al., 2007
MAL/00/2650-5	Maladeta	1,025	42,513	2650	31.4±2.4	Gibson et al., 2007
MAL/00/2765-1	Maladeta	1,025	42,514	2765	34.9±2.8	Gibson et al., 2007
MAL/00/2765-2	Maladeta	1,025	42,514	2765	20.4±1.6	Gibson et al., 2007
MAL/00/2870-1	Maladeta	1,024	42,518	2870	29.2±2.3	Gibson et al., 2007
MAL/00/2870-2	Maladeta	1,024	42,518	2870	26.4±2.1	Gibson et al., 2007
MAL/00/2870-7	Maladeta	1,024	42,518	2870	17.3±1.4	Gibson et al., 2007
MM/02/2440-2	Marimana	0,988	42,711	2440	37.7±3.0	Gibson et al., 2007
MM/00/2304-1	Marimana	0,983	42,706	2304	34.2±2.3	Gibson et al., 2007
MM/00/2200-2	Marimana	0,981	42,705	2200	32.3±2.6	Gibson et al., 2007
MM/00/2030-1	Marimana	0,976	42,705	2030	31.8±2.5	Gibson et al., 2007
MM/00/2030-2	Marimana	0,976	42,705	2030	34.3±2.7	Gibson et al., 2007
MM/00/2030-3	Marimana	0,976	42,705	2030	34.5±2.8	Gibson et al., 2007
ART/03/1480-2	Arties	0,8677	42,6734	1480	27.5±2.2	Gibson et al., 2007
3S-1/A	Trois Seigneurs	1,4401	42,8305	2199	41.3±3.3	Vacherat et al., 2014
3S-1/B	Trois Seigneurs	1,4401	42,8305	2199	47.0±3.8	Vacherat et al., 2014
3S-1/C	Trois Seigneurs	1,4401	42,8305	2199	40.9±3.3	Vacherat et al., 2014
3S-1/D	Trois Seigneurs	1,4401	42,8305	2199	42.4±3.4	Vacherat et al., 2014
3S-2/A	Trois Seigneurs	1,44	42,8272	2068	31.1±2.5	Vacherat et al., 2014
3S-2/B	Trois Seigneurs	1,44	42,8272	2068	34.2±2.7	Vacherat et al., 2014
3S-2/C	Trois Seigneurs	1,44	42,8272	2068	35.7±2.9	Vacherat et al., 2014
3S-2/D	Trois Seigneurs	1,44	42,8272	2068	35.1±2.8	Vacherat et al., 2014
3S-3/A	Trois Seigneurs	1,4409	42,8235	1915	37.0±3.0	Vacherat et al., 2014
3S-3/B	Trois Seigneurs	1,4409	42,8235	1915	43.2±3.5	Vacherat et al., 2014
3S-3/C	Trois Seigneurs	1,4409	42,8235	1915	44.3±3.5	Vacherat et al., 2014
3S-3/D	Trois Seigneurs	1,4409	42,8235	1915	38.0±3.0	Vacherat et al., 2014
3S-3/E	Trois Seigneurs	1,4409	42,8235	1915	35.4±2.8	Vacherat et al., 2014
3S-4/A	Trois Seigneurs	1,4387	42,8206	1772	37.8±3.0	Vacherat et al., 2014
3S-5/A	Trois Seigneurs	1,4357	42,8179	1700	34.0±2.7	Vacherat et al., 2014
3S-5/B	Trois Seigneurs	1,4357	42,8179	1700	33.4±2.7	Vacherat et al., 2014
3S-5/C	Trois Seigneurs	1,4357	42,8179	1700	33.9±2.7	Vacherat et al., 2014
3S-5/D	Trois Seigneurs	1,4357	42,8179	1700	32.7±2.6	Vacherat et al., 2014
3S-6/A	Trois Seigneurs	1,4371	42,8128	1598	47.6±3.8	Vacherat et al., 2014
3S-6/B	Trois Seigneurs	1,4371	42,8128	1598	55.8±4.5	Vacherat et al., 2014
3S-6/C	Trois Seigneurs	1,4371	42,8128	1598	49.0±3.9	Vacherat et al., 2014
3S-7/A	Trois Seigneurs	1,4415	42,8054	1459	36.9±3.0	Vacherat et al., 2014
3S-7/B	Trois Seigneurs	1,4415	42,8054	1459	37.4±3.0	Vacherat et al., 2014
3S-7/C	Trois Seigneurs	1,4415	42,8054	1459	33.0±2.6	Vacherat et al., 2014
3S-7/D	Trois Seigneurs	1,4415	42,8054	1459	38.1±3.1	Vacherat et al., 2014
Lac-1/A	Lacourt	1,1768	42,9341	451	36.5±2.9	Vacherat et al., 2014
Lac-1/B	Lacourt	1,1768	42,9341	451	37.6±3.0	Vacherat et al., 2014
Lac-1/C	Lacourt	1,1768	42,9341	451	37.9±3.0	Vacherat et al., 2014
Lac-1/D	Lacourt	1,1768	42,9341	451	29.9±2.4	Vacherat et al., 2014
Lac-2/A	Lacourt	1,2137	42,9078	493	37.2±3.0	Vacherat et al., 2014
Lac-2/B	Lacourt	1,2137	42,9078	493	27.7±2.2	Vacherat et al., 2014
Lac-2/D	Lacourt	1,2137	42,9078	493	36.7±2.9	Vacherat et al., 2014
Foi-1/A	Foix	1,5328	42,9646	488	34.5±2.8	Vacherat et al., 2014
Foi-1/B	Foix	1,5328	42,9646	488	50.9±4.1	Vacherat et al., 2014
Foi-1/C	Foix	1,5328	42,9646	488	55.0±4.4	Vacherat et al., 2014

Supplementary Table IV.2: List of apatite helium analytical data in the Central Pyrenees used for this study. (i) Longitude and latitude are in degree decimal unit. (ii) AHeA corresponds to apatite helium age.

Profile	Decrease cooling rate timing (Ma)	Cooling rate decrease time (Myrs)	Rate of cooling change (°C.Myrs^{-2})
Lacourt	30	15	0.7±0.1
Trois-Seigneurs	33	10	0.4±0.1
Riberot	28	9	1.8±0.3
Marimaña	25	7	1.5±0.1
Arties	20	9	2.4±0.3
Maladeta	20	7	2.0±0.2
Barruera	7	19	1.2±0.1
Nogueres	10	11	0.5±0.1

Supplementary Table IV.3: Summary of results from the thermal histories for each elevation profiles from north to south.

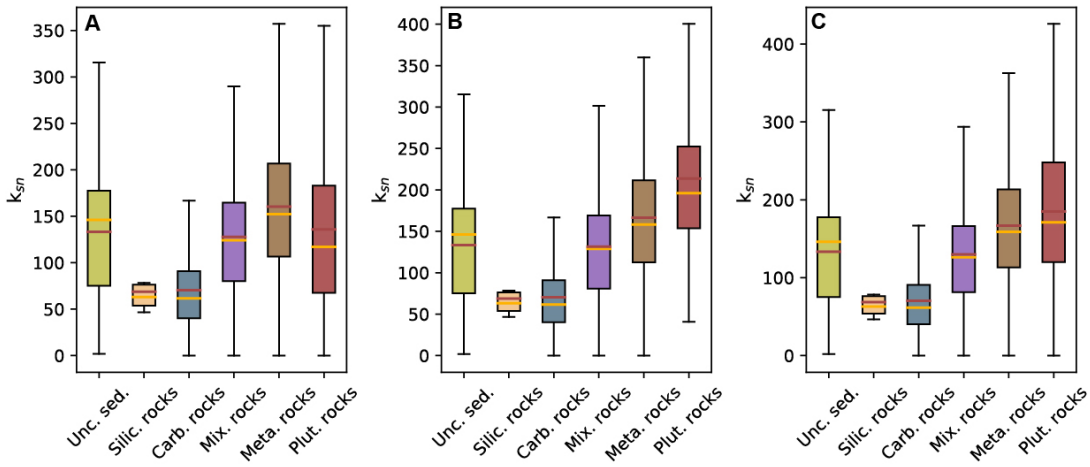

Supplementary Figure IV.2: Relation between lithologies and channel steepness for Noguera Pallaresa catchment with A) no consideration of potential glacial effect on channel steepness; B) consideration of glacial effect with removal of k_sn values above 1900 m; C) consideration of glacial effect with removal of k_sn values above 2100 m. Note highest mean and median k_sn values for plutonic rocks in panel B and C when removing ksn values above a limit elevation. Each box-and-whisker represent the minimal, 25th percentiles, 75th percentiles and maximal values in horizontal black lines while red and yellow horizontal lines represent respectively the mean and median values

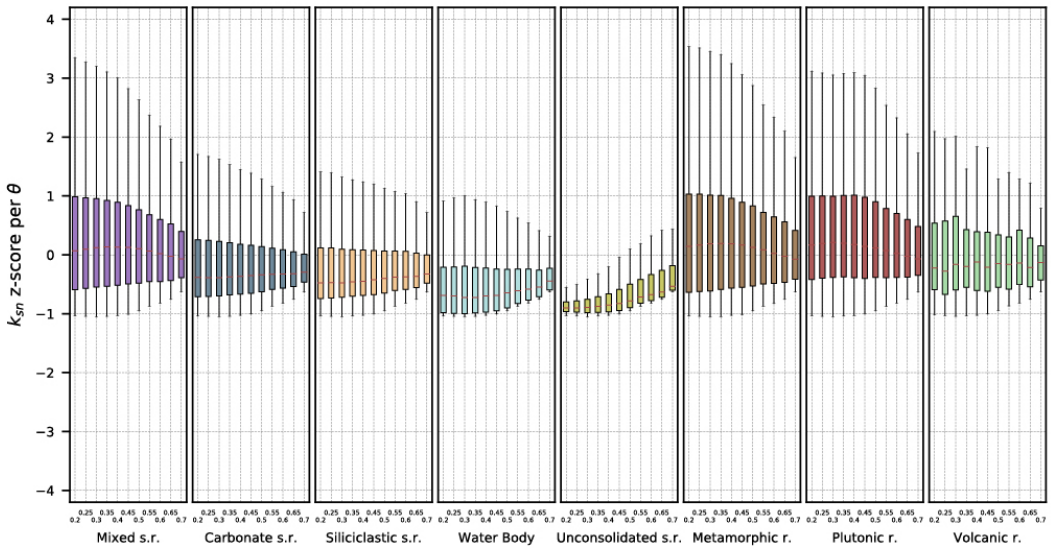

Supplementary Figure IV.3: k_sn z-score associated to the different lithologies as a function of different θ which correspond to the m/n ratio. From left to right each graphic plot corresponds to the k_sn z-score for different m/n ratio (0.2, 0.25, 0.3, 0.35, 0.4, 0.45, 0.5, 0.55, 0.6, 0.65 and 0.7) for each lithology (mixed sedimentary rocks, carbonate sedimentary rocks, siliciclastic sedimentary rocks, water body, unconsolidated sedimentary rocks, metamorphic rocks, plutonic rocks and volcanic rocks). The standard score or z-score corresponds to the number of standard deviations by which the value data is above or under the mean value. $Z - score = (x - \mu)/\sigma$ where μ is the mean and σ is the standard deviation.

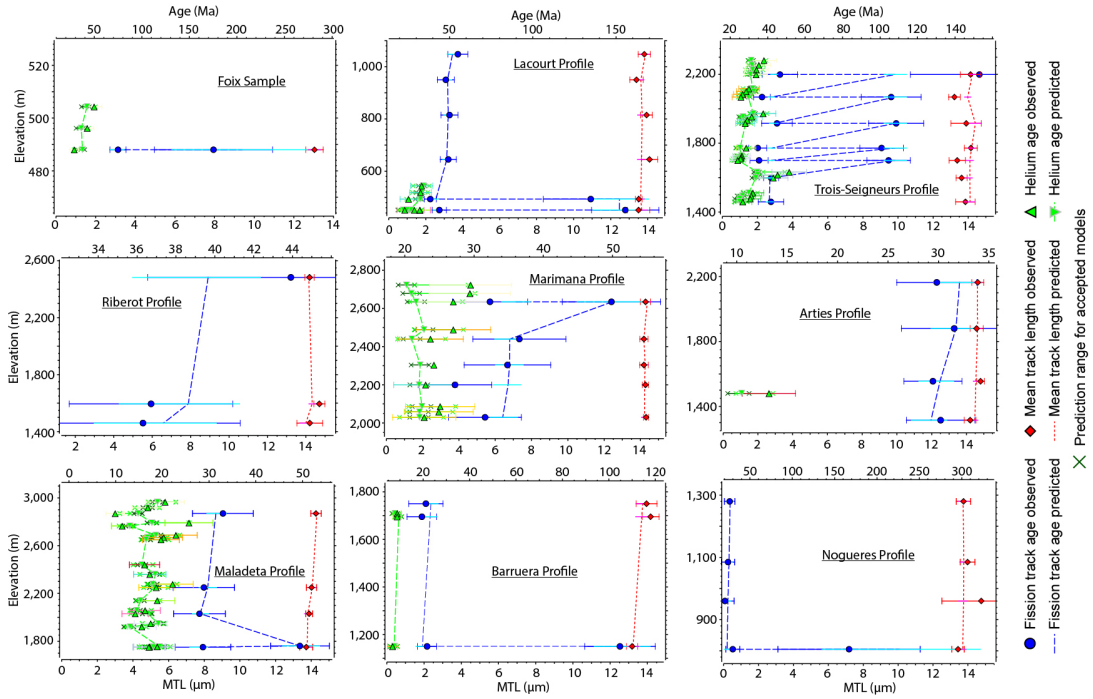

Supplementary Figure IV.4: Complete set of predictions from thermal history models compared to observed data. The predicted and observed values for all samples in the profiles are represented as a function of elevation. Normal green triangles, blue circles and red diamonds are respectively AHe ages, FT ages and mean track length (MTL) observed. Errors bars on AHe ages, FT ages and MTL are included and are represented by green, blue and red horizontal lines. Inverse green triangles, blue vertical lines and red vertical lines are the predicted AHe ages, FT ages and MTL respectively. The cyan, magenta, and green horizontal lines are the mean and 95% credible range for the predictions on FT ages, MTL and AHe ages, respectively. Green crosses correspond to the helium prediction range for accepted models. Yellow squares and horizontal lines are the prior kinetic parameters and error bars (multi-composition model of Ketcham et al., 2007 for apatite fission tracks data, Yamada, 2007 for zircon fission track data and the models of Gautheron et al., 2009 for helium data) used as inputs for inverse modelling. Yellow vertical lines are the predicted kinetic parameters while the modelled 95% credible range is shown as light yellow horizontal lines.

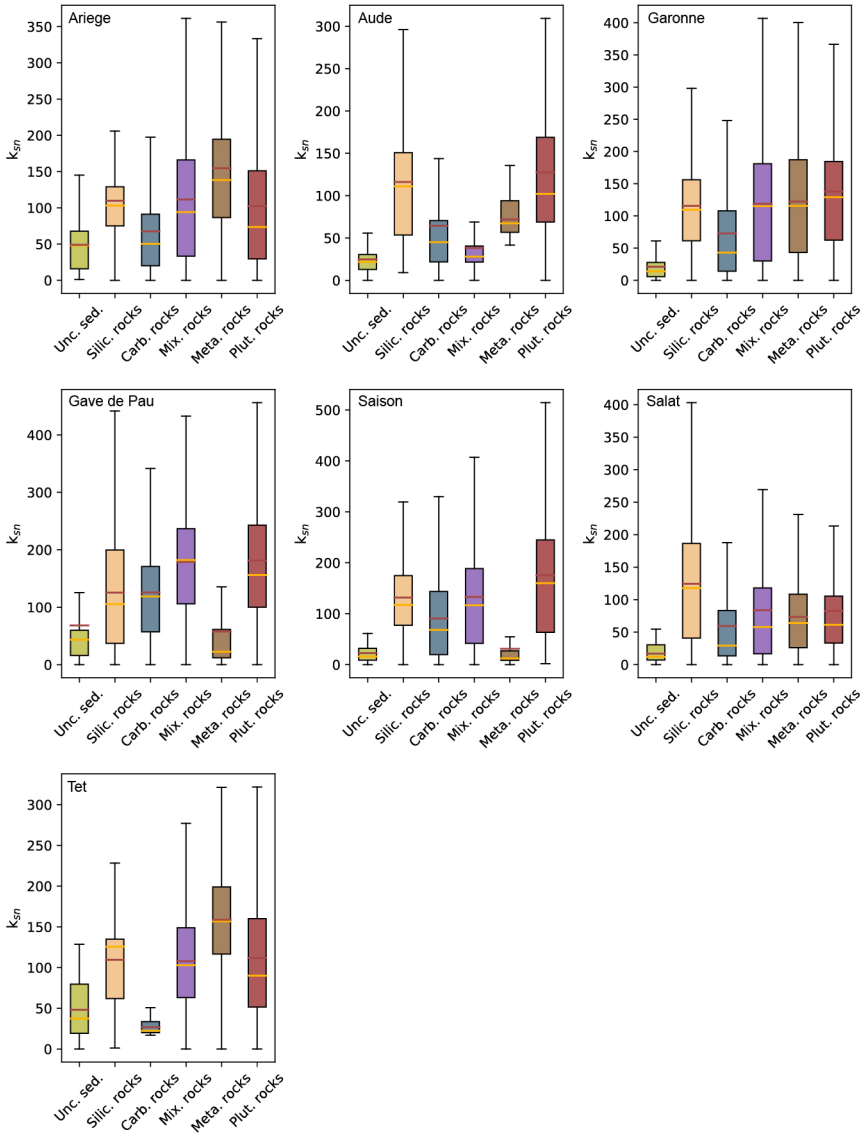

Supplementary Figure IV.5: Complete set of box and whisker plots of the range of ksn values associated with each lithology for the catchments of the northern Pyrenees. The different catchments are Saison, Gave de Pau, Garonne, Salat, Ariège, Aude and Tet. Colors of boxplots and lithology abbreviations are in accord with Figures IV.3 and IV.4. Each box-and-whisker represent the minimal, 25th percentiles, 75th percentiles and maximal values in horizontal black lines while red and yellow horizontal line represent respectively the mean and median values.

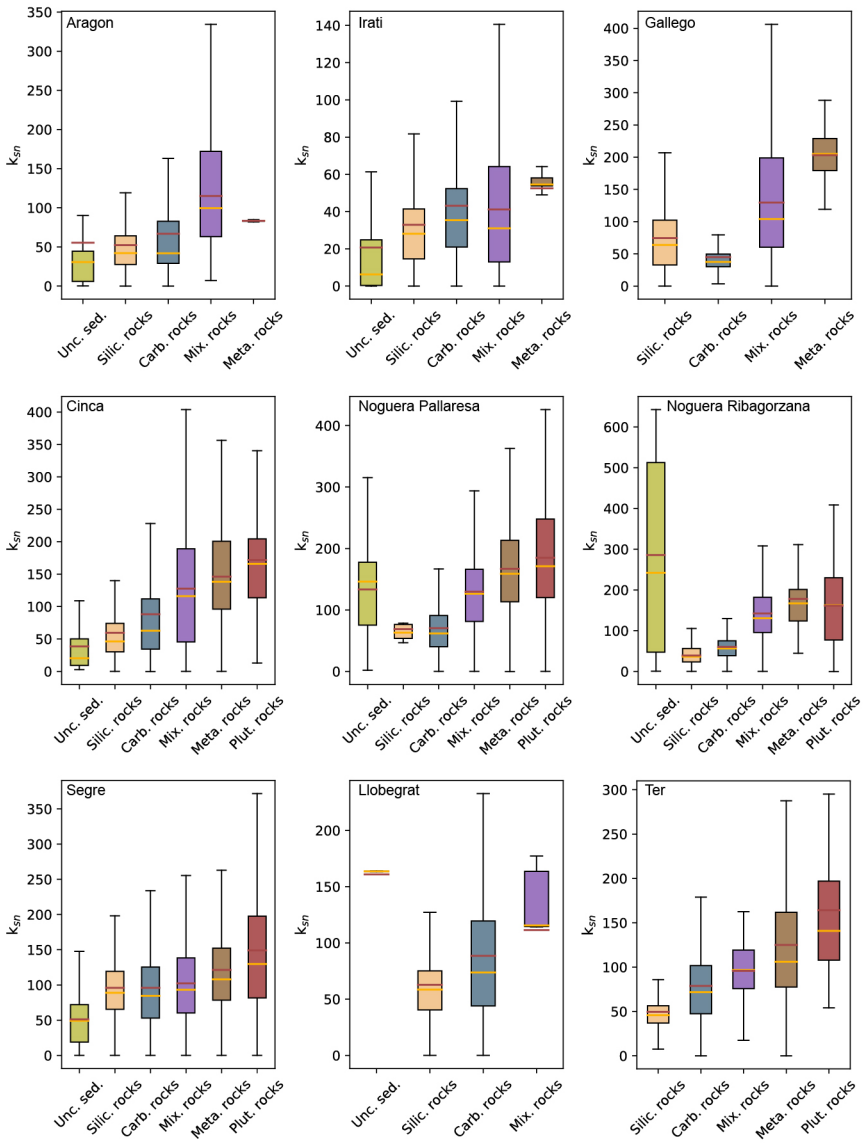

Supplementary Figure IV.6: Complete set of box and whisker plot of the range of ksn values associated with each lithology for the main catchments of the southern Pyrenees. The different catchments are Irati, Aragon, Gallego, Cinca, Noguera Ribagorzana, Noguera Pallaresa, Segre, Llobegrat and Ter. Each box-and-whisker represent the minimal, 25th percentiles, 75th percentiles and maximal values in horizontal black lines while red and yellow horizontal line represent respectively the mean and median values.

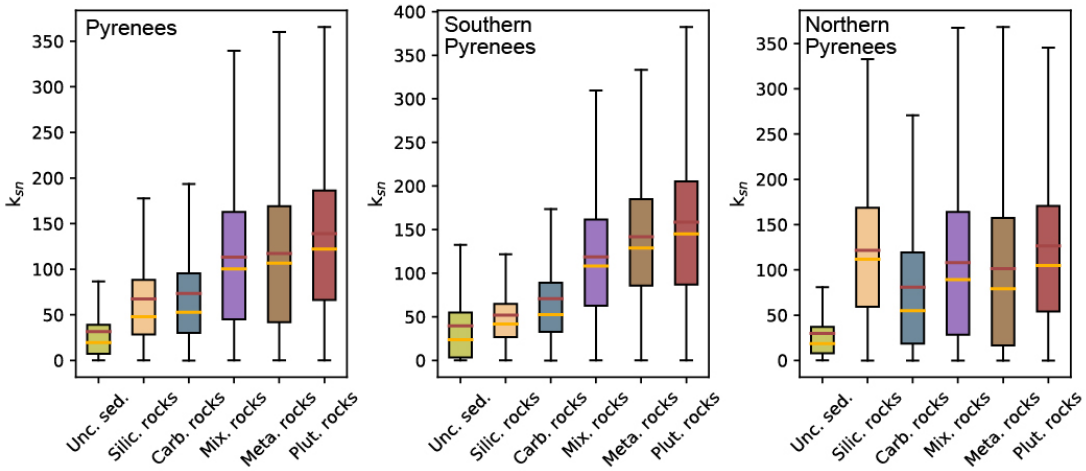

Supplementary Figure IV.7: Set of box and whisker plot of the range of ksn values associated to each lithology for the entire Pyrenees, northern Pyrenees and southern Pyrenees. The northern Pyrenees corresponds to Ariège, Aude, Garonne, Gave de Pau, Saison, Salat and Tet catchments. The southern Pyrenees corresponds to Aragon, Cinca, Gallego, Irati, Llobegrat, Noguera Pallaresa, Noguera Ribagorzana, Segre and Ter catchments. Each box-and-whisker represents the minimal, 25th percentiles, 75th percentiles and maximal values in horizontal black lines while red and yellow horizontal lines represent respectively the mean and median values.

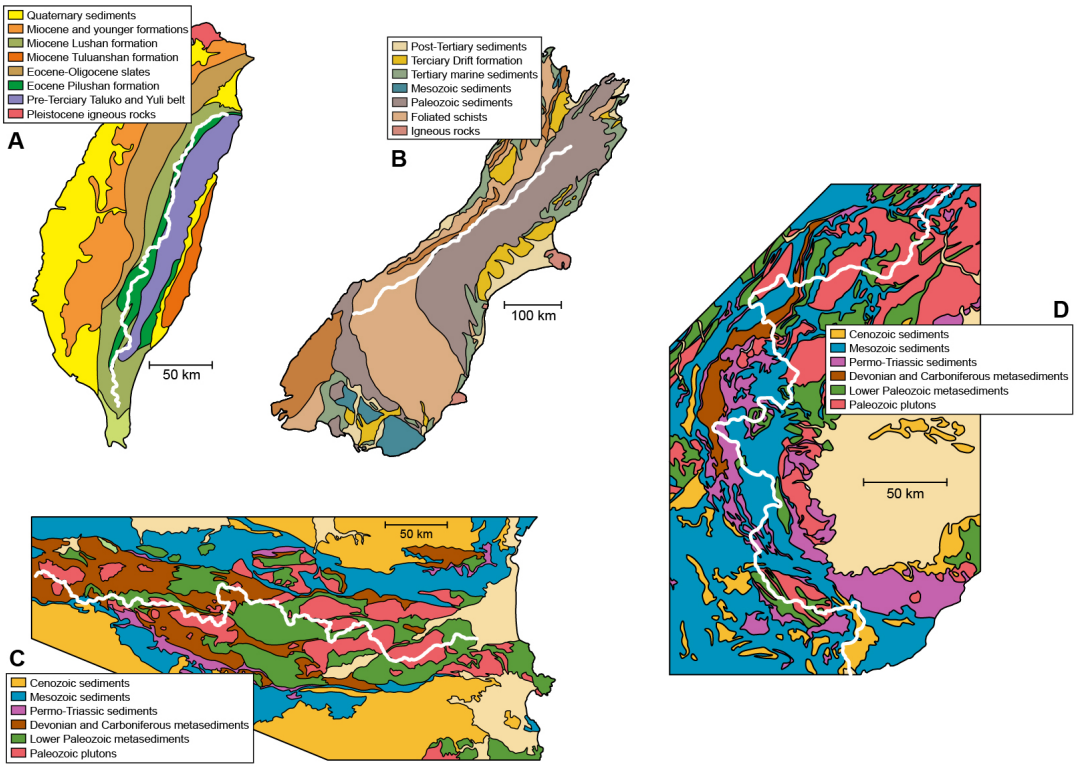

Supplementary Figure IV.8: Geologic map of A) Taiwan, B) Southern Alps of New Zealand, C) Pyrenees and D) Western European Alps showing the relation between the main drainage divide and the lateral variation of geologic units. Scale is not respected between the different orogens.

Chapter V

CATCHMENT VULNERABILITY AND DRAINAGE DIVIDE MIGRATION BY DIFFERENTIAL ROCK ERODIBILITY EXHUMATION

V.1 Abstract

Assessing the controls on erosive processes is required to understand dynamic and evolution of topographic landscape. While lithological rock type has been documented in mountains as an important parameter controlling landscape morphology, the impact of exhuming differential rock strengths through time on landscape dynamic remains unclear. In this study, we document the mobility of drainage divides in growing mountain ranges in response to exhuming harder lithologies. Our results are based on both two-dimensional landscape numerical modelling and topographic analyses of model outputs. We demonstrate that catchment vulnerability in transient landscapes can be constrained by analyses of the evolution of channel steepness. In response to exhumation of harder rocks within a catchment, channel steepness of tributaries upstream of the exhumed harder lithology are characterized by a reduction in channel steepness and erosion rates which contrasts with the surrounding areas that are unaffected. This disequilibrium in channel steepness located across drainage divides causes contrasts in the denudation rate across divides resulting in divide migration. This analysis proposes a previously unrecognised mechanism for catchment divide migrations associated with the exhumation of rock types of varying rock strength. Our interpretation is consistent

with ,mountain landscapes with high variability in rock lithologies such as the Central Pyrenees.

V.2 Introduction

Mountainous landscapes are produced by the long-term competition between multiple processes including crustal thickening, dynamic topography, climate and surfaces processes (erosion and deposition of sediment). The large-scale evolution of any convergent mountain belts will evolve toward a balance between crustal accretion provided by tectonic forcing and material removal by surface processes linked to climate (Beaumont et al., 1992; Willett & Brandon, 2002). In principle and assuming constant conditions, the landscape shape of a system that has reached a steady-state should stay relatively stable through time with no major drainage network reorganisation.

However, in most natural mountain ranges, a complete steady-state condition is unlikely because of multiple interactions and feedbacks between tectonics, climate and landscape shape. Many processes perturb uplift rate through time and space as varying the tectonic stress (Kirby & Whipple, 2012). Mantle processes at low amplitude and long wavelength through dynamic topography (Braun, Guillocheau, et al., 2014) affect uplift rate. Differential rock density triggers spatial variation of uplift (Braun, Simon-Labric, et al., 2014). Perturbations of climate affect tectonics by loading or unloading the lithosphere (Bettinelli et al., 2008; Doser & Rodriguez, 2011). In the same way, climate is affected by tectonics through volcanism (Zielinski, 2000) or in the landscape by modifying atmospheric circulation and orographic precipitation (Hoskins & Karoly, 1981; Roe et al., 2002). Active mountain ranges provide perfect conditions to study these important interactions (Champagnac et al., 2012). Debates are still relevant concerning whether climatic or geodynamic processes have the more important impact on the tectonic evolution, rock exhumation and landscape shaping as for example in the Himalayan or Andes belts (Burbank et al., 2003; Montgomery et al., 2001; Searle et al., 1997; Strecker et al., 2007; Thiede et al., 2004).

In addition, intrinsic geological parameters can also affect the efficiency of river channel erosion and modify landscape shape of mountain belts. These changes can be caused by spatial difference of fracture densities (Whipple, 2002) or rock strengths (Forte et al., 2016; Stock & Montgomery, 1999) generally associated to varying lithological

rock types in the landscape. Affected landscapes respond by transmitting signals upstream through the channel network (Perron & Royden, 2013; Whipple & Tucker, 1999). Resulting drainage network reorganisation by catchment captures or drainage divide migration leads to transient landscapes until new stable conditions are reached (Whipple et al., 2017; Willett et al., 2014). The dynamic state of transient landscapes has been widely studied using an integral channel analyses approach (Royden & Perron, 2013) in order to access potential catchment divide migration (Mouchené et al., 2017; Willett et al., 2014). However, as based solely on integration of the drainage area of each point of the channel from a base level reference, this method does not take into account differential uplift, climate or rock types and can result in misinterpretation.

V.3 Natural Landscape Motivation

There has been a renewal of interest in recent years on lithological controls on landscape evolution (Bernard et al., 2019; Darling et al., 2020; Flowers & Ehlers, 2018; Gallen, 2018; Zondervan et al., 2020). For example, experimental studies demonstrate that rocks with contrasting tensile strength influence the erosion rate along fluvial channels by a factor of 3 to 5 depending on the range of lithologies (Sklar & Dietrich, 2001). Flower and Ehlers (2018), show that changes of erosion determined by thermochronological data and associated thermal histories can be strongly affected by exhumation of variable rock erodibilities. Other studies directly demonstrated those effects on natural landscape. Gallen, (2019) show that in the Appalachian Mountains, important drainage reorganisation can be triggered by changes in the erodibility coefficient of different rock unit types. Bernard et al., (2019) show that lithologies with the highest rock strength control river channel steepness and the location of the modern drainage divide in the Pyrenees.

The comprehension of mountainous landscape evolution is critical in order to understand effects of varying external forces such as tectonics, climate or intrinsic conditions. In this contribution, we present analyses of the response of channel networks to spatial changes in rock erodibility in order to access the role of the exhumation of variable rock types on landscape evolution. Using numerical landscape evolution model experiments and analyses of topographic metrics, we explore the role of spatial variations in rock strength on river networks during orogenesis. We document through

time and at the scale of a mountain range, changes of channel steepness and denudation rate. A particular outcome of these experiments is the impact on upstream drainage evolution and divide migration in response to the exhumation of crystalline basement massifs.

V.4 Methods and Model Setup

In order to investigate evolution of transient river networks in a mountainous landscape, we perform 2-dimensional landscape numerical modelling using the Fastscape algorithm (Braun & Willett, 2013) available through the Xarray-Simlab package (Bovy, 2020). Erosion during landscape evolution are simulated by river channel and hillslope processes using the stream power incision model (Howard & Kerby, 1983; Whipple & Tucker, 1999) and linear diffusion law respectively. We setup a landscape model shape of 450 km in length and 150 km in width. The horizontal and vertical numbers of grid nodes are 300 and 100 respectively in order to keep an uniform spatial resolution of 1.5 km (Figure V.1). Landscape topography evolves under a linear gradient of rock uplift from 0 at the lower boundary to 1 mm.yr-1 at the upper boundary. When run to steady state, this set up generates an assymetric range with the main drainage divide located in the northern part of the model, comparable to many doubly-vergent mountain belts (eg. Taiwan and Olympic Mountains; Willett et al., 1993. We input an initial and constant background erodibility coefficient of $2\text{x}10^{-6}$ which decreases at a specific time and location in order to simulate the exhumation of more resistant rock types such as basement massifs. Studies have shown that the concavity index ($\theta = m/n$) generally ranges between 0.4 and 0.7 for landscape at an equilibrium state (Croissant & Braun, 2014; Lague, 2014; Stock & Montgomery, 1999). Here we setup an area exponent (n) of 0.6 and a slope exponent (n) of 1.5 giving a concavity index (θ) of 0.4 which correspond to concavity index found in natural landscape (Kirby & Whipple, 2012; Whipple & Meade, 2004; Whipple & Tucker, 1999).

We coupled the Fastscape landscape model outputs with the open-source topographic analysis algorithm from (Mudd et al., 2014). For each time-steps, we extract a series of topographic metrics from the model outputs. We particularly explore evolution of channel steepness index (k_{sn}) along catchment river channels. The channel steepness or rate of channel slope change normalized to drainage area has been shown to reflect

spatial patterns of uplift rate, climate or rock erodibility (Mudd et al., 2014; Wobus et al., 2006). Calculation of channel steepness is performed using the same concavity parameter as defined in the Fastscape modelling (i.e. $\theta = 0.4$) and a reference drainage area (A_0) of 1 m^2 for normalizing along the channel profile. We performed analyses only for basins with a minimum drainage area of 1x10^7 m^2.

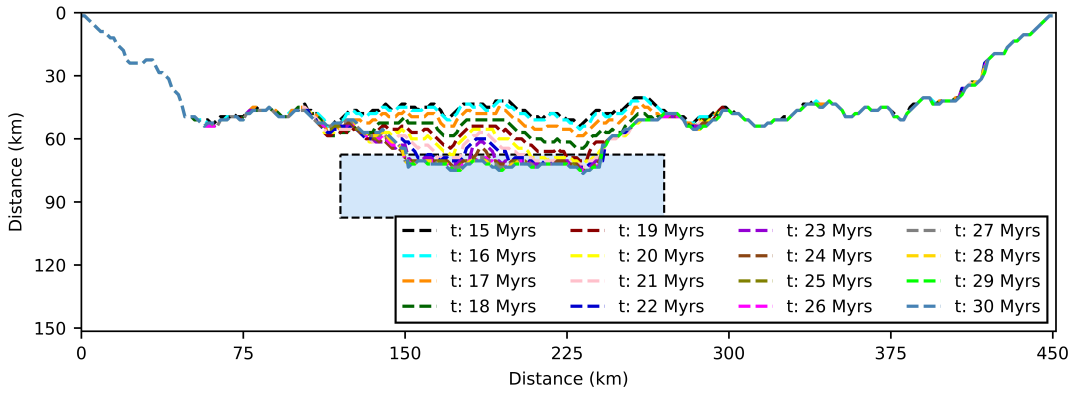

Figure V.1: Landscape numerical modelling result showing the main drainage divide position from 15 to 30 Myrs. Lower rock erodibility block are introduced in the model at 15 Myrs and represented by the square blue area. Dash colour lines correspond to the main drainage divide position at different time laps. After 30 Myrs the drainage divide remain relatively stable for the new erodibility conditions.

V.5 Results and Discussion

V.5.1 Landscape Dynamic by Numerical Modelling

We initiate the model with the following initial conditions: i) linear gradient in tectonic rock uplift rate and ii) spatially uniform erodibility coefficient (2x10^{-6}). At steady-state (i.e. after 15 Myrs), the topography is characterized by a main drainage divide located in the northern part of the model (Figure V.1) because of northward increasing uplift. These settings implies shorter and steeper northern catchments and longer and gentler southern catchments (Figures V.2A and V.3A). From 15 Myrs, we simulate the exhumation of harder rocks by introducing in the model a block with a lower erodibility coefficient (0.5x10^{-6}) (Figure V.1). The main response to these new conditions is a southward shift of the main drainage divide up to the northern limit of the lower erodibility block. After approximately 25 Myrs the system reaches a new steady-state

with a relatively stable drainage divide position (Figure V.1). Noted that the main drainage divide position does not entirely follow the upper part of the lower erodibility block, but instead, there is a systematic gap.

The transient response caused by the introduction of less erodible rocks is associated with the immediate formation of two knickpoints (G and H; Figure V.3B) in rivers flowing across harder rocks. From downstream to upstream, a first abrupt increase in normalised channel gradient (G; positive slope break) is observed at the southern border of the block and a second abrupt decrease in normalised channel gradient (H; negative slope break) is located at the northern border of the block. The initial transience is recorded by the upstream propagation of both of these slope breaks (Supplementary Figure V.1 and Figure V.3B and C). After approximately 1 Myr, the upper negative slope (H) break migrates through the whole upstream area and reaches the drainage divide (Supplementary Figure V.1 and Video V.1). After the migration phase, the upstream area situated just between the harder rocks and the drainage divide is characterized by a general rising and flattening as demonstrated by a decrease of channel steepness (Figure V.3) and longitudinal and transversal slope swath profile analyses (Supplementary Figures V.2 and V.3). Longer time (2 Myrs) is necessary for the first positive break-slope (G) to migrate upstream through the harder rocks (Figure V.3BC and Supplementary Video V.1). From 16 Myrs to about 20 Myrs (Figure V.3B-D), the upstream part of the southern catchment is progressively captured by the northern catchment resulting with the disappearance of the upstream knickpoint (H). A new knickpoint (I) is formed when rivers of the northern catchment reach harder rocks (Figure V.3E). From about 20 Myrs to 30 Myrs (Figure V.3EF) southward extension of the northern catchment continue until equilibrium of channel steepness across the divides is reached again.

The distribution of erosion rate also reveals a clear response to the exhumation of harder rocks (Figure V.2). Initially, as the model runs to steady state, the distribution of erosion is determined by the regional tilt (Figure V.2A). Shortly after exhumation of the more resistant rocks, the upstream area experience an abrupt decrease of erosion rate firstly located along the river channels (Supplementary Figure V.4) but rapidly through the whole catchment (Figure V.2B). The re-equilibration of erosion rates of the southern catchments is performed by the upstream propagation of channel erosion rate. This takes place initially through the more resistant block (Supplementary Figure V.4)

and secondly, through the upstream flattened area (Figure V.2C).

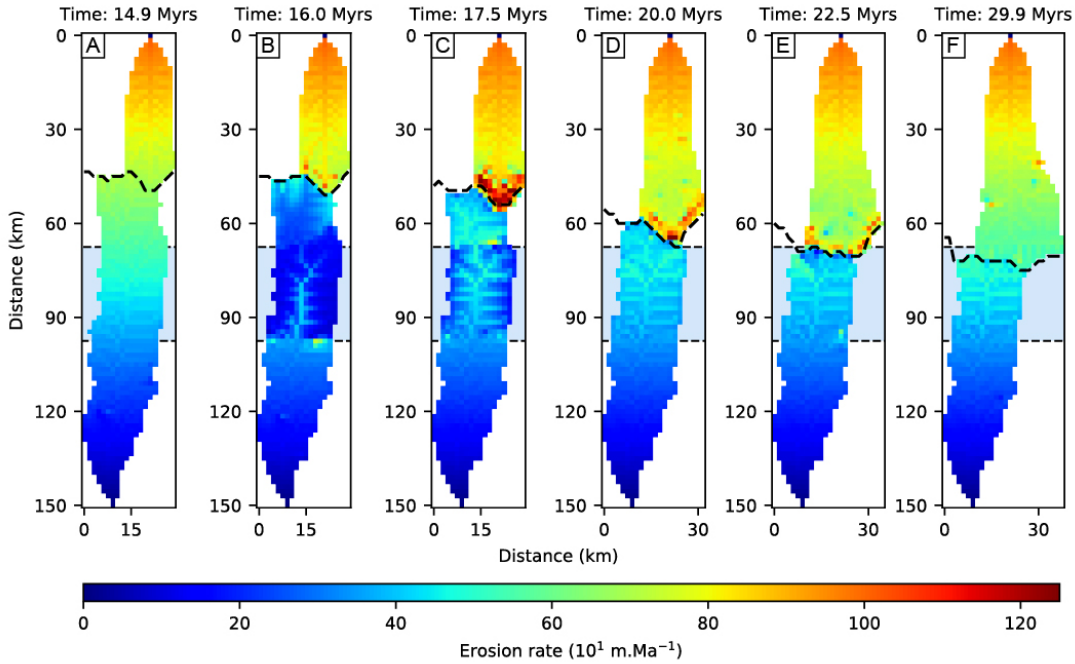

Figure V.2: Erosion rate pattern from Fastscape algorithm for two adjacent catchments located northward and southward of the main drainage divide and impacted by the change of rock erodibility. Erosion rate is represented in both catchments by colours from dark blue (low value) to dark red (high value) at different time laps (14.9, 16.0, 17.5, 20.0, 22.5 and 29.9 Myrs). Dash black lines correspond to the drainage divide between the two catchments. Lower rock erodibility are induced at 15 Myrs and located from 67.5 and 97.5 km. Initial erosion rate gradients are due to the gradient uplift from south to north. For first and last panels (i.e. 14.9 and 29.9 Myrs), low erosion rates contrast indicate relatively stable drainage divide compared to high contrast and instable drainage divide for intermediate panels. Square blue area indicate location of harder rocks.

Lowering of channel steepness in the upstream area of southern catchments contrasts with the surrounding unchanged channel steepness (Figure V.3B and Supplementary Figure V.3). The models demonstrate the vulnerability of these upper, low gradient portions of the southern catchments to capture, particularly by the northern catchments. In response to that disequilibrium, northern catchments capture the upstream part of the southern catchments with an associated drainage divide migration in order to rebalance channel steepness across the divide (Figure V.2). Transient drainage divides last up to

about 25 Myrs (i.e. 10 Myrs after the exhumation of harder rocks), which is when the landscape reaches a new steady-state with an equilibrium of channel steepness across the divides (Figure V.3EF). Disequilibrium is demonstrated by a pattern of denudation (Figure V.2B-E) with anomalously high erosion rates in the northern catchments close to the drainage divide. The relatively smooth gradient of erosion rate along the model indicate relatively stable landscape at about 30 Myrs (Figure V.2F). Importantly, the same pattern of vulnerability and divide migration is observed between affected and non-affected southern catchments on the left and right border of the harder rocks (Supplementary Figure V.5 and Supplementary Video V.1).

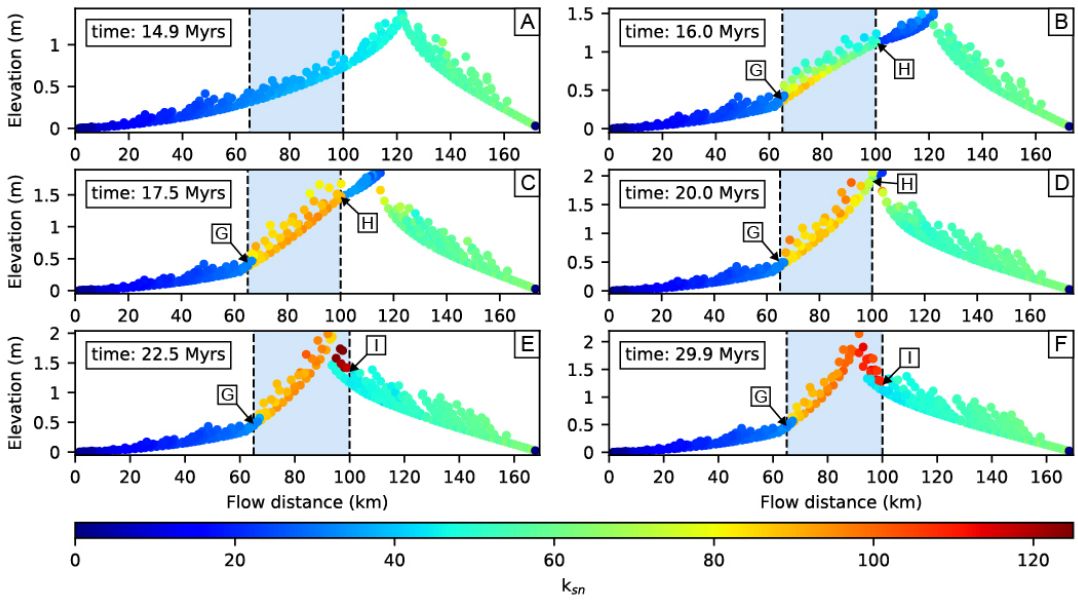

Figure V.3: Plot of channel steepness in function of flow distance and elevation for similar catchments and time laps to those in Figure V.2 from 14.9 to 29.9 Myrs. Channel steepness is represented by a succession of points along catchment river channels with colours from dark blue (low values) to dark red (high values). Channel steepness metric is calculated with LSDTopoTools from Fastscape landscape model outputs. Square blue area indicate location of harder rocks.

V.5.2 Natural Landscape Expression to Rock Erodibility Changes

Here we demonstrate that drainage divide migration may be the result of catchment vulnerabilities by exhumation of harder rocks within a catchment. A great deal of geomorphological research has questioned the relative degree to which climate or

tectonics are more likely to explain changes in erosion rate (Henck et al., 2011; Moon et al., 2011). This study shows that intrinsic landscape parameters (i.e. erodibility coefficient) have the ability to spatially regulate denudation rates and generate signals that may otherwise have required explanations in involving external forcings. Our model setup, which doesn't have the ultimate goal to mimic a natural landscape, but rather reproduce realistic processes and topographies, shows that the transient response to exhumation of hard roocks may last 10 Myrs. It is therefore challenging to record this transience in natural landscapes, but easier to identify the final product of this process. However, we may observe modern mountain ranges with steady-state drainage networks characterized by drainage divides that are mainly located on harder rock types and catchment geometries recording processes of previous capture both lateral and transverse to the range (see model scenarios) .

Analysis of the landscape shape of the Central Pyrenees around the main drainage divide reveals features which could correspond to the potential effect of varying lithological hardness (Figure V.4). The first-order signal is the simultaneous occurrence between the main drainage divide location and highly resistant Variscan basement massifs. This correlation is well defined between the Maladeta and Bassiès massifs where the main drainage divide runs transverse to the mountain front (Bernard et al., 2019) (Figure V.4A and B) in order to reach different basement massifs as shown by numerical modelling (Figure V.1). Another landscape expression is the upstream channel network of the Noguera Pallaresa catchment (Figure V.4C); the channel network proceeds around and behind the Maladeta and Marimaña massifs and may have resulted from an incision wave from the Noguera Pallaresa rivers into the Garonne catchment. The exact timing of exhumation of the Variscan basement is still debated but an Eocene-Oligocene age is realistic (i.e. 30-40 Myrs ago). We therefore observe a final steady-state response and interpret this to have resulted from the processes illustrated by the models (Figure V.3F) (Bernard et al., 2019). The additional level of complexity on this record is that of recent glaciation superimposed and modifying the fluvial profiles in the region.

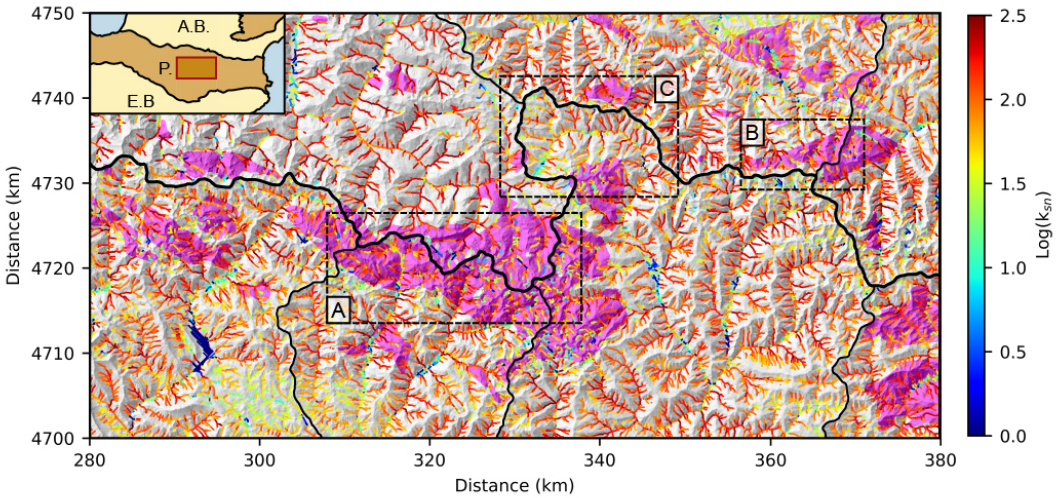

Figure V.4: Evidence of landscape shape response from spatial variation of rock strength type on the Central Pyrenees. A and B) Drainage divide capture by highly resistant rocks (Variscan granitoid basement). C) Longitudinal catchment capture behind highly resistant rocks. Channel steepness is represented by a succession of points along the river channels of different catchments (Garonne, Salat, Ariège, Cinca, Noguera Ribagorzana and Noguera Pallaresa) with colours from dark blue (low values) to dark red (high values). Pink patches indicate location of resistant granitic plutonic basements (i.e. lower erodibility). Thick black line correspond to the main drainage divide and black lines correspond to secondary catchment divides. A.B.: Aquitaine retro-foreland Basin; P.: Pyrenees; E.B.: Ebro pro-foreland Basin.

V.6 Conclusion

Based on experiments using a landscape evolution model, we found that the exhumation of harder rocks (i.e. lower erodibility) with the centre of a mountainous drainage catchment causes a general lowering of channel and hillslope gradients in the upstream area. This lowering of topographic gradients is associated with a reduction in erosion rates which contrasted with neighbouring headwaters of other catchments that are unaffected by the exhumation of harder lithologies. This disequilibrium across catchments forced drainage divides to migrate in order to rebalance the landscape. Again, this behaviour is supported by an increase of denudation rate for one side of the divide and generally pushing the drainage divide in the direction of the harder lithologies. Despite the noise in channel steepness on natural landscape associated with other processes, the correlation between drainage divides and resistant rocks and catchment forms around resistant rocks as in the Central Pyrenees suggest the processes revealed by the modelling are likely to have played a role in their origins. In addition, we have shown that landscape transience related to change of rock erodibility lasts a few millions of years as the network adapts rapidly to new conditions.

V.7 Supplementary Materials

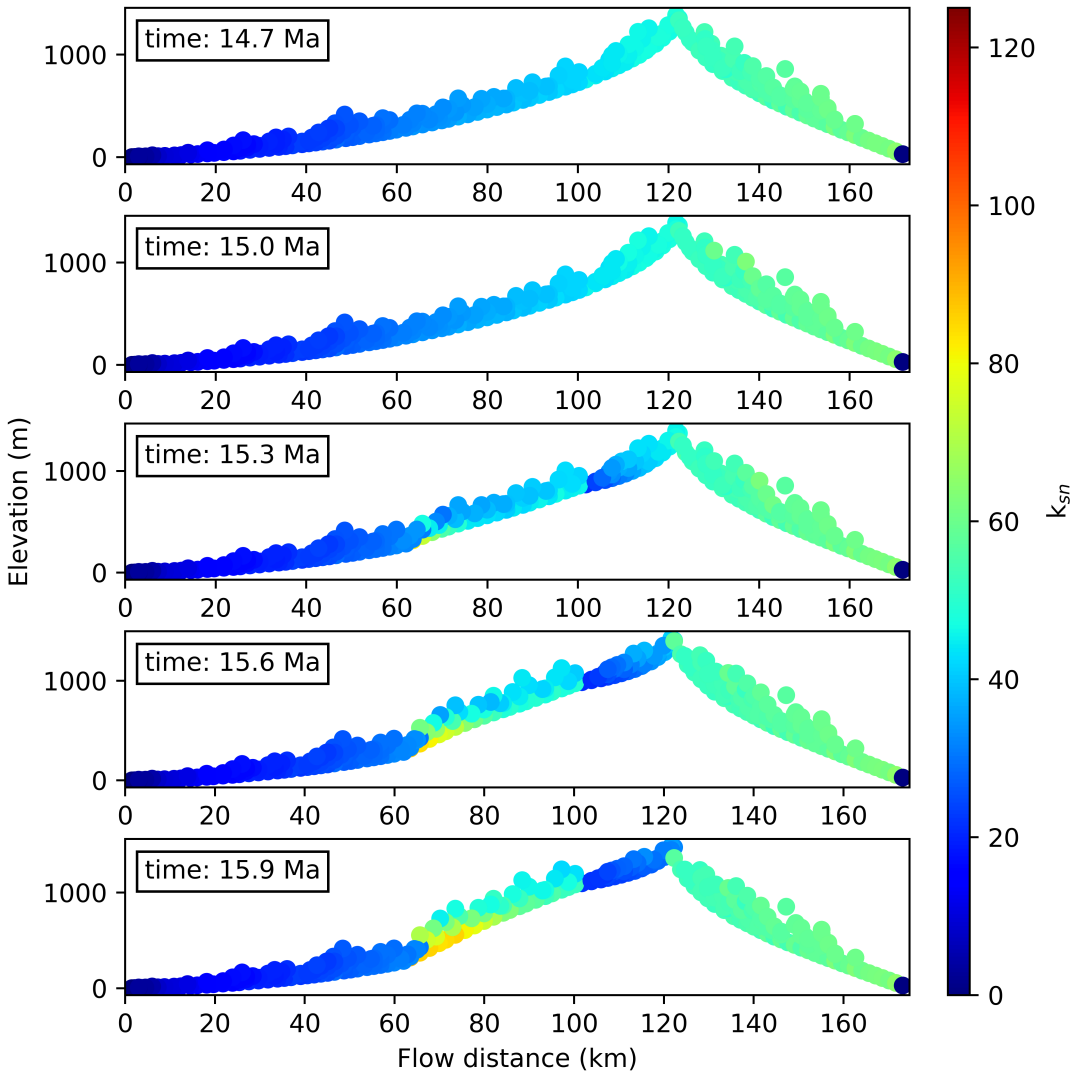

Supplementary Figure V.1: Plot of channel steepness in function of flow distance and elevation for similar catchments to those in Figure V.2 from 14.7 to 15.9 Myrs. Channel steepness is represented by a succession of points along catchment river channels with colours from dark blue (low values) to dark red (high values). Channel steepness metric is calculated with LSDTopoTools from Fastscape landscape model outputs. Square blue area indicate location of harder rocks.

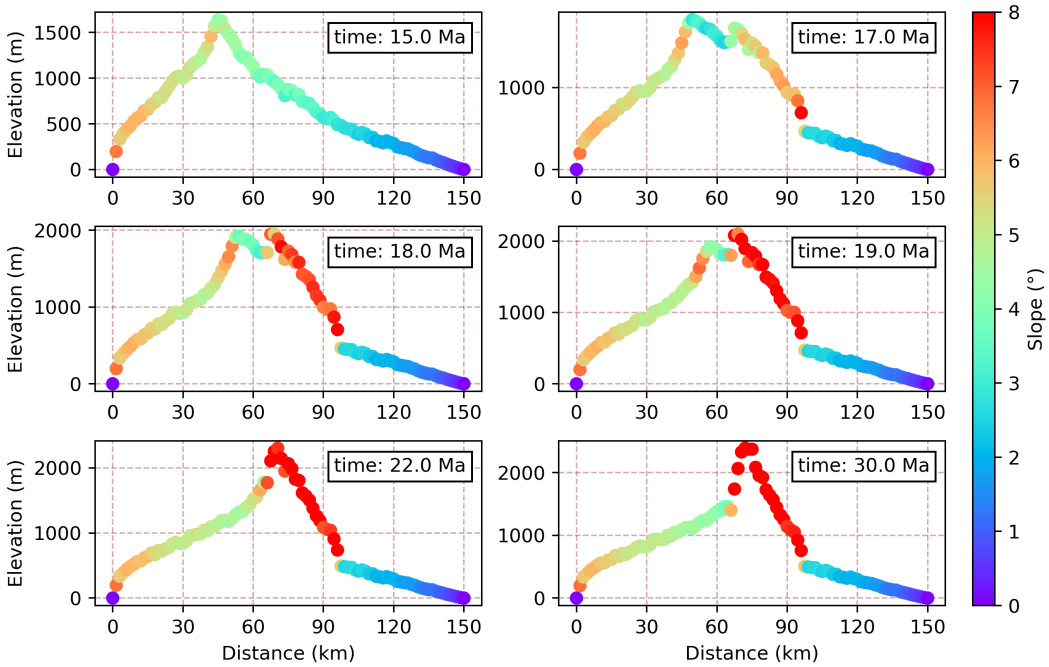

Supplementary Figure V.2: Swath profile plot of the slope and elevation in function of distance longitudinally to two catchments (northern and southern catchment) from 15 to 30 Myrs. Slope is represented with colours from dark blue (low values) to dark red (high values).

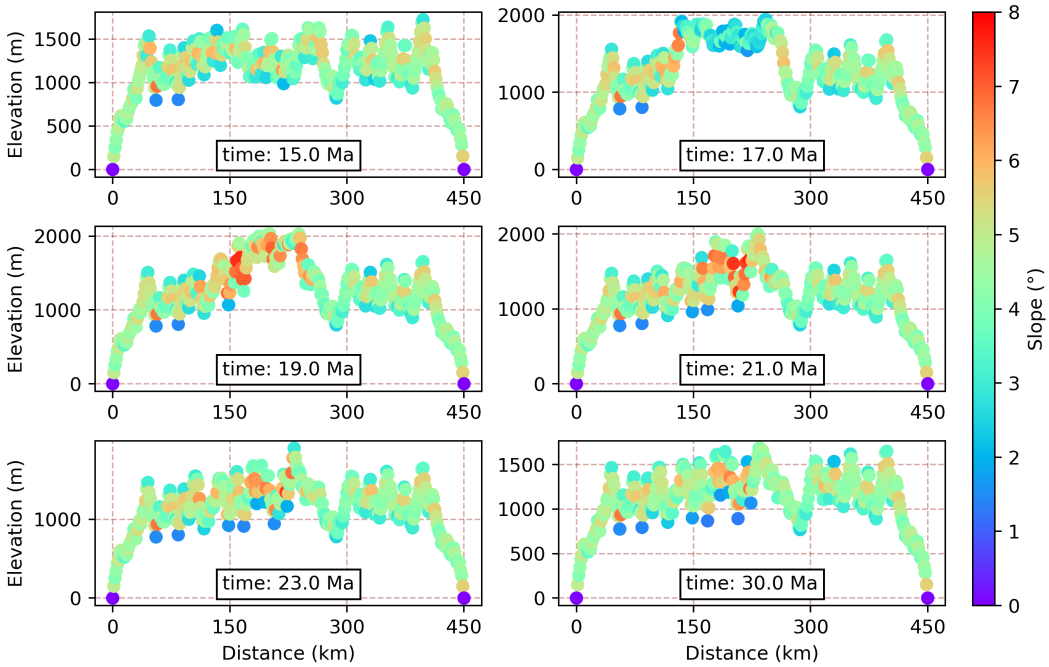

Supplementary Figure V.3: Swath profile plot of the slope and elevation in function of distance transversally to the model from 15 to 30 Myrs. Slope is represented with colours from dark blue (low values) to dark red (high values).

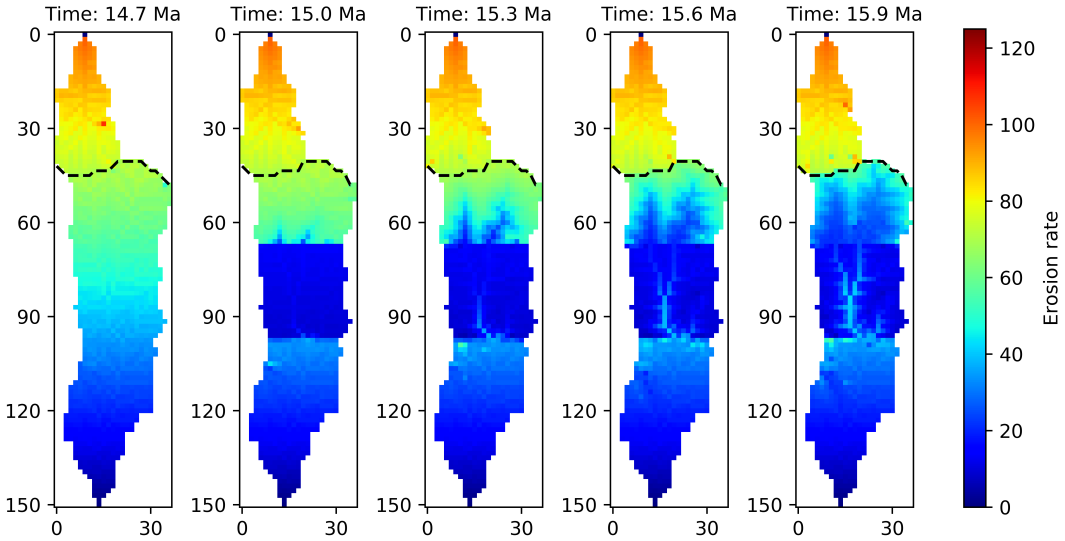

Supplementary Figure V.4: Erosion rate pattern from Fastscape algorithm for two adjacent catchments located northward and southward of the main drainage divide and impacted by the change of rock erodibility. Erosion rate is represented in both catchments by colours from dark blue (low value) to dark red (high value) at different time laps (14.7, 15.0, 15.3, 15.6 and 15.9 Myrs). Dash black lines correspond to the drainage divide between the two catchments. Lower rock erodibility are induced at 15 Myrs and located from 67.5 and 97.5 km. Initial erosion rate gradient are due to the gradient uplift from south to north. For first and last panels (i.e. 14.9), low erosion rate contrast indicates relatively stable drainage divide compared to high contrast and instable drainage divide for intermediate panels.

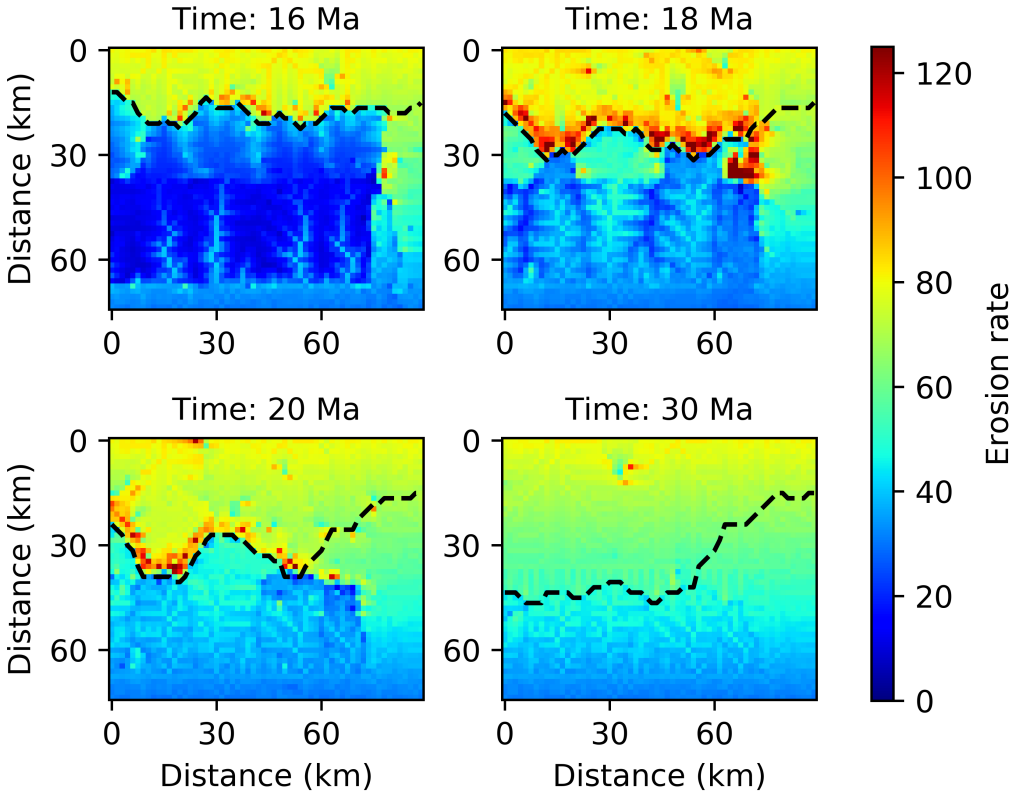

Supplementary Figure V.5: Erosion rate pattern from Fastscape algorithm for catchments crossing and not crossing through the exhumation of harder rocks. Erosion rate is represented in catchments by colours from dark blue (low value) to dark red (high value) at different time laps (16, 18, 20 and 30 Myrs). Dash black lines correspond to the main drainage divide between catchments.

Chapter VI

POST-OROGENIC SEDIMENT DRAPE IN THE NORTHERN PYRENEES EXPLAINED USING A BOX MODEL

Accepted as an article in "Basin Research" journal

Co-authors: Hugh D. Sinclair, Marc Naylor, Frédéric Christophoul and Mary Ford.

VI.1 Abstract

The transition to a post-orogenic state in mountain ranges has been identified by a change from active subsidence to isostatic rebound of the foreland basin. However, the nature of the interplay between isostatic rebound and sediment supply, and their impact on the topographic evolution of a range and foreland basin during this transition, has not been fully investigated. Here, we use a box model to explore the syn- to post-orogenic evolution of foreland basin/thrust wedge systems. Using a set of parameter values that approximate the northern Pyrenees and the neighbouring Aquitaine foreland basin, we evaluate the controls on sediment drape over the frontal parts of the retro-wedge following cessation of crustal thickening. Conglomerates preserved at approximately 600 m elevation, which is 300 m above the present mountain front in the northern Pyrenees are ca. 12 Ma, approximately 10 Myrs younger than the last evidence of crustal thickening in the wedge. Using the model, this post-orogenic sediment drape is explained by the combination of a sustained, high sediment influx from the range into the basin relative to the efflux out of the basin, combined with cessation of the generation of accommodation space through basin subsidence. Post-orogenic sediment drape is

considered a generic process that is likely to be responsible for elevated low-gradient surfaces and preserved remnants of continental sedimentation draping the outer margins of the northern Pyrenean thrust wedge.

VI.2 Introduction

Foreland basins are located at the outer edges of mountain belts (Dickinson, 1974). They are formed during mountain building and topographic growth. Flexure of the continental lithosphere is generated principally by topographic loads and controlled by the distribution of topography, internal density variations in the range and the flexural rigidity of the lithosphere (Beaumont, 1981; Jordan, 1981; Watts, 2001). The flexural basin forms the principle trap for sediments sourced from erosion of the neighbouring mountain range. Consequently, the stratigraphy, sedimentology and subsidence history of foreland basins contain an integrated record of orogenesis (Sinclair, 2012). Foreland basins have a typical asymmetric cross-section with a greater thickness at the orogenic margin and a wedge-shaped form that tapers out over the stable craton. The cratonic margin of a foreland basin is generally defined by the distal pinchout of the basin stratigraphy onto the region of forebulge uplift. During orogenesis, as a mountain range grows by increases in both width and elevation, it is expected that a large proportion of eroded sediment is trapped in the foreland basin (P. A. Allen et al., 1986; Sinclair & Naylor, 2012). However, transition to an inactive decaying mountain range results in a reduction of the topographic load on the lithosphere and an associated isostatic rebound of foreland basins implying a bypass of sediment through the foreland basin to more distal depocentres (Burbank et al., 1992; Cederbom et al., 2004; Champagnac et al., 2007).

A well documented example is the pro-foreland Ebro foreland basin of the Pyrenean system (Muñoz, 1992; Verges & Munoz, 1990). The Ebro basin is characterized by a period of continental conglomeratic deposition linked to a rapid phase of exhumation in the Central Pyrenean Axial Zone during Late Eocene-Early Oligocene times as demonstrated by low-temperature thermochronological data (Fitzgerald et al., 1999; Sinclair et al., 2005). The sediments generated during this period caused thick accumulations in the Ebro Basin that draped the South Pyrenean Thrust Belt (Coney et al., 1996) as a result of tectonic confinement and endorheic conditions (Fillon et al., 2013). It

has been proposed that piedmont aggradation for the Southern Pyrenees reduced the erosive capacity of rivers resulting in the development of high-elevation low-gradient surfaces within the internal zone of the belt (Babault, Van Den Driessche, et al., 2005). The presence of low-gradient surfaces on both side of the range (Babault, Van Den Driessche, et al., 2005; Bosch, Van Den Driessche, et al., 2016) has led to the proposal that similar processes were also active on the northern flank of the Pyrenees (Babault, Van Den Driessche, et al., 2005). However, there is no evidence for basin confinement in the north. A regional climatic control on base-level rise and subsequent fall across the mountain chain is also discussed by (Babault, Van Den Driessche, et al., 2005). Syn-tectonic conglomerates of the northern Pyrenees such as the Palassou and Toulouse Formations, were influenced by active structures of the Sub-Pyrenean Zone limiting their aggradation on the range. However, sedimentation continued during post-orogenesis with deposition of the undeformed Upper Carcassonne Group (i.e. Late Oligocene-Early Middle Miocene) which onlaps and seals structures of the northern Pyrenean flank (Ortiz et al., 2020; Rougier et al., 2016; Serrano et al., 2006). This raises the question of what controlled the accumulation of this drape during post-orogenic conditions (i.e. during isostatic rebound), and how this may have influenced the topography of the system.

Several studies have explored the effect of piedmont aggradation on the large-scale range topographic evolution by both numerical (Baldwin et al., 2003; Carretier & Lucazeaut, 2005; Pelletier, 2004) or analogue modelling (Babault, Bonnet, Crave, et al., 2005; Babault et al., 2007). Experiments show that piedmont sedimentation plays an important role on the timescale of lowered denudation rates by reducing range relief and hillslope gradients at high altitude (Babault, Bonnet, Crave, et al., 2005; Pelletier, 2004). However, our understanding of why piedmont sedimentation occurs during the onset of post-orogenic isostatic rebound of the thrust wedge and foreland basin is unclear.

Underpinning the transition to a post-orogenic state is the competition between erosion and crustal thickening. The balance of these processes determines the timing and magnitude of isostatic rebound and hence subsidence versus uplift of the foreland basin. It is expected that any change in the parameters controlling the balance of erosion versus crustal thickening of the range will impact the general vertical movements, topographic evolution of the foreland basin and sediment flux into surrounding depocentres, for example, continental margins. In order to explore these interactions, we take full

advantage of a simplification of the system represented in a box model that has been previously applied to the growth and decay of mountain belt/foreland basin systems (Tucker & van der Beek, 2013). In a series of experiments we simulate a counter-intuitive increase in sediment aggradation at the mountain front during the transition from syn- to post-orogenesis. We focus our analysis on the northern retro-wedge and retro-foreland Aquitaine Basin, and use this case study to define a range of parameter values for the model. We find a correlation between predicted post-orogenic sediment drape of the model, and the evidence of post-orogenic, late Miocene conglomerates draping the North Pyrenean Frontal Thrust. We conclude that an initial signal of post-orogenic decay of mountain belt/foreland basin systems is the aggradation of coarse and proximal sediments draping the frontal parts of the thrust wedge without the need for external forcing such as sediment ponding or changes in climate.

VI.3 Geologic setting of the Northern Pyrenees

VI.3.1 Pyrenean tectonics

The Pyrenean mountain belt is a doubly-vergent collisional orogen that constitutes a westerly segment of the Alpine-Himalayan belt caused by the closure of the Tethys Ocean (Roure et al., 1989). The Pyrenees form a linear east-west orographic barrier (450 km-long and 150 km-wide) between Spain and France with a steep and wet flank in the Northern Pyrenees compared with a gentler and dryer flank in the Southern Pyrenees. Its formation results from convergence between the Iberian micro-plate and the European plate from late Cretaceous time (i.e. 84 Ma) to early Miocene time (i.e. 20 Ma) (Roest & Srivastava, 1991). The Pyrenean mountain belt can be divided into different tectonic units (Figure VI.1; Muñoz, 1992; Seguret, 1972; Vergés et al., 2002). The South Central Pyrenean Thrust Belt comprises three main thrust sheets (Sierra Marginales, Montsec and Boixols) of mainly Mesozoic carbonate platform and siliciclastic Paleogene rocks (Muñoz, 1992). The Axial Zone in the central and eastern Pyrenees, comprises thick Precambrian and Paleozoic metamorphosed sedimentary successions intruded by Variscan granitoid massifs (Muñoz, 1992; Verges & Munoz, 1990). The North Pyrenean Thrust Belt (NPTB) involves Variscan basement massifs and Mesozoic to lower Eocene sedimentary cover rock. Two foreland basins associated with the Pyrenean orogeny developed simultaneously: the Ebro pro-foreland basin

(sensu Naylor and Sinclair, 2008) situated on the under-thrusting Iberian plate (Muñoz, 1992) and the Aquitaine retro-foreland basin situated on the over-thrusting European plate (Bourrouilh et al., 1995; Brunet, 1986).

Despite a large volume of research on the kinematic reconstruction of the Iberian plate with respect to the European plate, the total amount of shortening, the kinematics and timing and the rate of convergence are still a subject of debate (Beaumont et al., 2000; Macchiavelli et al., 2017; Mouthereau et al., 2014). Total amount of shortening of the Iberian plate indicates about 180 km of convergence (Olivet, 1996; Rosenbaum et al., 2002; Sibuet et al., 2004) and increasing from west to east (Vergés et al., 2002). However in the Central Pyrenees, different amounts of shortening have been proposed to interpret geological structures along the ECORS deep seismic line. Beaumont et al. (2000) estimates shortening of 160 km compared with Roure et al., (1989) and Mouthereau et al. (2014) who respectively indicate 100 and 92 km of shortening across the Central Pyrenees. Macchiavelli et al. (2017) proposes a N-S shortening of 125 km.

Estimation of shortening rates also varies in the Central Pyrenees: Mouthereau et al., (2014) indicates that the most rapid shortening happened during the onset of convergence at 80-60 Ma (3.5 mm/yr) followed by a period of constant shortening at 2.0 mm/yr. In contrast, Beaumont et al., (2000) model an initial convergence from late Cretaceous to Eocene time of 2.0 mm/yr followed by an increase of shortening rate of 4 mm/yr during Oligocene time. Macchiavelli et al., (2017) proposes a more complex shortening rate history but in better agreement with the model of Beaumont et al., (2000) for the Cenozoic history. Grool et al., (2018) use cross-section restoration and subsidence analyses to quantify convergence rates and find good accordance with the convergence rates from Macchiavelli et al., (2017).

Following the main phase of orogenesis, the eastern Pyrenees and Aquitaine basin have been affected by extensional tectonics related to the opening of the Gulf of Lyon during Oligocene-Miocene time (L. Jolivet et al., 2015).

VI.3.2 Exhumation of the central Pyrenees

The main phase of syn-orogenic exhumation in the Pyrenees has been documented in the Central Axial Zone and North Pyrenean Zone by an extensive data set of bedrock thermochronological ages (Figure VI.2). The first evidence of bedrock cooling was dated at about 55 Ma in the Northern Pyrenees using apatite and zircon fission track data

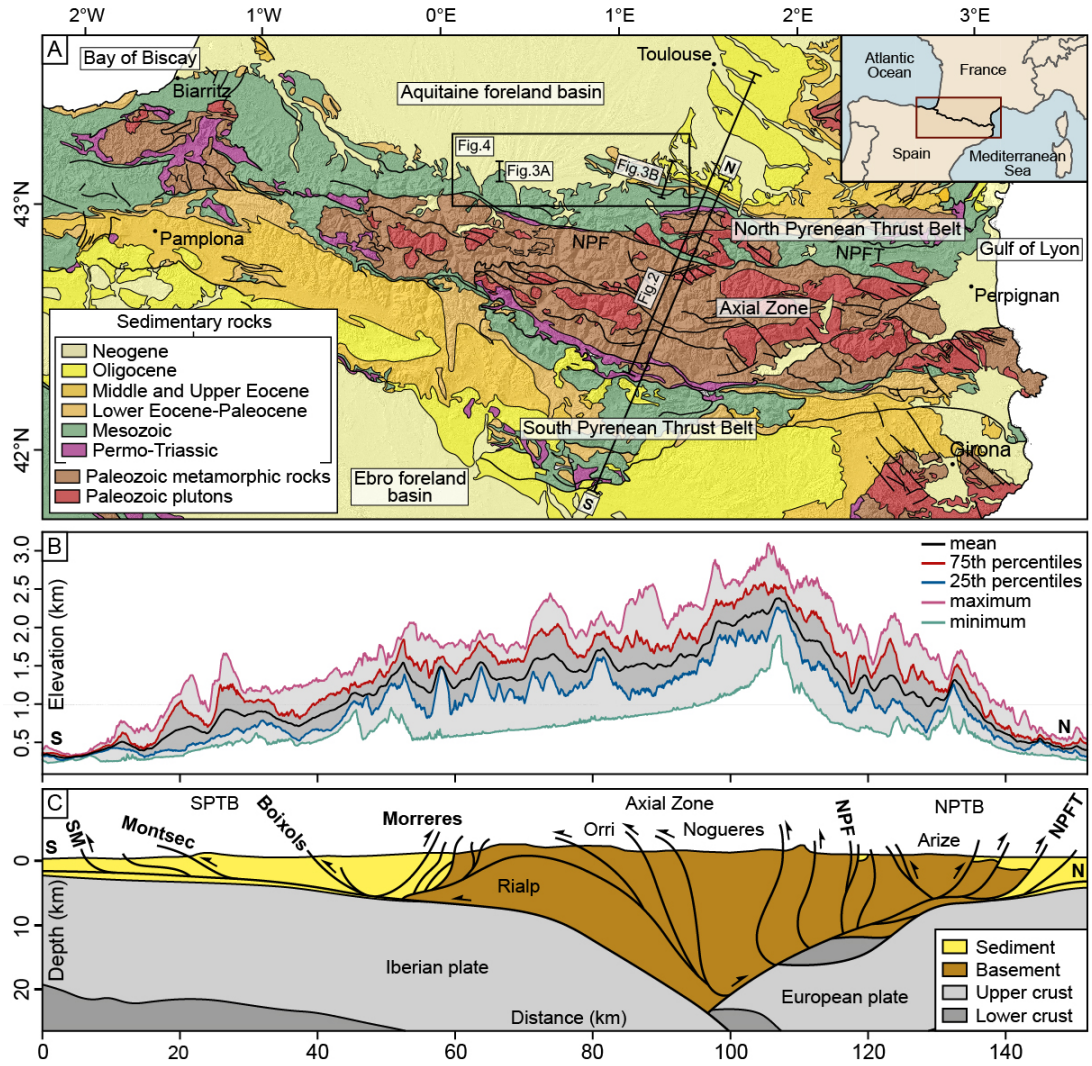

Figure VI.1: Geology of the Pyrenean system. A) Geologic map of the Pyrenees from the 1:1000000 BRGM geological map of France draped on a hillslope map from an SRTM digital topography with a resolution of 30 m. Black lines refer to locations of the elevation swath profile and geologic cross-section (panel B and C), the chronostratigraphic plot of Figure VI.2 and geologic cross-sections of Figure VI.3. Black square refers to the location of Figure VI.4. Cities are indicated by black dots. B) Swath profile of the central Pyrenees showing the mean (black lines), 75th percentile (red line), 25th percentile (blue line), maximum (magenta line) and minimum (cyan line) elevation. C) Simplified geologic cross-section of the central Pyrenees modified after Muñoz (1992); the distinction of basement and sediment relate to the contrasting densities used in the box model. NPF: North Pyrenean Fault. NPFT: North Pyrenean Frontal Thrust. SPTB: South Pyrenean Thrust Belt. NPTB: North Pyrenean Thrust Belt.

(Fitzgerald et al., 1999; Morris et al., 1998; Sinclair et al., 2005; Vacherat et al., 2016; Yelland, 1990). The main phase of exhumation is recorded during Mid-Eocene and Oligocene times by apatite fission track and Apatite helium data (Fitzgerald et al., 1999; Gibson et al., 2007; Metcalf et al., 2009; Sinclair et al., 2005). The main cooling phase is diachronous in the Central Pyrenees with exhumation younging from north to south (Fitzgerald et al., 1999; Sinclair et al., 2005). This diachroneity is interpreted as the record of an initial phase of structural inversion in the Northern Pyrenees followed by the progressive migration of deformation toward the south. Inverse modelling of thermochronological data indicate that cooling slowed significantly after 30-25 Ma (Bernard et al., 2019; Gibson et al., 2007) with the latest cooling in the Barruera massif located in the southern Axial Zone, which records the growth of the antiformal stack from 36 to 20 Ma (Sinclair et al., 2005; Gibson et al., 2007). Young cooling ages (i.e. 10-20 Ma) record local late exhumation in the southern Pyrenees (Gibson et al., 2007; Jolivet et al., 2007). Inverse modelling of a compilation of zircon and apatite fission track and apatite helium ages (Bernard et al., 2019) indicate that the transition from syn-orogenic shortening to post-orogenic quiescence in the Central Pyrenees is also diachronous and youngs southward (Figure VI.2).

VI.3.3 Stratigraphy of the Aquitaine Basin

As predicted by models of retro-foreland basin development (Naylor & Sinclair, 2008; Sinclair, 2012), the Aquitaine Basin preserves the full stratigraphic record of Pyrenean growth summarized in Figure VI.2 (adapted from Ford et al., 2016). Much of the western and central basin is superimposed on a pre-orogenic rifted crust. Sedimentation began during minor Permo-Triassic rifting between the Iberian and European plate; the sedimentary succession comprises red sandstones, evaporites and shallow marine deposits (Rougier et al., 2016). The Jurassic and Cretaceous periods were dominated by marine carbonate, marl and dolomite deposition (Biteau et al., 2006). During the principal rifting phase from Aptian to early Cenomanian a thick succession of deep marine clastics (Black Flysch group) and rim carbonates (Pierrelys group) was deposited in a series of distinct depocentres created under a transtensional regime (Debroas, 1990).

The Upper Cretaceous is dominated by marine flysch and marl sedimentation of the Grey Flysch Group deposited during post-rift thermal subsidence, followed by the Petites Pyrénées and Plantaurel Groups, which record accelerated subsidence during

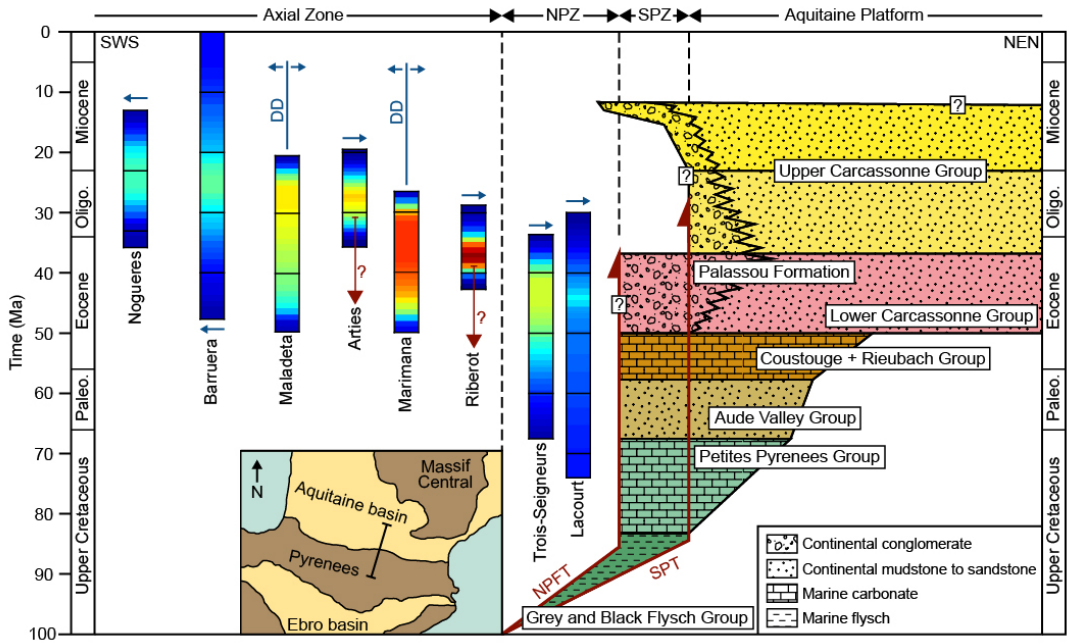

Figure VI.2: Relation between exhumation in the Pyrenean range and sedimentation in the north retro-foreland Aquitaine basin from Upper Cretaceous to Miocene time. Relative cooling rates based on thermochronology from Bernard et al., (2019) in the Axial Zone and North Pyrenean Zone is plotted (red: high cooling rate; blue: low cooling rate). Stratigraphy of the Aquitaine basin is adapted from Ford et al., (2016) and Rougier et al., (2016). Blue lines indicate the drainage divide position while blue arrows indicate flow water direction. Red lines indicate the main thrusts and their time of activity. NPFT: North Pyrenean Frontal Thrust. SPT: Sub-Pyrenean Thrust. NPZ: North Pyrenean Zone. SPZ: Sub-Pyrenean Zone.

early convergence between the Iberian and European plates (Ford et al., 2016; Monod et al., 2014; Rougier et al., 2016). A period with low tectonic subsidence during the early Paleocene (i.e. 66-59 Ma) is recorded by continental clastic deposits in the east (Aude Valley Group) and westward younging shallow marine deposits (Rieubach group). A second phase of subsidence starting during late Palaeocene times is first recorded by a short -lived marine incursion from the west across the whole foreland basin. In the eastern Pyrenees, sedimentation became predominantly continental during late Ypresian time (Ford et al., 2016) with deposition of the Carcassonne Group, while marine conditions continued further west. This marine-continental transition migrated as the basin infill prograded westward. The Carcassonne Group comprises a continental succession of mudstones with variable volumes of conglomerates, sandstones and limestones. Conglomerates sourced from the orogen occur mainly in the Sub-Pyrenean Zone (SPZ), adjacent to the thrust front (Palassou Formation, Figure VI.2; Ford et al., 2016).

Post-orogenic stratigraphy of the Northern Pyrenees (i.e. latest Oligocene to Miocene times) is characterized by the upper Carcassonne Group (Rougier et al., 2016; Ford et al., 2016; including the Armagnac, Agenais and Toulouse Formations); these comprise a fine grained detrital continental succession consisting of carbonate-rich siltstones, marls, dolomites and limestones deposited in fluvial, palustrine and lacustrine environments (Ford et al., 2016). Micaschist and quartz-rich pebble to cobble conglomerates and mica-rich sandstones were deposited across the Sub-Pyrenean zone and along the thrust front (Rougier et al., 2016). Across the whole Aquitaine platform the upper Carcassonne Group displays a high and constant thickness. The undeformed Upper Carcassonne Group onlaps eroded folds and reverse faults of the Sub-Pyrenean Zone and seals the Sub-Pyrenean Thrust and North Pyrenean Frontal Thrust (Figure VI.3). This indicates that the Sub-Pyrenean Thrust and North Pyrenean Frontal Thrust ceased to be active around late Oligocene - early Miocene time.

Miocene sediments of the Upper Carcassonne Group can be found in the foothills of the range (Figures VI.1, VI.2 and VI.4) from 300 to 600 m with a mean elevation of 500 m. Sediment drapes that are thought to be of Miocene age are principally found on the central portions of the northern Pyrenees and correspond to the deposition of large alluvial fans. From west to east, Miocene sediments are found in the Adour, Lannemezan and Salat fans (Figure VI.4). Miocene sediments preserved along the Adour

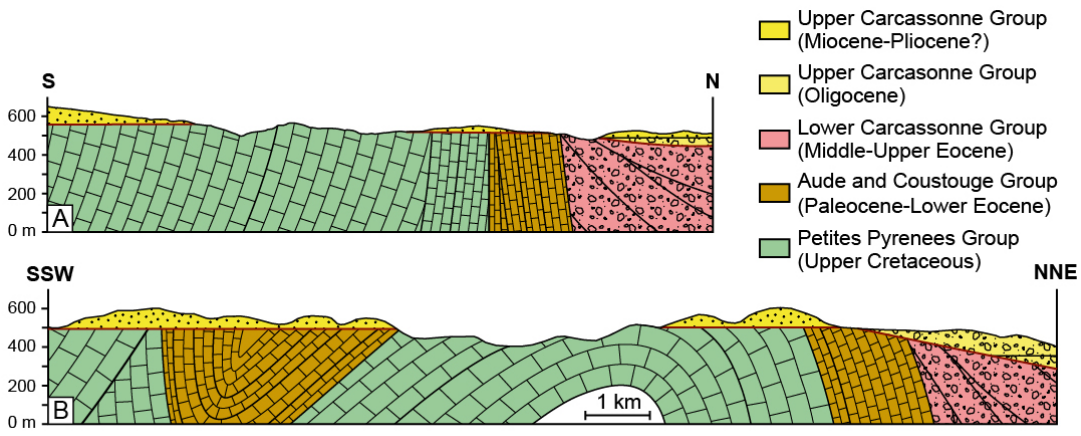

Figure VI.3: Geological cross-sections of the Central Northern Pyrenees showing draping by the Oligocene and Miocene sediments of eroded Pyrenean folds of the Sub-pyrenean Zone. A) Cross-section north to Bagneres-de-Bigorre from the 1:50000 BRGM geological map of Bagneres-de-Bigorre. B) Cross-section around St-Croix-Volvestre from the 1:50000 BRGM geological map of Le-Mas-d'Azil. Red lines on both cross-section highlight the stratigraphic unconformity recording the syn- to post-orogenic transition.

and Lannemezan fans show similar mean elevations of 500 to 550 m. The Lannemezan fan formed during middle to upper Miocene and Pliocene times and was abandoned when the Neste River was captured by the Garonne River during Quaternary times (Mouchené et al., 2017). Limited preservation of the Salat fan shows similar elevations to the Adour and Lannemezan fans, which suggests a similar mechanism of formation. As with the Lannemezan fan, the main stream network of the Salat fan was captured by the Garonne River. Miocene surfaces lying between the Lannemezan and Salat fan show lower mean elevations of 400 m (Figure VI.4). These surfaces could reflect deposition in a relatively lowland area between two fans.

VI.4 Methods

Our aim is to apply a parsimonious approach to the modelling of an orogenic system and associated foreland basin. Numerous models have been developed in order to investigate landscape evolution controlled by the coupling between tectonic deformation, flexural isostasy and surface processes. Two-dimensional models simulating mass transport from both fluvial and hillslope erosion through diffusive equations predict the relation-

ship between thrust deformation and sedimentation including grain-size distribution (Armitage et al., 2011; Flemings & Jordan, 1989; Simpson, 2006). More complex models take into account the dynamics of three-dimensional landscapes incorporating full fluvial networks (Garcia-Castellanos et al., 2002; Garcia-Castellanos et al., 2003; Johnson & Beaumont, 1995). Our approach aims to balance simplification of the system so that we can understand the main outputs of the model with approximating the first-order characteristics of the physical processes that govern the coupling in mountain range/foreland basin systems.

In order to investigate the coupling of topography and sediment flux during the evolution of a mountain range/foreland basin system, we use a modified version of a box-model introduced by Tucker and van der Beek (2013). We use this model to explore the relationship between crustal thickening, isostasy, topography and surface processes in the Pyrenees. The model analyses a single thrust wedge and foreland basin using two boxes that exchange mass with their surroundings by sediment transport, crustal thickening and tectonic accretion (Figure VI.5). Mass exchanges through the model follow two principles: i) mass conservation, which means that all material that exits a box has to be redistributed to its surroundings and ii) a correlation between topographic relief and sediment flux. The model is coupled with lithospheric flexural isostasy, which predicts the average deflection beneath the range and basin. Changes in the topographic elevation of the range (H_r)and basin (H_b) relative to a base level are then defined with the following equations:

$$\frac{dH_r}{dt} = (1 - \psi_r)\left(\frac{F_c + F_a - F_r}{\rho_r L_r}\right) \tag{VI.1}$$

$$\frac{dH_b}{dt} = \frac{F_r + -_a - F_b}{\rho_b L_b} - \psi_b \frac{d\eta_r}{dt} \tag{VI.2}$$

where F_c corresponds to accretionary flux of crustal rocks into the thrust wedge in response to plate convergence and underplating; F_a is the accretionary flux of basin sediments through frontal thrusting. F_r and F_b are respectively the sediment flux out of the range and sediment flux out of the basin; ρ_r and ρ_b are material density for the range and basin; L_r and L_b are the width of the range and basin perpendicular to their strike; η_r is the crustal thickness of the range and corresponds to $w_r + H_r$ where w_r is the isostatic deflection depth of the range; and ψ_r and ψ_b are flexural isostatic parameters for the range and basin respectively.

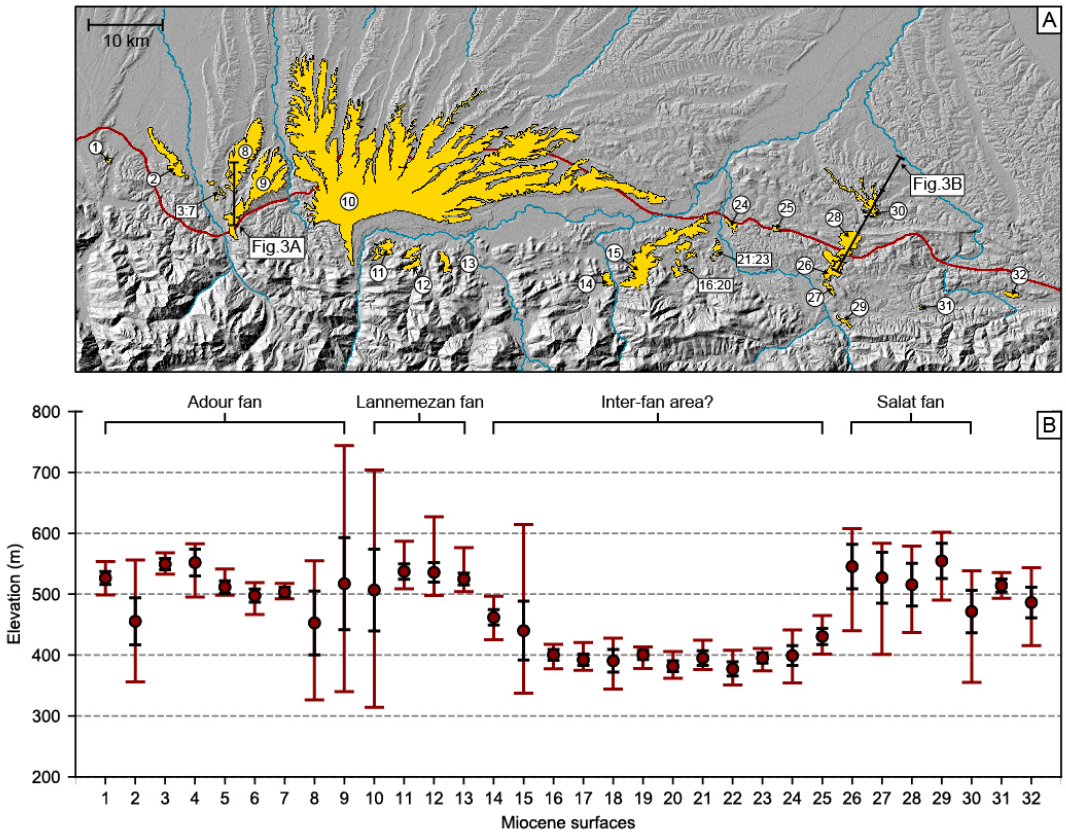

Figure VI.4: Miocene stratigraphic units of the northern Pyrenees at the boundary between the Aquitaine foreland basin and the Northern Pyrenean Thrust Belt highlighting their distribution across the Sub-Pyrenean Zone and North Pyrenean Zone. A) Middle Miocene-Pliocene surfaces (yellow areas) from the 1:50000 BRGM geologic map of Bagneres-de-Bigorre, Montrejeau, St-Gaudens, Le Mas-d'Azil, Aspet and St-Girons (Barrouquère et al., 1976; Paris et al., 1975; Paris & Monciardini, 1971; Souquet et al., 1977; Ternet et al., 1988) superimposed on a hillslope map from a SRTM with a resolution of 30 m. Black lines refer to locations of geologic cross-sections of Figure VI.3. B) Statistical elevation of the Miocene surfaces from West to East. The exact locations of the different Miocene surfaces are indicated in panel A. Red circles indicate the mean elevations. Black caps indicate the upper and lower standard deviations. Red caps indicate the maximum and minimum elevations.

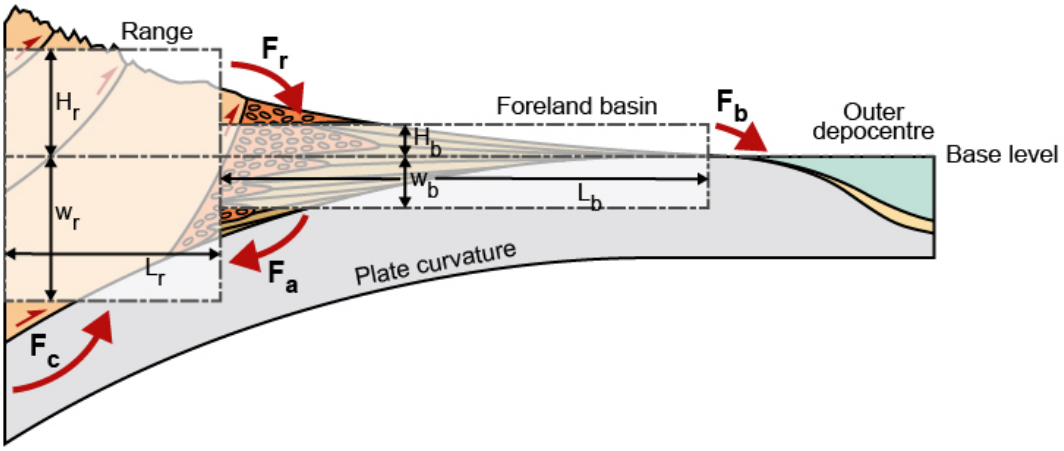

Figure VI.5: Cartoon summarising the main elements of the "box-model" modified after Tucker and van der Beek (2013). The orogenic system and associated foreland basin, shown schematically in the background are represented by two boxes, vertically positioned with respect to a horizontal base level that represents sea-level in this setting. F_r corresponds to the sediment flux from the range to the basin and F_b corresponds to the sediment flux from the basin to the outer depocentre. F_c corresponds to accretionary flux to the range due to plate convergence and underplating and F_a corresponds to accretionary flux from the basin to the range which in the case of many retro-wedge settings is negligible. All other parameters are defined in the text.

The accretionary flux (F_c) is expressed with the following equation:

$$F_c = V_c T_c \rho_r \alpha \tag{VI.3}$$

where V_c is the total convergence velocity, T_c is the thickness of the accreted rock. We introduce a new parameter α, which is not in the original model, where α is the proportion of the range formed by the pro- or retro-wedges (sensu Willett et al., 1993). Here, α is defined as L_r/L_t with L_t is the total width of the range and L_r the width of the retro or pro-wedge. It implies that in the model, the length of the retro or pro-wedge is strictly defined by the position of the drainage divide (Figure VI.1B). This study focuses on the growth of the retro-wedge of the northern Pyrenees where the topography is dominated by crustal rocks (Figure VI.2C), and where the accretionary flux from the basin (F_a) is negligible in terms of the contribution to topography. If modelling a pro-wedge such as the southern Pyrenees, an additional accretionary flux term is needed to describe the incorporation of accreted basin sediments to the front of the wedge; this is the same as equation (IV.3) but replaces ρ_r with ρ_b. The sediment flux from the range to the basin (F_r) and the sediment flux from the foreland basin (F_b) to the outer depocentre (Figure VI.5) are defined as follow:

$$\frac{F_r}{\rho_r L_r} = \frac{1}{\tau_r}(H_r - H_b) \tag{VI.4}$$

$$\frac{F_b}{\rho_b L_b} = \frac{1}{\tau_b} H_b \tag{VI.5}$$

where τ_r and $\tau_b$are the range and basin response times respectively and are defined as L^2/κ with L the width of the system and κ is the diffusive transport coefficient for the range or basin (P. A. Allen, 2008). We consider the ratio between the response times of the basin and the range to represent the relative efficiency of erosional processes between the basin and range. When the erosional response time ratio increases (i.e. the response time of the basin increases relative to the range), then the ability of the basin to transport sediment is less than that of the range to the basin, and so sediment will aggrade in the basin and the basin's elevation will increase. The average deflection beneath the range (ψ_r) and basin (ψ_r) are given by the following equation (Watts, 2001):

$$\psi_r = \frac{\rho_r}{\rho_m - \rho_b} \frac{e^{-2\lambda Lr}(e^{2\lambda Lr}(-1 + 4\lambda L_r) + cos(2\lambda L_r) - sin(2\lambda L_r))}{4\lambda L_r} \tag{VI.6}$$

$$\psi_b = \frac{\rho_r}{\rho_m - \rho_b} \frac{1}{3\pi - 4\lambda L_r} 2e^{-2\lambda Lr - 3\pi/4} (\sqrt{2} e^{\lambda Lr} (-1 + e^{2\lambda Lr}) cos(\lambda Lr) + e^{3\pi/4} (e^{2\lambda Lr} - cos(2\lambda Lr) + sin(2\lambda Lr))) \quad \text{(VI.7)}$$

with ρ_m is mantle density and λ is the inverse flexural parameter. The inverse flexural parameter λ is related to the flexural rigidity D and lithosphere elastic thickness T_e which correspond to the rigidity of the lithosphere and the ability of the lithosphere to support the mass of the range.

VI.5 Generic model sensitivity tests

We constructed a reference model with a simple history involving the growth, steady-state and decay of a retro-wedge/foreland basin system using general values for parameters derived from presently active mountain ranges (Batt & Braun, 1999). These values are $V_c = 10$ mm.yr^{-1}, $T_c = 20$ km, $T_e = 22$ km, $\alpha = 0.3$, response time ratio of 0.33 and duration of convergence deceleration T of 2.5 Myr. Convergence is active from 60 to 30 Ma followed by a post-orogenic stage lasting 30 Myrs (i.e. 30 to 0 Ma). These experiments are aimed at understanding the controls on elevation change in the foreland basin relative to the mountain belt. The main result is that in all model runs, there is a predicted increase in the elevation of the basin during the initial post-orogenic stage. This unexpected signal, already observed in Tucker and van der Beek (2013), can be broadly assigned to continued high rates of sediment supply from the mountain range due to the high elevation contrast between the range and basin, combined with the cessation of basin subsidence and hence of creation of accommodation space to capture the sediment. Diminution of accommodation space should therefore lead to sediment aggradation in the basin and contribute to the increase in basin elevation. We focus on this response through a set of experiments that aim to evaluate the principle controls on this signal (Figure VI.6).

The model indicates that different parameters influence the post-orogenic response of the foreland basin (i.e. after 30 Ma). The convergence velocity (V_c) and the thickness of the accreted rock (T_c), which govern tectonic accretion in the range, have a similar impact (Figure VI.6A and B). This impact is enhanced by an increase in topographic response of the foreland basin following cessation of convergence with higher V_c and T_c. The observed trend is due to higher uplift rate and sediment flux toward the basin. The difference in the modelled increase in the post-orogenic elevation of the foreland basin

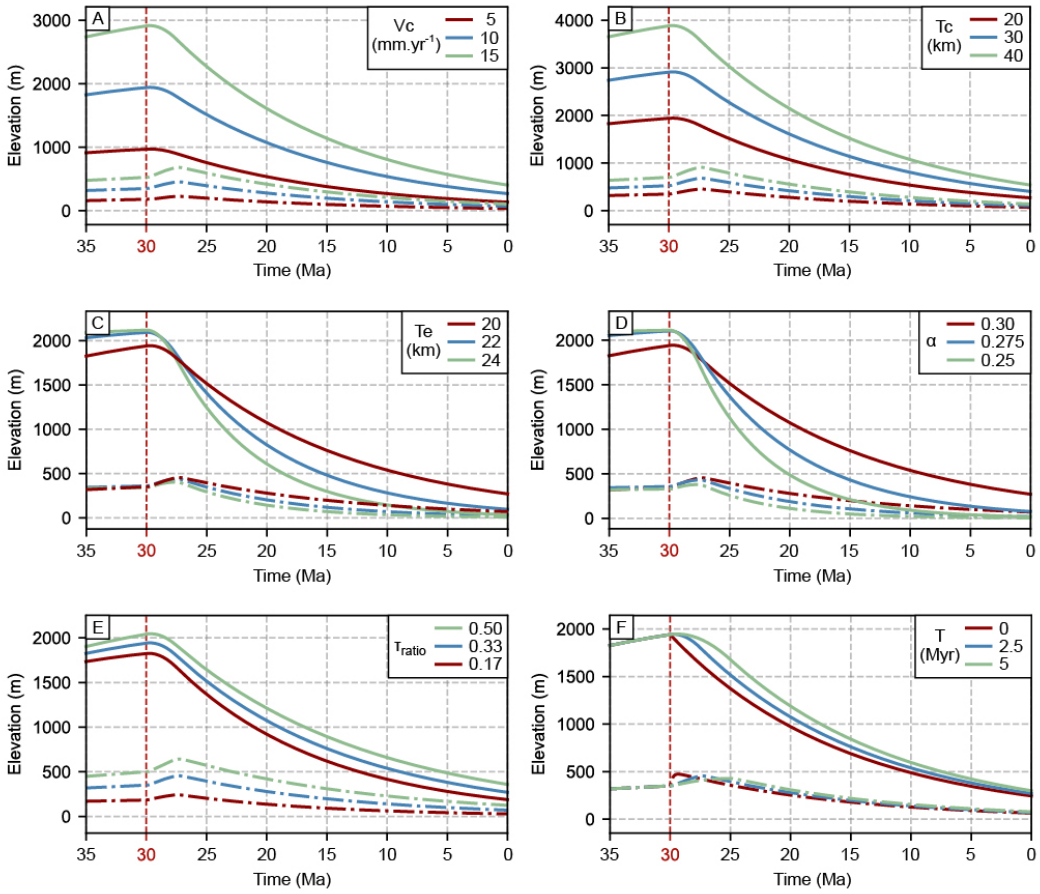

Figure VI.6: Effect of different parameters on the late syn- to post-orogenic mean elevation of a range (continuous lines) and adjacent foreland basin (dash lines). Convergence is active from 60 to 30 Ma and the transition from syn- to post-orogenesis is highlighted by a red vertical dashed line on each panel. The reference values that remain constant for the other models for each parameter is given in blue. A) Convergence velocity from 5 to 15 mm.yr^{-}1. B) Thickness of the accreted rock from 20 to 40 km. C) Lithosphere elastic thickness from 20 to 24 km. D) Relative proportion of the retro-wedge 0.25 to 0.30. E) Response time ratio between the range and foreland basin from 0.17 to 0.50. F) Time of convergence deceleration at the syn- to post-orogenic transition from 0 to 5 Ma.

is proportional to the maximum elevation achieved by the mountain range due to the changes of V_c or T_c. The lithosphere elastic thickness (T_e) corresponds to the rigidity of the lithosphere and the ability of the lithosphere to support the mass of the range. The relative proportion of the thrust-wedge width (α) compared with the full width of the range, directly determines the mass that loads the lithosphere and how much it will be flexed. These two parameters have therefore a similar effect on the foreland basin response. The main trend is a greater increase in elevation of the foreland basin after cessation of convergence at 30 Ma when T_e is lower or α is higher (Figure VI.6C and D). This effect is due to a greater flexural rebound after the cessation of convergence and therefore uplift of the basin after cessation of tectonics. Note that it takes longer for the system to reach steady-state during active convergence when T_e is lower or when α is higher. The inverse effect is also illustrated with a longer topographic elevation survival during the post-orogenic stage for both the range and the foreland basin when T_e is lower or when α is higher. The maximum elevation of the range at the end of the orogenic phase is also more important for an increase of the erosional response time ratio of the basin relative to the range, i.e. more sediment is delivered to the basin than can be removed (higher basin sedimentary influx than basin sedimentary outflux) (Figure VI.6E). Finally, the foreland basin shows different post-orogenic behaviour in response to varying the duration of convergence deceleration (T). When T increases, the basin elevation increase is lower, but elevation increases over a longer period (Figure VI.6F) as the isostatic rebound remains higher for a longer period of time.

In summary, the tendency for an increase in the elevation of the foreland basin relative to the range following the cessation of orogenesis is enhanced by: 1. Higher syn-orogenic convergence velocities; 2. Higher thickness of accreted material; 3. Lower lithosphere elastic thickness; 4. Higher proportion of range occupied by the retro-wedge; 5. A higher erosional response time ratio between the basin and the range; and 6. Shorter duration of convergence deceleration. We now apply the model to the northern Pyrenees using specific parameters and approximate the change in basin elevation of the modelled Aquitaine Basin during the transition to post-orogenesis. We explore the implications of this evolution for post-orogenic topography and stratigraphy of the Aquitaine Basin.

VI.6 Application to the Northern Pyrenees

VI.6.1 Northern Pyrenean parameters

We apply the model to the north Pyrenean case study using parameter values constrained by the geological history since the onset of active convergence (see section 2). As the construction of orogenic topography in the Pyrenean system started around Paleocene times, we set the model to run over 66 Myrs simulating the full Cenozoic evolution. The main phase of convergence runs from 56 to 23 Ma, and mimics the main phase of topographic growth in the Pyrenees, followed by post-orogenic decay during Neogene and Quaternary time (i.e. 23 to 0 Ma) (Figure VI.7). Tectonic accretion is simulated using a plate convergence velocity of 3.2 mm.yr^{-1} from 56 to 41 Ma, 2.4 mm.yr^{-1} from 41 to 34 Ma, 4 mm.yr^{-1} from 34 to 23 Ma and 0.2 mm.yr^{-1} from 23 to 0 Ma (Macchiavelli et al., 2017) and a thickness of accreted crustal material of 30 km (Muñoz, 1992). The proportion of the retro-wedge relative to the total range width of 150 km is defined by an alpha factor of 0.3 based on the modern position of the drainage divide in the central Pyrenees (Figure VI.1B). The lithosphere elastic thickness can vary from 15 to 40 km (Angrand et al., 2018; Brunet, 1986; Curry et al., 2019; Desegaulx et al., 1990). The transport coefficient is selected from values ranging from 100 to 5,000 m^2.yr^{-1} for the range and from 1,000 to 50,000 m2.yr^{-1} for the basin (Flemings and Jordan, 1989). Convergence deceleration starting at 23 Ma lasts from 2.5 to 7.5 Myrs.

VI.6.2 Inverse modelling approach

The applicability of the model to the north Pyrenean study is strengthened by an inverse modelling search for the most probable set of parameter values in order to replicate first order geologic data of the northern Pyrenees (Figure VI.7). The robustness of the different outputs is assessed by comparing them with: i) a maximum mean elevation of the range during orogenesis of about 2 km, which has been independently quantified both by 3D flexural deformation and stratigraphic restoration (Curry et al., 2019) and by oxygen stable-isotope records and morphologic-hydrologic modelling studies (Huyghe et al., 2012); ii) the estimated depth of the Aquitaine foreland basin at 23 Ma of about 4.5 km (Ford et al., 2016); iii) the present-day mean elevations of the Pyrenees and Aquitaine foreland basin of about 1.5 km (Curry et al., 2019) and 0.25 km respectively. This approach allows us to obtain results that reproduce the main geometric features

(i.e. range and basin topographic elevation and basin depth) of the Pyrenees (Figure VI.7).

In order to fully explore the parameter space during the inverse modelling search, a value is randomly chosen from a uniform distribution of the range of estimations of the controlling parameters (lithosphere elastic thickness, range transport coefficient, basin transport coefficient and convergence deceleration time). At each iteration, we calculate a root chi-square misfit function (χ) in order to measure the discrepancy between the observed (*obs*) data and the predicted (*pre*) results from the modified box-model:

$$\chi = \frac{1}{4}\sqrt{\frac{(H^{obs}_{r,max} - H^{pre}_{r,max})^2}{\delta H^{obs^2}_{r,max}} + \frac{(H^{obs}_{r,t0} - H^{pre}_{r,t0})^2}{\delta H^{obs^2}_{r,t0}} + \frac{(H^{obs}_{b,t0} - H^{pre}_{b,t0})^2}{\delta H^{obs^2}_{b,max}} + \frac{(w^{obs}_{b,t23} - w^{pre}_{b,t23})^2}{\delta w^{obs^2}_{b,t23}}} \tag{VI.8}$$

where $H_{r,max}$ is the maximum range elevation with uncertainty $\delta H_{r,max} = 0.2$ km; $H_{r,t0}$ is the modern range elevation with uncertainty $\delta H_{r,t0} = 0.15$ km; $H_{b,t0}$ is the modern basin elevation with uncertainty $\delta H_{b,t0}$= 0.025 km and $w_{b,t23}$ is the basin depth at 23 Ma with uncertainty $\delta w_{b,t23} = 0.45$ km.

VI.6.3 Inverse modelling results

From the initial grid space exploration of 100 000 iterations, the model proposes 500 solutions that converge towards a replication of the foreland basin depth, mean elevation of the range and basin and maximum elevation of the range with a misfit lower than 2 (Figure VI.8). The range of lithosphere elastic thickness in accepted models is 22.2±1.6 km. This value is in accordance with published lithosphere elastic thickness estimations for the northern Pyrenees. Brunet, (1986) and Desegaulx et al., (1990) calculate a lithosphere elastic thickness of 21.93 km and 15 to 20 km. Angrand et al., (2018) propose a lithosphere elastic thickness of 10 to 25 km that increases away from the range. Finally, Curry et al., (2019) estimate a lithosphere elastic thickness of 23 km.

Model results predict diffusive transport coefficient of 430±140 $m^2.yr^{-1}$ and 13200 ± 4400 $m^2.yr^{-1}$ for the range and the basin respectively. These values are in accordance with compiled transport coefficients from Flemings and Jordan (1989), which are of the order of 102-103 $m^2.yr^{-1}$ for the range and 104 $m2.yr^{-1}$ for the basin.

The duration of the deceleration in convergence impacts the timing and amount of elevation change of the basin (Figure VI.6F). However, this parameter cannot be quantified for the northern Pyrenees with available geological data. Therefore, we retain

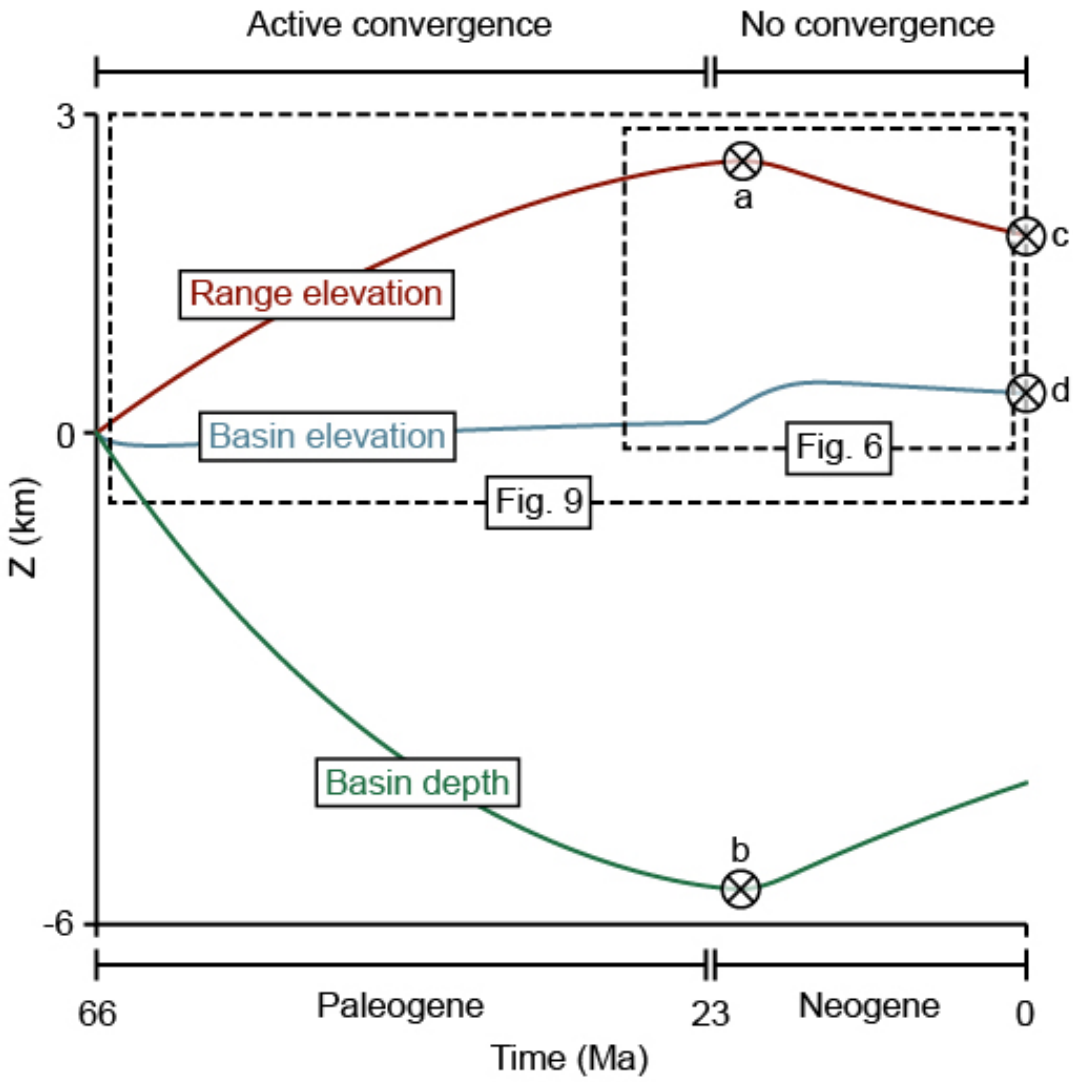

Figure VI.7: Schematic representation of the behaviour of measured parameters in the model during the evolution of an orogenic system from syn-orogenesis to post-orogenesis. For the Pyrenean case, active convergence occurred during Paleogene time. We highlight, with a circled x, the data from the model results that are compared with geologic data of the northern Pyrenees (a: maximum range elevation; b: depth of the basin at 23 Ma; c: present-day mean elevation of the range; d: present-day mean elevation of the basin). Note that for the generic experiments (Figure VI.6), the transition from active to no convergence is at 30 Ma. These schematic graphs are not to scale.

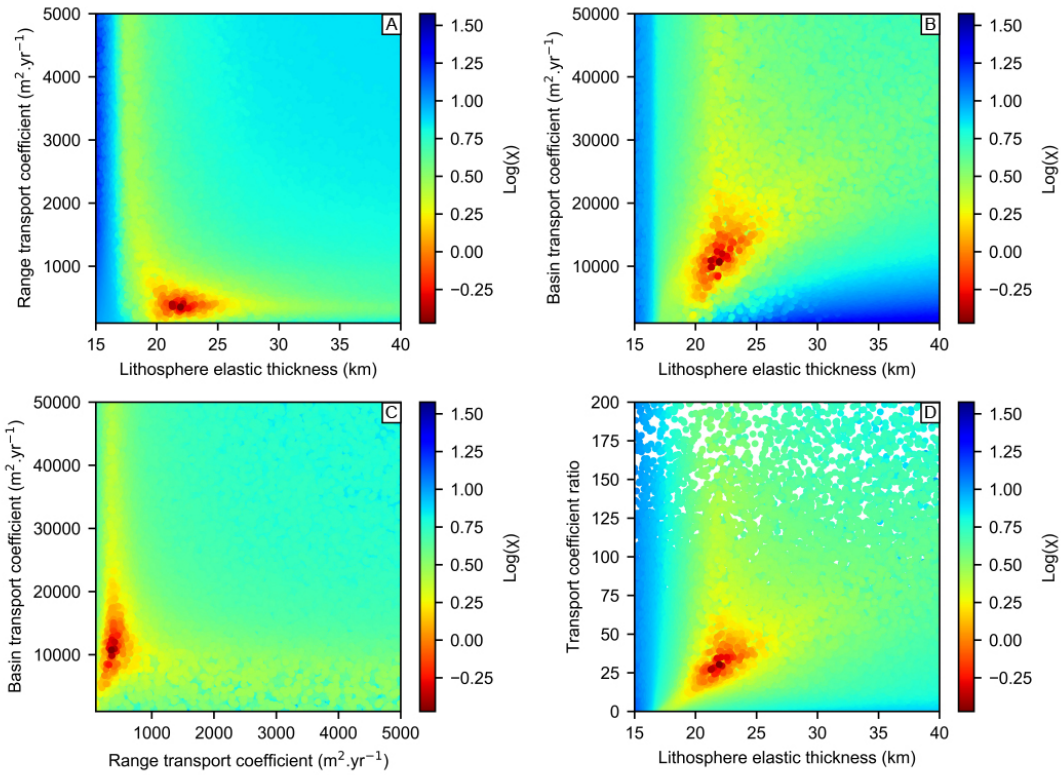

Figure VI.8: Misfit (χ results of the different model outputs for three varying parameters (i.e. lithosphere elastic thickness, range and basin transport coefficient). Each circles correspond to a single model results with a total of 100,000 iterations. For panel A (lithosphere elastic thickness versus range transport coefficient), B (lithosphere elastic thickness versus basin transport coefficient) and C (range versus basin transport coefficient), the 3D space misfit is plotted as a function of two parameters with a mean interpolation of the third parameters. For panel D (lithosphere elastic thickness versus transport coefficient ratio), the misfit is represented in 2D. Lower misfit (better models) is represented by warmer colours and higher misfit (worse model) is represented by colder colours. Model results are accepted for a misfit lower than $log(2) = 0.301$ (i.e. red to dark yellow dots).

the full range of proposed durations of convergence deceleration given by acceptable model solutions (i.e. 2.5 to 7.5 Myrs) (Supplementary Figure VI.1).

VI.6.4 Modelled topography results

During the main Pyrenean orogenic phase (i.e. 56 to 23 Ma), the modelled range topography increases through time in proportion to the convergence velocity (Figure VI.9A). The elevation of the range reaches a maximum mean topography of 1980 m at the end of the syn-orogenic phase (23 Ma), which is comparable to the predicted maximum elevation of the range derived in other studies (see above). The post-orogenic phase (i.e. 23 to 0 Ma) results in an exponential decline in the mean elevation of the range to a mean value of 1400 m at the end of the model run. This value also approximates the present mean elevation of the Pyrenean range.

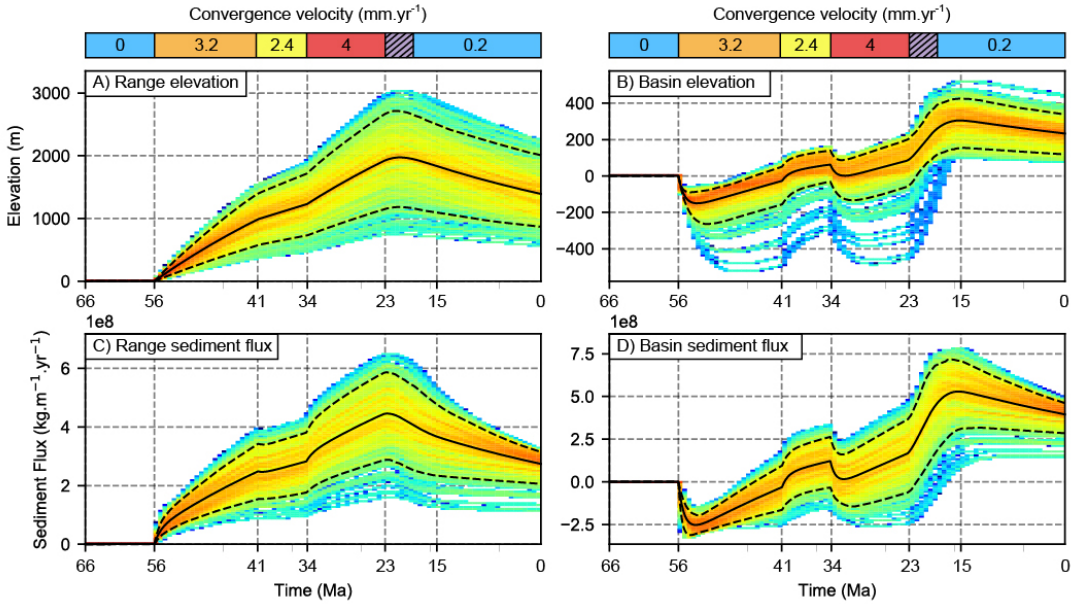

Figure VI.9: Model results for A) range elevation, B) basin elevation, C) sediment flux from the range to the basin and D) sediment flux from the basin to the outer basin through time. Colours correspond to the density model results with a misfit less than 0.15 from 100 000 iterations. Black lines correspond to the mean results while dash lines correspond to the upper and lower two standard deviations. Convergence velocity values through time are indicated above the four main panels. The purple dashed area indicates the phase of convergence deceleration starting at 23 Ma and lasting between 2.5 and 7.5 Myrs.

The elevation of the modelled foreland basin (Figure VI.9B) increases through time during the orogenic phase. Short periods of elevation decrease caused by the dominance of subsidence over sediment influx are recorded at the initiation of the higher convergence velocity phase (i.e. at 56 and 34 Ma). In contrast elevation increase is recorded at the onset of a phase of lower convergence velocity (i.e. 41 Ma). During the first stages of evolution of the modelled foreland basin, mean elevation of the basin remains negative meaning that it is underfilled. At 42 Ma, elevation becomes positive and the basin becomes filled by sediment coming from the range. The basin is again briefly underfilled from 33 to 29 Ma due to acceleration in the convergent velocity. The transition to post-orogenesis in the modelled foreland basin is marked by an increase in mean elevation from 85 to 310 m followed by a general decrease to the end of the model run. The phase of increased elevation following cessation of convergence lasts up to 8 Myrs (i.e. 23 to 15 Ma); this represents a period of basin elevation increase by isostatic rebound uplift and sediment aggradation. The mean elevation of the basin at the end of the model is 240 m, which is comparable to the present day mean height of the Aquitaine Basin.

VI.7 Discussion

VI.7.1 Model predictions for the post-orogenic Aquitaine Basin

Topographic and sediment flux predictions in the box model used here are underpinned by a number of assumptions relating to the coupling of thrust wedge development and foreland basin sedimentation: (i) The first main assumption is the application of a rectangle box-model to a wedge-shape mountain range; this approach is considered a first-order approximation for the interaction of the range and basin. The box-model is not intended to resolve localised deformation such as frontal accretion or internal thickening within a wedge which generate higher frequency, punctuated surface process signals (e.g. Naylor and Sinclair, 2007) (ii) We assume a constant lithospheric elastic thickness for the European lithosphere. Studies have demonstrated however that lithosphere rigidity can vary through space (Angrand et al., 2018) but also through time (Curry et al., 2019). The generic model suggests this could impact the magnitude of the flexural rebound and therefore the elevation increase signal of the foreland basin during the post-orogenic phase. (iii) Variable erosion or deposition is not resolved by the model in either the

range or foreland basin. Erosion rate and resulting sediment flux is defined by the elevation contrast between the mean height of the range and that of the basin. Whilst this does not reflect variations such as hillslope gradient, which assert an important control on erosion (Ahrens et al., 1970; Montgomery & Brandon, 2002) it could be seen as an approximation of channel steepness which underpins the stream power model for fluvial incision (e.g. Tucker and Whipple, 2002). Similarly, variations in the grainsize of the sediment are not accounted for here, but would affect the efficiency of sediment transport in the foreland basin (e.g. Duller et al., 2010). (iv) General evolutionary models coupling tectonics and surface processes indicate the development of a generally straight drainage divide roughly parallel with the mountain front and tracking the thickest part of a doubly-vergent wedge located above the S-point (Koons, 1990). The exact location of the drainage divide fluctuates around the S-point because of frontal accretion and underplating (Willett et al., 2001). The model approximates only the first order evolution of a thrust wedge/foreland basin system and therefore cannot address this natural variability.

Evolution of the foreland basin in the model is governed by three main processes: i) the flexure of the lithosphere, which can be negative when subsidence is active or positive during isostatic rebound, ii) the sedimentary influx from the range, which governs sediment accumulation of the foreland basin and iii) the sedimentary efflux from the basin to the outer basin, which simulates erosion and removal of material from the basin. During late syn-orogenesis, the majority of the sediment flux from the range is trapped in the foreland basin because of active lithospheric flexure (Figures VI.10A and VI.11A). Despite ongoing subsidence, foreland basin elevation increases because the sediment influx from the range to the basin is slightly greater than the accommodation space created by flexure (Figures VI.9B and VI.11A). However, tectonics and frontal thrust movements during active convergence should limit the formation of a sedimentary drape over the front of the range. During the early post-convergence phase (i.e. 23 to 20 Ma), the combination of reduced flexural subsidence, continued high sedimentary influx from the range and low basin outflux results in aggradation (Figure VI.10A) and hence an increased mean elevation of the foreland basin. Cessation of tectonic activity in the thrust wedge in combination with basin aggradation should allow sediments to drape and onlap the edge of the range (Figure VI.11B). From 23 Ma onwards, the topography of the range decays, causing an isostatic flexural rebound in

both the range and the foreland basin (Figures VI.10A and VI.11C). Increase in the elevation of the foreland basin is now (i.e. 20 to 15 Ma) mainly due to the isostatic uplift component. The sediment outflux from the foreland basin to the outer basin becomes more important and counterbalances the influx of sediment into the basin, thus limiting aggradation and onlap onto the range (Figures VI.10 and VI.11C). From the onset of post-orogenesis (i.e. 23 Ma) to the maximum elevation of the foreland basin (i.e. 15 Ma), the contribution of the sediment influx from the range to the basin is more important than the sediment outflux from the basin (Figure VI.8B). This phase of about 8 Myrs is mainly characterized by a decrease of range elevation and an increase of basin elevation (Figures VI.9AB and VI.10C). During the second part of the post-orogenic phase, sediment outflux from the foreland basin to the outer basin becomes more important than the sediment influx from the range, and this is associated with flexural rebound and uplift of the basin leading to net erosion (Figures VI.10 and VI.11D). Even if this last stage of erosion of the foreland basin is significant, evidence of sediment onlap onto the range from the early post-orogenic phase may be preserved as remnants on the mountain range (Figure VI.11D). This second phase from 15 Ma to present-day is characterized by a reduction in elevation of both the range and foreland basin (Figures VI.9AB and VI.10C).

VI.7.2 Topographic evolution and post-orogenic sediment drape in the Pyrenees

Topographic evolution of the Pyrenees during the Cenozoic period was recently modelled by Curry et al., (2019) through an inversion of the flexural subsidence of the foreland basins. They identify a limited decrease for the mean range elevation (i.e. 1800 to 1500 m) during the post-orogenic evolution, which is compatible with our results (Figure VI.9A). Our model results predict two main phases of topographic growth during Early Eocene and Early Oligocene times, controlled mainly by the convergence plate models of Macchiavelli et al., (2017). At contrary the main phase of topographic growth inferred by Curry et al., (2019) is limited to the Late Eocene based on the Aquitaine foreland basin record. A possible explanation for this main difference during Early Eocene is that we use a constant thickness of accreted material through time (i.e. 30 km). However, it is possible that the lithosphere thickness was lower during the Early Cenozoic limiting topographic growth during this period (Ford et al., 2016).

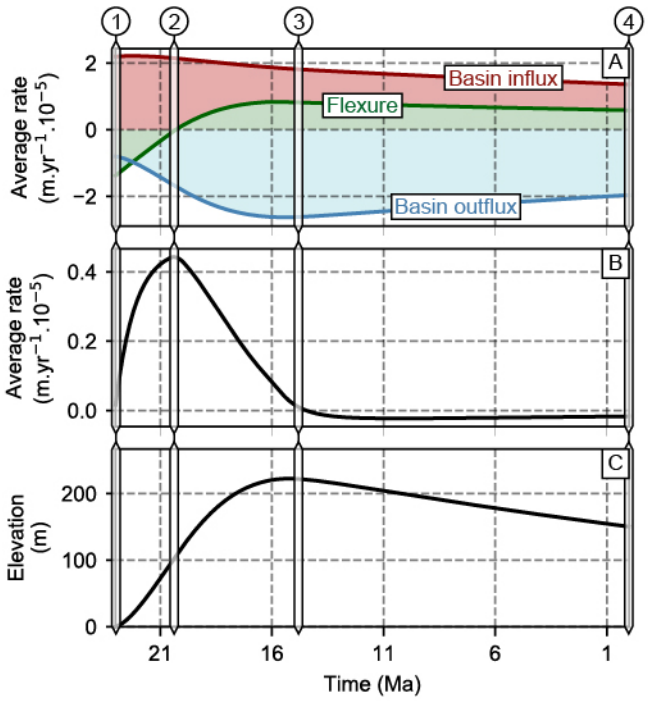

Figure VI.10: Contributions to the elevation of the foreland basin, inferred from the average result of accepted models, during the post-orogenic phase (i.e. 23 to 0 Ma) given as rates of range and basin sediment flux and basin flexure (A andB) and elevation (C) after cessation of active convergence. A) Contribution of different processes as rates through time. Red line corresponds to the sediment flux from the range to basin (basin influx). Blue line corresponds to the sediment flux from the basin to the outer basin (basin efflux). Basin outflux is negative as it contributes negatively to the elevation of the foreland basin. Green line corresponds to the flexure or vertical movement of the lithosphere or top basement (flexural subsidence or isostatic uplift). B) Basin elevation change evolution calculated as the sum of positive versus negative components in A. Positive or negative ratio means an increase or decrease respectively in elevation of the basin. C) Elevation accumulation of the basin through time from 23 to 0 Ma calculated from the integral of the average elevation change in panel B.

Our model predicts a maximum increase in mean elevation of about 220 m due to isostatic rebound and sediment aggradation above the previous height of the basin during the early post-orogenic stage (Figure VI.10C) with a maximum mean elevation of 310 m (Figure VI.9B). If we assume a constant slope through the foreland basin from the front ranges to a distal pinchout that approximates sea-level, the mean elevation of 310 m would correspond to a maximum elevation of 620 m on the proximal part of the basin. With a basin width of about 120 km across the Aquitaine Basin, this would imply a mean fluvial gradient of 0.32° across the basin, which is comparable to many modern fluvial gradients in similar settings (Blair & McPherson, 1994). This elevation range is in accordance with the maximum observed elevations of remnant modern Miocene sediment drapes in the Northern Pyrenees (i.e. 600-700 m) (Figure VI.4).

The transient period during which the elevated foreland basin existed at the beginning of the post-orogenic stage (Figure VI.9B) in the model is in agreement with the geological age of the sediment cover observed on the Sub-Pyrenean Zone and North Pyrenean Zone. The model predicts an elevated basin from 23 to 15 Ma, which corresponds to the Early and Middle Miocene age (Figure VI.2) of the sediment drape on the Northern Pyrenees (Figure VI.4). The age of the maximum elevation of the foreland basin as predicted by the model (15 Ma) is a little older than the youngest sedimentation in the Northern Pyrenees foothills, which is estimated as Upper Serravallian (i.e. 12 Ma). Recently, Ortiz et al., (2020) propose that generally the proximal part of the Aquitaine Basin during Early Miocene (i.e. 23-15 Ma) was in by-pass and sedimentation occurred mainly in the distal part of the basin. Our model cannot spatially differentiate if sedimentation occurs in the proximal or distal part of the basin. However, there is evidences of Early and Middle Miocene sediments on the Sub-Pyrenean Zone and proximal part of the Aquitaine Platform which strengthen our model results and geological data correlation.

VI.7.3 High elevation, low gradient surfaces and morphologic evolution of the Northern Pyrenees

Many of the locations that preserve sediment drapes are also characterised by low gradient surfaces in the landscape, which form an important feature of the Pyrenees on both sides of the range. It has been proposed that these surfaces result from planation near sea level and later uplift (Calvet & Gunnell, 2008; Gunnell et al., 2009)

or that they originally formed at high elevation by the inhibition of erosion because of piedmont sedimentation (Babault, Van Den Driessche, et al., 2005; Coney et al., 1996; Mellere, 1994). The latter has been demonstrated for the southern Pyrenees where thick continental deposits filled the Ebro foreland basin (Babault, Van Den Driessche, et al., 2005) and reached elevations up to 1700 m in the Southern Pyrenean Thrust Belt. However, comparably high signals are ambiguous in the northern Pyrenees. Elevation increase by post-orogenic sediment aggradation from our modelling results suggests a maximum mean elevation of 300 m above the deformation front (Fig. 9B) meaning an elevation of about 600 m at the Pyrenean range front. Projection of this surface into the range can explain the presence of low-gradient surfaces in the northern Pyrenees, which are generally at lower elevations compared to the southern Pyrenees (Bosch et al., 2016).

The topographic survival of post-orogenic mountain ranges has been an enigmatic problem (Baldwin et al., 2003). The Pyrenees still preserve high topography despite cessation of major convergence at the beginning of Miocene times (i.e. 23 Ma; Muñoz et al., 1992; Beaumont et al., 2000). Early research predicted a short period of topographic survival in a mountainous area by dividing the mean elevation of mountain ranges by the average denudation rate (Gilluly, 1955). Simple models of landscape evolution demonstrate an exponential decay of mountain topography (Stephenson, 1984; Tucker and van der Beek, 2013). Several factors can inhibit post-orogenic topographic decay such as resistant lithologies, isostatic response of the lithosphere and controls on fluvial erosion (Baldwin et al., 2003). One of the most important aspects of fluvial erosion in the persistence of topography is the relative roles for detachment-limited (i.e. bedrock) versus transport-limited (i.e. alluvial) river conditions. Numerical landscape evolution models incorporating both detachment and transport-limited conditions predict a transition to the transport-limited condition during post-orogenesis (Baldwin et al., 2003; Whipple, 2002) and an increase in decay times. Our results support this hypothesis where alluvial aggradation during the post-orogenic period inhibits channel erosion and allows for a longer persistence of mountain topography.

The current model cannot resolve fluvial transport and erosion, but the combination of low range transport coefficients and low lithosphere elastic thickness predicted by the inverse modelling (Figure VI.8) allow us to simulate limited topographic decay for the northern Pyrenees (Figure VI.9A) as proposed by Babault et al., (2005) and Curry et

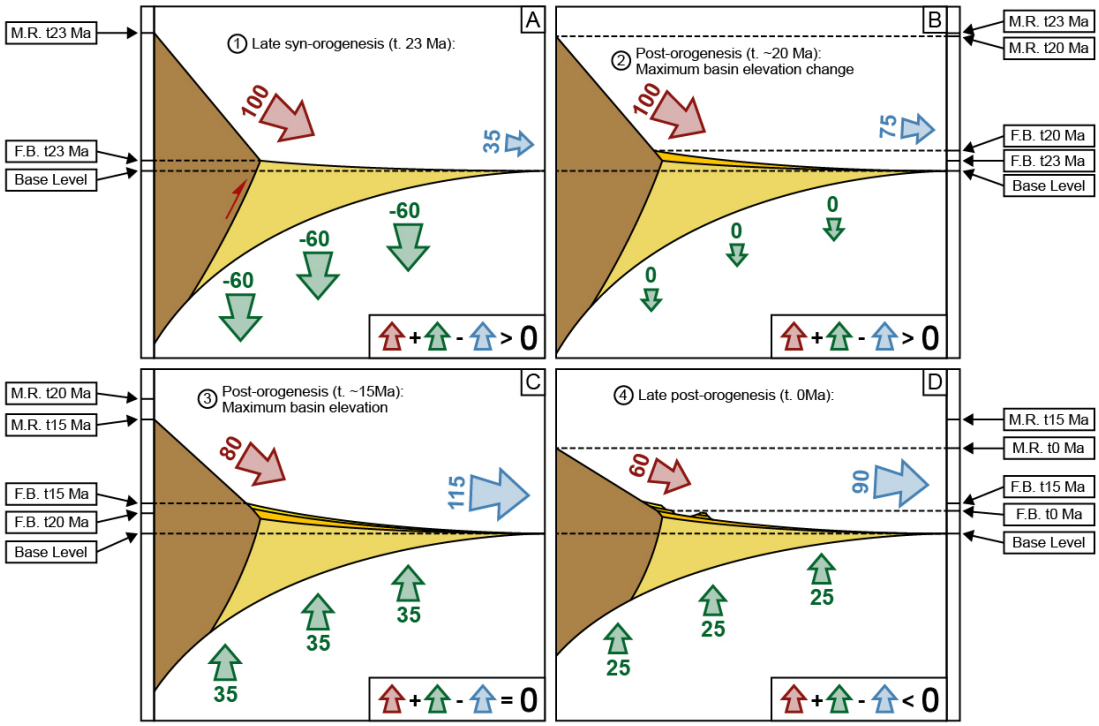

Figure VI.11: Schematic representation of the system evolution for four time frames during late syn- to post orogenesis. A) Late syn-orogenesis at 23 Ma. B) Early post-orogenesis at 20 Ma when positive elevation change of the foreland basin is maximum. C) Post-orogenesis at 15 Ma when elevation of the foreland basin is maximum. D) Post-orogenesis at 0 Ma when elevation of both the range and foreland basin are decreasing. Numbers for each time frame correspond to those in Figure VI.10 (i.e. 23, 20, 15 and 0 Ma). Red, green and blue arrows correspond respectively to the basin influx, lithospheric flexure and basin outflux with identical colours to those in Figure VI.10. Numbers next to the arrows indicate a percentage contribution to the basin elevation based on Figure VI.10. Black arrows indicate elevation of the range and foreland basin for the specific time frame and for the previous step for comparison.

al., (2019). Low values for the range transport coefficient limit erosion in the range and coupled with a low lithosphere elastic thickness imply an important isostatic effect to maintain topography in the thrust wedge through time. Relatively stable topography in the range is also maintained during the post-orogenic stage because of the elevated foreland basin (Figures VI.9B and VI.10), which reduces relief and inhibits erosion (Figure VI.9C) as demonstrated in Babault et al., (2005).

VI.7.4 Evidences from other mountain belt-foreland basin systems

The North Alpine Foreland Basin (NAFB) of the European Alps records deposition from Maastrichtian to middle Miocene. Sedimentation in the NAFB can be summarized by an early deep-water stage with deposition of the Ultrahelvetic flysch and North Helvetic flysch (P. A. Allen et al., 1991) followed by shallow-marine/continental flysch and molasse (P. A. Allen et al., 1991). First-order behaviour of the basin is characterized by an underfilled basin before mid-Oligocene time following by an overfilled basin (Sinclair & Allen, 1992). In Late Miocene, the basin switched from deposition to erosion as tectonic activity ceased because of isostatic rebound (Cederbom et al., 2004). The NAFB does not seem to record an overfilled trend but rather an erosive unconformity during the transition. The extent to which any deposits younger than the preserved uppermost Upper Freshwater Molasse (ca. 11 Ma; Bolliger, 1998) draped the outer margins of the thrust belt is unclear due principally to poor preservation. The NAFB and northern European Alps are a pro-wedge system with relatively higher convergence rate compare to the Pyrenean system. Isostatic rebound at the post-orogenic transition, also enhanced by a wetter climate change (Cederbom et al., 2004) and resulting unroofing erosion of the NAFB, may have been too high to preserve a deposition signal during the early post-orogenic phase. This suggest that the preservation of early post-orogenic sediments in foreland basins can be quite rare and requires relatively stable conditions without major external forces changes.

Although the NAFB does not preserved early post-orogenic sediments, an increase of sediment flux out of the system is recorded in surrounding depositional settings (i.e. Rhône Delta, Rhône Graben and North Sea; (Kuhlemann, 2000). This pattern is in agreement with our results, which indicate important erosional efflux out of the basin after cessation of tectonics (Figure VI.9D). Similar pattern is recorded for the Northern Pyrenees with an increase of sediment accumulation in the deep-sea plain of the margin

(i.e. Bay of Biscay) during the post-orogenic period (Ortiz et al., 2020).

VI.8 Conclusions

1. Topographic and geologic data from the northern Pyrenees characterise a post-orogenic sediment drape on the northern thrust wedge that corresponds to the deposition of large alluvial fans. Sediment drapes form low gradient-high elevation surfaces that range in elevation from 300 to 600 m.

2. Experiments using a box model which approximate dynamic coupling of a thrust wedge/foreland basin system indicate that at the transition from syn-orogenesis to post-orogenesis, sediment flux from the range remains high, while basin subsidence slows; this combination results in accumulation of continental sediment that can drape over the frontal portions of thrust wedges.

3. By deriving a set of parameter values that approximate the north Pyrenean thrust belt and Aquitaine Basin system, we propose a mechanism of early post-orogenic aggradation to explain the deposition of middle Miocene conglomerates that drape the Sub-Pyrenean zone and North Pyrenean Thrust Belt. The model suggests that this aggradation of the Aquitaine Basin continued to an elevation of 620 m on the proximal part of the foreland basin and lasted 8 Ma following the onset of post-orogenesis (i.e. 23 to 15 Ma). Miocene sediments that drape and seal tectonic structures of the Sub-Pyrenean Thrust and North Pyrenean Frontal Thrust are found at high elevations up to 600-700 m. Our modelling results indicate that these features are explained without evoking external forcing such as trapping of sediment or climate change.

4. Inverse modelling results explain the persistence of Pyrenean topography long after cessation of orogenic activity by low lithosphere elastic thickness and low range transport coefficient parameters and a reduction of relief between the range and basin.

VI.9 Supplementary Material

VI.9.1 Grid search and resulting space misfit

The inverse modelling used in this study can be resume as a grid search in order to replicate first-order geological evidences of the Northern Pyrenees. The multi-dimensional grid space is defined by different parameters controlling the model evolution (i.e. lithosphere elastic thickness, range and basin transport coefficients and time of convergence decrease). At each iteration, a random value is chosen for each parameter and a misfit is attributed. Misfit results for each iteration are calculated by comparing the discrepancy between the model results and the observed data. Observed data are: (i) the Aquitaine foreland basin depth of 4.5 km at 23 Ma based of subsidence analyses by Ford et al., (2015); (ii) the Pyrenean range elevation defined by a maximum mean elevation of 2 km and an actual mean elevation of 1.5 km. The maximum mean elevation is constrained by paleotopographic studies from oxygen stable-isotope records (Huyghe et al., 2012) and 3D flexural modelling results (Curry et al., 2019). (iii) A mean actual elevation of the Aquitaine basin of 0.25 km. The four observed data have the same contribution on the final misfit result.

As mentioned in the main text, the time of convergence decrease does not have impact on the misfit and is demonstrated by the Supplementary Figure VI.1 where there is no trend between time of convergence decrease and misfit. The consequence is that the misfit can be represented in a three dimension space defined by the lithosphere elastic thickness, the range transport coefficient and the basin transport coefficient (Supplementary Figures VI.2 and VI.3).

VI.9.2 Model cross-section evolution

The model (Tucker and van der Beek, 2013) supports lithospheric flexural isostasy and allow to predict depth for both the range and foreland basin through time. Thickness of the basin can then be access by the sum between the basin topography and basin flexure (Supplementary Figure VI.4). In the case of the range, the total thickness is access by the sum of the range topography, range flexure and initial convergence thickness (i.e. 30km) (Supplementary Figure VI.5).

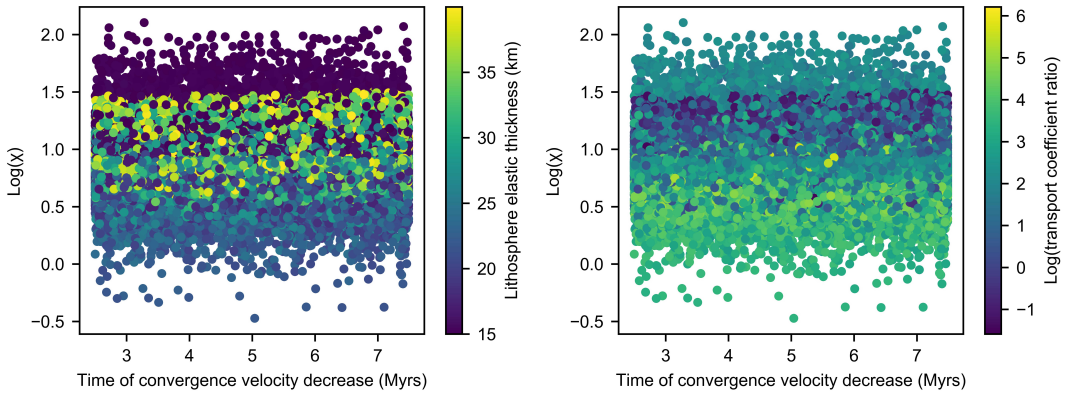

Supplementary Figure VI.1: Effect of the convergence velocity decrease time on the misfit results. Left: plot of the misfit in function of the time of convergence decrease. Color is scaled on the lithosphere elastic thickness. Right: plot of the misfit in function of the time of convergence decrease. Color is scaled on the transport coefficient ratio logarithm. Both panels show no major trends between the misfit and time of convergence decrease.

VI.9.3 Range and foreland basin mass change

The two dimensional mass of the range can be access by the following equation:

$$m_r = (H_r + w_r)L_r\rho_r \tag{VI.9}$$

With H_r the elevation of the range; w_r the depth of the range; L_r the length of the range; and ρ_r the material density of the range. Any change of mass for the range can be calculated by subtracting the tectonic accretion flux (F_c) from the range sediment flux (F_r):

$$\frac{dm_r}{dt} = F_c - F - r \tag{VI.10}$$

Same properties can be translated to the foreland basin with the basin mass (m_r):

$$m_b = (H_b + w_b)L_b\rho_b \tag{VI.11}$$

With H_b the elevation of the basin; w_b the depth of the basin; L_b the width of the basin and ρ_b the material density of the basin. Change of mass through time for the basin can be calculating by subtracting the range sediment flux (F_r) from the basin sediment flux (F_b):

$$\frac{dm_b}{dt} = F_r - F - b \tag{VI.12}$$

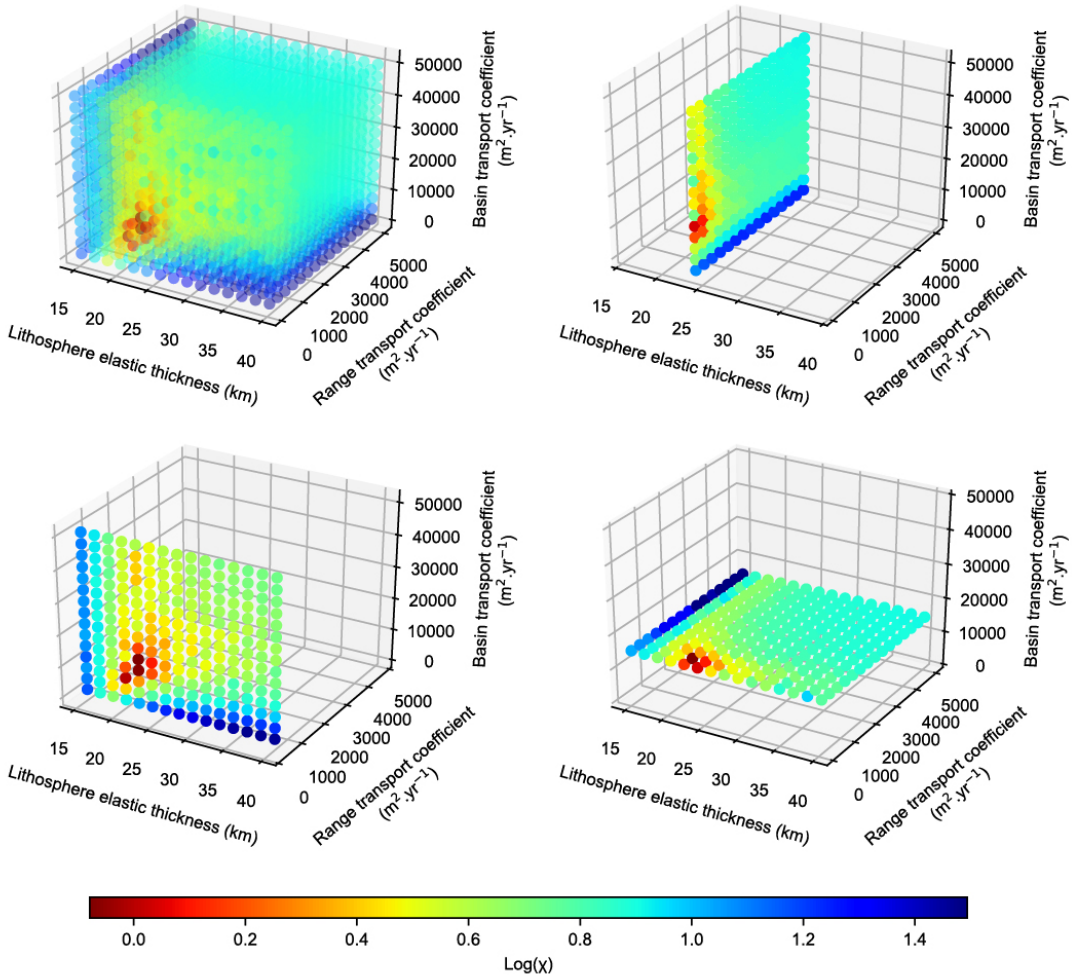

Supplementary Figure VI.2: Three dimensional plot of the interpolated misfit in function of the lithosphere elastic thickness, range transport coefficient and basin transport coefficient. Upper left: Overall misfit plot through the space grid. Upper right: Misfit slice through the space grid depending a fixed lithosphere elastic thickness. Lower left: Misfit slice through the space grid depending a fixed range transport coefficient. Lower right: Misfit slice through the space grid depending a fixed basin transport coefficient. Each slices are focused on the lower misfit area.

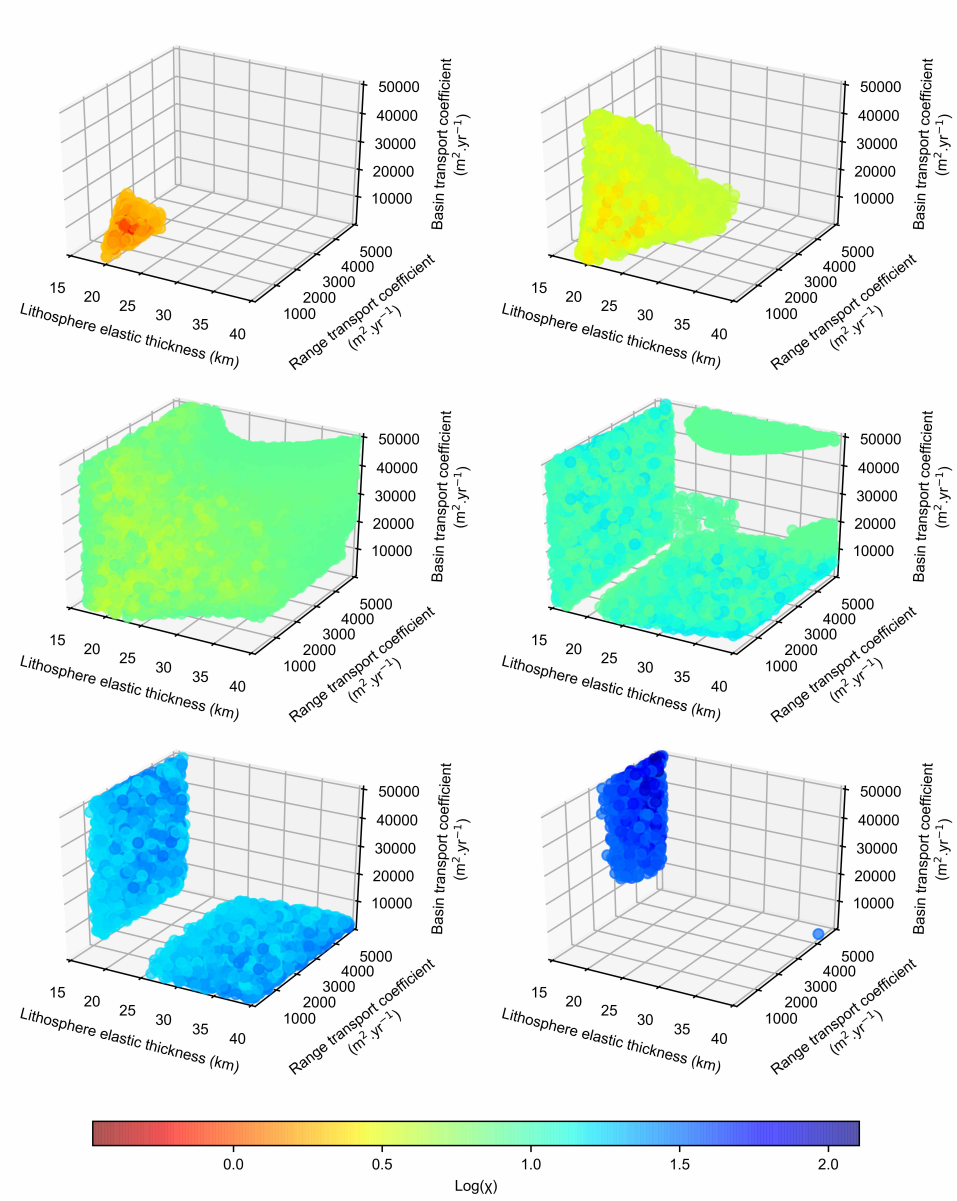

Supplementary Figure VI.3: Three dimensional plot of the misfit in function of the lithosphere elastic thickness, range transport coefficient and basin transport coefficient for different range of misfit. Upper left: misfit plot with values lower than 0.3. Upper right: misfit plot with values ranging from 0.3 to 0.6. Middle left: misfit plot with values ranging from 0.6 to 0.9. Middle right: misfit plot with values ranging from 0.9 to 1.2. Lower Left: misfit plot with values ranging from 0.9 to 1.5. Lower right: misfit plot with values higher than 1.5.

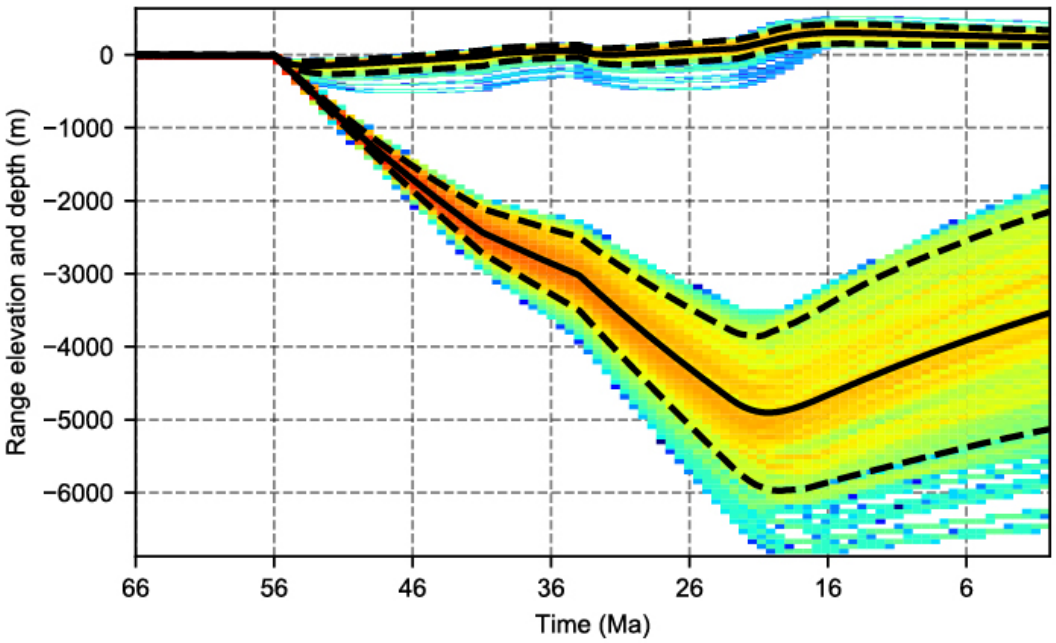

Supplementary Figure VI.4: Basin topography and flexure thought time.

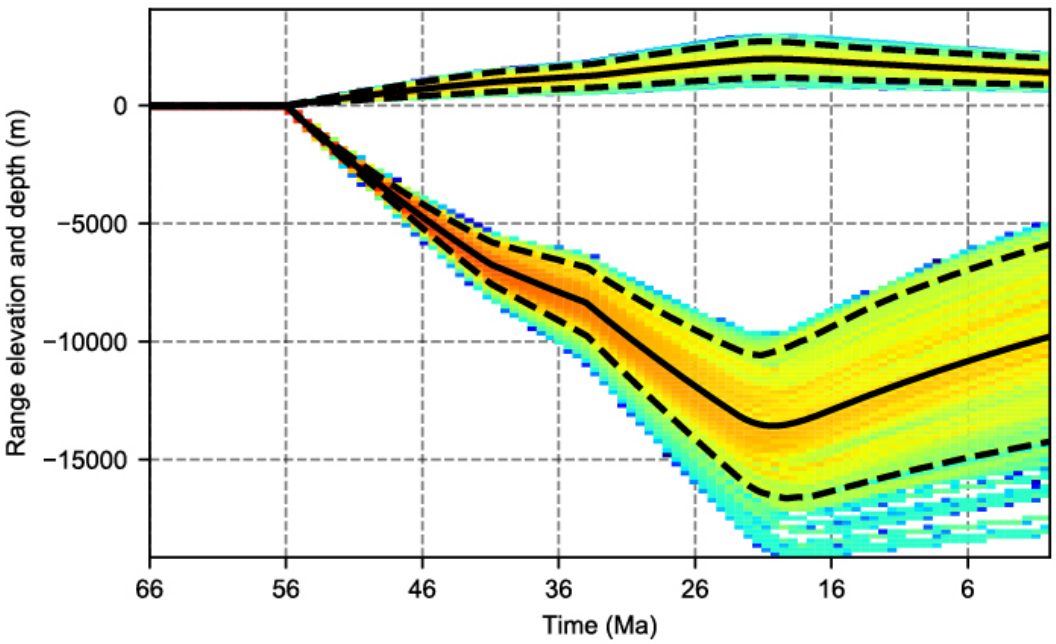

Supplementary Figure VI.5: Range topography and flexure through time.

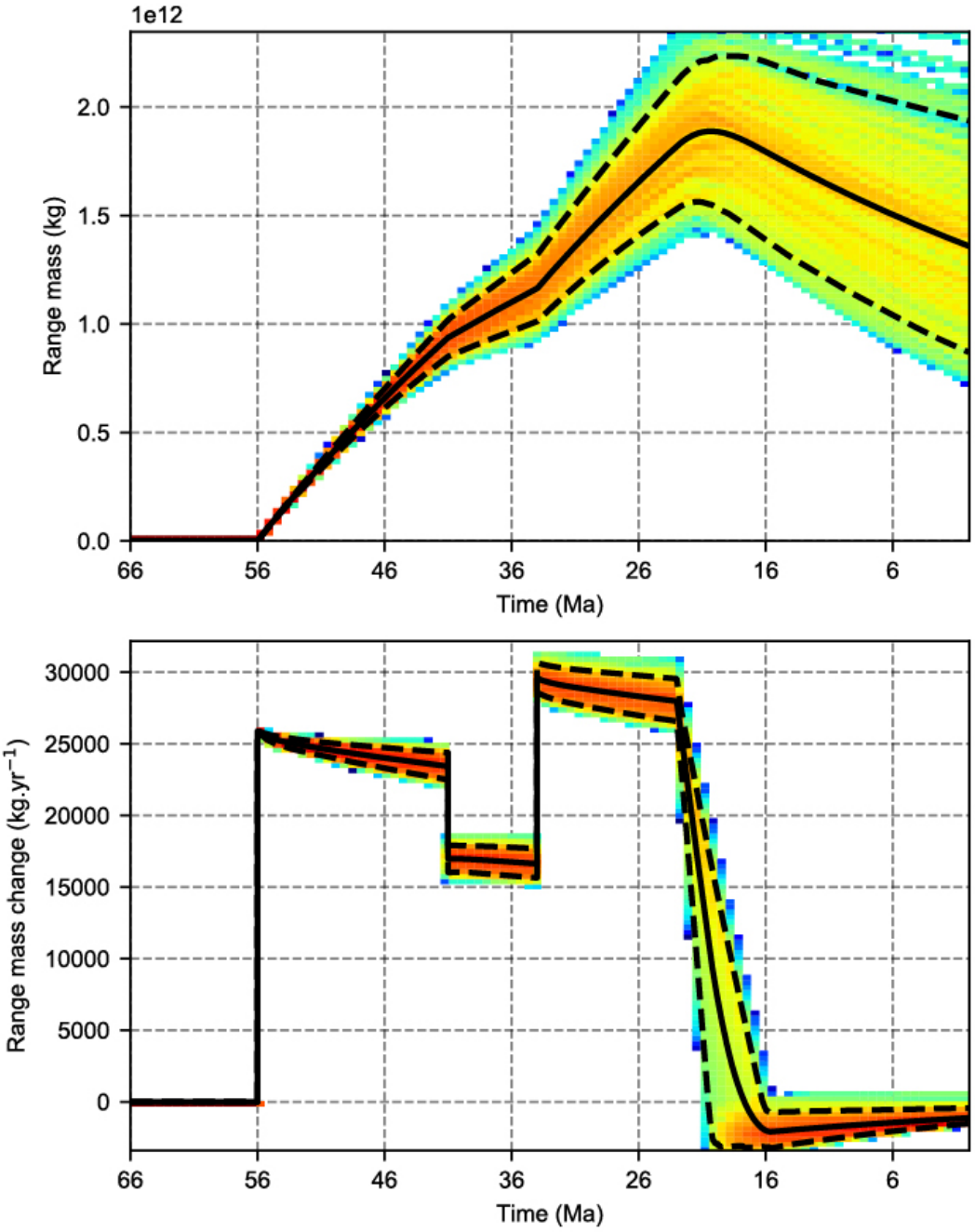

Supplementary Figure VI.6: Evolution through time of the range mass (upper panel) and the range mass change (lower panel).

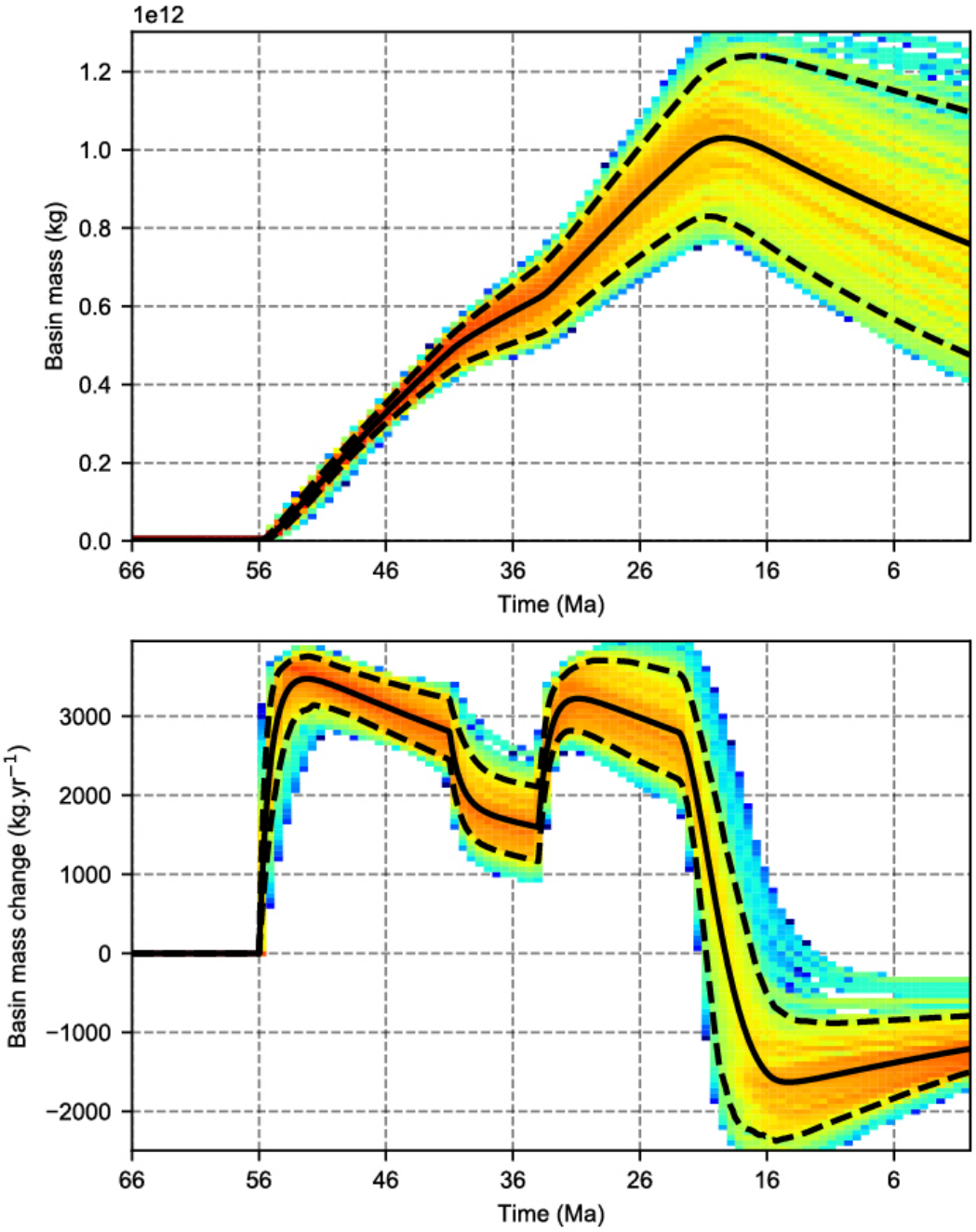

Supplementary Figure VI.7: Evolution through time of the basin mass (upper panel) and the basin mass change (lower panel).

Chapter VII

PRELIMINARY EXPERIMENTS OF POST-OROGENIC EVOLUTION

Results obtained with a relatively simple model (i.e. "box-model") in Chapter VI highlight the complexity of a mountain range and foreland basin system during the post-orogenic stage. These studies have raised new questions regarding the post-orogenic evolution of mountain range and foreland basin systems, especially about: i) the long -term persistence of topography and relief during post-orogenesis and ii) The evolution of sediment flux towards surrounding continental margins. Moreover, in Chapter V we show strong potential for the model "Fastscape", which incorporates more robust equations for erosion, transport and deposition processes in both continental and marine domains to efficiently resolve landscape evolution problems. Therefore, in this chapter, we explore some new preliminary experiments of post-orogenic evolution at the scale of a mountain range and foreland basin with the intention of expanding on these in the future. We start with initial studies using the "Fastscape" algorithm in order to explore what parameters and at what extent they affect the long-term persistence of topography and relief during post-orogenesis. We also compare the evolution of sediment accumulation during syn- and post-orogenic times between model predictions of mountain range and foreland basin systems and stratigraphic data from the Alpine and Pyrenean systems. Finally we present predictions of ^{4}He profiles depending on different the late post-orogenic scenarios that the data aim to test. We demonstrate that the ^{4}He/^{3}He system has the resolution to distinguish between those late events where traditional isotopic systems (i.e. fission tracks and apatite helium) were not able. These initial post-orogenic explorations are topics for future deeper investigations.

VII.1 Post-Orogenic Modelling with "Fastscape"

VII.1.1 Long-persistence of topography and relief

The modern topography of the Pyrenees is high with several summits which reach 3 km of elevation. For example, the "Pico d'Aneto" which is the highest summit of the Pyrenees has an elevation of 3404 m. In the Axial Zone, valley floors are situated at low elevations ranging down to about 900 m which result in high relief of up to about 2 km. The long persistence of mountainous topography in post-orogenic belts is still not a fully solved geomorphologic problem (Baldwin et al., 2003). An example of an ancient mountain belt is the Appalachian Mountains characterized also by significant topography which seems to have been maintained for hundreds of millions of years after the cessation of orogenic processes (Pazzaglia & Brandon, 1996). High peaks of the Adirondack, White and Green Mountain ranges of the New England Appalachians reach elevations up to 1500 m. In the Blue Ridge mountains of Virginia, summits rise over 1000m with significant relief. Other post-orogenic mountain ranges with notable topography include the Ural Mountains, Caledonides, Canadian Rockies and several Paleozoic ranges in Central Asia).

Previous modelling studies have tried to explain the long persistence of topography in ancient mountain ranges by the addition of multiple processes (i.e. isostatic rebound and flexural strength, transition to transport-limited conditions, critical threshold for erosion and stochastic variability of flood magnitudes; Baldwin et al., 2003). In our modelling (Chapter VI), survival of topography is explained by the combination between low lithosphere elastic thickness, low range transport coefficient and late sediment aggradation. A low lithosphere elastic thickness allow important isostatic rebound of the orogenic root and support the decaying topography as demonstrated by early work of Baldwin et al., (2003). The effect of unusually resistant bedrock in the landscape is also a key controlling factor in the preservation of elevation. It was shown for example in the Appalachian Mountain (Pazzaglia and Brandon, 1996) or by modelling (Pelletier, 2004) that the presence of high resistant basement have influenced the late evolution of mountain range. We have shown a similar effect for the Pyrenees (Chapter IV) where the occurrence of highly resistant Variscan granitoid bedrock (i.e. high rock strength) are systematically associated with the highest elevation and relief relatively to the surrounding area. Finally, elevation increase of the foreland basin during the

early post-orogenic stage (Chapter VI) play an important role in the time scale of mountain belt denudation (Babault et al., 2007; Babault, Van Den Driessche, et al., 2005; Pelletier, 2004). Piedmont aggradation sets the base level and reduces relief and therefore reduces erosion efficiency in the mountain range. However, in our modelling, we do not investigate at which degree each parameters influence on the long persistence of topography.

Here, we simulate similar long-term persistence of topography with "Fastscape" which take into account proper erosion, transport and deposition laws (Figure VII.1). We first test the influence of flexural isostatic rebound on the topographic evolution of the range by varying the lithosphere elastic thickness from 13 to 29 km (Figure VII.1A). The decrease of both maximum and mean elevation of the range is lower through time (i.e. longer persistence of topography) for a mountain range/foreland basin system with a lower lithosphere elastic thickness (Figure VII.1A). The effect of rock resistance to erosion in the range is tested by varying the range erodibility. We change the range erodibility from 2.10^{-8} to 9.10^{-7} (Figure VII.1B). For a lower range erodibility, elevation of the range remain higher through time. Noted that for a high range erodibility (i.e. 7.10^{-7} and 9.10^{-7}) decrease of the maximum elevation of the range is very important. Finally, we simulate the piedmont elevation of the basin by varying the basin erodibility from 1.10^{-8} to 9.10^{-8} (Figure VII.1C). Change of basin erodibility result in a proximal basin elevation of 180 m to 600 m. Longer topographic survival is predicted with a higher proximal basin elevation. However, the degree of change compare to experiments with different lithosphere elastic thickness or range erodibility.

To summarize, in our "Fastscape" experiments, topographic survival is greatly enhanced for system with a lower lithosphere elastic thickness which support the range by isostatic rebound. Lower range erodibility which surely simulate the presence of resistant rocks in the range enhanced the persistence of topography. Piedmont elevation increase during the early post-orogenic phase also contribute to topographic survival.

VII.1.2 Sediment Accumulation in Surrounding Continental Margins

During post-orogenic time the erosional products of the mountain range are combined with the sediment eroded from the foreland basins because of isostatic rebound of the lithosphere. A main hypothesize is therefore that the majority of sediment delivered toward surrounding continental margins happened during post-orogenic time when

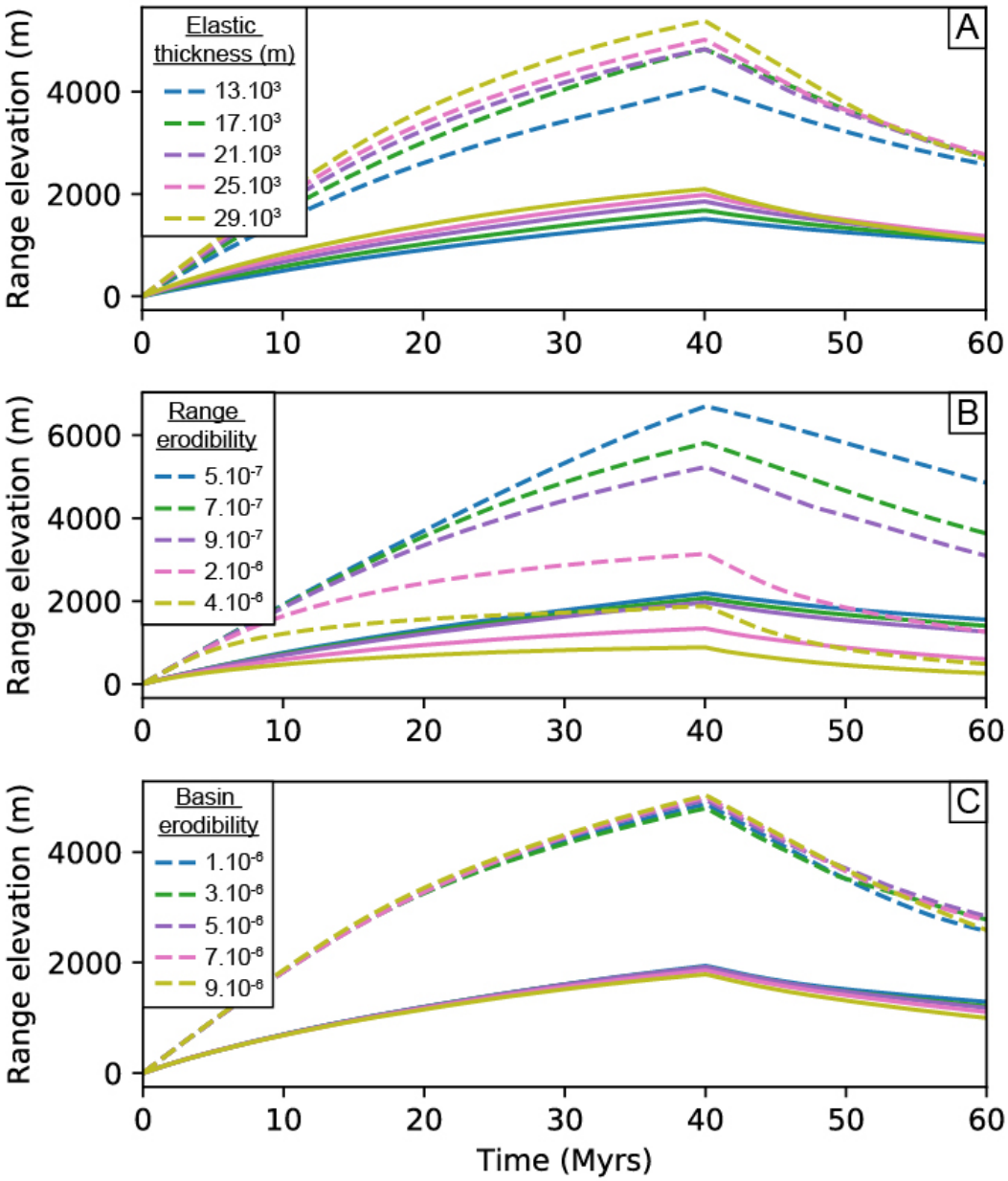

Figure VII.1: Effect of A) the lithosphere elastic thickness, B) the range erodibility and C) the basin erodibility on the range topographic evolution simulated with Fastscape. Uplift is active from 0 to 40 Myrs. Continue lines and dash lines correspond to the mean and maximum elevations respectively while colours indicate the range topographic evolution for different parameter values (i.e. lithosphere elastic thickness and range and basin erodibility). Basin erodibility control directly the basin elevation and reflect the piedmont elevation and therefore relief between the range and basin. For a basin erodibility of 1.10^{-6}, 3.10^{-6}, 5.10^{-6}, 7.10^{-6} and 9.10-6 the basin piedmont elevation at the post-orogenic transition is about 180, 200, 250, 350 and 600 m respectively.

shortening decelerates. In this study, we tested this hypothesize with a "box-model" (Chapter VI) and showing that the basin sediment efflux leaving the system (i.e. going toward surrounding continental margins) dramatically increased during the early post-orogenic phase. Application of the model to the Northern Pyrenean system predicts an increase of the basin efflux from 2.5 to 5 $kg.m^{-1}.yr^{-1}$ at the post-orogenic transition. Sediment efflux toward surrounding continental margin remains higher during the post-orogenic phase than at the maximum convergence during the syn-orogenic phase for the Pyrenean case. This prediction is also tested with the Fastscape algorithm with simulation of erosion, transport and deposition in a thrust-wedge/foreland basin system (Figure VII.3). The model predicts that at the syn- to post- orogenic transition, the foreland basin progressively shifts from a depositional to an erosionalbest of tyc system (Figure VII.3D). Because topographic survival are significant in the thrust-wedge, erosional efflux from the range to the basin remain relatively high during the post-orogenic phase (Figure VII.3A). High range efflux and erosion of the foreland basin are combined to produce an increase of sediment efflux toward sediment efflux. In this 3-dimensional model, sediment efflux increase goes from about $1.0e^4$ to $1.8e^4$ $m^3.yrs^{-1}$.

The degree to which post-orogenic sediment efflux increases toward surrounding continental margins will depend on a number of different parameters. The main controlling intrinsic parameters of the system are again the range and basin erodibility and the elastic thickness of the modelled lithosphere (Figure VII.4). As demonstrated in Figure VII.4A, if the range erodibility is too high (i.e. high range erosional products) relatively to the basin erodibility, the post-orogenic basin sediment efflux increase is no longer observable. In this case, the erosional product from the range overpassed and cover the effect of erosion in the basin. On another way, if the basin erodibility is too low (i.e. low basin erosional products), erosion in the basin become limited and the post-orogenic sediment efflux is only governed by the erosional product from the range with no observable increase (Figure VII.4B). A lower lithosphere elastic thickness tends to increase the isostatic rebound and resulting erosion in the basin during the post-orogenic phase. Therefore, the basin sediment efflux is more important for a lower lithosphere elastic thickness (Figure VII.4C). To resume the basin sediment efflux toward surrounding continental margins is highlighted for a lower range erodibility, a higher basin erodibility and a lower lithosphere elastic thickness.

Several mountain range/foreland basin systems highlight this post-orogenic be-

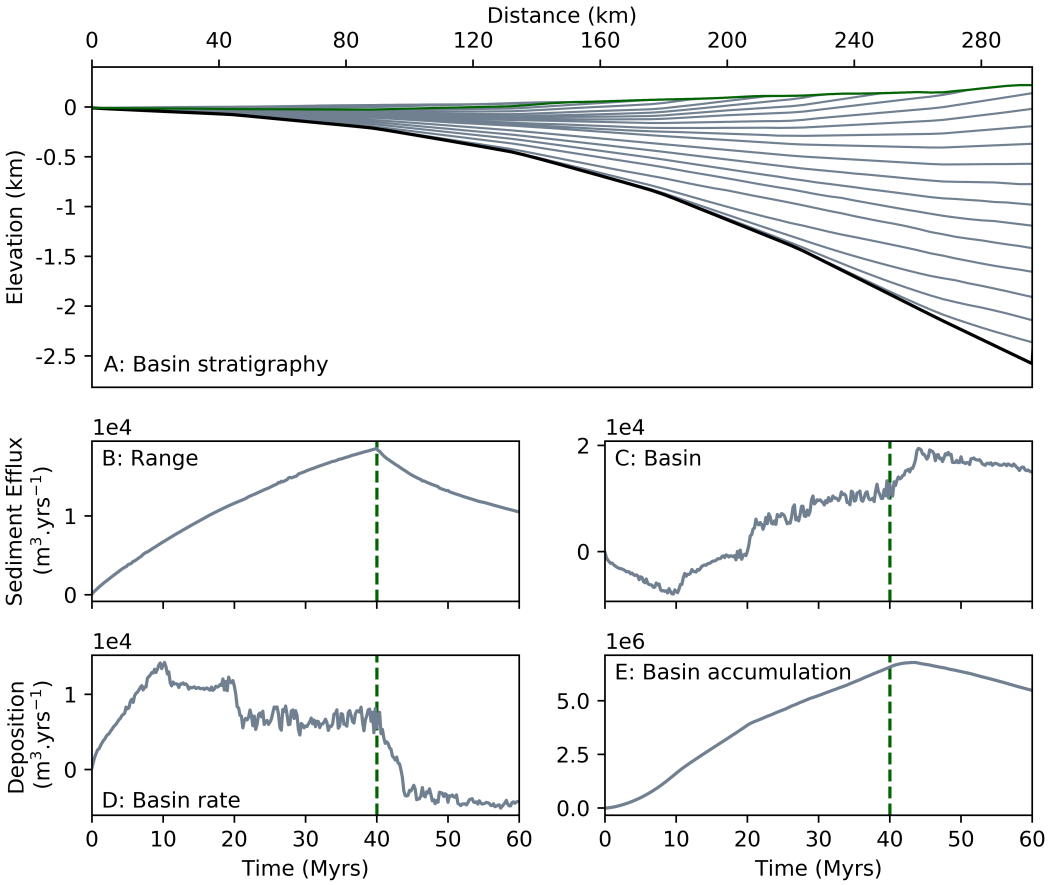

Figure VII.2: Pattern of sediment flux and deposition in a foreland basin through times during syn- and post-orogenesis modelled with Fastscape. Foreland basin respond to the evolution of a simulated thrust wedge during 60 Myrs which undergoes active convergence from 0 to 40 Myrs. A) Stratigraphic preview of the foreland basin at the end of the simulation (i.e. 60 Myrs). Black stratigraphic line corresponds to the basin base. B) Evolution of the sediment efflux of the range toward the basin. C) Evolution of the sediment efflux of the basin out of the system. D) Evolution of the rate of deposition in the foreland basin through time. E) Evolution of the basin accumulation through time. Green vertical dash line highlight the end of active convergence in the system.

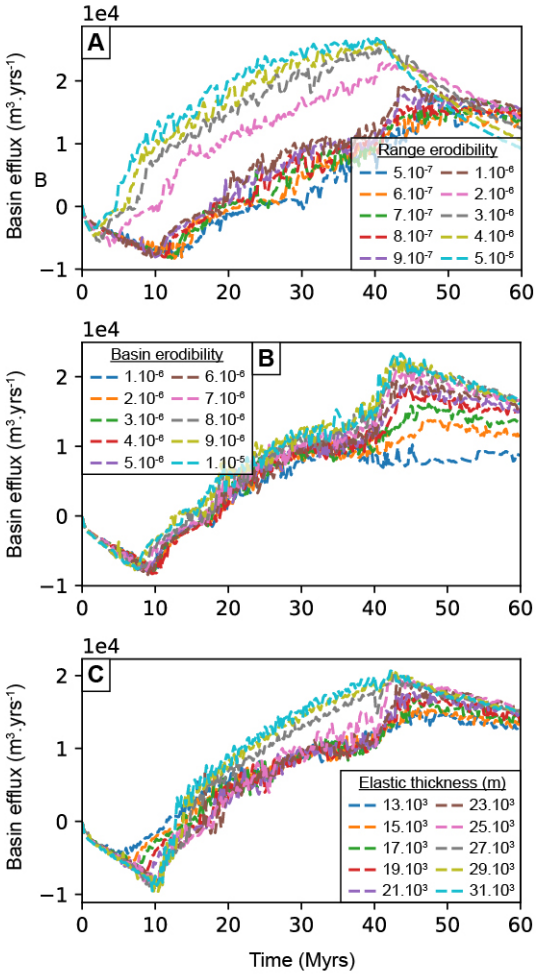

Figure VII.3: Evolution through time of the basin efflux toward surrounding continental margins for different A) range erodibilities, B) basin erodibilities and C) lithosphere elastic thickness. Convergence is active from 0 to 40 Myrs. Each colour curves correspond to a basin efflux evolution for a different range erodibility, basin erodibility or elastic thickness.

haviour. The syn- to post-orogenic transition is associated with first a drastic reduction of sediment accumulation rate in the foreland basin and second an increase of sedimentation accumulation rate in surrounding continental margins. The sediment rooting system of the Northern Pyrenees show that the Aquitaine foreland basin records a decrease of sediment rate at 23 Ma which coincides with the timing of post-orogenic transition (Figure VII.5). The deep-sea margin of the Bay of Biscay records higher preservation of sediment starting during Oligocene time (Ortiz et al., 2020) (Figure VII.5). The North Alpine Foreland Basin and associated Rhône system records a similar trend. Cessation of sedimentation in the North Alpine Foreland Basin occurred around 8 Ma and increase of sediment in the surrounding depositional settings (Rhône Delta) around 6 Ma (Figure VII.6) (Kuhlemann et al., 2002). It coincide with the timing of post-orogenesis in the Alps and the start of isostatic rebound in the basin around 5-6 Ma (Cederbom et al., 2004).

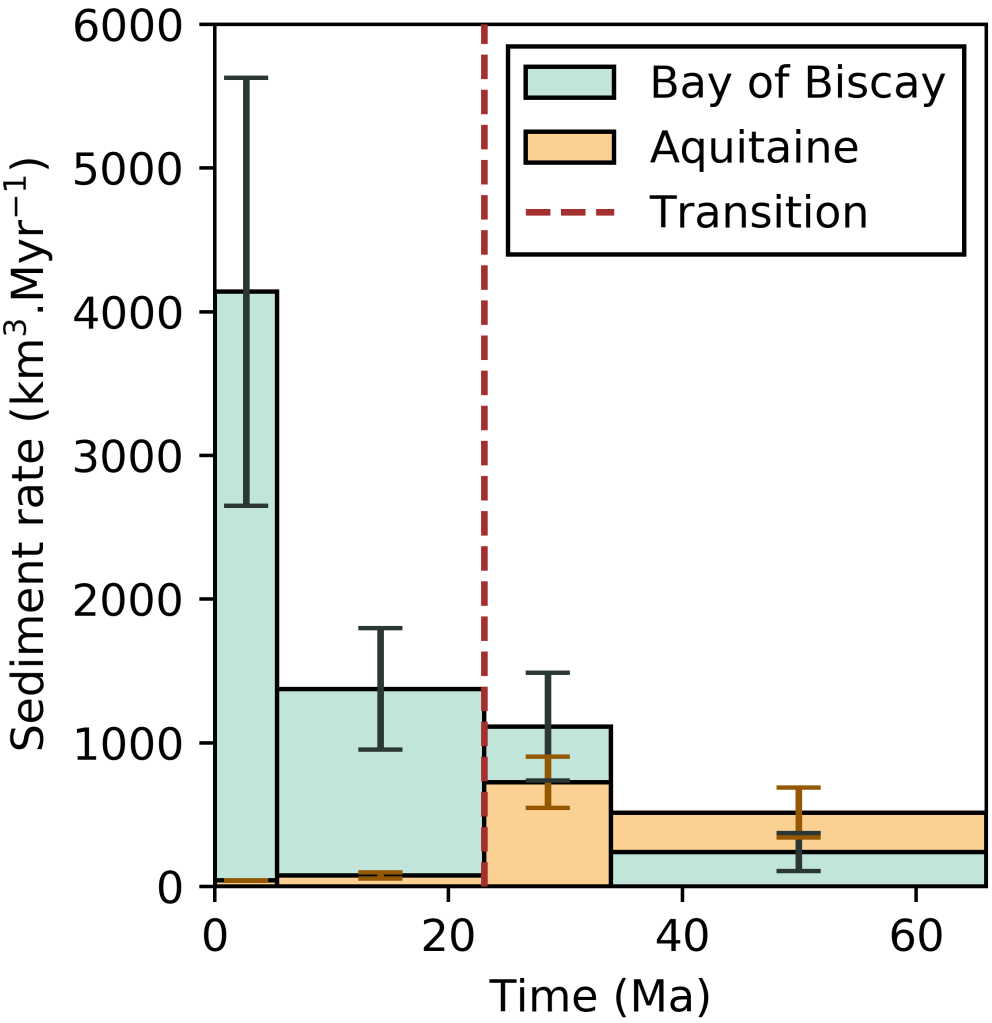

Figure VII.4: Evolution of sediment accumulation rate in the Aquitaine retro-foreland basin and deep-sea Bay of Biscay during Cenozoic time from Ortiz et al. (2020).

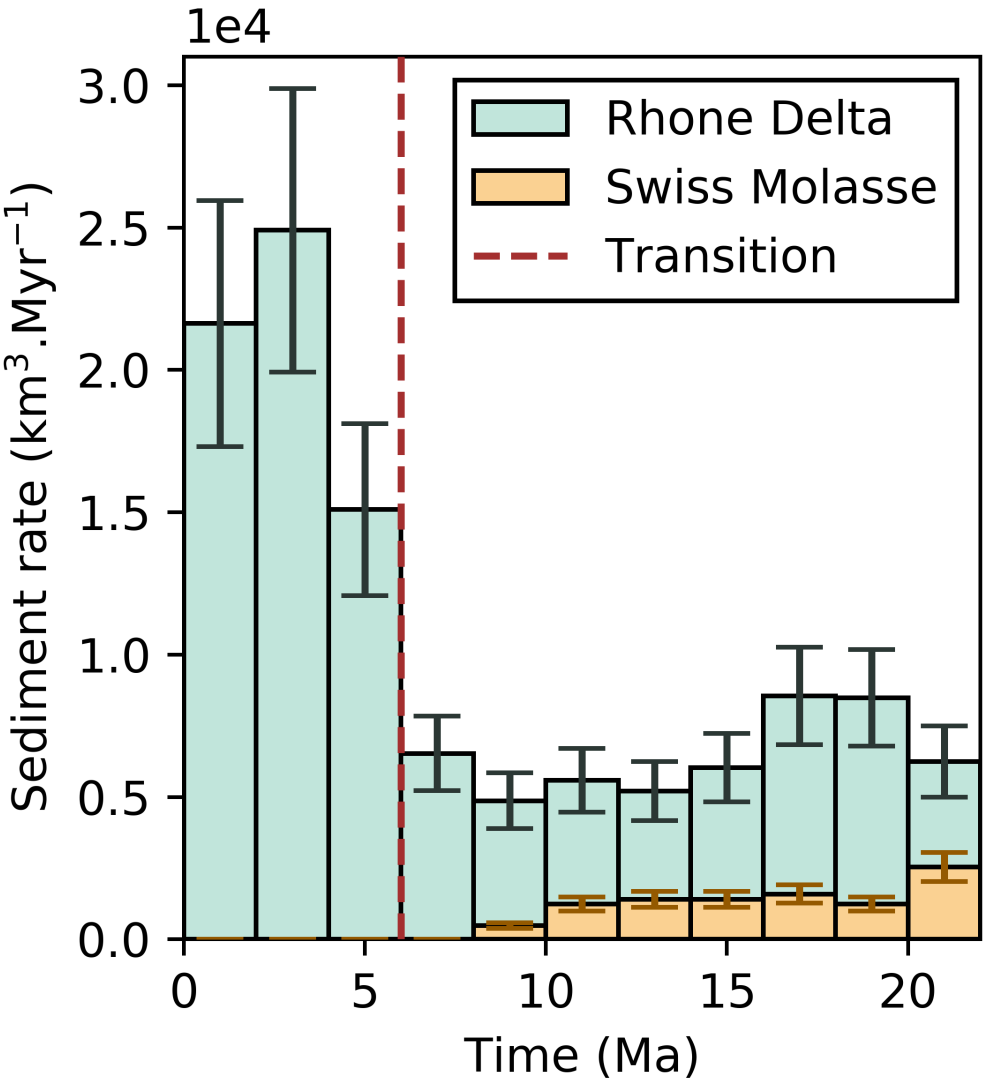

Figure VII.5: Evolution of sediment accumulation rate in the North Alpine Foreland Basin and surrounding depositional settings of the Rhône Delta during Miocene and Quaternary time from (Kuhlemann et al., 2002).

VII.2 Late Post-Orogenic Exhumation of the Pyrenees

VII.2.1 Late exhumation scenario

Forward modelling of thermochronologic data from the Maladeta massif (Besiberri profile) of the Southern Pyrenees (Fitzgerald et al., 1999) already suggests that a post-orogenic component is required to completely explain apatite fission track ages and mean track lengths. The amount of exhumation suggested for the post-orogenic rejuvenation phase is 2-3 km with a best-fit timing between 10 and 5 Ma in order to reveal the partial annealing zone recorded by the dataset. However, the Besiberri profile is the only one to clearly record a recent phase of post-orogenic exhumation. Our inverse modelling (Chapter IV) or previous ones (Sinclair et al., 2005; Gibson et al., 2007) for the same massif do not record post-orogenic exhumation. Moreover, there is no evidence in the Central Pyrenees of tectonic structures or metamorphic relationships that might suggest that the Central Pyrenees have experienced tectonic denudation through low angle normal faults.

It has been proposed that a possible explanation for the topographic rejuvenation during the late stage of the Pyrenees may be due to abrupt re-excavation of the Ebro Basin during Miocene-Pliocene time (Garcia-Castellanos et al., 2003; Fillon et al., 2012). The Ebro Basin was buried and filled by continental sandstone and conglomerate sediments with the deposition of up to 3 km in thickness (Coney et al., 1996) leading to the backfilling of the Southern Pyrenean Thrust Belt and possibly the southern flank of the Pyrenees as a whole. During Late-Middle Miocene time the Ebro River cuts through the Catalan Coastal Ranges (Gaspar-Escribano et al., 2001) leading to excavation of the sedimentary infill of the Ebro basin and possibly the southern flank of the Axial Zone (Coney et al., 1996). The timing and origin of this major drainage change is still not completely resolve but eustatic sea-level change (Calvo et al., 1992), lake capture or sediment overfilling (Garcia-Castellanos et al., 2003) have been proposed.

Another cause for the late rejuvenation hypothesis is a global worldwide climate change with a switch from a rather equable climate during Neogene time to a period of frequent and abrupt changes in temperature, rainfall and vegetation from late Pliocene (England & Molnar, 1993). Such climate change has been proposed as the driving mechanism for accelerated exhumation and erosion in the Central European Alps (Cederbom et al., 2004). Early Pliocene global climate change signal has been used to

explain the preservation of peneplains for the Pyrenees and their subsequent dissection (Babault, Van Den Driessche, et al., 2005).

Finally, a more recent agent for late rejuvenation is glaciation. The predominant modern erosive agent for the Pyrenees is fluvial erosion with the majority of valleys being filled by rivers. However, the geomorphology of the preserved landscape of the Pyrenees records evidence of past glacial processes with deep U-shaped valleys and cirques. Considerable evidence, such as mapping of moraines, has highlighted that glaciers once extended far down the valleys (see Chapter I.3.7). Record of glacial valley incision has been documented in the European Alps using very low-temperature thermochronology (i.e. $^{4}He/^{3}He$ thermochronometer) (Valla et al., 2011) and attributed to the global mid-Pleistocene climate transition from symmetric 41,000-year to strongly asymmetric 100,000-year glacial/interglacial oscillation (Lisiecki, 2010). Even if glaciation in the Pyrenees was not as extensive as in the European Alps, a mid-Pleistocene signal is possible.

VII.2.2 Low-temperature thermochronological predictions

The effect of a possible late thermal exhumation events on low-temperature isotopic systems can be investigated by modifying a pre-existing modelled thermal history from the Maladeta massif. Modified time-temperature cooling histories (Chapter IV) were obtained by implementing different late events to the likelihood model (i.e. the thermal history which best predict the observed data; Gallagher, 2012). A first scenario (Figure VII.7A) implies that the whole cooling occurred during Late Eocene and Oligocene time (i.e. from 40 to 25 Ma) following by a clear cessation up to actual time. This scenario suggests that since the main cooling phase, the topography of the Pyrenees has stayed relatively stable as proposed in chapter IV. A second scenario (Figure VII.7B) proposes two distinct phases of cooling. The first one is still associated with the main phase of growth of the Pyrenees during Late Eocene and Oligocene times following by a second cooling phase during Pliocene time. This cooling history may be associated to Neogene perturbations (Fitzgerald et al., 1999) such as opening of the Ebro Basin or climate change during Pliocene time. The exact timing for the start of the second cooling phase depends on the change nature. Finally, the third scenario (Figure VII.7C) proposes that the main phase of cooling is followed by a constant exhumation during Neogene and Quaternary time. This scenarios could result from a constant topographic decrease of

the Pyrenees during the post-orogenic phase.

For each thermal history scenario (Figure VII.7A, B and C), it is possible to predict thermochronological data (fission track and apatite helium ages and fission mean track lengths) and compare them against the observed ones using a forward modelling (Figure VII.7D, E and F). Dataset predictions of the different scenarios are in good accordance with the observed dataset meaning that the proposed late events are not in disagreement with the pre-existing low-temperature dataset. Predictions stay also relatively similar between the different t-T paths suggesting that fission tracks or apatite helium thermochronometers don't have the resolution to detect these events. Slightly younger predicted helium ages are recorded for the second scenario because of longer period of time close to the partial retention zone for the lower samples. However, change for the predicted helium ages stay in the range of the observed age uncertainties.

In the same way than fission track and apatite helium dataset, forward modelling of the proposed thermal histories allows a prediction of the ^{4}He helium profiles associated to the different t-T paths (Figure VII.8D, E and F). A thermal history with a rapid cooling through the PRZ with no subsequent cooling (Figure VII.8A) produces a square helium profile with full helium retention in the inner part of the crystal radius (Figure VII.8D). In contrast, a thermal history like for scenario 2 (Figure VII.8B) will result with a rounder helium profile and less retention of 4He in the inner part of the crystal (Figure VII.8E). The thermal history of scenario 3 which implies constant late cooling produces a helium profile between the two other ones (Figure VII.8C and F). The main pattern from this experiment is that a t-T path which stays longer and closer to the PRZ will result in a rounder helium profile and less retention of ^{4}He in the inner part of the crystal. Depending on sample elevations, the predicted helium profile will differ (Figure VII.9). Even if direct comparison is difficult to be made because of different radius effects, samples at higher elevations (Figure VII.9D) have a more square helium profile and more 4He retention compared to a sample at lower elevation (Figure VII.9A). This effect is observed because lower samples, in our example, are more susceptible to staying close to the PRZ for a longer period of time (Figure VII.8A and B). Another implication is that the change of helium profiles for the different scenarios are more marked for a sample situated at lower elevation (Figure VII.9A, B and C) compared to a sample situated at higher elevation (Figure VII.9D, E and F). Finally, different helium profiles for the same thermal history and sample can be different depending the

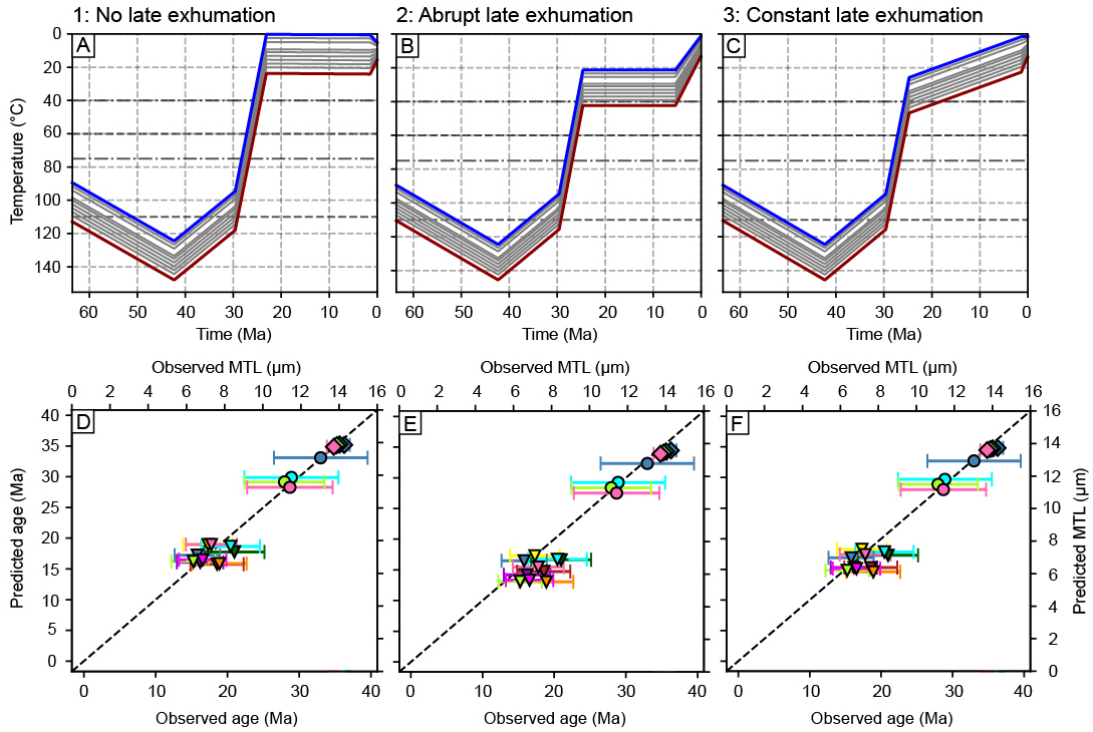

Figure VII.6: Thermal histories (A, B and C) and their associated observed versus predicted dataset (D, E and F) for different late evolution: i) no late exhumation (A and D); ii) Abrupt late exhumation (B and E), iii) Constant late exhumation (C and F). Blue, red and grey lines for thermal histories are t-T paths for the upper, lower and intermediate samples respectively. Horizontal black dash lines correspond to the partial annealing zone while the horizontal black point-dash lines correspond to the partial helium retention zone. Triangles, circles and diamonds in the observed versus predicted dataset correspond to the helium ages, fission track ages and mean track lengths respectively. Diagonal black dash line corresponds to the hypothetical best prediction line.

radius of the crystal analysed (Figure VII.10). The main effect is that for a crystal with a low radius, the loss of helium goes deeper through the crystal (Figure VII.10A, B and C). In contrast, a high radius crystal will result in a loss of helium restricted in the outer part of the crystal radius (Figure VII.10D, E and F).

To conclude, here we show that in contrast to fission tracks and apatite helium isotopic systems, $^{4}He/^{3}He$ thermochronometry has the resolution to detect different post-orogenic exhumation signals. Application of this technique to key massifs, as started during this thesis, should bring new information on the late evolution of the Pyrenees and enable a distinction between the scenarios outlined previously. .

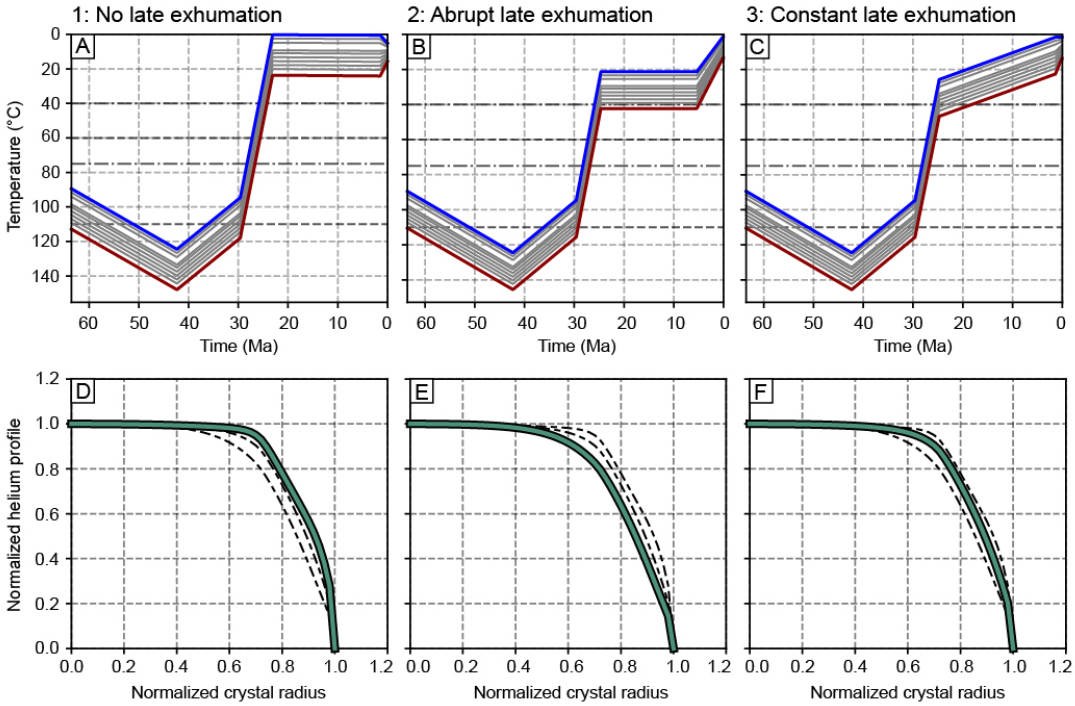

Figure VII.7: Thermal histories (A, B and C) and their associated predicted helium profiles for different late evolutions: i) no late exhumation (A and D); ii) Abrupt late exhumation (B and E), iii) Constant late exhumation (C and F). Blue, red and grey lines for thermal histories are t-T paths for the upper, lower and intermediate samples respectively. Horizontal black dash lines correspond to the partial annealing zone while the horizontal black point-dash lines correspond to the partial helium retention zone. Helium profiles in green are predicted for the lower sample and an apatite radius of 71 μm.

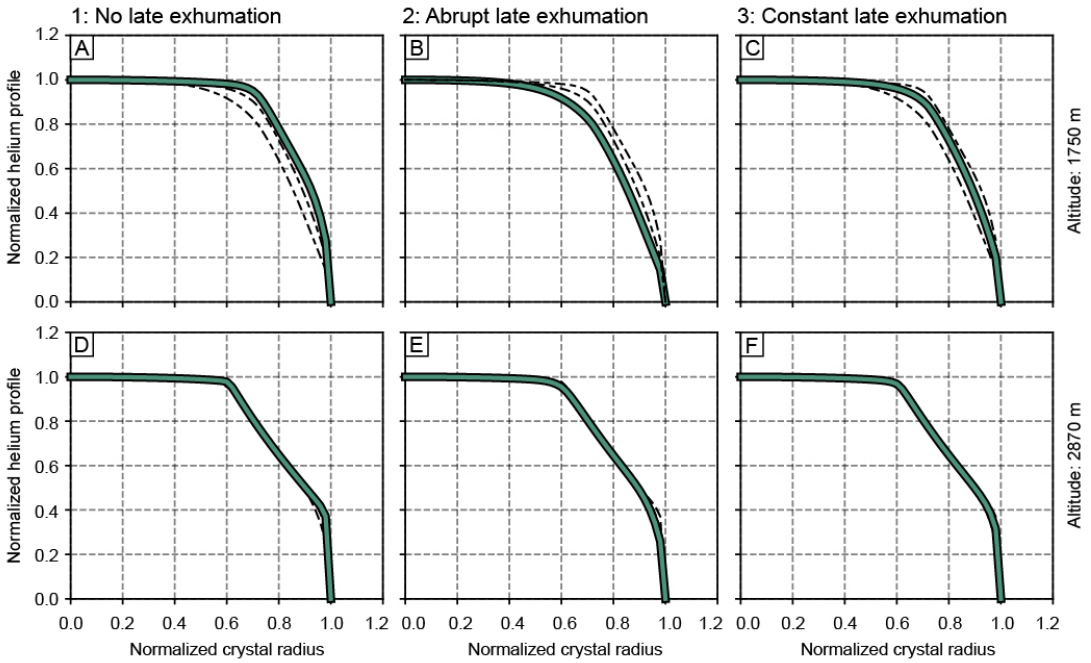

Figure VII.8: Helium profile predictions for different late evolutions (A and D: No late exhumation; B and E: Abrupt late exhumation, C and D: Constant late exhumation) and for different elevations (A, B and C: low altitude; D, E and F: high altitude).

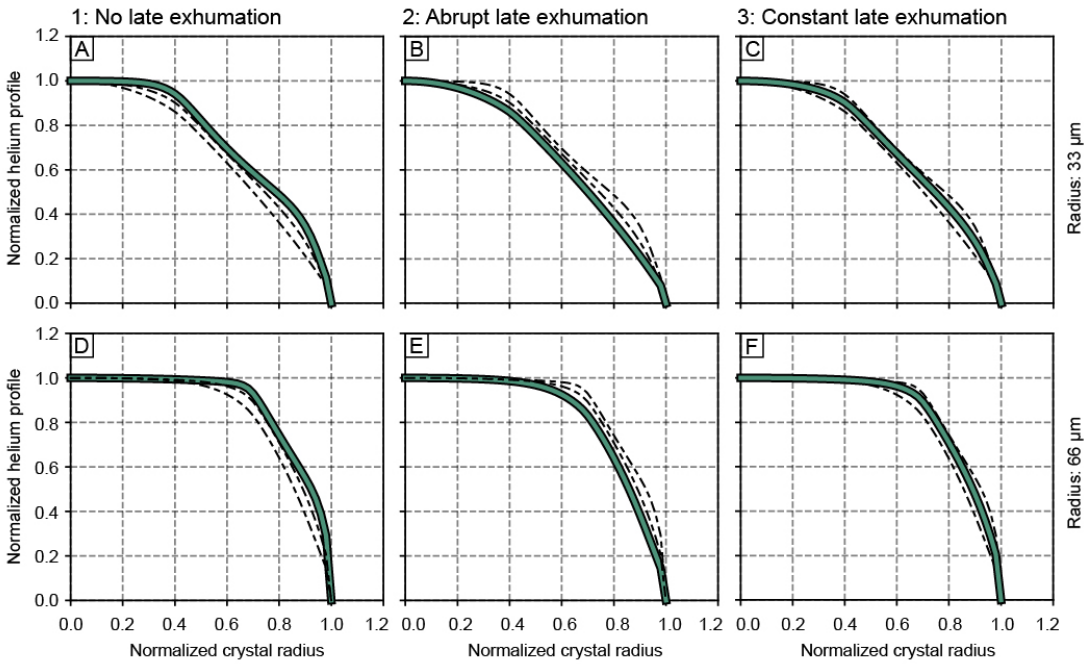

Figure VII.9: Helium profile predictions for different late evolutions (A and D: No late exhumation; B and E: Abrupt late exhumation; C and F: Constant late exhumation) and for different apatite radius (A, B and C: low radius; D, E and F: high radius).

Chapter VIII

CONCLUSION

The main conclusions of this thesis are highlighted in figure VIII.1 and are summarised below:

1. The post-orogenic topography of the Pyrenees is influenced by variations in the rock strength of the main lithological units. Rock strength of the different lithologies are quantified using elastic rebound measurements that demonstrate that the granitoid lithologies of the Variscan massifs have the greatest strength compared to Palaeozoic metasediments, Mesozoic and Tertiary cover rocks. The strength of rocks are also revealed by the elevation and channel steepness of rivers; high elevation and channel steepness broadly correlate with areas of high rock strength across the Pyrenees. The main drainage divide preferentially tracks the highly elevated and resistant Variscan granitoid massifs of the Axial Zone and suggests that, during the recent evolution of the Pyrenees, lithology has played a dominant role in defining the range topography.

2. Numerical landscape evolution modelling shows that the progressive exhumation of harder rocks in mountainous areas trigger a transient fluvial response. The landscape response involves a decrease in channel steepness and erosive capability in the upstream parts of a catchment. The reduced erosive capacity of this upstream part of the catchment make it vulnerable to drainage capture by neighbouring river catchments that have not been affected by the exhumation of harder rocks. The predicted response is that opposing catchments consume catchment area until the drainage divide stabilises over the location of the harder rock type. Neighbouring catchments may also migrate laterally at the headwaters resulting in a distinct drainage pattern that appears to 'wrap around' the harder lithology

of the affected victim catchment. It is possible that this explains some similar catchment geometries in the Pyrenees and the Alps.

3. Modelling of a thermochronological dataset from the Central Pyrenees confirms that the main phase of exhumation is diachronous through time and younging from north to south. Additionally, the modelled thermal histories indicate a southward migration of the timing of abrupt decelerations of cooling in granitic massifs. By combining data from landscape numerical modelling, topographic analyses and low-temperature thermochronology we suggest that exhumation of crystalline basement following removal of overlying sedimentary cover is likely to have influenced the syn-tectonic erosional history of the range.

4. Topographic and geological data of the northern Pyrenees are characterized by post-orogenic sediments that drape and seal tectonic structures of the Sub-Pyrenean Thrust and North Pyrenean Frontal Thrust and corresponds to the deposition of large alluvial fans. Sediment drapes form low gradient-high elevation surfaces that range in elevation from 300 to 600 m. Application of a box-model to the Northern Pyrenees demonstrate that at the transition from syn-orogenesis to post-orogenesis, sediment flux from the range remains high, while basin subsidence slows; this combination results in accumulation of continental sediment that can drape over the frontal portions of thrust wedges. The model suggests that this aggradation of the Aquitaine Basin continued to an elevation of 620 m on the proximal part of the foreland basin and lasted 8 Ma following the onset of post-orogenesis (i.e. 23 to 15 Ma). Results confirm the presence of Miocene sediment at high elevation, up to 600-700 m, without invoking external forcing such as trapping of sediment or climate change.

5. An important signal related to the late syn- to post-orogenic transition of a mountain range and foreland basin system is a diminution of sediment accumulation in the foreland basin and an increase of sediment accumulation in surrounding continental margins. This signal is explained by the combination of continue high erosion and sediment flux from the range and sediments eroded from the foreland basins because of isostatic rebound of the system. We found natural post-orogenic systems highlighting this behaviour as for the Northern Pyrenean or Western Alpine systems. In both case, sedimentation in foreland basins (i.e. Aquitaine

Basin and North Alpine Foreland Basin) decrease at the post-orogenic transition whereas sediment accumulation in surrounding depocenters accelerate (i.e. Bay of Biscay and Rhône Delta).

6. Long persistence of topography in the Pyrenees after cessation of tectonic activity is explained by: i) Root isostatic rebound (i.e. low lithosphere elastic thickness); ii) Presence of highly resistant basement rocks (i.e. low range transport coefficient) and; iii) An increase in basin elevation driving a reduction in relief between the range and basin).

7. We highlight that in contrast to the conventional fission tracks and apatite helium isotopic systems, 4He/3He thermochronometers have the resolution to record potential post-orogenic exhumation signals. This system will be used to test the following post-orogenic scenarios: i) topographic rejuvenation due to abrupt re-excavation of the Ebro basin during Miocene-Pliocene time; ii) worldwide climate change from equable climate during the Neogene to a climate with frequent changes of temperature and rainfall from late Pliocene; iii) intensification of glaciation during mid-Pleistocene time.

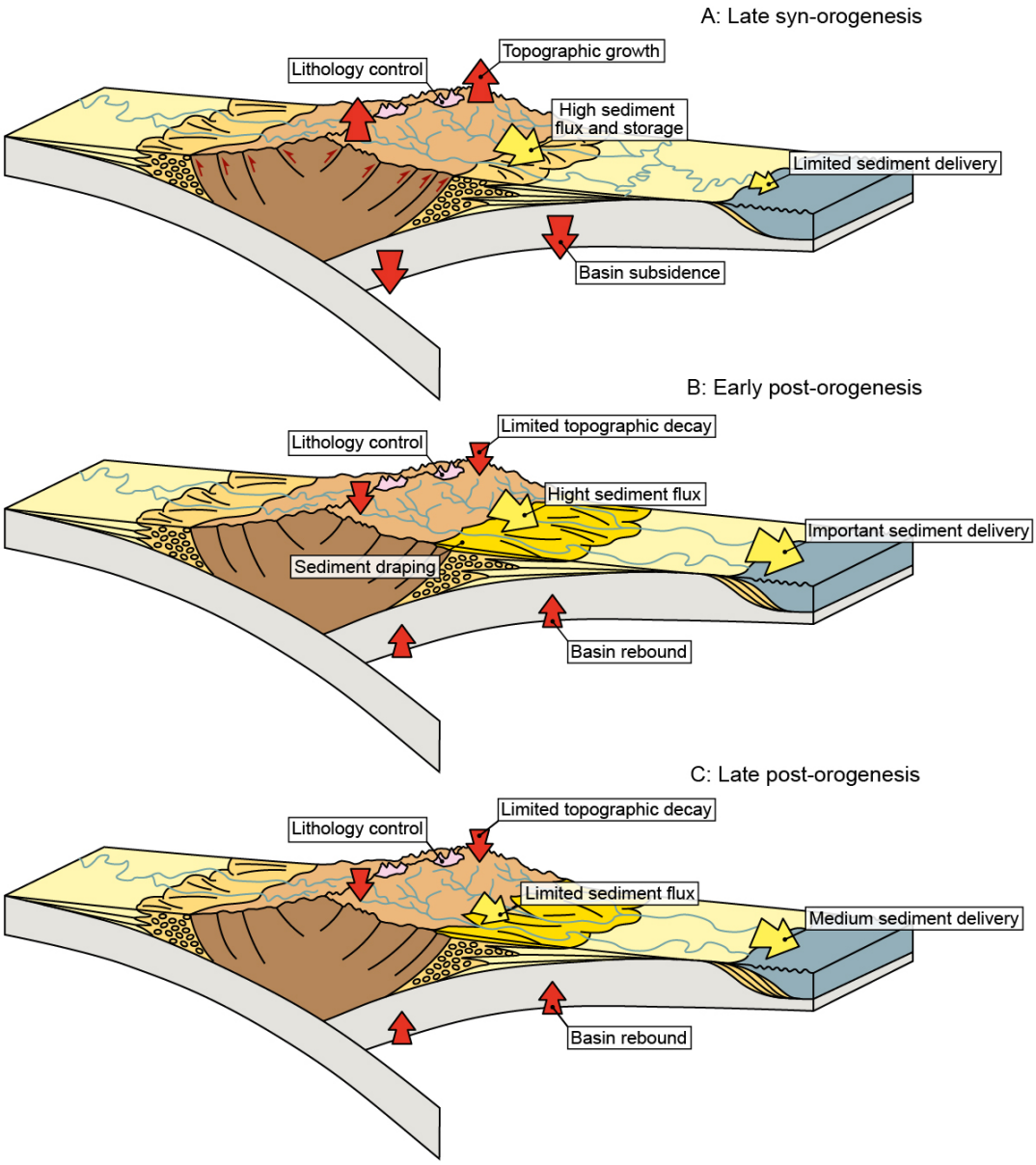

Figure VIII.1: Schematic representation of the main conclusions from this thesis. Main changes associated to the late syn- to post-orogenic evolution of a mountain-foreland system are only highlighted for the northern retro-side. Figure is not to scale.

Bibliography

Ahrens, T. J., Fleischer, R. L., Price, P. B., & Woods, R. T. (1970). Erasure of fission tracks in glasses and silicates by shock waves. *Earth and Planetary Science Letters*, *8*(6), 420–426. https://doi.org/10.1016/0012-821X(70)90145-7

Allen, P. A. (2008). Time scales of tectonic landscapes and their sediment routing systems. *Geological Society, London, Special Publications*, *296*(1), 7–28. https://doi.org/10.1144/sp296.2

Allen, P. A., & Allen, J. R. (2005). Basin Analysis. https://doi.org/10.1364/JOSA.66.001025

Allen, P. A., Crampton, S. L., & Sinclair, H. D. (1991). The inception and early evolution of the north Alpine foreland basin, Switzerland. *Basin Research*, *3*(3), 143–163. https://doi.org/10.1111/j.1365-2117.1991.tb00124.x

Allen, P. A., Homewood, P., & Williams, G. D. (1986). Foreland Basins: An Introduction, In *Foreland basins*. https://doi.org/10.1002/9781444303810.ch

Andrieu-Ponel, V., Hubschman, J., Jalut, G., & Hérail, G. (1988). Chronologie de la dégladation des Pyrénées françaises. Dynamique de sédimentation et contenu pollinique des paléolacs ; application à l'interprétation du retrait glaciaire. *Bulletin de l'Association française pour l'étude du quaternaire*, *25*(2-3), 55–67. https://doi.org/10.3406/quate.1988.1866

Angevine, C. L., Heller, P. L., & Christopher, P. (1990). Quantitative sedimentary basin modelling. *AAPG Continuing Education Course Notes*, *47*, 121–178.

Angrand, P., Ford, M., & Watts, A. B. (2018). Lateral Variations in Foreland Flexure of a Rifted Continental Margin: The Aquitaine Basin (SW France). *Tectonics*, *37*(2), 430–449. https://doi.org/10.1002/2017TC004670

Armitage, J. J., Duller, R. A., Whittaker, A. C., & Allen, P. A. (2011). Transformation of tectonic and climatic signals from source to sedimentary archive. *Nature Geoscience*, *4*(4), 231–235. https://doi.org/10.1038/ngeo1087

Armstrong, P. A., Ehlers, T. A., Chapman, D. S., Farley, K. A., & Kamp, P. J. J. (2003). Exhumation of the central Wasatch Mountains, Utah: 1. Patterns and timing of exhumation deduced from low-temperature thermochronology data. *Journal of Geophysical Research: Solid Earth*, *108*(B3). https://doi.org/10.1029/2001JB001708

Babault, J., Bonnet, S., Crave, A., & Van Den Driessche, J. (2005). Influence of piedmont sedimentation on erosion dynamics of an uplifting landscape: An experimental approach. *Geology*, *33*(4), 301–304. https://doi.org/10.1130/G21095.1

Babault, J., Bonnet, S., Van Den Driessche, J., & Crave, A. (2007). High elevation of low-relief surfaces in mountain belts: Does it equate to post-orogenic surface uplift? *Terra Nova*, *19*(4), 272–277. https://doi.org/10.1111/j.1365-3121.2007.00746.x

Babault, J., & Van Den Driessche, J. (2005). L'érosion des chaînes de montagnes: Influence de la sédimentation de piedmont. *Comptes Rendus - Geoscience*, *337*(16), 1431–1438. https://doi.org/10.1016/j.crte.2005.09.010

Babault, J., Van Den Driessche, J., Bonnet, S., Castelltort, S., & Crave, A. (2005). Origin of the highly elevated Pyrenean peneplain. *Tectonics*, *24*(2). https://doi.org/10.1029/2004TC001697

Bahr, R., Lippolt, H. J., & Wernicke, R. S. (1994). Temperature-induced 4He degassing of specularite and botryoidal hematite: a 4He retentivity study. *Journal of Geophysical Research*, *89*(B9), 17695–17707. https://doi.org/10.1029/94JB01055

Baldwin, J. A., Whipple, K. X., & Tucker, G. E. (2003). Implications of the shear stress river incision model for the timescale of postorogenic decay of topography. *Journal of Geophysical Research: Solid Earth*, *108*(B3). https://doi.org/10.1029/2001jb000550

Barbey, P., Cheilletz, A., & Laumonier, B. (2001). The Canigou orthogneisses (Eastern Pyrenees, France, Spain): an Early Ordovician rapakivi granite laccolith and its contact aureole. *Comptes Rendus de l'Académie des Sciences - Series IIA - Earth and Planetary Science*, *332*(2), 129–136. https://doi.org/10.1016/S1251-8050(00)01506-8

Barrouquère, G., Roux, L., Souquet, P., Peybernes, B., Rey, J., Debroas, E. J., & Bambier, J. P. (1976). Carte géol. France (1/50000), feuille 18 — EAGE BERNARD et al. ST-GIRONS (1074). *Orléans: Bureaux de recherches géologiques et minières.*

Batt, G. E., & Braun, J. (1997). On the thermomechanical evolution of compressional orogens. *Geophysical Journal International*, *128*(2), 364–382. https://doi.org/10.1111/j.1365-246X.1997.tb01561.x

Batt, G. E., & Braun, J. (1999). The tectonic evolution of the Southern Alps, New Zealand: Insights from fully thermally coupled dynamical modelling. *Geophysical Journal International*, *136*(2), 403–420. https://doi.org/10.1046/j.1365-246X.1999.00730.x

Beamud, E., Muñoz, J. A., Fitzgerald, P. G., Baldwin, S. L., Garcés, M., Cabrera, L., & Metcalf, J. R. (2011). Magnetostratigraphy and detrital apatite fission track thermochronology in syntectonic conglomerates: Constraints on the exhumation of the South-Central Pyrenees. *Basin Research*, *23*(3), 309–331. https://doi.org/10.1111/j.1365-2117.2010.00492.x

Beaumont, C., Jamieson, R. A., Nguyen, M. H., & Lee, B. (2001). Himalayan tectonics explained by extrusion of a low-viscosity crustal channel coupled to focused surface denudation. *Nature*, *414*(6865), 738–742. https://doi.org/10.1038/414738a

Beaumont, C. (1981). Foreland basins. *Geophysical Journal of the Royal Astronomical Society*, *65*(2), 291–329. https://doi.org/10.1111/j.1365-246X.1981.tb02715.x

Beaumont, C., Fullsack, P., & Hamilton, J. (1992). Erosional control of active compressional orogens, In *Thrust tectonics*. https://doi.org/10.1007/978-94-011-3066-0{_}1

Beaumont, C., Kamp, P. J. J., Hamilton, J., & Fullsack, P. (1996). The continental collision zone, South Island, New Zealand: Comparison of geodynamical models and observations. *Journal of Geophysical Research*, *101*(B2), 3333–3359. https://doi.org/10.1029/95jb02401

Beaumont, C., Munoz, J. A., Hamilton, J., & Fullsack, P. (2000). Factors controlling the Alpine evolution of the central Pyrenees inferred from a comparison of ... *Journal of Geophysical Research*, *105*(B4), 8121–8145.

Bernard, T., Sinclair, H. D., Gailleton, B., Mudd, S. M., & Ford, M. (2019). Lithological control on the post-orogenic topography and erosion history of the Pyrenees. *Earth and Planetary Science Letters*, *518*, 53–66. https://doi.org/10.1016/j.epsl.2019.04.034

Bernard, T., Steer, P., Gallagher, K., Szulc, A., Whitham, A., & Johnson, C. (2016). Evidence for Eocene-Oligocene glaciation in the landscape of the East Greenland margin. *Geology*, *44*(11), 895–898. https://doi.org/10.1130/G38248.1

Bernet, M., & Garver, J. I. (2005). Fission-track analysis of detrital zircon. *Reviews in Mineralogy and Geochemistry*, *58*(1), 205–237. https://doi.org/10.2138/rmg.2005.58.8

Bernet, M., Zattin, M., Garver, J. I., Brandon, M. T., & Vance, J. A. (2001). Steady-state exhumation of the European Alps. *Geology*, *29*(1), 35–38. https://doi.org/10.1130/0091-7613(2001)029⟨0035:SSEOTE⟩2.0.CO;2

Bettinelli, P., Avouac, J. P., Flouzat, M., Bollinger, L., Ramillien, G., Rajaure, S., & Sapkota, S. (2008). Seasonal variations of seismicity and geodetic strain in the Himalaya induced by surface hydrology. *Earth and Planetary Science Letters*, *266*(3-4), 332–344. https://doi.org/10.1016/j.epsl.2007.11.021

Bhandari, N., Bhat, S. G., Lal, D., Rajagopalan, G., Tamhane, A. S., & Venkatavaradan, V. S. (1971). Fission fragment tracks in apatite: recordable track lengths. *Earth and Planetary Science Letters*, *13*(1), 191–199. https://doi.org/10.1016/0012-821X(71)90123-3

Biteau, J.-J., Le Marrec, A., Le Vot, M., & Masset, J.-M. (2006). The Aquitaine Basin. *Petroleum Geoscience*, *6*(2), 295–306. https://doi.org/10.1144/1354-079305-674

Blair, T. C., & McPherson, J. G. (1994). Alluvial fans and their natural distinction from rivers based on morphology, hydraulic processes, sedimentary processes, and facies assemblages. *Journal of Sedimentary Research A: Sedimentary Petrology & Processes*, *64*(3a), 450–489. https://doi.org/10.1306/d42681b2-2b26-11d7-8648000102c1865d

Bolliger, T. (1998). Age and geographic distribution of the youngest Upper Freshwater Molasse (OSM) of eastern Switzerland. *Eclogae Geologicae Helvetiae*, *91*(3), 321–332.

Bosch, G. V., Teixell, A., Jolivet, M., Labaume, P., Stockli, D., Domènech, M., & Monié, P. (2016). Timing of Eocene-Miocene thrust activity in the Western Axial Zone and Chaînons Béarnais (west-central Pyrenees) revealed by multi-method thermochronology. *Comptes Rendus - Geoscience*, *348*(3-4), 246–256. https://doi.org/10.1016/j.crte.2016.01.001

Bosch, G. V., Van Den Driessche, J., Babault, J., Robert, A., Carballo, A., Le Carlier, C., Loget, N., Prognon, C., Wyns, R., & Baudin, T. (2016). Peneplanation and lithosphere dynamics in the Pyrenees. *Comptes Rendus - Geoscience*, *348*(3-4), 194–202. https://doi.org/10.1016/j.crte.2015.08.005

Bourrouilh, R., Richert, J. P., & Zolnai, G. (1995). The north Pyrenean Aquitaine Basin, France: evolution and hydrocarbons. *American Association of Petroleum Geologists Bulletin*, *79*(6), 831–853. https://doi.org/10.1306/8D2B1BC4-171E-11D7-8645000102C1865D

Bovy, B. (2020). fastscape-lem/fastscape 0.1.0beta (Version 0.1.0beta). *Zenodo*.

Braun, J. (2002). Quantifying the effect of recent relief changes on age-elevation relationships. *Earth and Planetary Science Letters*, *29*(6), 787–794. https://doi.org/10.1016/S0012-821X(02)00638-6

Braun, J., Guillocheau, F., Robin, C., Baby, G., & Jelsma, H. (2014). Rapid erosion of the Southern African plateau as it climbs over a mantle superswell. *Journal of Geophysical Research: Solid Earth*, *199*(7), 6093–6112. https://doi.org/10.1002/2014JB010998

Braun, J., Simon-Labric, T., Murray, K. E., & Reiners, P. W. (2014). Topographic relief driven by variations in surface rock density. *Nature Geoscience*, *7*(7), 534–540. https://doi.org/10.1038/ngeo2171

Braun, J., van der Beek, P., Valla, P., Robert, X., Herman, F., Glotzbach, C., Pedersen, V., Perry, C., Simon-Labric, T., & Prigent, C. (2012). Quantifying rates of landscape evolution and tectonic processes by thermochronology and numerical modeling of crustal heat transport using PECUBE. *Tectonophysics*, *524*, 1–28. https://doi.org/10.1016/j.tecto.2011.12.035

Braun, J., & Willett, S. D. (2013). A very efficient O(n), implicit and parallel method to solve the stream power equation governing fluvial incision and landscape evolution. *Geomorphology*, *180*, 170–179. https://doi.org/10.1016/j.geomorph.2012.10.008

Brix, M. R., Stöckhert, B., Seidel, E., Theye, T., Thomson, S. N., & Küster, M. (2002). Thermobarometric data from a fossil zircon partial annealing zone in high pressure-low temperature rocks of eastern and central Crete, Greece. *Tectonophysics*, *349*(1-4), 309–326. https://doi.org/10.1016/S0040-1951(02)00059-8

Brocklehurst, S. H., & Whipple, K. X. (2002). Glacial erosion and relief production in the Eastern Sierra Nevada, California. *Geomorphology*, *42*(1-2), 1–24. https://doi.org/10.1016/S0169-555X(01)00069-1

Brunet, M. F. (1986). The influence of the evolution of the Pyrenees on adjacent basins. *Tectonophysics*, *129*(1-4), 343–354. https://doi.org/10.1016/0040-1951(86)90260-X

Burbank, D. W., Blythe, A. E., Putkonen, J., Pratt-Sitaula, B., Gabet, E., Oskin, M., Barros, A., & Ojha, T. P. (2003). Decoupling of erosion and precipitation in the Himalayas. *Nature*, *426*(6967), 652–655. https://doi.org/10.1038/nature02187

Burbank, D. W., & Verges, J. (1994). Reconstruction of topography and related depositional systems during active thrusting. *Journal of Geophysical Research*, *99*(B10), 20281–20297. https://doi.org/10.1029/94jb00463

Burbank, D. W., Verges, J., Munoz, J. A., & Bentham, P. (1992). Coeval hindward- and forward-imbricating thrusting in the south- central Pyrenees, Spain: timing and rates of shortening and deposition. *Geological Society of America Bulletin*, *104*(1), 3–17. https://doi.org/10.1130/0016-7606(1992)104⟨0003:CHAFIT⟩2.3.CO;2

Burbank, D. W. (1992). Causes of recent Himalayan uplift deduced from deposited patterns in the Ganges basin. *Nature*, *357*(6380), 680–683. https://doi.org/10.1038/357680a0

Burgess, P. M., & Gayer, R. A. (2000). Late Carboniferous tectonic subsidence in South Wales: Implications for Variscan basin evolution and tectonic history in SW Britain. *Journal of the Geological Society*, *157*(1), 93–104. https://doi.org/10.1144/jgs.157.1.93

Burgess, P. M., Gurnis, M., & Moresi, L. (1997). Formation of sequences in the cratonic interior of North America by interaction between mantle, eustatic, and stratigraphic processes. *Bulletin of the Geological Society of America*, *109*(12), 1515–1535. https://doi.org/10.1130/0016-7606(1997)109⟨1515:FOSITC⟩2.3.CO;2

Calvet, M. (1996). *Morphogenèse d'une montagne méditerranéenne: les Pyrénées orientales* (Doctoral dissertation).

Calvet, M. (2004). The Quaternary glaciation of the Pyrenees. *Developments in Quaternary Science*, *2*, 199–128. https://doi.org/10.1016/S1571-0866(04)80062-9

Calvet, M., & Gunnell, Y. (2008). Planar landforms as markers of denudation chronology: an inversion of East Pyrenean tectonics based on landscape and sedimentary

basin analysis. *Geological Society, London, Special Publications*, *296*(1), 147–166. https://doi.org/10.1144/SP296.10

Calvo, J., Daams, R., Morales, J., López-Martínez, N., Agustí, J., Anadón, P., Armenteros, I., Cabrera, L., Civis, J., Corrochano, A., Diaz-Molina, M., Elizaga, E., Hoyos, M., Martín-Suárez, E., Martínez, J., Moissenet, E., Muñoz, A., Perez - García, A., Pérez-González, A., ... Mein, P. (1992). Up to date Spanish continental Neogene synthesis and paleclimatic interpretation. *Revista de la Sociedad Geológica de España*, *6*(3-4), 29–40.

Carbrera, L., Roca, E., & Santanach, P. (1988). Basin formation at the end of a strike-slip fault: the Cerdanya Basin (eastern Pyrenees). *Journal - Geological Society (London)*, *145*(2), 261–268. https://doi.org/10.1144/gsjgs.145.2.0261

Cardozo, N., & Jordan, T. (2001). Causes of spatially variable tectonic subsidence in the Miocene Bermejo Foreland Basin, Argentina. *Basin Research*, *13*(3), 335–357. https://doi.org/10.1046/j.0950-091X.2001.00154.x

Carlson, W. D. (1990). Mechanisms and kinetics of apatite fission-track annealing. *American Mineralogist*, *75*(9-10), 1120–1139.

Carretier, S., & Lucazeaut, F. (2005). How does alluvial sedimentation at range fronts modify the erosional dynamics of mountain catchments? *Basin Research*, *17*(3), 361–381. https://doi.org/10.1111/j.1365-2117.2005.00270.x

Casas, A., Kearey, P., Rivero, L., & Adam, C. R. (1997). Gravity anomaly map of the Pyrenean region and a comparison of the deep geological structure of the western and eastern Pyrenees. *Earth and Planetary Science Letters*, *150*(1-2), 65–78. https://doi.org/10.1016/s0012-821x(97)00087-3

Cederbom, C. E., Sinclair, H. D., Schlunegger, F., & Rahn, M. K. (2004). Climate-induced rebound and exhumation of the European Alps. *Geology*, *32*(8), 709–712. https://doi.org/10.1130/G20491.1

Champagnac, J. D., Molnar, P., Anderson, R. S., Sue, C., & Delacou, B. (2007). Quaternary erosion-induced isostatic rebound in the western Alps. *Geology*, *35*(3), 195–198. https://doi.org/10.1130/G23053A.1

Champagnac, J. D., Molnar, P., Sue, C., & Herman, F. (2012). Tectonics, climate, and mountain topography. *Journal of Geophysical Research: Solid Earth*, *117*(B2). https://doi.org/10.1029/2011JB008348

Chapple, W. M. (1978). Mechanics of thin-skinned fold-and-thrust belts. *Bulletin of the Geological Society of America*, *89*(9), 1189–1198. https://doi.org/10.1130/0016-7606(1978)89⟨1189:MOTFB⟩2.0.CO;2

Chevrot, S., Villasenor, A., Sylvander, M., Benahmed, S., Beucler, E., Cougoulat, G., Delmas, P., Blanquat, M. D. S., Diaz, J., Gallart, J., Grimaud, F., Lagabrielle, Y., Manatschal, G., Mocquet, A., Pauchet, H., Paul, A., Péquegnat, C., Quillard, O., Roussel, S., … Wolyniec, D. (2014). High-resolution imaging of the Pyrenees and Massif Central from the data of the PYROPE and IBERARRAY portable array deployments. *Journal of Geophysical Research: Solid Earth*, *119*(8), 6399–6420. https://doi.org/10.1002/2014JB010953

Choukroune, P. (1989). The Ecors Pyrenean deep seismic profile reflection data and the overall structure of an orogenic belt. *Tectonics*, *8*(1), 23–39. https://doi.org/10.1029/TC008i001p00023

Choukroune, P., & Mattauer, M. (1978). Tectonique des plaques et Pyrenees; sur le fonctionnement de la faille transformante nord-pyreneenne; comparaisons avec des modeles actuels. *Bulletin de la Société Géologique de France*, *7*(5), 689–700. https://doi.org/10.2113/gssgfbull.s7-xx.5.689

Choukroune, P., Roure, F., Pinet, B., & Ecors Pyrenees Team. (1990). Main results of the ECORS Pyrenees profile. *Tectonophysics*, *173*(1-4), 411–423. https://doi.org/10.1016/0040-1951(90)90234-Y

Coney, P. J., Munoz, J. A., McClay, K. R., & Evenchick, C. A. (1996). Syntectonic burial and post-tectonic exhumation of the southern Pyrenees foreland fold-thrust belt. *Journal of the Geological Society*, *153*(1), 9–16. https://doi.org/10.1144/gsjgs.153.1.0009

Corrigan, J. (1991). Inversion of apatite fission track data for thermal history information. *Journal of Geophysical Research*, *96*(B3), 10347–10360. https://doi.org/10.1029/91jb00514

Costa, E., Garcés, M., López-Blanco, M., Beamud, E., Gómez-Paccard, M., & Larrasoaña, J. C. (2010). Closing and continentalization of the South Pyrenean foreland basin (NE Spain): Magnetochronological constraints. *Basin Research*, *22*(6), 904–917. https://doi.org/10.1111/j.1365-2117.2009.00452.x

Croissant, T., & Braun, J. (2014). Constraining the stream power law: A novel approach combining a landscape evolution model and an inversion method. *Earth Surface Dynamics*, *2*(1), 155–166. https://doi.org/10.5194/esurf-2-155-2014

Crowley, K. d., Cameron, M., & Schaefer, R. l. (1991). Experimental studies of annealing of etched fission tracks in fluorapatite. *Geochimica et Cosmochimica Acta*, *55*(5), 1149–1465. https://doi.org/10.1016/0016-7037(91)90320-5

Crowley, K. D. (1993). LENMODEL: A forward model for calculating length distributions and fission-track ages in apatite. *Computers and Geosciences*, *19*(5), 619–626. https://doi.org/10.1016/0098-3004(93)90098-P

Curry, M. E., van der Beek, P., Huismans, R. S., Wolf, S. G., & Muñoz, J. A. (2019). Evolving paleotopography and lithospheric flexure of the Pyrenean Orogen from 3D flexural modeling and basin analysis. *Earth and Planetary Science Letters*, *515*, 26–37. https://doi.org/10.1016/j.epsl.2019.03.009

Dahlen, F. A. (1984). Noncohesive critical Coulomb wedges: An exact solution. *Journal of Geophysical Research*, *89*(B12), 10125–10133. https://doi.org/10.1029/JB089iB12p10125

Dahlen, F. A. (1990). Critical taper model of fold-and-thrust belts and accretionary wedges. *Annual Review of Earth & Planetary Sciences*, *18*(1), 55–99. https://doi.org/10.1146/annurev.ea.18.050190.000415

Daignieres, M., Gallart, J., Banda, E., & Hirn, A. (1982). Implications of the seismic structure for the orogenic evolution of the Pyrenean Range. *Earth and Planetary Science Letters*, *57*(1), 88–100. https://doi.org/10.1016/0012-821X(82)90175-3

Darling, A., Whipple, K. X., Bierman, P., Clarke, B., & Heimsath, A. (2020). Resistant rock layers amplify cosmogenically-determined erosion rates. *Earth Surface Processes and Landforms*, *45*(2), 312–330. https://doi.org/10.1002/esp.4730

Davis, D., Suppe, J., & Dahlen, F. A. (1983). Mechanics of fold-and- thrust belts and accretionary wedges. *Journal of Geophysical Research*, *88*(B2), 1153–1172. https://doi.org/10.1029/JB088iB02p01153

Davis, W. M. (1899). The Geographical Cycle. *The Geographical Journal*, *14*(5), 481–504. https://doi.org/10.2307/1774538

Debroas, E. J. (1990). Le Flysch noir albo-cenomanien temoin de la structuration albienne a senonienne de la Zone nord-pyreneenne en Bigorre (Hautes-Pyrenees,

France). *Bulletin - Societe Geologique de France*. https://doi.org/10.2113/gssgfbull.vi.2.273

DeCelles, P. G., & Giles, K. A. (1996). Foreland basin systems. *Basin Research*, *8*(2), 105–123. https://doi.org/10.1046/j.1365-2117.1996.01491.x

Deffontaines, B., Lee, J. C., Angelier, J., Carvalho, J., & Rudant, J. (1994). New geomorphic data on the active Taiwan Orogen: a multisource approach. *Journal of Geophysical Research*, *99*(B10), 20243–20266. https://doi.org/10.1029/94jb00733

Denèle, Y., Paquette, J. L., Olivier, P., & Barbey, P. (2012). Permian granites in the Pyrenees: The Aya pluton (Basque Country). *Terra Nova*, *24*(2), 105–113. https://doi.org/10.1111/j.1365-3121.2011.01043.x

Denison, D. G., Holmes, C. C., Mallick, B. K., & Smith, A. F. (2002). Bayesian methods for nonlinear classification and regression. *John Wiley & Sons*, *386*.

Deramond, J., Souquet, P., Fondecave-Wallez, M. J., & Specht, M. (1993). Relationships between thrust tectonics and sequence stratigraphy surfaces in foredeeps: Model and examples from the Pyrenees (Cretaceous-Eocene, France, Spain). *Geological Society Special Publication*, *71*(1), 193–219. https://doi.org/10.1144/GSL.SP.1993.071.01.09

Desegaulx, P., Roure, F., & Villein, A. (1990). Structural evolution of the Pyrenees: tectonic inheritance and flexural behaviour in the continental crust. *Tectonophysics*, *182*(3-4), 211–225. https://doi.org/10.1016/0040-1951(90)90164-4

Dickinson, W. R. (1974). Plate tectonics and sedimentation, In *Tectonics and sedimentation*. https://doi.org/10.2110/pec.74.22.0001

Dodson, M. H. (1973). Closure temperature in cooling geochronological and petrological systems. *Contributions to Mineralogy and Petrology*, *40*(3), 259–274. https://doi.org/10.1007/BF00373790

Donelick, R. A. (1991). Crystallographic orientation dependence of mean etchable fission track lenglh in apatite: An empirical model and experimental observations. *American Mineralogist*, *76*(1-2), 83–91. https://doi.org/0003-004x/91/0102-0083{\$}02.00

Donelick, R. A. (2005). Apatite Fission-Track Analysis. *Reviews in Mineralogy and Geochemistry*, *58*(1), 49–94. https://doi.org/10.2138/rmg.2005.58.3

Donelick, R. A., & Miller, D. S. (1991). Enhanced tint fission track densities in low spontaneous track density apatites using 252Cf-derived fission fragment tracks: A model and experimental observations. *International Journal of Radiation Applications and Instrumentation. Part*, *18*(3), 301–307. https://doi.org/10.1016/1359-0189(91)90022-A

Doser, D. I., & Rodriguez, H. (2011). A seismotectonic study of the Southeastern Alaska Region. *Tectonophysics*, *497*(1-4), 105–113. https://doi.org/10.1016/j.tecto.2010.10.019

Duller, R. A., Whittaker, A. C., Fedele, J. J., Whitchurch, A. L., Springett, J., Smithells, R., Fordyce, S., & Allen, P. A. (2010). From grain size to tectonics. *Journal of Geophysical Research: Earth Surface*, *115*(F3). https://doi.org/10.1029/2009JF001495

Ehlers, T. A. (2005). Crustal Thermal Processes and the Interpretation of Thermochronometer Data. *Reviews in Mineralogy and Geochemistry*, *58*(1), 315–350. https://doi.org/10.2138/rmg.2005.58.12

Ehlers, T. A., & Farley, K. A. (2003). Apatite (U-Th)/He thermochronometry: Methods and applications to problems in tectonic and surface processes. *Earth and Planetary Science Letters*, *206*(1-2), 1–14. https://doi.org/10.1016/S0012-821X(02)01069-5

Elliott, D. (1976). A Discussion on natural strain and geological structure - The energy balance and deformation mechanisms of thrust sheets. *Philosophical Transactions of the Royal Society of London. Series A, Mathematical and Physical Sciences*, *283*(1312), 289–312. https://doi.org/10.1098/rsta.1976.0086

England, P., & Molnar, P. (1993). Cause and effect among thrust and normal faulting, anatectic melting and exhumation in the Himalaya. *Geological Society Special Publication*, *74*(1), 401–411. https://doi.org/10.1144/GSL.SP.1993.074.01.27

Ewing, R. C., Weber, W. J., & Clinard, F. W. (1995). Radiation effects in nuclear waste forms for high-level radioactive waste. *Progress in Nuclear Energy*, *29*(2), 63–127. https://doi.org/10.1016/0149-1970(94)00016-Y

Farías, M., Charrier, R., Carretier, S., Martinod, J., Fock, A., Campbell, D., Cáceres, J., & Comte, D. (2008). Late Miocene high and rapid surface uplift and its erosional response in the Andes of central Chile (33° - 35°S). *Tectonics*, *27*(1). https://doi.org/10.1029/2006TC002046

Farley, K. A. (2000). Helium diffusion from apatite: General behavior as illustrated by Durango fluorapatite. *Journal of Geophysical Research: Solid Earth*, *105*(B2), 2903–2914. https://doi.org/10.1029/1999JB900348

Farley, K. A. (2002). (U-Th)/He Dating: Techniques, Calibrations, and Applications. *Reviews in Mineralogy and Geochemistry*, *47*(1), 819–844. https://doi.org/10.2138/rmg.2002.47.18

Farley, K. A., Wolf, R. A., & Silver, L. T. (1996). The effects of long alpha-stopping distances on (U-Th)/He ages. *Geochimica et Cosmochimica Acta*, *60*(21), 4223–4229. https://doi.org/10.1016/S0016-7037(96)00193-7

Fechtig, H., & Kalbitzer, S. (1966). The diffusion of argon in potassium bearing solids. *Schaeffer, O.A., and Zahringer, J., eds., Potassium-Argon Dating*, *60*(21), 4223–4229.

Fillon, C., Gautheron, C., & van der Beek, P. (2013). Oligocene–Miocene burial and exhumation of the Southern Pyrenean foreland quantified by low-temperature thermochronology. *Journal of the Geological Society*, *170*(1), 67–77. https://doi.org/10.1144/jgs2012-051

Fillon, C., & van der Beek, P. (2012). Post-orogenic evolution of the southern Pyrenees: Constraints from inverse thermo-kinematic modelling of low-temperature thermochronology data. *Basin Research*, *24*(4), 418–436. https://doi.org/10.1111/j.1365-2117.2011.00533.x

Fischer, M. W. (1984). Thrust tectonics in the North Pyrenees. *Journal of Structural Geology*, *6*(6), 721–726. https://doi.org/10.1016/0191-8141(84)90011-7

Fitzgerald, P. G., Muñoz, J. A., Coney, P. J., & Baldwin, S. L. (1999). Asymmetric exhumation across the Pyrenean orogen: Implications for the tectonic evolution of a collisional orogen. *Earth and Planetary Science Letters*, *173*(3), 157–170. https://doi.org/10.1016/S0012-821X(99)00225-3

Fitzgerald, P. G. (1992). The Transantarctic Mountains of southern Victoria Land: The application of apatite fission track analysis to a rift shoulder uplift. *Tectonics*, *11*(3), 634–662. https://doi.org/10.1029/91TC02495

Fitzgerald, P. G., Sorkhabi, R. B., Redfield, T. F., & Stump, E. (1995). Uplift and denudation of the central Alaska Range: A case study in the use of apatite fission track thermochronology to determine absolute uplift parameters. *Journal of*

Geophysical Research: Solid Earth, *100*(B10), 20175–20191. https://doi.org/10.1029/95JB02150

Fitzgerald, P. G., & Stump, E. (1997). Cretaceous and Cenozoic episodic denudation of the Transantarctic Mountains, Antarctica: New constraints from apatite fission track thermochronology in the Scott Glacier region. *Journal of Geophysical Research: Solid Earth*, *102*(B4), 7747–7765. https://doi.org/10.1029/96JB03898

Fleischer, R. L., Price, P. B., & Walker, R. M. (1975). *Nuclear tracks in solids: principles and applications*. https://doi.org/9780520026650

Flemings, P. B., & Jordan, T. E. (1989). A synthetic stratigraphic model of foreland basin development. *Journal of Geophysical Research*, *94*(B4), 3851–3866. https://doi.org/10.1029/JB094iB04p03851

Flemings, P. B., & Jordan, T. E. (1990). Stratigraphic modeling of foreland basins: Interpreting thrust deformation and lithosphere rheology. *Geology*, *18*(5), 430–434. https://doi.org/10.1130/0091-7613(1990)018⟨0430:SMOFBI⟩2.3.CO;2

Flint, J. J. (1974). Stream gradient as a function of order, magnitude, and discharge. *Water Resources Research*, *10*(5), 969–973. https://doi.org/10.1029/WR010i005p00969

Flowers, R. M., & Ehlers, T. A. (2018). Rock erodibility and the interpretation of low-temperature thermochronologic data. *Earth and Planetary Science Letters*, *482*, 312–323. https://doi.org/10.1016/j.epsl.2017.11.018

Flowers, R. M., Ketcham, R. A., Shuster, D. L., & Farley, K. A. (2009). Apatite (U-Th)/He thermochronometry using a radiation damage accumulation and annealing model. *Geochimica et Cosmochimica Acta*, *73*(8), 2347–2365. https://doi.org/10.1016/j.gca.2009.01.015

Ford, M., Hemmer, L., Vacherat, A., Gallagher, K., & Christophoul, F. (2016). Retro-wedge foreland basin evolution along the ECORS line, eastern Pyrenees, France. *Journal of the Geological Society*, *173*(3), 419–437. https://doi.org/10.1144/jgs2015-129

Forte, A. M., Yanites, B. J., & Whipple, K. X. (2016). Complexities of landscape evolution during incision through layered stratigraphy with contrasts in rock strength. *Earth Surface Processes and Landforms*, *41*(12), 1736–1757. https://doi.org/10.1002/esp.3947

Galbraith, R. F., & Laslett, G. M. (1993). Statistical models for mixed fission track ages. *Nuclear Tracks and Radiation Measurements*, *21*(4), 459–470. https://doi.org/10.1016/1359-0189(93)90185-C

Galbraith, R. F., & Laslett, G. M. (1997). Statistical modelling of thermal annealing of fission tracks in zircon. *Chemical Geology*, *140*(1-2), 123–135. https://doi.org/10.1016/S0009-2541(97)00016-8

Galbraith, R. F., Laslett, G. M., Green, P. F., & Duddy, I. R. (1990). Apatite fission track analysis: geological thermal history analysis based on a three- dimensional random process of linear radiation damage. *Philosophical Transactions of the Royal Society of London*, *332*(1627), 419–438. https://doi.org/10.1098/rsta.1990.0124

Gallagher, K. (2005). Exploiting 3D Spatial Sampling in Inverse Modeling of Thermochronological Data. *Reviews in Mineralogy and Geochemistry*, *58*(1), 375–387. https://doi.org/10.2138/rmg.2005.58.14

Gallagher, K., Brown, R., & Johnson, C. (1998). Fission track analysis and its applications to geological problems. *Annual Review of Earth and Planetary Sciences*, *26*(1), 519–572. https://doi.org/10.1146/annurev.earth.26.1.519

Gallagher, K. (2012). Transdimensional inverse thermal history modeling for quantitative thermochronology. *Journal of Geophysical Research: Solid Earth*, *117*(B2). https://doi.org/10.1029/2011JB008825

Gallagher, K., Charvin, K., Nielsen, S., Sambridge, M., & Stephenson, J. (2009). Markov chain Monte Carlo (MCMC) sampling methods to determine optimal models, model resolution and model choice for Earth Science problems. *Marine and Petroleum Geology*, *26*(4), 525–535. https://doi.org/10.1016/j.marpetgeo.2009.01.003

Gallen, S. F. (2018). Lithologic controls on landscape dynamics and aquatic species evolution in post-orogenic mountains. *Earth and Planetary Science Letters*, *493*, 150–160. https://doi.org/10.1016/j.epsl.2018.04.029

Garcia-Castellanos, D., Fernández, M., & Torne, M. (2002). Modeling the evolution of the Guadalquivir foreland basin (southern Spain). *Tectonics*, *21*(3), 9–17. https://doi.org/10.1029/2001TC001339

Garcia-Castellanos, D. (2002). Interplay between lithospheric flexure and river transport in foreland basins. *Basin Research*, *14*(2), 89–104. https://doi.org/10.1046/j.1365-2117.2002.00174.x

Garcia-Castellanos, D., Vergés, J., Gaspar-Escribano, J., & Cloetingh, S. (2003). Interplay between tectonics, climate, and fluvial transport during the Cenozoic evolution of the Ebro Basin (NE Iberia). *Journal of Geophysical Research: Solid Earth*, *108*(B7). https://doi.org/10.1029/2002JB002073

Garver, J. I., & Brandon, M. T. (1994). Fission-track ages of detrital zircons from Cretaceous strata, southern British Columbia: Implications for the Baja BC hypothesis. *Tectonics*, *12*(2), 401–420. https://doi.org/10.1029/93TC02939

Garver, J. I., Brandon, M. T., Roden-Tice, M., & Kamp, P. J. J. (1999). Exhumation history of orogenic highlands determined by detrital fission-track thermochronology. *Geological Society, London, Special Publications*, *154*(1), 283–304. https://doi.org/10.1144/GSL.SP.1999.154.01.13

Gaspar-Escribano, J. M., Van Wees, J. D., Ter Voorde, M., Cloetingh, S., Roca, E., Cabrera, L., Muñoz, J. A., Ziegler, P. A., & Garcia-Castellanos, D. (2001). Three-dimensional flexural modelling of the Ebro Basin (NE Iberia). *Geophysical Journal International*, *145*(2), 349–367. https://doi.org/10.1046/j.1365-246X.2001.01379.x

Gautheron, C., & Tassan-Got, L. (2010). A Monte Carlo approach to diffusion applied to noble gas/helium thermochronology. *Chemical Geology*, *273*(3-4), 212–224. https://doi.org/10.1016/j.chemgeo.2010.02.023

Gautheron, C., Tassan-Got, L., Barbarand, J., & Pagel, M. (2009). Effect of alpha-damage annealing on apatite (U-Th)/He thermochronology. *Chemical Geology*, *266*(3-4), 157–170. https://doi.org/10.1016/j.chemgeo.2009.06.001

Gibson, M., Sinclair, H. D., Lynn, G. J., & Stuart, F. M. (2007). Late- to post-orogenic exhumation of the central Pyrenees revealed through combined thermochronological data and modelling. *Basin Research*, *19*(3), 323–334. https://doi.org/10.1111/j.1365-2117.2007.00333.x

Gilbert, G. (1877). Land Sculptures - Geology of the Henry Mountains. *Monograph*. https://doi.org/10.1038/022266c0

Gilks, W. R., Richardson, S., & Spiegelhalter, D. J. (1996). Introducing markov chain monte carlo. *Markov chain Monte Carlo in practice*, *1*, 19.

Gilluly, J. (1955). Geologic contrasts between continents and ocean basins. *Geol. Soc. Amer*, 7–18.

Gleadow, A. J. W. (1981). Fission-track dating methods: What are the real alternatives? *Nuclear Tracks*, *5*(1-2), 3–14. https://doi.org/10.1016/0191-278X(81)90021-4

Gleadow, A. J. W., & Duddy, I. R. (1981). A natural long-term track annealing experiment for apatite. *Nuclear Tracks*, *5*(1-2), 169–174. https://doi.org/10.1016/0191-278X(81)90039-1

Gleadow, A. J. W., Duddy, I. R., Green, P. F., & Hegarty, K. A. (1986). Fission track lengths in the apatite annealing zone and the interpretation of mixed ages. *Earth and Planetary Science Letters*, *78*(2-3), 245–254. https://doi.org/10.1016/0012-821X(86)90065-8

Glotzbach, C., van der Beek, P. A., & Spiegel, C. (2011). Episodic exhumation and relief growth in the Mont Blanc massif, Western Alps from numerical modelling of thermochronology data. *Earth and Planetary Science Letters*, *304*(3-4), 417–430. https://doi.org/10.1016/j.epsl.2011.02.020

Green, P. F. (1981). "Track-in-track" length measurements in annealed apatites. *Nuclear Tracks*, *5*(1-2), 121–128. https://doi.org/10.1016/0191-278X(81)90034-2

Green, P. F., & Duddy, I. R. (2006). Interpretation of apatite (U-Th)/He ages and fission track ages from cratons. *Earth and Planetary Science Letters*, *244*(3-4), 541–547. https://doi.org/10.1016/j.epsl.2006.02.024

Green, P. F., Duddy, I. R., Gleadow, A. J. W., Tingate, P., & Laslett, G. M. (1986). Thermal annealing of fission tracks in apatite 1. Variable temperature behaviour. *Chemical Geology: Isotope Geoscience Section*, *73*(1), 25–38. https://doi.org/10.1016/0168-9622(88)90019-X

Green, P. F., Duddy, I. R., Laslett, G. M., Hegarty, K. A., Gleadow, A. J. W., & Lovering, J. F. (1989). Thermal annealing of fission tracks in apatite 4. Quantitative modelling techniques and extension to geological timescales. *Chemical Geology: Isotope Geoscience Section*, *79*(2), 155–182. https://doi.org/10.1016/0168-9622(89)90018-3

Green, P. F., & Hurford, A. J. (1984). Thermal neutron dosimetry for fission track dating. *Nuclear Tracks and Radiation Measurements (1982)*, *9*(3-4), 231–241. https://doi.org/10.1016/0735-245X(84)90190-X

Grool, A. R., Ford, M., Vergés, J., Huismans, R. S., Christophoul, F., & Dielforder, A. (2018). Insights Into the Crustal-Scale Dynamics of a Doubly Vergent Orogen From a Quantitative Analysis of Its Forelands: A Case Study of the Eastern Pyrenees. *Tectonics*, *37*(2), 450–476. https://doi.org/10.1002/2017TC004731

Guenthner, W. R., Reiners, P. W., Ketcham, R. A., Nasdala, L., & Giester, G. (2013). Helium diffusion in natural zircon: radiation damage, anisotropy, and the interpretation of zircon (U-TH)/He thermochronology. *American Journal of Science*, *313*(3), 145–198. https://doi.org/10.2475/03.2013.01

Gunnell, Y., Calvet, M., Brichau, S., Carter, A., Aguilar, J. P., & Zeyen, H. (2009). Low long-term erosion rates in high-energy mountain belts: Insights from thermo- and biochronology in the Eastern Pyrenees. *Earth and Planetary Science Letters*, *278*(3-4), 208–218. https://doi.org/10.1016/j.epsl.2008.12.004

Hack, J. T. (1973). Stream-profile analysis and stream-gradient index. *Journal of Research of the US Geological Survey*, *1*(4), 421–429.

Hancock, G. S., Anderson, R. S., & Whipple, K. X. (1998). Beyond power: Bedrock river incision process and form, In *Geophysical monograph series*. https://doi.org/10.1029/GM107p0035

Harel, M. A., Mudd, S. M., & Attal, M. (2016). Global analysis of the stream power law parameters based on worldwide 10Be denudation rates. *Geomorphology*, *268*, 184–196. https://doi.org/10.1016/j.geomorph.2016.05.035

Harkins, N., Kirby, E., Heimsath, A., Robinson, R., & Reiser, U. (2007). Transient fluvial incision in the headwaters of the Yellow River, northeastern Tibet, China. *Journal of Geophysical Research: Earth Surface*, *112*(F3). https://doi.org/10.1029/2006JF000570

Hartmann, J., & Moosdorf, N. (2012). The new global lithological map database GLiM: A representation of rock properties at the Earth surface. *Geochemistry, Geophysics, Geosystems*, *13*(12). https://doi.org/10.1029/2012GC004370

Heller, P. L., Angevine, C. L., Winslow, N. S., & Paola, C. (1988). Two-phase stratigraphic model of foreland-basin sequences. *Geology*, *16*(6), 501–504. https://doi.org/10.1130/0091-7613(1988)016⟨0501:TPSMOF⟩2.3.CO;2

Henck, A. C., Huntington, K. W., Stone, J. O., Montgomery, D. R., & Hallet, B. (2011). Spatial controls on erosion in the Three Rivers Region, southeastern Tibet

and southwestern China. *Earth and Planetary Science Letters*, *303*(1-2), 71–83. https://doi.org/10.1016/j.epsl.2010.12.038

Hetzel, R., Dunkl, I., Haider, V., Strobl, M., von Eynatten, H., Ding, L., & Frei, D. (2011). Peneplain formation in southern Tibet predates the India-Asia collision and plateau uplift. *Geology*, *39*(10), 983–986. https://doi.org/10.1130/G32069.1

Hilley, G. E., & Strecker, M. R. (2004). Steady state erosion of critical Coulomb wedges with applications to Taiwan and the Himalaya. *Journal of Geophysical Research: Solid Earth*, *109*(B1). https://doi.org/10.1029/2002jb002284

Hobley, D. E., Sinclair, H. D., Mudd, S. M., & Cowie, P. A. (2011). Field calibration of sediment flux dependent river incision. *Journal of Geophysical Research: Earth Surface*, *116*(F4). https://doi.org/10.1029/2010JF001935

Hodges, K. V., Wobus, C., Ruhl, K., Schildgen, T., & Whipple, K. X. (2004). Quaternary deformation, river steepening, and heavy precipitation at the front of the Higher Himalayan ranges. *Earth and Planetary Science Letters*, *220*(3-4), 379–389. https://doi.org/10.1016/S0012-821X(04)00063-9

Hoskins, B. J., & Karoly, D. J. (1981). The steady linear response of a spherical atmosphere to thermal and orographic forcing. *Journal of the Atmospheric Sciences*, *38*(6), 1179–1196. https://doi.org/10.1175/1520-0469(1981)038⟨1179:TSLROA⟩2.0.CO;2

House, M. A., Farley, K. A., & Stockli, D. (2000). Helium chronometry of apatite and titanite using Nd-YAG laser heating. *Earth and Planetary Science Letters*, *183*(3-4), 365–368. https://doi.org/10.1016/S0012-821X(00)00286-7

House, M. A., Wernicke, B. P., & Farley, K. A. (1998). Dating topography of the Sierra Nevada, California, using apatite (U–Th)/He ages. *Nature*, *396*(6706), 66–69. https://doi.org/10.1038/23926

House, M. A., Farley, K. A., & Kohn, B. P. (1999). An empirical test of helium diffusion in apatite: Borehole data from the Otway basin, Australia. *Earth and Planetary Science Letters*, *170*(4), 463–474. https://doi.org/10.1016/S0012-821X(99)00120-X

Howard, A. D. (1980). Thresholds in river regimes. *Thresholds in geomorphology*, *227*, 227–258.

Howard, A. D., & Kerby, G. (1983). Channel changes in badlands. *Geological Society of America Bulletin*, *94*(6), 739–752. https://doi.org/10.1130/0016-7606(1983)94⟨739:CCIB⟩2.0.CO;2

Hurford, A. J. (1986). Cooling and uplift patterns in the Lepontine Alps South Central Switzerland and an age of vertical movement on the Insubric fault line. *Contributions to Mineralogy and Petrology*, *92*(4), 413–247. https://doi.org/10.1007/BF00374424

Hurford, A. J. (1990). Standardization of fission track dating calibration: Recommendation by the Fission Track Working Group of the I.U.G.S. Subcommission on Geochronology. *Chemical Geology: Isotope Geoscience Section*, *80*(2), 171–178. https://doi.org/10.1016/0168-9622(90)90025-8

Hurford, A. J., & Carter, A. (1991). The role of fission track dating in discrimination of provenance. *Geological Society, London, Special Publications*, *57*(1), 67–78. https://doi.org/10.1144/GSL.SP.1991.057.01.07

Hurford, A. J., & Green, P. F. (1982). A users' guide to fission track dating calibration. *Earth and Planetary Science Letters*, *59*(2), 343–354. https://doi.org/10.1016/0012-821X(82)90136-4

Hurley, A. C. (1954). The electrostatic calculation of molecular energies-II. Approximate wave functions and the electrostatic method. *Proceedings of the Royal Society of London. Series A. Mathematical and Physical Sciences*, *226*(1165), 179–192.

Huyghe, D., Mouthereau, F., & Emmanuel, L. (2012). Oxygen isotopes of marine mollusc shells record Eocene elevation change in the Pyrenees. *Earth and Planetary Science Letters*, *345*, 131–141. https://doi.org/10.1016/j.epsl.2012.06.035

Jaeger, J. C., & Carslaw, H. S. (1959). Conduction of heat in solids. *Clarendon P.*

Jamieson, R. A., & Beaumont, C. (1988). Orogeny and metamorphism: A model for deformation and pressure-temperature-time paths with applications to the central and southern Appalachians. *Tectonics*, *7*(3), 417–445. https://doi.org/10.1029/TC007i003p00417

Jammes, S., Manatschal, G., Lavier, L., & Masini, E. (2009). Tectonosedimentary evolution related to extreme crustal thinning ahead of a propagating ocean: Example of the western Pyrenees. *Tectonics*, *28*(4). https://doi.org/10.1029/2008TC002406

Jiménez-Sánchez, M., Rodríguez-Rodríguez, L., García-Ruiz, J. M., Domínguez-Cuesta, M. J., Farias, P., Valero-Garcés, B., Moreno, A., Rico, M., & Valcárcel, M. (2013). A review of glacial geomorphology and chronology in northern Spain: Timing and regional variability during the last glacial cycle. *Geomorphology*, *196*, 50–64. https://doi.org/10.1016/j.geomorph.2012.06.009

Johnson, D. D., & Beaumont, C. (1995). Preliminary results from a planform kinematic model of orogen evolution, surface processes and the development of clastic foreland basin stratigraphy, In *Stratigraphic evolution of foreland basins*. https://doi.org/10.2110/pec.95.52.0003

Jolivet, L., Gorini, C., Smit, J., & Leroy, S. (2015). Continental breakup and the dynamics of rifting in back-arc basins: The Gulf of Lion margin. *Tectonics*, *34*(4), 662–679. https://doi.org/10.1002/2014TC003570

Jolivet, M., Labaume, P., Monié, P., Brunel, M., Arnaud, N., & Campani, M. (2007). Thermochronology constraints for the propagation sequence of the south Pyrenean basement thrust system (France-Spain). *Tectonics*, *26*(5). https://doi.org/10.1029/2006TC002080

Jordan, T. E. (1981). Thrust loads and foreland basin evolution, Cretaceous, western United States. *AAPG Bulletin*, *65*(12), 2506–2520.

Judson, S., & Ritter, D. F. (1964). Rates of regional denudation in the United States. *Journal of Geophysical Research*, *69*(16), 3395–3401. https://doi.org/10.1029/jz069i016p03395

Karner, G. D., & Watts, A. B. (1983). Gravity anomalies and flexure of the lithosphere at mountain ranges. *Journal of Geophysical Research*, *88*(B12), 10449–10477. https://doi.org/10.1029/JB088iB12p10449

Kasuya, M., & Naeser, C. W. (1988). The effect of α-damage on fission-track annealing in zircon. *International Journal of Radiation Applications and Instrumentation. Part*, *14*(4), 477–480. https://doi.org/10.1016/1359-0189(88)90008-8

Ketcham, R. A. (2005). Forward and Inverse Modeling of Low-Temperature Thermochronometry Data. *Reviews in Mineralogy and Geochemistry*, *58*(1), 275–314. https://doi.org/10.2138/rmg.2005.58.11

Ketcham, R. A., Carter, A., Donelick, R. A., Barbarand, J., & Hurford, A. J. (2007). Improved modeling of fission-track annealing in apatite. *American Mineralogist*, *92*(5-6), 799–810. https://doi.org/10.2138/am.2007.2281

Ketcham, R. A., Donelick, R. A., & Carlson, W. D. (1999). Variability of apatite fission-track annealing kinetics: III. Extrapolation to geological time scales. *American Mineralogist*, *84*(9), 1235–1255. https://doi.org/10.2138/am-1999-0903

Ketcham, R. A., Donelick, R. A., & Donelick, M. B. (2003). AFTSolve: A program for multi-kinetic modeling of apatite fission-track data. *American Mineralogist*, *2*(1), 1–32.

Kirby, E., & Whipple, K. X. (2001). Quantifying differential rock-uplift rates via stream profile analysis. *Geology*, *29*(5), 415–418. https://doi.org/10.1130/0091-7613(2001)029⟨0415:QDRURV⟩2.0.CO;2

Kirby, E., & Whipple, K. X. (2012). Expression of active tectonics in erosional landscapes. *Journal of Structural Geology*, *44*, 54–75. https://doi.org/10.1016/j.jsg.2012.07.009

Knight, J. (1999). Morphology and palaeoenvironmental interpretation of deformed soft-sediment clasts: Examples from within Late Pleistocene glacial outwash, Tempo Valley, Northern Ireland. *Sedimentary Geology*, *128*(3-4), 293–306. https://doi.org/10.1016/S0037-0738(99)00080-9

Kohn, B. P., Belton, D. X., Brown, R. W., Gleadow, A. J. W., Green, P. F., & Lovering, J. F. (2003). Comment on: "Experimental evidence for the pressure dependence of fission track annealing in apatite" by A.S. Wendt et al. [Earth Planet. Sci. Lett. 201 (2002) 593-607]. *Earth and Planetary Science Letters*, *215*(1-2), 299–306. https://doi.org/10.1016/S0012-821X(03)00077-3

Koons, P. O. (1989). The topographic evolution of collisional mountain belts: a numerical look at the Southern Alps, New Zealand. *American Journal of Science*, *289*(9), 1041–1069. https://doi.org/10.2475/ajs.289.9.1041

Koons, P. O. (1990). Two-sided orogen: collision and erosion from the sandbox to the Southern Alps, New Zealand. *Geology*, *18*(8), 679–682. https://doi.org/10.1130/0091-7613(1990)018⟨0679:TSOCAE⟩2.3.CO;2

Koons, P. O., Upton, P., & Barker, A. D. (2012). The influence of mechanical properties on the link between tectonic and topographic evolution. *Geomorphology*, *137*(1), 168–180. https://doi.org/10.1016/j.geomorph.2010.11.012

Kuhlemann, J., Frisch, W., Székely, B., Dunkl, I., & Kázmér, M. (2002). Post-collisional sediment budget history of the Alps: Tectonic versus climatic control. *Interna-*

tional Journal of Earth Sciences, *91*(5), 818–837. https://doi.org/10.1007/s00531-002-0266-y

Kuhlemann, J. (2000). Post-collisional sediment budget of circum-Alpine basins (Central Europe). *Mem. Sci. Geol. Padova*, *52*(1), 1–91.

Lague, D. (2014). The stream power river incision model: Evidence, theory and beyond. *Earth Surface Processes and Landforms*, *39*(1), 38–61. https://doi.org/10.1002/esp.3462

Lamb, S., & Davis, P. (2003). Cenozoic climate change as a possible cause for the rise of the Andes. *Nature*, *425*(6960), 792–797. https://doi.org/10.1038/nature02049

Laslett, G. M., & Galbraith, R. F. (1996). Statistical modelling of thermal annealing of fission tracks in apatite. *Geochimica et Cosmochimica Acta*, *60*(24), 5117–5131. https://doi.org/10.1016/S0016-7037(96)00307-9

Laslett, G. M., Galbraith, R. F., & Green, P. F. (1994). The analysis of projected fission track lengths. *Radiation Measurements*, *23*(1), 103–123. https://doi.org/10.1016/1350-4487(94)90028-0

Laslett, G. M., Gleadow, A. J. W., & Duddy, I. R. (1984). The relationship between fission track length and track density in apatite. *Nuclear Tracks and Radiation Measurements (1982)*, *9*(1), 29–38. https://doi.org/10.1016/0735-245X(84)90019-X

Laslett, G. M., Green, P. F., Duddy, I. R., & Gleadow, A. J. W. (1987). Thermal annealing of fission tracks in apatite 2. A quantitative analysis. *Chemical Geology: Isotope Geoscience Section*, *65*(1), 1–13. https://doi.org/10.1016/0168-9622(87)90057-1

Laslett, G. M., Kendall, W. S., Gleadow, A. J. W., & Duddy, I. R. (1982). Bias in measurement of fission-track length distributions. *Nuclear Tracks and Radiation Measurements (1982)*, *6*(2-3), 79–85. https://doi.org/10.1016/0735-245X(82)90031-X

Lewis, C. J., McDonald, E. V., Sancho, C., Peña, J. L., & Rhodes, E. J. (2009). Climatic implications of correlated Upper Pleistocene glacial and fluvial deposits on the Cinca and Gállego Rivers (NE Spain) based on OSL dating and soil stratigraphy. *Global and Planetary Change*, *67*(3-4), 141–152. https://doi.org/10.1016/j.gloplacha.2009.01.001

Lippolt, H. J., Leitz, M., Wernicke, R. S., & Hagedorn, B. (1994). (Uranium + thorium)/helium dating of apatite: experience with samples from different geochem-

ical environments. *Chemical Geology*, *112*(1-2), 179–191. https://doi.org/10.1016/0009-2541(94)90113-9

Lisiecki, L. E. (2010). Links between eccentricity forcing and the 100,000-year glacial cycle. *Nature Geoscience*, *3*(5), 349–352. https://doi.org/10.1038/ngeo828

López-Blanco, M., Marzo, M., & Munoz, J. A. (2003). Low-amplitude, synsedimentary folding of a deltaic complex: Roda Sandstone (lower Eocene), South-Pyrenean Foreland Basin. *Basin Research*, *15*(1), 73–96. https://doi.org/10.1046/j.1365-2117.2003.00193.x

Lucas, C. (1985). *Essai sur la géodynamique de dépôts continentaux du Permien et du Trias: le grès rouge du versant nord des Pyrénées* (Doctoral dissertation).

Lutz, T. M., & Omar, G. (1991). An inverse method of modeling thermal histories from apatite fission-track data. *Earth and Planetary Science Letters*, *104*(2-4), 181–195. https://doi.org/10.1016/0012-821X(91)90203-T

Lynn, G. J. (2005). *Macrogeomorphology and erosional history of the postorogenic Pyrenean mountain belt* (Doctoral dissertation).

Lyon-Caen, H., & Molnar, P. (1985). Gravity anomalies, flexure of the Indian Plate, and the structure, support and evolution of the Himalaya and Ganga Basin. *Tectonics*, *4*(6), 513–538. https://doi.org/10.1029/TC004i006p00513

Macchiavelli, C., Vergés, J., Schettino, A., Fernàndez, M., Turco, E., Casciello, E., Torne, M., Pierantoni, P. P., & Tunini, L. (2017). A New Southern North Atlantic Isochron Map: Insights Into the Drift of the Iberian Plate Since the Late Cretaceous. *Journal of Geophysical Research: Solid Earth*, *122*(12), 9603–9626. https://doi.org/10.1002/2017JB014769

MacGregor, K. R., Anderson, R. S., Anderson, S. P., & Waddington, E. D. (2000). Numerical simulations of glacial-valley longitudinal profile evolution. *Geology*, *28*(11), 1031–1034. https://doi.org/10.1130/0091-7613(2000)028⟨1031:NSOGVL⟩2.3.CO;2

Manatschal, G., & Bernoulli, D. (1999). Architecture and tectonic evolution of nonvolcanic margins: Present-day Galicia and ancient Adria. *Tectonics*, *18*(6), 1099–1119. https://doi.org/10.1029/1999TC900041

Mațenco, L. (2017). Tectonics and exhumation of Romanian carpathians: Inferences from kinematic and thermochronological studies, In *Springer geography*. https://doi.org/10.1007/978-3-319-32589-7{_}2

Maurel, O., Moniè, P., Pik, R., Arnaud, N., Brunel, M., & Jolivet, M. (2008). The Meso-Cenozoic thermo-tectonic evolution of the Eastern Pyrenees: An 40Ar/39Ar fission track and (U-Th)/He thermochronological study of the Canigou and Mont-Louis massifs. *International Journal of Earth Sciences*, *97*(3), 565–584. https://doi.org/10.1007/s00531-007-0179-x

Meesters, a., & Dunai, T. (2002). Solving the production – diffusion equation for finite diffusion domains of various shapes Part II . Application to cases with a-ejection and nonhomogeneous distribution of the source. *Chemical Geology*, *186*(1-2), 57–73. https://doi.org/10.1016/S0009-2541(01)00422-3

Meigs, A. J., Vergés, J., & Burbank, D. W. (1996). Ten-million-year history of a thrust sheet. *Bulletin of the Geological Society of America*, *108*(12), 1608–1625. https://doi.org/10.1130/0016-7606(1996)108⟨1608:TMYHOA⟩2.3.CO;2

Mellere, D. (1994). Thrust-generated, back-fill stacking of alluvial fan sequences, south-central Pyrenees, Spain (La Pobla de Segur Conglomerates). *Tectonic controls and signatures in sedimentary successions*, *40*, 259.

Mellere, D. (2009). Thrust-Generated, Back-Fill Stacking of Alluvial Fan Sequences, South-Central Pyrenees, Spain (La Pobla De Segur Conglomerates), In *Tectonic controls and signatures in sedimentary successions*. https://doi.org/10.1002/9781444304053.ch14

Metcalf, J. R., Fitzgerald, P. G., Baldwin, S. L., & Muñoz, J. A. (2009). Thermochronology of a convergent orogen: Constraints on the timing of thrust faulting and subsequent exhumation of the Maladeta Pluton in the Central Pyrenean Axial Zone. *Earth and Planetary Science Letters*, *287*(3-4), 488–503. https://doi.org/10.1016/j.epsl.2009.08.036

Michael, N. A., Whittaker, A. C., Carter, A., & Allen, P. A. (2014). Volumetric budget and grain-size fractionation of a geological sediment routing system: Eocene Escanilla Formation, south-central Pyrenees. *Bulletin of the Geological Society of America*, *126*(3-4), 585–599. https://doi.org/10.1130/B30954.1

Mitrovica, J. X., Beaumont, C., & Jarvis, G. T. (1989). Tilting of continental interiors by the dynamical effects of subduction. *Tectonics*, *8*(5), 1079–1094. https://doi.org/10.1029/TC008i005p01079

Monod, B., Bourroullec, I., Chèvremont, P., LeBayon, B., Nehlig, P., Aretz, M., & Blanquat, M. (2014). Carte géologique numérique à 1/250 000 de la région Midi-Pyrénées, Notice.

Monod, B., Regard, V., Carcone, J., Wyns, R., & Christophoul, F. (2016). Postorogenic planar palaeosurfaces of the central Pyrenees: Weathering and neotectonic records. *Comptes Rendus - Geoscience*, *348*(3-4), 184–193. https://doi.org/10.1016/j.crte.2015.09.005

Montgomery, D. R., Balco, G., & Willett, S. D. (2001). Climate, tectonics, and the morphology of the Andes. *Geology*, *29*(7), 579–582. https://doi.org/10.1130/0091-7613(2001)029⟨0579:CTATMO⟩2.0.CO;2

Montgomery, D. R., & Brandon, M. T. (2002). Topographic controls on erosion rates in tectonically active mountain ranges. *Earth and Planetary Science Letters*, *201*(3-4), 481–489. https://doi.org/10.1016/S0012-821X(02)00725-2

Moon, S., Page Chamberlain, C., Blisniuk, K., Levine, N., Rood, D. H., & Hilley, G. E. (2011). Climatic control of denudation in the deglaciated landscape of the Washington Cascades. *Nature Geoscience*, *4*(7), 469–473. https://doi.org/10.1038/ngeo1159

Morisawa, M. E. (1962). Quantitative geomorphology of some watersheds in the appalachian plateau. *Bulletin of the Geological Society of America*, *73*(9), 1025–1046. https://doi.org/10.1130/0016-7606(1962)73[1025:QGOSWI]2.0.CO;2

Morris, R. G., Sinclair, H. D., & Yelland, A. J. (1998). Exhumation of the Pyrenean Orogen: implications for sediment discharge. *Basin Research*, *10*(1), 69–86. https://doi.org/10.1046/j.1365-2117.1998.00053.x

Mouchené, M., van der Beek, P., Mouthereau, F., & Carcaillet, J. (2017). Controls on Quaternary incision of the Northern Pyrenean foreland: Chronological and geomorphological constraints from the Lannemezan megafan, SW France. *Geomorphology*, *281*, 78–93. https://doi.org/10.1016/j.geomorph.2016.12.027

Mouthereau, F., Filleaudeau, P. Y., Vacherat, A., Pik, R., Lacombe, O., Fellin, M. G., Castelltort, S., Christophoul, F., & Masini, E. (2014). Placing limits to shortening evolution in the Pyrenees: Role of margin architecture and implications for the Iberia/Europe convergence. *Tectonics*, *33*(12), 2283–2314. https://doi.org/10.1002/2014TC003663

Mudd, S. M., Attal, M., Milodowski, D. T., Grieve, S. W., & Valters, D. A. (2014). A statistical framework to quantify spatial variation in channel gradients using the integral method of channel profile analysis. *Journal of Geophysical Research: Earth Surface*, *119*(2), 138–152. https://doi.org/10.1002/2013JF002981

Mudd, S. M., Clubb, F. J., Gailleton, B., & Hurst, M. D. (2018). How concave are river channels? *Earth Surface Dynamics Discussions*, *6*(2), 505–523. https://doi.org/10.5194/esurf-2018-7

Muñoz, J. A. (1992). Evolution of a continental collision belt: ECORS-Pyrenees crustal balanced cross-section, In *Thrust tectonics*. https://doi.org/10.1007/978-94-011-3066-0{_}21

Naylor, M., & Sinclair, H. D. (2007). Punctuated thrust deformation in the context of doubly vergent thrust wedges: Implications for the location of uplift and exhumation. *Geology*, *35*(6), 559–562. https://doi.org/10.1130/G23448A.1

Naylor, M., & Sinclair, H. D. (2008). Pro- vs. retro-foreland basins. *Basin Research*, *20*(3), 285–303. https://doi.org/10.1111/j.1365-2117.2008.00366.x

Naylor, M., Sinclair, H. D., Willett, S., & Cowie, P. A. (2005). A discrete element model for orogenesis and accretionary wedge growth. *Journal of Geophysical Research: Solid Earth*, *110*(B12). https://doi.org/10.1029/2003JB002940

Nijman, W. (1998). Cyclicity and basin axis shift in a piggybank basin: towards modelling of the Eocene Tremp-Ager Basin, South Pyrenees, Spain. *Geological Society Special Publication*, *134*(1), 135–162. https://doi.org/10.1144/GSL.SP.1998.134.01.07

Norris, R. J., Koons, P. O., & Cooper, A. F. (1990). The obliquely-convergent plate boundary in the South Island of New Zealand: implications for ancient collision zones. *Journal of Structural Geology*, *12*(5-6), 715–725. https://doi.org/10.1016/0191-8141(90)90084-C

Olivet, J. L. (1996). La cinématique de la plaque ibérique. *Bulletin des Centres de Recherches Elf Exploration Production*, *20*(1), 131–195.

Ortiz, A., Guillocheau, F., Lasseur, E., Briais, J., Robin, C., Serrano, O., & Fillon, C. (2020). Sediment routing system and sink preservation during the post-orogenic evolution of a retro-foreland basin: The case example of the North Pyrenean (Aquitaine, Bay of Biscay) Basins. *Marine and Petroleum Geology*, *112*. https://doi.org/10.1016/j.marpetgeo.2019.104085

Ortuño, M., Martí, A., Martín-Closas, C., Jiménez-Moreno, G., Martinetto, E., & Santanach, P. (2013). Palaeoenvironments of the late miocene prüedo basin: Implications for the uplift of the central pyrenees. *Journal of the Geological Society*, *170*(1), 79–92. https://doi.org/10.1144/jgs2011-121

O'Sullivan, P. B., & Parrish, R. R. (1995). The importance of apatite composition and single-grain ages when interpreting fission track data from plutonic rocks: a case study from the Coast Ranges, British Columbia. *Earth and Planetary Science Letters*, *132*(1-4), 213–224. https://doi.org/10.1016/0012-821X(95)00058-K

Paris, J. P., Icole, M., Tegyey, A., Monciardini, C., Andreieff, P., & Collignon, M. (1975). Carte géol. France (1/50000), feuille MONTREJEAU (1054). *Orléans: Bureaux de recherches géologiques et minières.*

Paris, J. P., & Monciardini, C. (1971). Carte géol. France (1/50000), feuille ST-GAUDENS. *Orléans: Bureaux de recherches géologiques et minières.*

Pazzaglia, F. J., & Brandon, M. T. (1996). Macrogeomorphic evolution of the post-Triassic Appalachian mountains determined by deconvolution of the offshore basin sedimentary record. *Basin Research*, *8*(3), 255–278. https://doi.org/10.1046/j.1365-2117.1996.00274.x

Pedreira, D., Pulgar, J. A., Gallart, J., & Torné, M. (2007). Three-dimensional gravity and magnetic modeling of crustal indentation and wedging in the western Pyrenees-Cantabrian Mountains. *Journal of Geophysical Research: Solid Earth*, *112*(B2). https://doi.org/10.1029/2007JB005021

Pelletier, J. D. (2004). The influence of piedmont deposition on the time scale of mountain-belt denudation. *Geophysical Research Letters*, *31*(15). https://doi.org/10.1029/2004GL020052

Peper, T., Beekman, F., & Cloetingh, S. (1992). Consequences of thrusting and intraplate stress fluctuations for vertical motions in foreland basins and peripheral areas. *Geophysical Journal International*, *11*(1), 104–126. https://doi.org/10.1111/j.1365-246X.1992.tb00558.x

Perron, T. J., & Royden, L. H. (2013). An integral approach to bedrock river profile analysis. *Earth Surface Processes and Landforms*, *38*(6), 570–576. https://doi.org/10.1002/esp.3302

Pinet, P., & Souriau, M. (1988). Continental erosion and large-scale relief. *Tectonics*, *7*(3), 563–582. https://doi.org/10.1029/TC007i003p00563

Plafker, G., Naeser, C. W., Zimmermann, R. A., Lull, J. S., & Hudson, T. (1992). Cenozoic uplift history of the Mount McKinley area in the central Alaska Range based on fission-trace dating. *US Geological Survey Bulletin*, 202–212.

Pocoví, A. (1978). Estudio geológico de las Sierras Marginales Catalanas (Prepirineo de Lérida). *Acta Geológica Hispánica*.

Pollack, H. N., Hurter, S. J., & Johnson, J. R. (1993). Heat flow from the Earth's interior: Analysis of the global data set. *Reviews of Geophysics*, *31*(3), 267–280. https://doi.org/10.1029/93RG01249

Prezzi, C. B., Uba, C. E., & Götze, H. J. (2009). Flexural isostasy in the Bolivian Andes: Chaco foreland basin development. *Tectonophysics*, *474*(3-4), 526–543. https://doi.org/10.1016/j.tecto.2009.04.037

Puigdefàbregas, C., Muñoz, J. A., & Marzo, M. (1986). Thrust Belt Development in the Eastern Pyrenees and Related Depositional Sequences in the Southern Foreland Basin, In *Foreland basins*. https://doi.org/10.1002/9781444303810.ch12

Puigdefàbregas, C., & Souquet, P. (1986). Tecto-sedimentary cycles and depositional sequences of the Mesozoic and Tertiary from the Pyrenees. *Tectonophysics*, *129*(1-4), 173–203. https://doi.org/10.1016/0040-1951(86)90251-9

Rahn, M. K., Brandon, M. T., Batt, G. E., & Garver, J. I. (2004). A zero-damage model for fission-track annealing in zircon. *American Mineralogist*, *89*(4), 473–484. https://doi.org/10.2138/am-2004-0401

Reiners, P. W., & Farley, K. A. (1999). Helium diffusion and (U-Th)/He thermochronometry of titanite. *Geochimica et Cosmochimica Acta*, *63*(22), 3845–3859. https://doi.org/10.1016/S0016-7037(99)00170-2

Reiners, P. W., Farley, K. A., & Hickes, H. J. (2002). He diffusion and (U-Th)/He thermochronometry of zircon: Initial results from Fish Canyon Tuff and Gold Butte. *Tectonophysics*, *349*(1-4), 297–308. https://doi.org/10.1016/S0040-1951(02)00058-6

Roca, E. (1996). The Neogene Cerdanya and Seu d'Urgell intramontane basins (Eastern Pyrenees), In *Tertiary basins of spain*. https://doi.org/10.1017/cbo9780511524851.019

Roe, G. H., Montgomery, D. R., & Hallet, B. (2002). Effects of orographic precipitation variations on the concavity of steady-state river profiles. *Geology*, *30*(2), 143–146. https://doi.org/10.1130/0091-7613(2002)030⟨0143:EOOPVO⟩2.0.CO;2

Roe, G. H., Montgomery, D. R., & Hallet, B. (2003). Orographic precipitation and the relief of mountain ranges. *Journal of Geophysical Research: Solid Earth*, *108*(B6). https://doi.org/10.1029/2001jb001521

Roe, G. H., Stolar, D. B., & Willett, S. D. (2006). Response of a steady-state critical wedge orogen to changes in climate and tectonic forcing. *Special Paper of the Geological Society of America*, *398*, 227. https://doi.org/10.1130/2005.2398(13)

Roest, W. R., & Srivastava, S. P. (1991). Kinematics of the plate boundaries between Eurasia, Iberia, and Africa in the North Atlantic from the Late Cretaceous to the present. *Geology*, *19*(6), 613–616. https://doi.org/10.1130/0091-7613(1991)019⟨0613:KOTPBB⟩2.3.CO;2

Rosenbaum, G., Lister, G. S., & Duboz, C. (2002). Relative motions of Africa, Iberia and Europe during Alpine orogeny. *Tectonophysics*, *359*(1-2), 117–129. https://doi.org/10.1016/S0040-1951(02)00442-0

Rougier, G., Ford, M., Christophoul, F., & Bader, A. G. (2016). Stratigraphic and tectonic studies in the central Aquitaine Basin, northern Pyrenees: Constraints on the subsidence and deformation history of a retro-foreland basin. *Comptes Rendus - Geoscience*, *348*(3-4), 224–235. https://doi.org/10.1016/j.crte.2015.12.005

Roure, F., Choukroune, P., Berastegui, X., Munoz, J. A., Villien, A., Matheron, P., Bareyt, M., Seguret, M., Camara, P., & Deramond, J. (1989). Ecors deep seismic data and balanced cross sections: Geometric constraints on the evolution of the Pyrenees. *Tectonics*, *8*(1), 41–50. https://doi.org/10.1029/TC008i001p00041

Royden, L. H. (1993). The tectonic expression slab pull at continental convergent boundaries. *Tectonics*, *12*(2), 303–325. https://doi.org/10.1029/92TC02248

Royden, L. H., & Karner, G. D. (1984). Flexure of the continental lithosphere beneath Apennine and Carpathian foredeep basins. *Nature*, *309*(5964), 142–144. https://doi.org/10.1038/309142a0

Royden, L. H., & Perron, T. J. (2013). Solutions of the stream power equation and application to the evolution of river longitudinal profiles. *Journal of Geophysical Research: Earth Surface*, *118*(2), 497–518. https://doi.org/10.1002/jgrf.20031

Rutherford, E. (1905). Radio-activity. *University press.*

Savostin, L. A., Sibuet, J. C., Zonenshain, L. P., Le Pichon, X., & Roulet, M. J. (1986). Kinematic evolution of the Tethys belt from the Atlantic ocean to the pamirs

since the Triassic. *Tectonophysics*, *123*(1-4), 1–35. https://doi.org/10.1016/0040-1951(86)90192-7

Scharf, T. E., Codilean, A. T., De Wit, M., Jansen, J. D., & Kubik, P. W. (2013). Strong rocks sustain ancient postorogenic topography in southern Africa. *Geology*, *41*(3), 331–334. https://doi.org/10.1130/G33806.1

Schumm, S. a. (1963). The disparity between present rates of denudation and orogeny. *USGS Professional Paper*.

Searle, M. P., Parrish, R. R., Hodges, K. V., Hurford, A. J., Ayres, M. W., & Whitehouse, M. J. (1997). Shisha Pangma leucogranite, south Tibetan Himalaya: Field relations, geochemistry, age, origin, and emplacement. *Journal of Geology*, *105*(3), 295–318. https://doi.org/10.1086/515924

Seguret, M. (1972). Étude tectonique des nappes et séries décollées de la partie centrale du versant sud des Pyrénées. *Pub. Estela, Ser geol. struct.*, *2*, 1–155.

Serrano, O., Delmas, J., Hanot, F., Vially, R., Herbin, J.-P., Houel, P., & Tourlière, B. (2006). Le bassin d'Aquitaine: valorisation des données sismiques, cartographique structurale et potentiel pétrolier. *BRGM, Orléans*.

Shuster, D. L., & Farley, K. A. (2004). 4He/3He thermochronometry. *Earth and Planetary Science Letters*, *217*(1-2), 1–17. https://doi.org/10.1016/S0012-821X(03)00595-8

Shuster, D. L., & Farley, K. A. (2005). 4He/3He thermochronometry: Theory, practice, and potential complications. *Reviews in Mineralogy and Geochemistry*, *58*(1), 181–203. https://doi.org/10.2138/rmg.2005.58.7

Shuster, D. L., Farley, K. A., Sisterson, J. M., & Burnett, D. S. (2004). Quantifying the diffusion kinetics and spatial distributions of radiogenic 4He in minerals containing proton-induced 3He. *Earth and Planetary Science Letters*, *217*(1-2), 19–32. https://doi.org/10.1016/S0012-821X(03)00594-6

Shuster, D. L., Flowers, R. M., & Farley, K. A. (2006). The influence of natural radiation damage on helium diffusion kinetics in apatite. *Earth and Planetary Science Letters*, *249*(3-4), 148–161. https://doi.org/10.1016/j.epsl.2006.07.028

Sibuet, J. C., Srivastava, S. P., & Spakman, W. (2004). Pyrenean orogeny and plate kinematics. *Journal of Geophysical Research: Solid Earth*, *109*(B8). https://doi.org/10.1029/2003JB002514

Sibuet, J. C., Srivastava, S., & Manatschal, G. (2007). Exhumed mantle-forming transitional crust in the Newfoundland-Iberia rift and associated magnetic anomalies.

Journal of Geophysical Research: Solid Earth, *112*(B6). https://doi.org/10.1029/2005JB003856

Simpson, G. (2006). Influence of erosion and deposition on deformation in fold belts. *Special Paper of the Geological Society of America*, *398*, 267. https://doi.org/10.1130/2006.2398(16)

Sinclair, H. D. (2012). Thrust wedge/foreland basin systems. *Tectonics of Sedimentary Basins: Recent Advances, First Edition*, 522–537.

Sinclair, H. D., & Allen, P. A. (1992). Vertical versus horizontal motions in the Alpine orogenic wedge: Stratigraphic response in the foreland basin. *Basin Research*, *4*(3-4), 215–232. https://doi.org/10.1111/j.1365-2117.1992.tb00046.x

Sinclair, H. D., Coakley, B. J., Allen, P. A., & Watts, A. B. (1991). Simulation of Foreland Basin Stratigraphy using a diffusion model of mountain belt uplift and erosion: An example from the central Alps, Switzerland. *Tectonics*, *10*(3), 599–620. https://doi.org/10.1029/90TC02507

Sinclair, H. D., Gibson, M., Naylor, M., & Morris, R. G. (2005). Asymmetric growth of the Pyrenees revealed through measurement and modeling of orogenic fluxes. *American Journal of Science*, *305*(5), 369–406. https://doi.org/10.2475/ajs.305.5.369

Sinclair, H. D., & Naylor, M. (2012). Foreland basin subsidence driven by topographic growth versus plate subduction. *Bulletin of the Geological Society of America*, *124*(3-4), 368–379. https://doi.org/10.1130/B30383.1

Sklar, L. S., & Dietrich, W. E. (1998). River longitudinal profiles and bedrock incision models: Stream power and the influence of sediment supply, In *Geophysical monograph series*. https://doi.org/10.1029/GM107p0237

Sklar, L. S., & Dietrich, W. E. (2001). Sediment and rock strength controls on river incision into bedrock. *Geology*, *29*(12), 1087–1090. https://doi.org/10.1130/0091-7613(2001)029⟨1087:SARSCO⟩2.0.CO

Sklar, L. S., & Dietrich, W. E. (2004). A mechanistic model for river incision into bedrock by saltating bed load. *Water Resources Research*, *40*(6). https://doi.org/10.1029/2003WR002496

Sobel, E. R., Chen, J., & Heermance, R. V. (2006). Late Oligocene-Early Miocene initiation of shortening in the Southwestern Chinese Tian Shan: Implications

for Neogene shortening rate variations. *Earth and Planetary Science Letters*, *247*(1-2), 70–81. https://doi.org/10.1016/j.epsl.2006.03.048

Souquet, P., Rey, J., Peybernès, B., Bilotte, M., Cosson, J., Cavaillé, A., & Bambier, A. (1977). Carte géol. France (1/50000), feuille LE MAS-D'AZIL (1056). *Orléans: Bureaux de recherches géologiques et minières.*

Souriau, A., Chevrot, S., & Olivera, C. (2008). A new tomographic image of the Pyrenean lithosphere from teleseismic data. *Tectonophysics*, *460*(1-4), 206–214. https://doi.org/10.1016/j.tecto.2008.08.014

Souriau, A., & Granet, M. (1995). A tomographic study of the lithosphere beneath the Pyrenees from local and teleseismic data. *Journal of Geophysical Research*, *100*(B9), 18117–18134. https://doi.org/10.1029/95jb01053

Srivastava, S. P., Roest, W. R., Kovacs, L. C., Oakey, G., Lévesque, S., Verhoef, J., & Macnab, R. (1990). Motion of Iberia since the Late Jurassic: Results from detailed aeromagnetic measurements in the Newfoundland Basin. *Tectonophysics*, *184*(3-4), 229–260. https://doi.org/10.1016/0040-1951(90)90442-B

Srivastava, S. P., Sibuet, J. C., Cande, S., Roest, W. R., & Reid, I. D. (2000). Magnetic evidence for slow seafloor spreading during the formation of the Newfoundland and Iberian margins. *Earth and Planetary Science Letters*, *182*(1), 61–76. https://doi.org/10.1016/S0012-821X(00)00231-4

Stephenson, R. (1984). Flexural models of continental lithosphere based on the long-term erosional decay of topography. *Geophysical Journal of the Royal Astronomical Society*, *77*(2), 385–413. https://doi.org/10.1111/j.1365-246X.1984.tb01940.x

Stewart, J., & Watts, A. B. (1997). Gravity anomalies and spatial variations of flexural rigidity at mountain ranges. *Journal of Geophysical Research: Solid Earth*, *102*(B3), 5327–5352. https://doi.org/10.1029/96jb03664

Stock, J. D., & Montgomery, D. R. (1999). Geologic constraints on bedrock river incision using the stream power law. *Journal of Geophysical Research: Solid Earth*, *104*(B3), 4983–4993. https://doi.org/10.1029/98JB02139

Stockli, D. F., Farley, K. A., & Dumitru, T. A. (2000). Calibration of the apatite (U-Th)/He thermochronometer on anexhumed fault block, White Mountains, California. *Geology*, *28*(11), 983–986. https://doi.org/10.1130/0091-7613(2000)28⟨983:COTAHT⟩2.0.CO;2

Stockmal, G. S., & Beaumont, C. (1987). Geodynamic Models of Convergent Margin Tectonics: The Southern Canadian Cordillera and the Swiss Alps. *Sedimentary Basins and Basin-Forming Mechanisms*.

Stockmal, G. S., Beaumont, C., & Boutilier, R. (1986). GEODYNAMIC MODELS OF CONVERGENT MARGIN TECTONICS: TRANSITION FROM RIFTED MARGIN TO OVERTHRUST BELT AND CONSEQUENCES FOR FORELAND-BASIN DEVELOPMENT. *American Association of Petroleum Geologists Bulletin*. https://doi.org/10.1306/94885656-1704-11D7-8645000102C1865D

Stolar, D. B., Willett, S. D., & Roe, G. H. (2006). Climatic and tectonic forcing of a critical orogen. *Special Paper of the Geological Society of America*. https://doi.org/10.1130/2006.2398(14)

Strecker, M., Alonso, R., Bookhagen, B., Carrapa, B., Hilley, G., Sobel, E., & Trauth, M. (2007). Tectonics and Climate of the Southern Central Andes. *Annual Review of Earth and Planetary Sciences*. https://doi.org/10.1146/annurev.earth.35.031306.140158

Strutt, R. J. (1905). On the Radio-Active Minerals. *Proceedings of the Royal Society A: Mathematical, Physical and Engineering Sciences*. https://doi.org/10.1098/rspa.1905.0006

Suppe, J. (1981). Mechanics of mountain building and metamorphism in Taiwan.

Tagami, T., Galbraith, R. F., Yamada, R., & Laslett, G. M. (1998). Revised Annealing Kinetics of Fission Tracks in Zircon and Geological Implications, In *Advances in fission-track geochronology*. https://doi.org/10.1007/978-94-015-9133-1{_}8

Tagami, T., Ito, H., & Nishimura, S. (1990). Thermal annealing characteristics of spontaneous fission tracks in zircon. *Chemical Geology: Isotope Geoscience Section*. https://doi.org/10.1016/0168-9622(90)90024-7

Tagami, T., & O'Sullivan, P. B. (2005). Fundamentals of fission-track thermochronology. *Reviews in Mineralogy and Geochemistry*, *58*(1), 19–47. https://doi.org/10.2138/rmg.2005.58.2

Taillefer, F. (1967). Extent of Pleistocene glaciation in the Pyrenees. *Indiana University Press*.

Taillefer, F. (1969). Les glaciations des Pyrénées. *Études Francaises sur le Quaternaire. VIII Congrés INQUA*, 19–32.

Taillefer, F. (1957). Glaciaire pyrénéen : versant nord et versant sud. *Revue géographique des Pyrénées et du Sud-Ouest*. https://doi.org/10.3406/rgpso.1957.1459

Ternet, Y., Crouzel, F., Mirabail, H., Rey, E., Bouvier, A., Mediavilla, F., & Gatinot, F. (1988). Carte géol. France (1/50000), feuille BAGNÈRES-DE-BIGORRE. *Orléans: Bureaux de recherches géologiques et minières*.

Thiede, R. C., Bookhagen, B., Arrowsmith, J. R., Sobel, E. R., & Strecker, M. R. (2004). Climatic control on rapid exhumation along the Southern Himalayan Front. *Earth and Planetary Science Letters*, *222*(3-4), 791–806. https://doi.org/10.1016/j.epsl.2004.03.015

Torné, M., De Cabissole, B., Bayer, R., Casas, A., Daignières, M., & Rivero, A. (1989). Gravity constraints on the deep structure of the Pyrenean belt along the ECORS profile. *Tectonophysics*, *165*(1-4), 105–116. https://doi.org/10.1016/0040-1951(89)90039-5

Tucker, G. E., & van der Beek, P. (2013). A model for post-orogenic development of a mountain range and its foreland. *Basin Research*, *25*(3), 241–259. https://doi.org/10.1111/j.1365-2117.2012.00559.x

Tucker, G. E., & Whipple, K. X. (2002). Topographic outcomes predicted by stream erosion models: Sensitivity analysis and intermodel comparison. *Journal of Geophysical Research: Solid Earth*, *107*(B9). https://doi.org/10.1029/2001jb000162

Vacher, P., & Souriau, A. (2001). A three-dimensional model of the Pyrenen deep structure based on gravity modelling, seismic images and petrological constrainst. *Geophysical Journal International*, *145*(2), 460–470. https://doi.org/10.1046/j.0956-540X.2001.01393.x

Vacherat, A., Mouthereau, F., Pik, R., Bellahsen, N., Gautheron, C., Bernet, M., Daudet, M., Balansa, J., Tibari, B., Pinna Jamme, R., & Radal, J. (2016). Rift-to-collision transition recorded by tectonothermal evolution of the northern Pyrenees. *Tectonics*, *35*(4), 907–933. https://doi.org/10.1002/2015TC004016

Valla, P. G., Shuster, D. L., & Van Der Beek, P. A. (2011). Significant increase in relief of the European Alps during mid-Pleistocene glaciations. *Nature Geoscience*, *4*(10), 688–692. https://doi.org/10.1038/ngeo1242

Valla, P. G., Van Der Beek, P. A., Shuster, D. L., Braun, J., Herman, F., Tassan-Got, L., & Gautheron, C. (2012). Late Neogene exhumation and relief development of the Aar and Aiguilles Rouges massifs (Swiss Alps) from low-temperature ther-

mochronology modeling and 4He/3He thermochronometry. *Journal of Geophysical Research: Earth Surface*, *117*(F1). https://doi.org/10.1029/2011JF002043

Vergés, J., Millán, H., Roca, E., Muñoz, J. A., Marzo, M., Cirés, J., Bezemer, T. D., Zoetemeijer, R., & Cloetingh, S. (1995). Eastern Pyrenees and related foreland basins: pre-, syn- and post-collisional crustal-scale cross-sections. *Marine and Petroleum Geology*, *12*(8), 903–915. https://doi.org/10.1016/0264-8172(95)98854-X

Verges, J., & Munoz, J. A. (1990). Thrust sequences in the southern central Pyrenees. *Bulletin de la Société Géologique de France*, *6*(2), 265–271. https://doi.org/10.2113/gssgfbull.VI.2.265

Vergés, J., Fernàndez, M., & Martìnez, A. (2002). The Pyrenean orogen: Pre-, syn-, and post-collisional evolution. *Journal of the Virtual Explorer*, *8*, 55–74. https://doi.org/10.3809/jvirtex.2002.00058

Vergés, J., Marzo, M., Santaeularia, T., Serra-Kiel, J., Burbank, D. W., Muñoz, J. A., & Gimenez-Montsant, J. (1998). Quantified vertical motions and tectonic evolution of the SE Pyrenean foreland basin. *Geological Society, London, Special Publications*, *134*(1), 107–134. https://doi.org/10.1144/GSL.SP.1998.134.01.06

Vielzeuf, D., & Kornprobst, J. (1984). "Crustal splitting and the emplacement of Pyrenean lherzolites and granulites"-A reply to M.W. Fischer. *Earth and Planetary Science Letters*, *70*(2), 439–443. https://doi.org/10.1016/0012-821X(84)90028-1

Vincent, S. J. (2001). The Sis palaeovalley: A record of proximal fluvial sedimentation and drainage basin development in response to Pyrenean mountain building. *Sedimentology*, *48*(6), 1235–1276. https://doi.org/10.1046/j.1365-3091.2001.00421.x

Vissers, R. L., & Meijer, P. T. (2012). Iberian plate kinematics and Alpine collision in the Pyrenees. *Earth-Science Reviews*, *114*(1-2), 61–83. https://doi.org/10.1016/j.earscirev.2012.05.001

Wagner, G. A. (1988). Apatite fission-track geochrono-thermometer to 60°C: Projected length studies. *Chemical Geology: Isotope Geoscience Section*, *72*(2), 145–153. https://doi.org/10.1016/0168-9622(88)90062-0

Wagner, G. A., & Hejl, E. (1991). Apatite fission-track age-spectrum based on projected track-length analysis. *Chemical Geology: Isotope Geoscience Section*, *87*(1), 1–9. https://doi.org/10.1016/0168-9622(91)90029-V

Wagner, G. A., & Reimer, G. M. (1972). Fission track tectonics: The tectonic interpretation of fission track apatite ages. *Earth and Planetary Science Letters*, *14*(2), 263–268. https://doi.org/10.1016/0012-821X(72)90018-0

Wagner, M., Altherr, R., & Van Den Haute, P. (1992). Apatite fission-track analysis of Kenyan basement rocks: constraints on the thermotectonic evolution of the Kenya dome. A reconnaissance study. *Tectonophysics*, *204*(1-2), 93–110. https://doi.org/10.1016/0040-1951(92)90272-8

Wang, Y., Chevrot, S., Monteiller, V., Komatitsch, D., Mouthereau, F., Manatschal, G., Sylvander, M., Diaz, J., Ruiz, M., Grimaud, F., Benahmed, S., Pauchet, H., & Martin, R. (2016). The deep roots of the western Pyrenees revealed by full waveform inversion of teleseismic P waves. *Geology*, *44*(6), 475–478. https://doi.org/10.1130/G37812.1

Warnock, A. C., Zeitler, P. K., Wolf, R. A., & Bergman, S. C. (1997). An evaluation of low-temperature apatite U-Th/He thermochronometry. *Geochimica et Cosmochimica Acta*, *61*(24), 5371–5377. https://doi.org/10.1016/S0016-7037(97)00302-5

Watts, A. B. (2001). *Isostasy and Flexure of the Lithosphere*.

Wendt, A. S., Vidal, O., & Chadderton, L. T. (2002). Experimental evidence for the pressure dependence of fission track annealing in apatite. *Earth and Planetary Science Letters*, *201*(3-4), 593–607. https://doi.org/10.1016/S0012-821X(02)00727-6

Whipple, K. X. (2002). Implications of sediment-flux-dependent river incision models for landscape evolution. *Journal of Geophysical Research*, *107*(B2). https://doi.org/10.1029/2000jb000044

Whipple, K. X., Forte, A. M., DiBiase, R. A., Gasparini, N. M., & Ouimet, W. B. (2017). Timescales of landscape response to divide migration and drainage capture: Implications for the role of divide mobility in landscape evolution. *Journal of Geophysical Research: Earth Surface*, *122*(1), 248–273. https://doi.org/10.1002/2016JF003973

Whipple, K. X., Hancock, G. S., & Anderson, R. S. (2000). River incision into bedrock: Mechanics and relative efficacy of plucking, abrasion, and cavitation. *Bulletin of the Geological Society of America*, *112*(3), 490–503. https://doi.org/10.1130/0016-7606(2000)112⟨490:RIIBMA⟩2.0.CO;2

Whipple, K. X., & Meade, B. J. (2004). Controls on the strength of coupling among climate, erosion, and deformation in two-sided, frictional orogenic wedges at steady state. *Journal of Geophysical Research: Earth Surface*, *109*(F1). https://doi.org/10.1029/2003jf000019

Whipple, K. X., & Tucker, G. E. (1999). Dynamics of the stream-power river incision model: Implications for height limits of mountain ranges, landscape response timescales, and research needs. *Journal of Geophysical Research: Solid Earth*, *104*(B8), 17661–17674. https://doi.org/10.1029/1999jb900120

Whitchurch, A. L., Carter, A., Sinclair, H. D., Duller, R. A., Whittaker, A. C., & Allen, P. A. (2011). Sediment routing system evolution within a diachronously uplifting orogen: Insights from detrital zircon thermochronological analyses from the South-Central pyrenees. *American Journal of Science*, *311*(5), 442–482. https://doi.org/10.2475/05.2011.03

Willett, S. D. (1992). Dynamic and kinematic growth and change of a Coulomb wedge, In *Thrust tectonics*. https://doi.org/10.1007/978-94-011-3066-0{_}2

Willett, S. D. (1999). Orogeny and orography: The effects of erosion on the structure of mountain belts. *Journal of Geophysical Research: Solid Earth*, *104*(B12), 28957–28981. https://doi.org/10.1029/1999JB900248

Willett, S. D., Beaumont, C., & Fullsack, P. (1993). Mechanical model for the tectonics of doubly vergent compressional orogens. *Geology*, *21*(4), 371–374. https://doi.org/10.1130/0091-7613(1993)021⟨0371:MMFTTO⟩2.3.CO;2

Willett, S. D., & Brandon, M. T. (2002). On steady states in mountain belts. *Geology*, *30*(2), 175–178. https://doi.org/10.1130/0091-7613(2002)030⟨0175:OSSIMB⟩2.0.CO;2

Willett, S. D., McCoy, S. W., Taylor Perron, J., Goren, L., & Chen, C. Y. (2014). Dynamic reorganization of River Basins. *Science*, *343*(6175). https://doi.org/10.1126/science.1248765

Willett, S. D., Schlunegger, F., & Picotti, V. (2006). Messinian climate change and erosional destruction of the central European Alps. *Geology*, *34*(8), 613–616. https://doi.org/10.1130/G22280.1

Willett, S. D., Slingerland, R., & Hovius, N. (2001). Uplift, shortening, and steady state topography in active mountain belts. *American Journal of Science*, *301*(4-5), 455–485. https://doi.org/10.2475/ajs.301.4-5.455

Wobus, C., Whipple, K. X., Kirby, E., Snyder, N., Johnson, J., Spyropolou, K., Crosby, B., & Sheehan, D. (2006). Tectonics from topography: Procedures, promise, and pitfalls. *Special Paper 398: Tectonics, Climate, and Landscape Evolution*, *398*(55). https://doi.org/10.1130/2006.2398(04)

Wolf, R. A., Farley, K. A., & Kass, D. M. (1998). Modeling of the temperature sensitivity of the apatite (U-Th)/He thermochronometer. *Chemical Geology*, *148*(1-2), 105–114. https://doi.org/10.1016/S0009-2541(98)00024-2

Wolf, R. A., Farley, K. A., & Silver, L. T. (1996). Helium diffusion and low-temperature thermochronometry of apatite. *Geochimica et Cosmochimica Acta*, *60*(21), 4231–420. https://doi.org/10.1016/S0016-7037(96)00192-5

Xie, X., & Heller, P. L. (2009). Plate tectonics and basin subsidence history. *Bulletin of the Geological Society of America*, *121*(1-2), 55–64. https://doi.org/10.1130/B26398.1

Yamada, K., Tagami, T., & Shimobayashi, N. (2003). Experimental study on hydrothermal annealing of fission tracks in zircon. *Chemical Geology*, *201*(3-4), 351–357. https://doi.org/10.1016/j.chemgeo.2003.08.009

Yamada, R., Murakami, M., & Tagami, T. (2007). Statistical modelling of annealing kinetics of fission tracks in zircon; Reassessment of laboratory experiments. *Chemical Geology*, *236*(1-2), 75–91. https://doi.org/10.1016/j.chemgeo.2006.09.002

Yamada, R., Tagami, T., Nishimura, S., & Ito, H. (1995). Annealing kinetics of fission tracks in zircon: an experimental study. *Chemical Geology*, *122*(1-4), 249–258. https://doi.org/10.1016/0009-2541(95)00006-8

Yamada, R., Yoshioka, T., Watanabe, K., Tagami, T., Nakamura, H., Hashimoto, T., & Nishimura, S. (1998). Comparison of experimental techniques to increase the number of measurable confined fission tracks in zircon. *Chemical geology*, *149*(1-2), 99–107.

Yelland, A. J. (1990). Fission track thermotectonics in the Pyrenean orogen. *International Journal of Radiation Applications and Instrumentation. Part*, *17*(3), 293–299. https://doi.org/10.1016/1359-0189(90)90049-4

Young, E. J., Myers, A. T., Munson, E. L., & Conklin, N. M. (1969). Mineralogy and geochemistry of fluoapatite from Cerro de Mercado, Durango, Mexico. *Geological Survey Research 1969 - Professional Paper 650*.

Yuan, X. P., Braun, J., Guerit, L., Rouby, D., & Cordonnier, G. (2019). A New Efficient Method to Solve the Stream Power Law Model Taking Into Account Sediment Deposition. *Journal of Geophysical Research: Earth Surface*, *124*(6), 1346–1365. https://doi.org/10.1029/2018JF004867

Yuan, X. P., Braun, J., Guerit, L., Simon, B., Bovy, B., Rouby, D., Robin, C., & Jiao, R. (2019). Linking continental erosion to marine sediment transport and deposition: A new implicit and O(N) method for inverse analysis. *Earth and Planetary Science Letters*, *524*. https://doi.org/10.1016/j.epsl.2019.115728

Zaprowski, B. J., Pazzaglia, F. J., & Evenson, E. B. (2005). Climatic influences on profile concavity and river incision. *Journal of Geophysical Research: Earth Surface*, *100*(F3). https://doi.org/10.1029/2004JF000138

Zeitler, P. K., Herczeg, A. L., McDougall, I., & Honda, M. (1987). U-Th-He dating of apatite: A potential thermochronometer. *Geochimica et Cosmochimica Acta*, *51*(10), 2865–2868. https://doi.org/10.1016/0016-7037(87)90164-5

Zeitler, P. K. (1985). Cooling history of the NW Himalaya, Pakistan. *Tectonics*, *4*(1), 127–151. https://doi.org/10.1029/TC004i001p00127

Zeitler, P. K., Johnson, N. M., Naeser, C. W., & Tahirkheli, R. A. (1982). Fission-track evidence for Quaternary uplift of the Nanga Parbat region, Pakistan. *Nature*, *298*(5871), 255–257. https://doi.org/10.1038/298255a0

Ziegler, J. F. (1977). *Stopping cross-sections for energetic ions in all elements*.

Zielinski, G. A. (2000). Use of paleo-records in determining variability within the volcanism-climate system. *Quaternary Science Reviews*, *19*(1-5), 417–438. https://doi.org/10.1016/s0277-3791(99)00073-6

Zoetemeijer, R., Desegaulx, P., Cloetingh, S., Roure, F., & Moretti, I. (1990). Lithospheric dynamics and tectonic-stratigraphic evolution of the Ebro Basin. *Journal of Geophysical Research*, *95*(B3), 2701–2711. https://doi.org/10.1029/JB095iB03p02701

Zondervan, J. R., Stokes, M., Boulton, S. J., Telfer, M. W., & Mather, A. E. (2020). Rock strength and structural controls on fluvial erodibility: Implications for drainage divide mobility in a collisional mountain belt. *Earth and Planetary Science Letters*, *538*. https://doi.org/10.1016/j.epsl.2020.116221

Zwart, H. J. (1986). The variscan geology of the Pyrenees. *Tectonophysics*, *129*(1-4), 9–27. https://doi.org/10.1016/0040-1951(86)90243-X